Novel Properties of Graphene and Other 2D Materials with Potential Applications in Energy Devices and Related Areas

A Thesis
Submitted for the Degree of
Doctor of Philosophy

by
Gopalakrishnan K

Chemistry and Physics of Materials Unit
Jawaharlal Nehru Centre for Advanced Scientific Research, Bangalore-560064, India
December 2016

Dedicated to my *Guru*

Prof. C. N. R. Rao

DECLARATION

I hereby declare that the matter embodied in the thesis entitled "**Novel properties of graphene and other 2D materials with potential applications in energy devices and related areas**" is the result of investigations carried out by me at Chemistry and Physics of Materials Unit, Jawaharlal Nehru Centre for Advanced Scientific Research, Bangalore, India under the supervision of Prof. C. N. R. Rao, FRS and it has not been submitted elsewhere for the award of any degree or diploma.

In keeping with the general practice in reporting scientific observations, due acknowledgement has been made whenever the work described is based on the findings of other investigators.

_____

Gopalakrishnan K

CERTIFICATE

I hereby declare that the matter embodied in this thesis entitled "**Novel properties of graphene and other 2D materials with potential applications in energy devices and related areas**" has been carried out by Mr. Gopalakrishnan K at Chemistry and Physics of Materials Unit, Jawaharlal Nehru Centre for Advanced Scientific Research, Bangalore, India under my supervision and it has not been submitted elsewhere for the award of any degree or diploma.

_____

Prof. C. N. R. Rao

(Research Supervisor)

PREFACE

The thesis consists of four parts. Part 1 describes the supercapacitor performances of graphene, borocarbonitrides and other 2D materials. In this Part, Section 1.1 provides a brief overview of 2D layered materials and their performance in supercapacitor applications. Supercapacitor performance of nitrogen-doped graphene and borocarbonitrides are discussed in Sections 1.2 and 1.3. Supercapacitor characteristics of heavily-nitrogen doped graphene prepared by microwave method in Section 1.4 is noteworthy for possible application. Section 1.4 discusses the supercapacitor performance of composites of polyaniline with N-RGO, borocarbonitrides, MoS_2 and WS_2. Supercapacitor performance of MoS_2-RGO nanocomposites is discussed in Section 1.5, while Section 1.6 describe the performance of covalently linked BN-graphene composites in supercapacitor applications.

Oxygen reduction reaction catalysts based on graphene, borocarbonitrides and other 2D materials are discussed in Part 2. Section 2.1 gives a brief overview of fuel cells and the catalytic activity of 2D layered materials in the oxygen reduction reaction. Section 2.2 discuss the electrocatalytic of heavily nitrogen-doped graphene in the oxygen reduction reaction. Section 2.3 deals with the oxygen reduction reaction activity of BN-graphene composites.

Part 3 discusses the physico-chemical properties of nitrogen- and boron-doped graphene, where Section 3.1 describes the photocatalytic activity of its composites with TiO_2. Section 3.3 presents the interaction of N and B-doped graphene with electron donor and acceptor molecules.

Part 4 reports reversible chemical storage of halogens in few-layer graphene.

ACKNOWLEDGEMENTS

I am extremely thankful to Prof. C. N. R. Rao, FRS for giving me this opportunity to work under his guidance. I hereby take this opportunity to express my immense gratitude to him. The position where I stand now is because of him. He has taught me various facts of materials science and always helped me in understanding the problems and how tactfully handle them in times of hardship. I thank him once again for the constant inspiration in my scientific and research life.

I would like to thank Dr. A. Govindaraj, Dr. A. Gomathi, Dr. K. S. Subrahmanyam and Dr. L. S. Panchakarla for helping me in various experiments and for the scientific discussions.

I would like to thank JNCASR for funding and providing me all the facilities. I also thank ICMS, RAK-CAM and SSL for the Sheikh Saqr Fellowship.

I am thankful to the present and past chairmen of CPMU, Prof. N. Chandrabhas Prof. S. Balasubramanian and Prof. G.U. Kulkarni for allowing me to use various facilities.

I would like to thank, Prof. G.U. Kulkarni, Prof. K. S. Narayan, Prof. N. Chandrabhas Prof. S. Balasubramanian, Prof. A. Sundaresan, Prof. S. M. Shivaprasad, Prof. M. Eswaramoorthy, Dr. T. Govindaraju and Dr. Ranjan Datta for their valuable suggestions.

I would like to thank Dr. K. Moses, Dr. U. Maitra, Mr. K. Pramoda, Mr. Ram Kumar and Mr. Sreedhara, Dr. Prashant Kumar, Dr. H. Joshi, Dr. S. Sultan, Ms. Mahima, Ms. Chaitra for the collaborative work and various discussions.

I thank the office staff of CPMU. I also thank the office staff of CSIR-COE, Mrs. Sashi, Mrs. Sudha, Mr. H. Gowda and Mr. Victor for their help.

My sincere thanks to all the technical staff of CPMU and NCU, specially Mrs. Usha, Mrs. Selvi, Dr. Basawaraja, Mr. Vasu, Mr. Srinath, Mr. Mahesh, Mr. Sivakumar and Mr. Anil for their help in various characterization techniques. I am thankful to Mr. Somnath for the four-probe measurements.

A special thanks to Dr. A. Sundar Rajan for helping me in electrochemical measurements.

I am thankful the computer lab staff for their help.

I would like to thank JNC academic staff Dr. Princy, Mrs. Sukanya and Mr. Bannaiah for their help in various academic help. I also thank the admin staff of JNC specially Mr. Jayachandra, Mr. Sarma, Mr. Venkatesalu, Mrs. Sunitha for the help. I also thank Prof. Bhat for adding me in various POCE activities.

I am extremely thankful to all my past and present labmates, Dr. Gomathi, Dr. Subrahmanyam, Dr. Leela, Dr. Neenu, Dr. Sashi, Dr. Urmimala, Dr. Nitesh, Dr. Moses, Pramoda, Sunita Dey, Ram Kumar, Rana Saha, Lingampalli, Sreedhara, Manjeet, Uttam, Anand Roy, Manoj, Dr. Deepa, Dr. Manjunath, Dr. Pratap, Manjunath, Dr. Manish, Manaswee and Monis.

My deepest thanks to Mrs. Indumati Rao and Mr. Sanjay Rao for their love, affection and hospitality extended to all of us during the course of my association with them.

My special thanks to my school Chemistry teacher Mrs. G. L. Vidhya Barathi for helping in me various ways.

I would like to thank my friends Dr. N. Prakash and Dr. Nikhil Gupta for helping me in various ways.

I would like to thank Sweta, Kiruthika, Vijay, Suresh and Ram for their treats and for being with me for such a long time.

I also thank Raagesh, Rajaji, Dr. Suresh Perumal, Dr. Sridevi, Manoj, Shashi, Susheela, Swati, for their kind gestures and for having their lunch with me. I also thank Vijay, Lakshmeesha, Arpit, Amrutha and Asutosh for their friendship and for playing table tennis with me.

I thank my Telecom Layout friends, Mr. Ananda Raman, Mr. Boopathi, Mr. Hari, Mr. Karthi, Sankar, Veera, Devaraj, Vijay Mohan, Mohammed and their families for their kind gestures, love, friendship and for playing badminton with me.

I also thank Dhanvantri doctors, Dr. Archana, Dr. Kavitha,Dr. Subbarao, Dr. Chandralekha, Dr. Nagabhushan, Mrs. Uma and Ms. Thara for taking care of me. Thanks a lot.

I thank the hostel wardens, staff, mess workers and Mr. Harish for making the stay pleasant. I also thank the DG room staffs.

I would like to thank JNC security staff members, specially Mr. Michael for his love and good wishes.

I would like thank Mr. Jairamaiah, Gardener for making the campus beautiful.

I like to thank Google, Wiki, YouTube for the knowledge they shared with me.

Last but not least, I would like to thank my Uncle-Aunt, my parents, my grandmother, my sisters, brothers and brother-in-law for their love, affection and the support they gave.

CONTENTS

PART 3 PHYSICO-CHEMICAL STUDIES BASED ON CHEMICALLY DOPED GRAPHENES

3.1 Selectivity in the photocatalytic properties of the composites of TiO_2 nanoparticles with b- and n-doped graphenes

3.2 A Raman study of the interaction of electron-donor and -acceptor molecules with chemically doped graphene

PART 1

SUPERCAPACITORS BASED ON GRAPHENE, BOROCARBONITRIDES AND OTHER 2D MATERIALS

"After a brief introduction to 2D materials and supercapacitors, results obtained from a detailed study of supercapacitor performance of graphene, borocarbonitrides and other 2D materials are described in this part of thesis. Of the various materials studied, heavily nitrogen-doped graphene oxide shows the best supercapacitor performance. We have been able to make a device using this material."

PART 1

SUPERCAPACITORS BASED ON GRAPHENE, BOROCARBONITRIDES AND OTHER 2D MATERIALS

1.1 Brief overview

1.1.1 Introduction

Energy storage devices are prevalent in our everyday lives, from powering laptops to mobile phones and to serve as backup energy supplies in numerous electronic applications [1]. The emerging electronic markets and technologies will continue to increase the importance of lightweight, affordable and long-life energy storage devices. Batteries and capacitors are widely used devices in energy storage applications. Traditional capacitors store energy through electrostatic charging at their electrode-electrolyte interfaces under an applied potential, whereas batteries store energy through electrochemical reactions that typically occur throughout the entire bulk of the electrode active material [2]. This is the reason why batteries store more energy than capacitors. The power/energy densities of the devices are captured in the Ragone plot shown Figure 1. Energy density is a measure of energy stored in a given size or mass. A device with higher energy density can power a load longer than a low energy density device for the same physical size or mass and its unit is Wh/kg. Power density measures how quickly the device can deliver energy. In other words, it is equivalent to the maximum current one can draw from a device of a given size and its unit is W/kg [2].

Although capacitors are not viable for large-scale or high-energy storage, they have found commercial use in applications that need fast, pulsed power (car acceleration, tramways, cranes, forklifts, emergency systems etc.,) and levelling of current fluctuations in control electronics [3]. Capacitors have certain advantages over batteries in low-energy applications because they are cost-effective, can be charged significantly faster and have longer lifetimes. The latter two features are result of the absence of electrochemical reactions in appropriately designed capacitors [2].

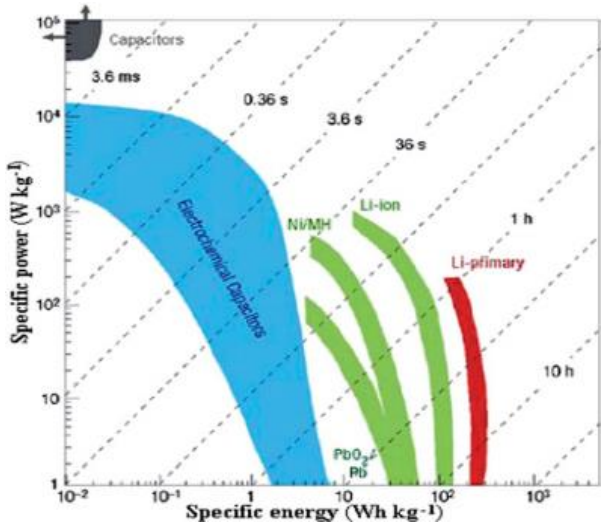

Figure 1. Ragone plots for an array of energy storage and energy conversion devices [4].

1.1.2 Electrochemical supercapacitors

Electrochemical supercapacitors are passive, static electrical energy storage devices which store a high amount of energy compared to conventional capacitors but less than that of batteries. They are similar to conventional capacitors except that metal electrodes are replaced by a highly porous electrode [5]. A supercapacitor comprises two nonreactive electrodes immersed in an electrolyte and ion-conducting porous membrane acts as separator. A potential difference is created at the electrode-electrolyte interface upon the application of a voltage potential across the electrodes. On the basis of energy storage mechanism, supercapacitors can be classified into two types [6]. One is the electrical double layer capacitor (EDLC) where the charge storage mechanism is non-Faradaic; this means that during charging and discharging no charge transfer occurs across the electrode-electrolyte interface and energy storage is completely electrostatic. The second type is the pseudocapacitor, with fast and reversible charge-transfer reactions between electrode surface and electrolyte ions. These processes are Faradaic. The above two mechanisms can function simultaneously depending on the nature of electrode material.

1.1.2.1 Electrical double-layer capacitors

Unlike a ceramic capacitor, the electrical double layer capacitor contains no conventional dielectric. Instead, an electrolyte (solid or liquid) is filled between two electrodes with a

non-conducting separator membrane. Charge separation occurs on polarization at the electrode/electrolyte interface, producing Helmholtz [2] double-layer capacitance, C according to: $C = \varepsilon_r \varepsilon_0 A/d$, where ε_r is the relative dielectric constant of the electrolyte, ε_0 the dielectric constant of vacuum, d the effective thickness of the double layer (charge separation distance) and A is the surface area of the interface. Positive and negative ions in electrolyte accumulate at the surface of solid electrode and compensate for electronic charge at electrode surface (Figure 2). The thickness of the double layer depends on concentration of electrolyte and on size of ions and is therefore strongly dependent on surface area of the electrode material. Therefore, using material which has large surface area for electrodes, enables EDLC to have high capacitance. Porous carbon materials ranging from activated carbon to the recently discovered graphene have been investigated as supercapacitor electrodes. These carbon materials are used as supercapacitor electrodes because of their low cost and versatile existing forms such as powders, fibres, composites, mats and foils [7].

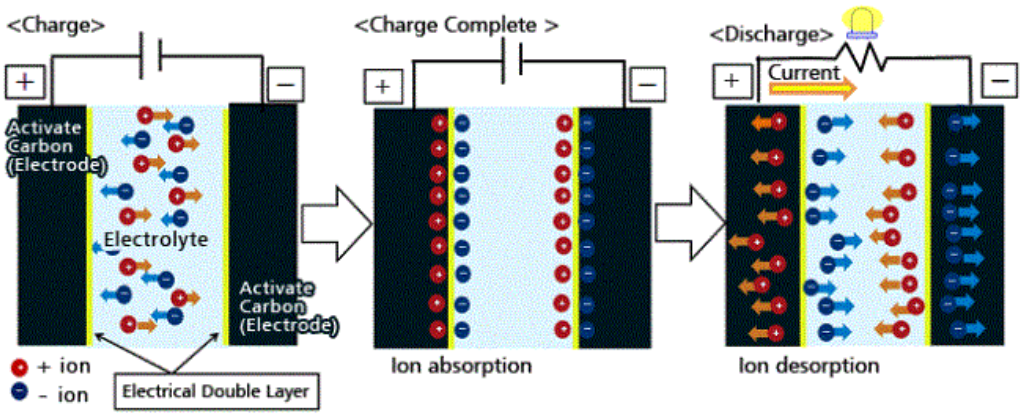

Figure 2. Charging and discharging of a electrical double layer capacitor

1.1.2.1.1 Carbon based supercapacitors

Activated Carbons: The most common materials used in commercial supercapacitors are activated carbons (ACs). ACs are generally produced from physical or chemical activation of different carbonaceous materials such as wood, coal etc [7]. In physical activation, carbon precursors are treated in the presence of steam, CO_2 and air at high temperatures ranging from 700 to 1200 ^{o}C. Chemical activation is generally carried out

at lower temperatures (from 400 to 700 ^{o}C) with activating agents like phosphoric acid, potassium hydroxide and sodium hydroxide [8]. The activated carbons contain a distribution of pore sizes. Brunauer, Emmett and Teller (BET) surface areas of activated carbons are in the 1000-3000 m^2/g range. Irrespective of the high surface area, activated carbons show relatively low specific capacitance >10 mF/cm^2 (80–110 F/g in organic electrolytes and 100–160 F/g in aqueous electrolytes), which is considerably lower than the theoretical EDL capacitance (15-25 mF/cm^2) [6]. This indicates that not all pores are effective in charge accumulation. Since a substantial fraction of the surface area resides in unpercolated pores which are inaccessible to ion migration and are unable to support an electrical double layer as shown in Figure 3. Ions can migrate to some of the larger pores, and this result in an increased resistance of the electrolyte, causing a decrease in capacitance. The main reason for the low electrolyte accessibility is due to the mismatch of the ion size of an electrolyte and pore size of the electrode material [9]. In order to solve this problem, the pore size of the electrode must be suitable for the ion size of the electrolyte, so that the ions are fully utilized to form the double layer and contribute to energy storage.

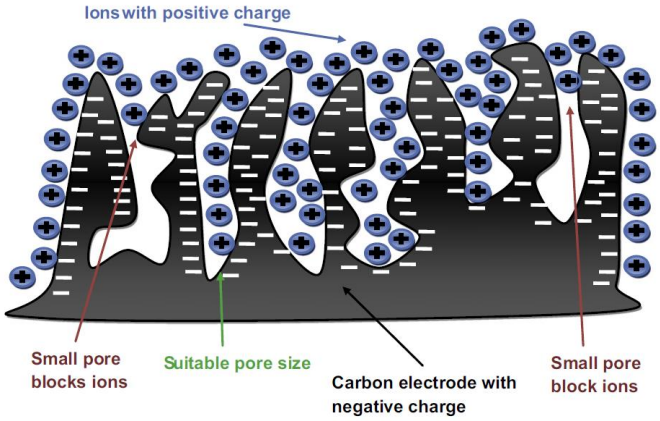

Figure 3. Schematic of the ion size and pore size effect on nanoporous carbon electrode [9].

Carbon nanotubes: Carbon nanotubes (CNTs) possess many remarkable properties, such as high specific surface area, high aspect ratio, remarkable electrical and thermal conductivity, chemical stability and low mass [10]. In 1997, Niu et al. [11] suggested that CNTs could be used in supercapacitors. Multi-walled carbon nanotubes (MWCNTs), treated with nitric acid to create functional groups on the surface, have a specific area of

430 m^2/g, a gravimetric capacitance of 102 F/g and an energy density of 0.5 Wh/kg in 38 % sulfuric acid electrolyte. Beguin et al. [12] studied the role of structure and diameter of CNTs, micro-texture and elemental composition of the materials on the capacitance. The capacitance increased with increase in the specific surface area. The mesopores in the central canal or the entanglement are found to be responsible for the easy accessibility of the ions to the electrode/electrolyte interface for charging the electrical double layer as shown in Figure 4 (a & b). The specific capacitance varies from 40 to 135 F/g depending upon the type of nanotubes and the post-treatment. Even with a moderate specific surface area of ~470 m^2/g, the MWCNTs are attractive supercapacitor material as compared to the best activated carbons due to the accessibility of the mesopores. The specific surface area and capacitance performance of CNTs are lower than those of activated carbon electrodes (specific surface area up to 3000 m^2/g) or mesoporous carbons (up to 1730 $m^2\ g^{-1}$) [13, 14] . There are several reports on the surface modification of carbon nanotubes for improvising the supercapacitor performance [7].

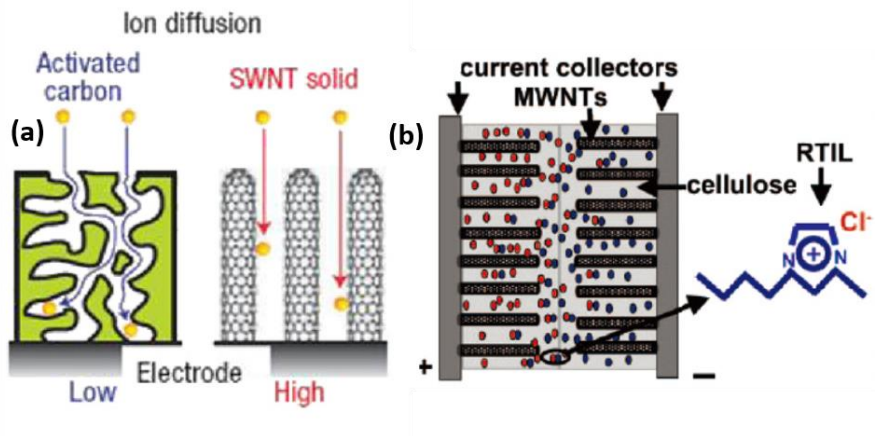

Figure 4. (a) Ion diffusion in activated carbon and oriented CNTs (b) Fabrication of nanocomposite electrochemical capacitor with additive Room-temperature ionic liquid (RTIL) electrolytes [12].

Graphene: Graphene, the one-atom-thick 2D single layer sp^2-bonded carbon, has been considered as the parent of all graphitic forms (Figure 5) [15, 16]. It is distinctly different from carbon nanotubes (CNTs), fullerenes, activated carbons and exhibits unique properties [15]. It has a large theoretical specific surface area (2630 m^2/g), high intrinsic

mobility (200 000 $cm^2/v.s$), high Young's modulus (~1.0 TPa), thermal conductivity (~5000 W/m.K) and optical transmittance (~97.7%) and good electrical conductivity [17]. The electronic properties of graphene are dependent on arrangement and number of graphene layers. Bi-layer and few-layer graphenes contain 2 or 3-10 layers of two-dimensional sheets, respectively [17]. Graphene structures consisting of more than 10 layers are considered as to be like graphite and are of less scientific interest. Few-layer graphenes also possess electronic structures different from bulk graphite.

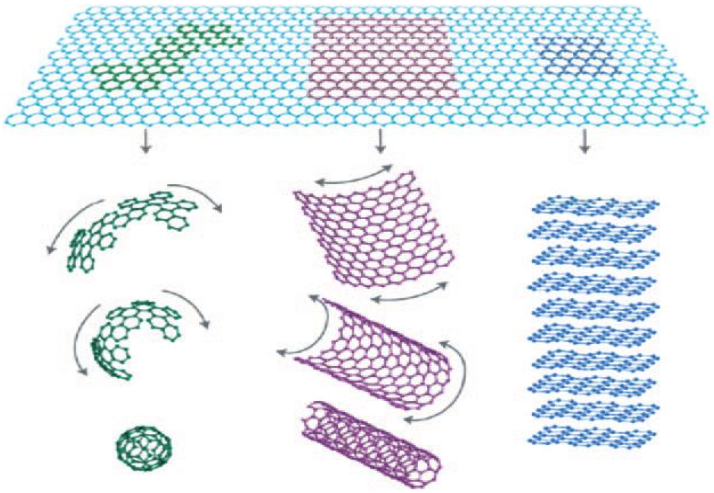

Figure 5. Graphene: the parent of all graphitic forms [18]

Several methods are available for the synthesis of graphene [19-21]. Graphene has been synthesized in various ways on different substrates [15]. Graphene was first exfoliated mechanically from graphite in 2004 by Geim et al. [16]. Besides mechanical cleavage of graphite, the other important methods employed to produce graphene samples are epitaxial growth on an insulator surface (such as SiC), chemical vapour deposition (CVD) on the surfaces of single crystals of metals [15]. These methods allow studying the properties of single-layer or bi-layer graphene. The methods are not suitable for large scale synthesis of single-layer or few-layer graphenes. One can synthesize graphene on a large-scale synthesis by two different ways: (i) exfoliation of graphite and (ii) exfoliation of graphite oxide followed by reduction. The latter method gives sheets of reduced graphite oxide (RGO), some of which could be single-layer.

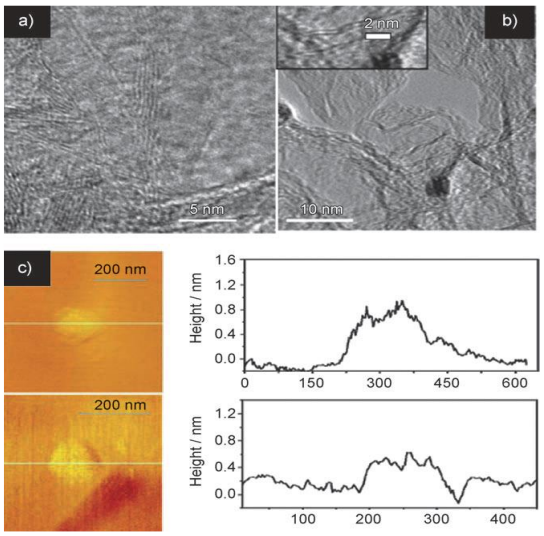

Figure 6 (a & b) High resolution TEM images of graphene (HG) prepared by the arc-discharge method (inset in (b) shows clearly a bi-layer graphene). c) AFM images and height profiles (1–4 layers) [22].

Single-layer graphene can be produced in good yields by solution-phase exfoliation of graphite in an organic solvent, such as N-methylpyrrolidone (NMP) [23]. The energy required to exfoliate graphite is balanced by the solvent-graphene interaction. RGO with properties similar to that of graphene is also prepared through chemical, thermal, or electrochemical reduction pathways. Lin et al. [24] have prepared graphene by rapid reduction and expansion exfoliation of sulfuric acid intercalated graphite oxide at temperature just above 100 ^{o}C in ambient atmosphere. The product consists of mostly single layer graphene sheets with a mean diameter of 1.07 μm after dispersion in DMF. Arc-discharge is one of the best method to synthesize few-layer graphene in gram quantity [22]. To prepare graphene (HG), direct current arc evaporation of graphite was carried out in a water-cooled stainless steel chamber filled with a mixture of hydrogen and helium in different proportions, without using a catalyst. The discharge current was in the 100-150 A range, with a maximum open circuit voltage of 60 V. The arc-discharge deposits formed on the inner walls of the reaction chamber. Figure 6(a & b) shows the TEM and (c) shows AFM images with height profiles. The deposit mainly contained few-layer graphene (1–4 layers).

Graphene-based supercapacitors: The outstanding properties enable graphene and graphene-based materials to find applications in supercapacitors. Rao and co-workers first explored the supercapacitor performances of graphene [25]. The graphene samples were prepared by exfoliation of graphitic oxide (EG) or transformation of nanodiamond

(DG). The Brunauer-Emmett-Teller (BET) surface areas of EG and DG were 925 and 520 m^2/g respectively. EG showed the highest specific capacitance of 117 F/g when compared to DG (35 F/g) in 1 M H_2SO_4. In an ionic liquid these samples showed specific capacitance values of 75 F/g and 40 F/g for EG and DG respectively. Figure 7(a) shows the cyclic voltammogram curves of EG, DG and CG whereas Figure 7(b) shows the specific capacitance as a function of scan rate. The values of the maximum energy density stored using these capacitors were 31.9 and 17.0 Wh kg^{-1} respectively for EG and DG. Ruoff et al. [26] have used chemically modified graphene with surface area of 705 $m^2\ g^{-1}$, to obtain specific capacitances of 135 and 99 F g^{-1} in aqueous (5.5 KOH) and organic ($TEABF_4$) electrolytes respectively. Theoretically, the specific surface area of single-layer graphene can reach up to 2675 $m^2\ g^{-1}$ and can show a supercapacitance of 550 F g^{-1} [27].

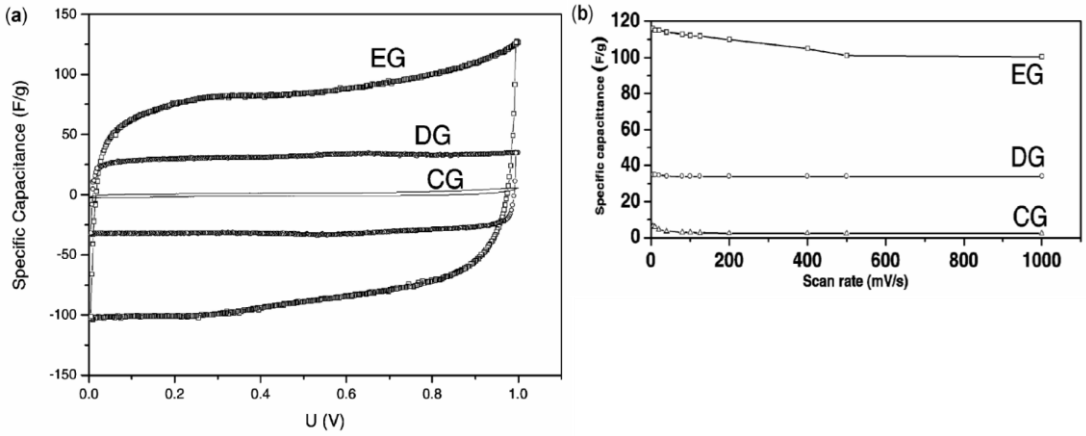

Figure 7. (a) Voltammetry characteristics of a capacitor built from graphene electrodes at a scan rate of 100 mV/s using (a) aqueous H2SO4 (1 M) and (b) specific capacitance as a function of scan rate.

Conventional supercapacitors based on curved graphene in an ionic liquid typically show 100-250 F/g at a high current density of 1 A/g with a discharge voltage of 4.0 V and exhibited an energy density of 85.6 Wh/kg [28]. Microwave exfoliated graphite oxide (MEGO) gives a specific capacitance as high as 191 F g^{-1} in KOH [29], the surface area also being large (463 m^2/g). When chemically activated, the surface area of microwave exfoliated graphite oxide (a-MEGO) goes up to ~2400 m^2/g with high electrical conductivity and a low oxygen and hydrogen content [30]. A specific capacitance value of ~166 F g^{-1} is obtained at a current density in the 1.4-5.7 A/g range.

The corresponding volumetric capacitance and the energy density were ~60 F cm^{-3} and ~70 Wh/kg respectively. Even after 10,000 constant current charge-discharge cycles at a current density of 2.5 A/g, 97% of the capacitance was retained.

Doped graphene: Graphene has recently emerged as a sensational nanocarbon with unusual properties [15, 18]. It is a gapless material with ballistic conduction at room temperature and high carrier mobility. These characteristics belong to single-layer graphene. Two-, three- and few-layer graphenes also exhibit novel properties although they are not be gapless as the single-layer material. The problem with single-layer graphene is that for many applications it is necessary to create a band-gap. Thus, to use graphene in nano-electronic devices, a band-gap has to be engineered which will in turn reduce its electron mobility. Such a band-gap can be created by surface modification or chemical doping [31]. Doping graphene with heteroatoms can effectively tune its electronic structure and other intrinsic properties. Doping graphene with nitrogen or boron creates a band-gap and makes it a n-type or p-type material. The band structure of single layer graphene showing p- and n-type doping with respect to the Fermi level is shown in Figure 8. Such chemically doped materials have unique properties, for example, nitrogen-doped graphene is a good electron-donor and these unique properties can be used in many energy-related areas.

Nitrogen doping helps to manipulate the electronic structure of graphene in a desirable fashion [32]. A change in electronic structure of graphene allows enhanced binding of electrolyte ions in the solution, thus enhances the capacitance. With nitrogen-doped graphene prepared by the reduction of graphene oxide with urea, Zhao et al. [33] obtained a specific capacitance of 255 F/g at 0.5 A/g in an aqueous electrolyte (6 M KOH). The graphene electrode showed 43 % decrease in the initial capacitance at a current density of 30 A/g. Nitrogen doped graphene obtained from hydrothermal method showed a specific capacitance of 326 F/g at 0.2 A/g in an aqueous electrolyte with superior cyclic stability and nearly 99% coulombic efficiency [34]. The maximum energy density obtained was 35.05 Wh/kg at a power density of 175 W/kg. Nitrogen-doped graphene hydrogels showed a specific capacitance of 308 F/g at 3 A/g [35]. The energy density of supercapacitors can be increased using organic solvents or ionic liquids as electrolytes [36]. Nitrogen doped graphene prepared under plasma conditions shows

capacitance 4 times higher than that of pristine graphene in an organic electrolyte (1 M tetraethylammonium tetrafluoroborate in acetonitrile) and showed superb cyclic stability of 100,000 cycles [37].

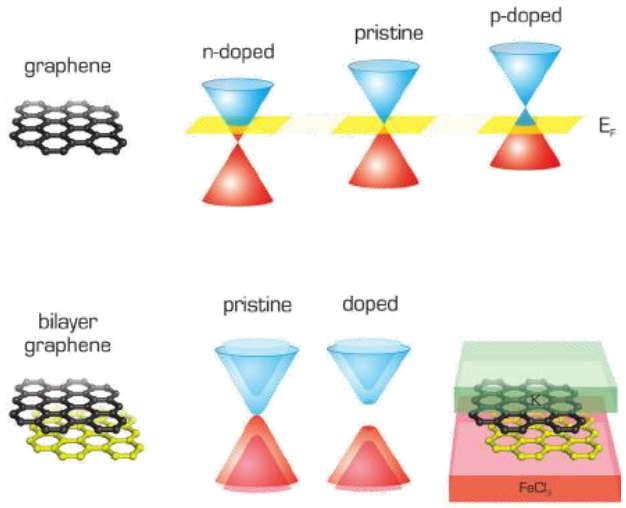

Figure 8. Band structure of single layer graphene showing p- and n-type doping with respect to the Fermi level, and band gap opening in bilayer graphene caused by doping [38].

Boron-doped graphene (BG) made by the 'Fried ice' method gives a specific capacitance of 281 F/g in aqueous electrolyte (2M H_2SO_4) [39]. BG prepared by a simple pyrolysis process using GO and boric acid shows a specific capacitance of 172.5 F/g at 0.5 A/g and maintains 96.5% of the initial capacity after a continuous cycling of 5000 times [40]. Solid-state supercapacitors based on three-dimensional (3D) nitrogen and boron co-doped monolithic graphene aerogels (BN-GAs) show a specific capacitance of ~62 F/g, an enhanced energy density of ~8.65 Wh/kg and a power density of ~1600 W/kg [41]. Boron-doped reduced graphene oxide (1.1 at. % B) synthesized via the reduction of graphene oxide by borane-tetrahydrofuran has a high surface area of 466 m^2/g and showed a specific capacitance of 200 F/g in aqueous electrolyte with good cyclic stability of more than 4500 cycles [42].

1.1.2.1.2 Borocarbonitrides

Borocarbonitrides with the general formula of $B_xC_yN_z$ constitute a new family of 2D materials, whose composition can be varied over a wide range [43]. These materials are generally nanoplatelets containing graphene and BN domains, possibly along with BCN

rings. If the ratio of BN to carbon is 1:1 the composition would be BCN. $B_xC_yN_z$ compositions contain hexagonal networks of B–C, B–N, C–N and C–C bonds but no B–B or N–N bonds. On the other hand, lateral integration of graphene and hexagonal boron nitride (*h*-BN) permits the intricate design of a hybrid heterostructure in which the electronic characteristics can be tuned as required for a particular application [44].

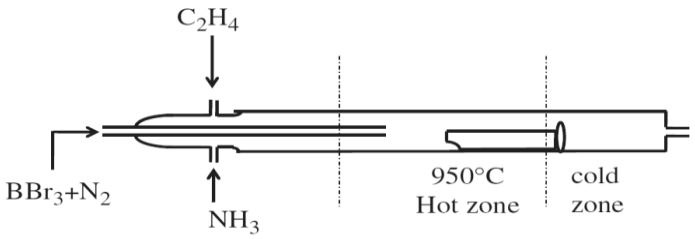

Figure 9 Experimental set-up for gas phase synthesis of borocarbonitrides [45].

Different structures and compositions of $B_xC_yN_z$ have been reported in the literature including those containing separated layers of BN and carbon or an outer BC_2N layer with inner graphitic layers. Pyrolysis of the BH_3–trimethylamine adduct is reported to yield $B_xC_yN_z$ nanotubes [46]. Multiwalled B_5CN_5 nanotubes have been obtained by chemical vapour deposition [47]. $B_xC_yN_z$ type materials have been prepared by the nitridation of boric acid and carbonization of saccharose in molten urea [48]. Urea gives NH_3 on heating and acts as a good nitrogen source. Such products of solid state synthesis seem to give rise to borocarbonitrides with well-defined compositions, but they are unlikely to possess entirely homogeneous compositions of B, C and N atoms throughout the structure. Spectroscopic and theoretical studies suggest these compositions to contain graphene-like networks, without long-range registry along the c-direction. Gas phase synthesis of BxCyNz by the reaction of a hydrocarbon such as CH_4 with ammonia and BCl_3 was carried out sometime ago by Bartlett and co-workers [49]. Recently, a similar reaction of BBr_3, NH_3 and ethylene has been found to give borocarbonitrides [45]. Composites containing hybrid structures of BN and graphene have also been prepared. Some of the composites contain stacks of graphene and BN or involve deposition of graphene on BN surfaces [44].

BN/reduced graphene oxide (BN/RGO) nanocomposites synthesized by liquid-phase exfoliation show a specific capacitance of 140 F g^{-1} at 2 A g^{-1}, with a rate performance of 71.5 F g^{-1} at 50 A g^{-1}, and good cyclic stability [50]. Shi et al. [51] have fabricated the thinnest nanocapacitor electrode consisting of h-BN and graphene with different layers h-BN ranging from bulk to 2 layers. The electrode with thickness of 0.8 nm (h-BN=2 layers) shows highest capacitance of ~ 12 pF.

1.1.2.1.3 MoS_2

MoS_2 is a special layered material which exhibits variety of properties of vital interest to physical as well as materials sciences [43, 52, 53]. Single layer MoS_2 can be a p-type semiconductor or a metal, depending on the way it is generated. Li intercalation of MoS_2 using *n*-butyllithium can be used to prepare dispersions of single layered materials [54]. Li intercalation can be carried electrochemically with the layered material as the cathode and a Li-foil as the anode [55]. Subsequent sonication in water or ethanol yielded 2D layered nanosheets. On Li intercalation, the stable 2H structures of MoS_2 change to the less stable 1T forms. 2H-MoS_2 has trigonal prismatic coordination of the metal and chalcogen atoms with AbA BaB packing. The 1T form has octahedral or trigonal anti-prismatic coordination with AbC AbC packing [56]. Figure 10 shows the structure of MoS_2.

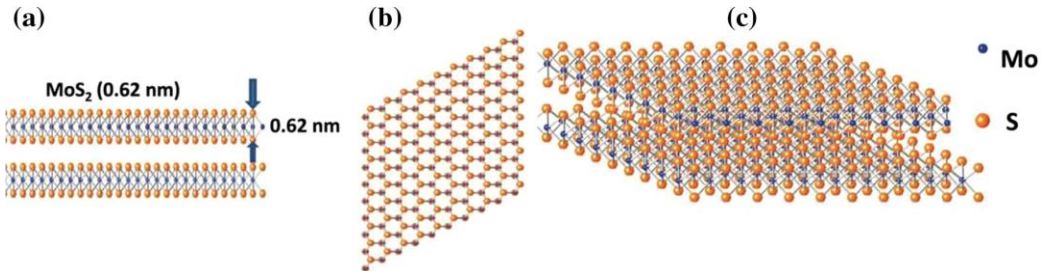

Figure 10 Structure of MoS_2: (a) side view and (b & c) top view [52].

MoS_2 consists of a metal Mo layer sandwiched between two S layers, with these triple layers stacked together to form the layered structure. Such 2D electron-electron correlations among Mo atoms enhance the supercapacitance characteristics of MoS_2 [53]. Figure 11 show the TEM images of single-layered MoS_2 showing (a) zig-zag edges and (b)

bends (arising from defects) in the layers. Three-dimensional (3D) flower-like MoS_2 nanostructures prepared by a one pot hydrothermal method show a maximum capacitance of 218 F/g at a scan rate of 5 mV/s (1 M KCl) [57]. Flexible supercapacitors based on MoS_2 hierarchical nanospheres show good electrochemical performance such as high capacitance 368 F/g at a scan rate of 5 mV/s [58]. The supercapacitor inherits good characteristics such as lightweight, low cost, portability, high flexibility and long term cycling stability. Few-layered MoS_2 obtained by liquid phase exfoliation of bulk MoS_2 powder in 1-dodecyl-2-pyrrolidinone exhibited capacitances ~2 mF/cm^2 whereas for bulk MoS_2 the capacitance was ~0.5 mF/cm^2 in KOH electrolyte [59]. Flowerlike MoS_2 nanospheres synthesized through hydrothermal route with mean diameters of 300 nm shows supercapacitive behaviour in 1 M KCl [60]. The specific capacitance of the flower-like MoS_2 is found to be 114 F/g at 2 mV/s. Hydrothermally synthesized of MoS_2 nanosheets show a specific capacitance of 129.2 F/g at 1.0 A/g [61]. Acerce et al. [62] have reported nanosheets of MoS_2 synthesized through chemical exfoliation to contain a high concentration of the metallic 1T phase. These chemically exfoliated MoS_2 nanosheets exhibited extraordinary efficiency and showed capacitance values ranging from ~400 to ~700 F/cm^3 in various aqueous electrolytes.

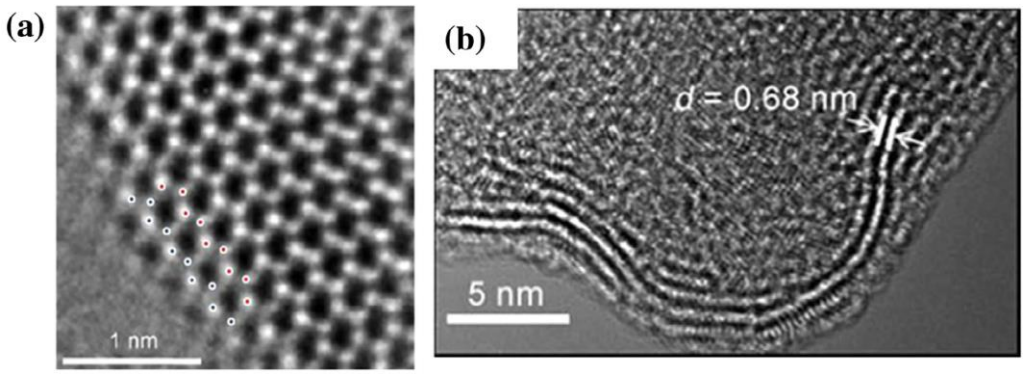

Figure 11 High-resolution TEM image of (a) single-layered MoS2 showing zig-zag edges and (b) bends in few-layer MoS_2 arising because of defects at the edges [54].

1.1.2.2 Pseudocapacitors

EDLCs can provide ultrahigh power density and excellent life cycle because of the non-degradative processes between the electrode and the electrolyte [5]. In a pseudocapacitor, the fast and reversible Faradaic reaction near the surface determines

its energy storage capability. Pseudocapacitors are, therefore, preferred in applications where high capacitance is required. Typical active pseudocapacitive materials include transition metal oxides such as RuO_2, Fe_3O_4, NiO, and MnO_2 and conducting redox polymers such as polyanilines, polypyrroles, and polythiophenes [63, 64]. The energy densities of pseudocapacitors are greater than EDLCs, but the phase changes within the electrode due to the Faradic reaction limits their lifetime and power density. To resolve this problem, carbonaceous materials (CNTs and graphene) with high electrical conductivity and ductility have been utilized to prepare composites. Graphene composites show improved capacitance due their enhanced electronic conductivity and 2D nanostructure [53].

1.1.2.2.1 Pseudocapacitors based on two dimensional materials

Graphene-Conducting polymer composites: Electronically conducting π-electrons polymers (ECPs) are promising electrode materials for supercapacitors because of their high specific capacitance, high conductivity and ease of preparation. Polypyrrole (PPy), polyaniline (PANI), and polythiophene (PT) as well as their derivatives are commonly used ECPs. These polymers can be synthesized chemically or electrochemically. However, the main drawback of conducting polymers is their low stability. Electro-reduction or electro-oxidation of a polymer generates a charge, which is balanced by oppositely charged counter ions entering or leaving the polymer film to maintain its neutrality. Therefore, electrochemical charging and discharging irreversibly changes the structure of polymers due to swelling and shrinking. This problem can be solved by making composites with outstanding carbon material like graphene. The resulting composites synergistically combine properties of graphene with high electrical conductivity and surface area.

Polyaniline (PANI) possesses high conductivity and chemical stability. Its electrochemical behaviour is complex due to the presence of several oxidation states of PANI including the fully reduced leucoemeraldine form, the intermediate emeraldine form, and the fully oxidized pernigraniline form as shown in Figure 12. The specific capacity of PANI depends upon three parameters such as the preparation procedure

used, morphology and thickness. Chemically modified graphene and polyaniline nanofiber composites have been prepared by in situ polymerization of aniline monomer in the presence of graphene oxide under acid conditions [65]. The graphene oxide/PANI composites with different mass ratios were reduced to graphene using hydrazine followed by reoxidation and reprotonation of the reduced PANI to give the graphene/PANI nanocomposites. The BET surface areas of these composites were in the 4.3-20.2 m^2/g range and the highest specific capacitance achieved was 480 F/g at a current density of 0.1 A/g.

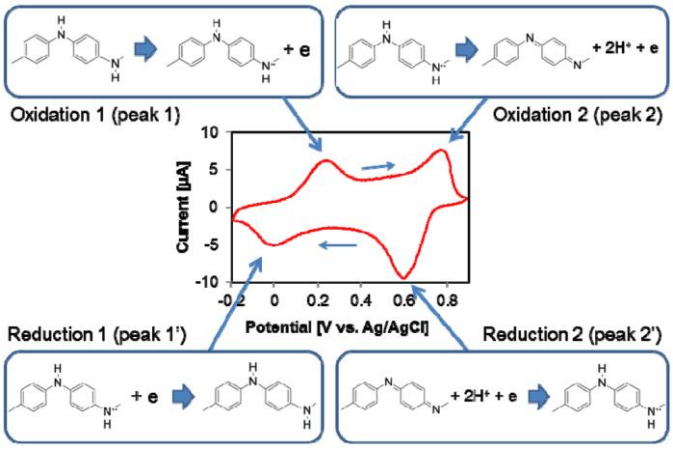

Figure 12 A typical cyclic voltammetry (CV) curve of polyaniline in HCl showing two sets of redox couples [66].

PANI sandwiched graphene layers prepared by mixed dispersion of chemically converted graphene (CCG) and polyaniline nanofibers (PANI-NFs) show high conductivity (44% higher than CCG (5.5102 S/m) and 10 times that of a PANI-NF film) [66]. Supercapacitor performance is excellent with a capacitance of 210 F/g at 0.3 A/g. Doping of PANI with graphene also shows good electrochemical performance with capacitance of 531 F/g [67]. Change in size of raw graphite flakes plays an important role in the electrochemical performance [68]. The specific capacitances are 746 F/g for 12500 mesh and 627 F/g for 500 mesh compared to PANI of 216 F/g at 0.200 A/g. Polyaniline-grafted reduced graphene oxide (PANI-*g*-rGO) composite synthesized using *in-situ* oxidative polymerization shows fibrillar morphology with a room-temperature electrical conductivity as high as 8.66 S/cm and a capacitance of 250 F/g with good cycling stability.

Other than PANI, polypyrrole is a widely studied conducting polymer for energy storage devices. A polypyrrole-reduced graphite oxide core-shell composite fabricated through electrostatic interactions and π- π accumulation shows remarkable performance as a supercapacitor electrode material with a specific capacitance of 557 F/g at a current density of 0.5 A/g and retains a high value after 1000 charge–discharge processes [69]. The maximum energy density of the fabricated supercapacitor is calculated to be 49.5 W at a power density of 0.22 kW/kg. The improved capacitance is due to the higher conductivity and the crumpled surface of the composite. Interfacial/*in-situ* oxidative polymerization of polypyrrole in the presence of functionalized graphene sheets produces high quality composites for supercapacitors [70].

Graphene-transition metal oxide composites: Transition metal oxides such as RuO_2, MnO_2, Fe_3O_4 and NiO have been used as supercapacitor electrodes due to their high surface area and theoretical capacitance [17,18]. The poor electrical conductivity of these metal oxides affects their specific capacitance. A good strategy to increase the performance of metal oxides is to form composites with carbon materials such as graphene and carbon nanotubes. Manganese dioxide (MnO_2) is a low-cost material with a large theoretical capacity (1370 F/g). It is abundant, eco-friendly and is a promising electrode material for supercapacitors. Due to the poor electrical conductivity of MnO_2 (10^{-5} to 10^{-6} S/cm) some results have been achieved on ultrathin films. Composites of MnO_2 with conducting carbon materials enhance their conductivity and electrochemical performance. Wang et al. [71] reported a straightforward method to intercalate and adsorb MnO_2 nanoparticles on graphene oxide sheets via a simple soft chemical route in water/isopropanol to prepare GO-MnO_2 nanocomposites. The specific capacitance for MnO_2 reaches about 211 F/g and it was 216 F/g at 0.2 A/g for GO-MnO_2 composite in 1 M Na_2SO_4 aqueous electrolyte. In addition, the GO-MnO_2 composite electrode retains about 84.1% (165.9 F/g) of the initial capacitance after 1000 cycles, while the MnO_2 nanoparticles retain only about 69.0% (145.7 F/g). The increase in capacitance is attributed from the combination of double-layer and pseudocapacitive process of graphene and MnO_2 respectively. Controlled deposition of nanostructured MnO_2 on conducting graphene-coated textiles has been achieved through electrochemical deposition [72]. Graphene also provides electrical conducting channels and increases the

capacitance. Composites of graphene with nickel oxide (NiO) exhibit a high specific capacitance of ~816 F g^{-1} at a scan rate of 5 mV/s and a stable cycling performance without any decrease in specific capacitance after 2000 cycles [73]. Graphene sheet /porous NiO hybrid films prepared by electrophoretic deposition show excellent pseudocapacitive behavior with pseudocapacitances of 400 F/g at 2 A/g with an energy density of 16.8 Wh/kg [74].

1.1.3 Characterization Techniques

Several spectroscopic and microscopic techniques have been used to characterize the prepared nanomaterials and to study its properties in the thesis.

Field emission scanning electron microscopy (FESEM) and Energy-dispersive X-ray spectroscopy (EDS): Field emission scanning electron microscopy (FESEM) measurements were performed using a Nova NanoSEM 600 equipment (FEI Co., The Netherlands). Energy dispersive spectroscopic (EDS) mapping was performed using EDAX Genesis V4.52 (USA) attached to the SEM column. The EDS mapping was performed at 10-15 kV with a beam current of 0.1 - 2 nA.

Transmission electron microscopy (TEM) and Electron Diffraction (ED): Transmission electron microscopy (TEM) measurements were carried out with a JEOL-3010 instrument operating at 300 kV (λ = 0.0196 Å) and selected area electron diffraction (SAED) patterns were collected at a camera length 20 cm (calibrated with respect to the standard polycrystalline Au thin film). Samples for TEM were prepared by depositing a drop of the nanomaterial on a holey carbon copper grid, allowing it to dry in a desiccator overnight. This grid was used for TEM and selected area electron diffraction (SAED) analysis.

Atomic force microscopy (AFM): Atomic force microscopy (AFM) imaging was carried out using Multimode, Veeco digital instruments, USA with Nanoscope IV controller and

Veeco diInnova SPM with Nanodrive controller. Tapping and contact (lateral force) mode imaging was carried out using standard etched Si or Si_3N_4 cantilevers, respectively.

Raman spectroscopy: Raman spectra were recorded with a LabRAM HR high resolution Raman spectrometer (Horiba Jobin Yvon) using He–Ne Laser (λ=630 nm)/ Ar laser (λ =514nm). Signal accumulation was performed for 30 s with a spot size of ~ 2 μm.

UV-Vis and IR spectroscopy: UV-visible spectra were recorded using a Perkin-Elmer Lambda 900 UV/vis/NIR spectrophotometer using 1 mm path length cuvette. Fourier transform infrared (FTIR) measurements were done using a Bruker IFS66 v/s spectrometre.

X-ray diffraction (XRD): The structural analysis of the nanomaterials were carried out by X-ray diffraction using Bruker D8 Discover diffractometer attached with temperature and humidity controlled stage. Cu Kα (λ = 1.5419 Å) was used as an X-ray source. Samples were prepared by depositing the materials in the form of films on glass slides and typical scan rate of 1 deg/min was used. The X-ray tube was set at 40 kV and 30 mA. With a receiving slit of 0.3 mm wide and a scintillation counter as a detector, the θ - 2θ scans were performed.

Electrochemical measurements: The electrochemical properties were investigated in two-electrode or three-electrode configuration. The electrochemical performance of the electrodes is determined by testing the cyclic voltammetry (CV), galvanostatic charge–discharge curves and electrochemical impedance spectroscopy (EIS) using PG262A potentiostat/galovanostat, (Technoscience Ltd, Bangalore, India).
Specific capacitance (C_{sp}) is calculated using the formula,

$$C_{sp} = \quad 2(i_+ - i_-)/(m \times \text{scan rate})$$

where, i_+ and i_- are the maximum values of current in the positive scan and negative scan respectively and m is the mass of the single electrode.

Specific capacitance is calculated from constant current charge-discharge curves using the formula,

$$C_{sp} = \quad 2(i)/(m \times s)$$

where, i is the discharge current and s is the slope of the discharge curve.
Energy densities (E) and power densities (P) are calculated using the formulae,

$$E=1/2CV^2$$

$$P = E/t$$

where, C is the specific capacitance, V is the operational potential window (0-1 V) and t is the discharge time.

Electrochemical impedance measurements were carried out at a DC bias of 0 V over a frequency range of 100 kHz to 10 mHz by applying an AC voltage with 10 mV perturbation.

References

[1] Pandolfo T, Ruiz V, Sivakkumar S, Nerkar J. General Properties of Electrochemical Capacitors. Supercapacitors: Wiley-VCH Verlag GmbH & Co. KGaA; 2013. p. 69-109.

[2] Conway BE. Similarities and Differences between Supercapacitors and Batteries for Storing Electrical Energy. Electrochemical Supercapacitors: Scientific Fundamentals and Technological Applications. Boston, MA: Springer US; 1999. p. 11-31.

[3] McCloskey BD. Expanding the Ragone Plot: Pushing the Limits of Energy Storage. J Phys Chem Lett. 2015;6:3592-3.

[4] Simon P, Gogotsi Y. Materials for electrochemical capacitors. Nat Mater. 2008;7:845-54.

[5] KÃ¶tz R, Carlen M. Principles and applications of electrochemical capacitors. Electrochimica Acta. 2000;45:2483-98.

[6] Wang S, Zhang L, Xia Z, Roy A, Chang DW, Baek J-B, et al. BCN Graphene as Efficient Metal-Free Electrocatalyst for the Oxygen Reduction Reaction. Angewandte Chemie International Edition. 2012;51:4209-12.

[7] Candelaria SL, Shao Y, Zhou W, Li X, Xiao J, Zhang J-G, et al. Nanostructured carbon for energy storage and conversion. Nano Energy.1:195-220.

[8] Zhang LL, Zhao XS. Carbon-based materials as supercapacitor electrodes. Chemical Society Reviews. 2009;38:2520-31.

[9] Li X, Wei B. Supercapacitors based on nanostructured carbon. Nano Energy. 2013;2:159-73.

[10] Park S, Vosguerichian M, Bao Z. A review of fabrication and applications of carbon nanotube film-based flexible electronics. Nanoscale.5:1727-52.

[11] Niu C, Sichel EK, Hoch R, Moy D, Tennent H. High power electrochemical capacitors based on carbon nanotube electrodes. Applied Physics Letters. 1997;70:1480-2.

[12] Frackowiak E, Metenier K, Bertagna V, Beguin F. Supercapacitor electrodes from multiwalled carbon nanotubes. Applied Physics Letters. 2000;77:2421-3.

[13] Liu CG, Fang HT, Li F, Liu M, Cheng HM. Single-walled carbon nanotubes modified by electrochemical treatment for application in electrochemical capacitors. Journal of Power Sources. 2006;160:758-61.

[14] Fuertes AB, Pico F, Rojo JM. Influence of pore structure on electric double-layer capacitance of template mesoporous carbons. Journal of Power Sources. 2004;133:329-36.

[15] Rao CNR, Sood AK, Subrahmanyam KS, Govindaraj A. Graphene: The New Two-Dimensional Nanomaterial. Angewandte Chemie International Edition. 2009;48:7752-77.

[16] Novoselov KS, Geim AK, Morozov SV, Jiang D, Zhang Y, Dubonos SV, et al. Electric Field Effect in Atomically Thin Carbon Films. Science. 2004;306:666-9.

[17] Zhu Y, Murali S, Cai W, Li X, Suk JW, Potts JR, et al. Graphene and Graphene Oxide: Synthesis, Properties, and Applications. Adv Mater. 2010;22:3906-24.

[18] Geim AK, Novoselov KS. The rise of graphene. Nat Mater. 2007;6:183-91.

[19] Rao CNR, Subrahmanyam KS, Matte HSSR, Abdulhakeem B, Govindaraj A, Barun D, et al. A study of the synthetic methods and properties of graphenes. Sci Tech Adv Mater. 2010;11:054502.

[20] Subrahmanyam KS, Vivekchand SRC, Govindaraj A, Rao CNR. A study of graphenes prepared by different methods: characterization, properties and solubilization. J Mater Chem. 2008;18:1517-23.

[21] Rao CNR, Maitra U, Matte HSSR. Synthesis, Characterization, and Selected Properties of Graphene. Graphene: Wiley-VCH Verlag GmbH & Co. KGaA; 2012. p. 1-47.

[22] Subrahmanyam KS, Panchakarla LS, Govindaraj A, Rao CNR. Simple Method of Preparing Graphene Flakes by an Arc-Discharge Method. The Journal of Physical Chemistry C. 2009;113:4257-9.

[23] Hernandez Y, Nicolosi V, Lotya M, Blighe FM, Sun Z, De S, et al. High-yield production of graphene by liquid-phase exfoliation of graphite. Nat Nano. 2008;3:563-8.

[24] Hong Y, Wang Z, Jin X. Sulfuric Acid Intercalated Graphite Oxide for Graphene Preparation. Sci Rep.3.

[25] Vivekchand SRC, Rout C, Subrahmanyam KS, Govindaraj A, Rao CNR. Graphene-based electrochemical supercapacitors. Journal of Chemical Sciences. 2008;120:9-13.

[26] Stoller MD, Park S, Zhu Y, An J, Ruoff RS. Graphene-Based Ultracapacitors. Nano Letters. 2008;8:3498-502.

[27] Xia J, Chen F, Li J, Tao N. Measurement of the quantum capacitance of graphene. Nat Nano. 2009;4:505-9.

[28] Liu C, Yu Z, Neff D, Zhamu A, Jang BZ. Graphene-Based Supercapacitor with an Ultrahigh Energy Density. Nano Letters.10:4863-8.

[29] Zhu Y, Murali S, Stoller MD, Velamakanni A, Piner RD, Ruoff RS. Microwave assisted exfoliation and reduction of graphite oxide for ultracapacitors. Carbon.48:2118-22.

[30] Zhu Y, Murali S, Stoller MD, Ganesh KJ, Cai W, Ferreira PJ, et al. Carbon-Based Supercapacitors Produced by Activation of Graphene. Science.332:1537-41.

[31] Rao CNR, Gopalakrishnan K, Govindaraj A. Synthesis, properties and applications of graphene doped with boron, nitrogen and other elements. Nano Today. 2014;9:324-43.

[32] Wang H, Maiyalagan T, Wang X. Review on Recent Progress in Nitrogen-Doped Graphene: Synthesis, Characterization, and Its Potential Applications. ACS Catalysis.2:781-94.

[33] Lei Z, Lu L, Zhao XS. The electrocapacitive properties of graphene oxide reduced by urea. Energy & Environmental Science.5:6391-9.

[34] Sun L, Wang L, Tian C, Tan T, Xie Y, Shi K, et al. Nitrogen-doped graphene with high nitrogen level via a one-step hydrothermal reaction of graphene oxide with urea for superior capacitive energy storage. RSC Advances.2:4498-506.

[35] Guo H-L, Su P, Kang X, Ning S-K. Synthesis and characterization of nitrogen-doped graphene hydrogels by hydrothermal route with urea as reducing-doping agents. Journal of Materials Chemistry A.1:2248-55.

[36] Kim TY, Lee HW, Stoller M, Dreyer DR, Bielawski CW, Ruoff RS, et al. High-Performance Supercapacitors Based on Poly(ionic liquid)-Modified Graphene Electrodes. ACS Nano.5:436-42.

[37] Jeong HM, Lee JW, Shin WH, Choi YJ, Shin HJ, Kang JK, et al. Nitrogen-Doped Graphene for High-Performance Ultracapacitors and the Importance of Nitrogen-Doped Sites at Basal Planes. Nano Letters.11:2472-7.

[38] Pykal M, Jurecka P, Karlicky F, Otyepka M. Modelling of graphene functionalization. Phys Chem Chem Phys. 2016;18:6351-72.

[39] Zuo Z, Jiang Z, Manthiram A. Porous B-doped graphene inspired by Fried-Ice for supercapacitors and metal-free catalysts. Journal of Materials Chemistry A.1:13476-83.

[40] Niu L, Li Z, Hong W, Sun J, Wang Z, Ma L, et al. Pyrolytic synthesis of boron-doped graphene and its application as electrode material for supercapacitors. Electrochimica Acta.108:666-73.

[41] Wu Z-S, Winter A, Chen L, Sun Y, Turchanin A, Feng X, et al. Three-Dimensional Nitrogen and Boron Co-doped Graphene for High-Performance All-Solid-State Supercapacitors. Advanced Materials.24:5130-5.

[42] Han J, Zhang LL, Lee S, Oh J, Lee K-S, Potts JR, et al. Generation of B-Doped Graphene Nanoplatelets Using a Solution Process and Their Supercapacitor Applications. ACS Nano. 2013;7:19-26.

[43] Kumar N, Moses K, Pramoda K, Shirodkar SN, Mishra AK, Waghmare UV, et al. Borocarbonitrides, BxCyNz. J Mater Chem A. 2013;1:5806-21.

[44] Ci L, Song L, Jin C, Jariwala D, Wu D, Li Y, et al. Atomic layers of hybridized boron nitride and graphene domains. Nat Mater. 2010;9:430-5.

[45] Kumar N, Raidongia K, Mishra AK, Waghmare UV, Sundaresan A, Rao CNR. Synthetic approaches to borocarbonitrides, BCxN (x=1–2). J Solid State Chem. 2011;184:2902-8.

[46] Sen R, Satishkumar BC, Govindaraj A, Harikumar KR, Raina G, Zhang J-P, et al. B–C–N, C–N and B–N nanotubes produced by the pyrolysis of precursor molecules over Co catalysts. Chem Phys Lett. 1998;287:671-6.

[47] Kim SY, Park J, Choi HC, Ahn JP, Hou JQ, Kang HS. X-ray Photoelectron Spectroscopy and First Principles Calculation of BCN Nanotubes. J Am Chem Soc. 2007;129:1705-16.

[48] Hubáček M, Sato T. Preparation and Properties of a Compound in the B-C-N System. J Solid State Chem. 1995;114:258-64.

[49] Kaner RB, Kouvetakis J, Warble CE, Sattler ML, Bartlett N. Boron-carbon-nitrogen materials of graphite-like structure. Mater Res Bull. 1987;22:399-404.

[50] Gao T, Gong L-j, Wang Z, Yang Z-k, Pan W, He L, et al. Boron nitride/reduced graphene oxide nanocomposites as supercapacitors electrodes. Materials Lett. 2015;159:54-7.

[51] Shi G, Hanlumyuang Y, Liu Z, Gong Y, Gao W, Li B, et al. Boron Nitride–Graphene Nanocapacitor and the Origins of Anomalous Size-Dependent Increase of Capacitance. Nano Lett. 2014;14:1739-44.

[52] Rao CNR, Maitra U, Waghmare UV. Extraordinary attributes of 2-dimensional MoS2 nanosheets. Chem Phys Lett. 2014;609:172-83.

[53] Rao CNR, Gopalakrishnan K, Maitra U. Comparative Study of Potential Applications of Graphene, MoS2, and Other Two-Dimensional Materials in Energy Devices, Sensors, and Related Areas. ACS App Mater Interfaces. 2015;7:7809-32.

[54] Ramakrishna Matte HSS, Gomathi A, Manna AK, Late DJ, Datta R, Pati SK, et al. MoS2 and WS2 Analogues of Graphene. Angew Chem Int Ed. 2010;122:4153-6.

[55] Zeng Z, Yin Z, Huang X, Li H, He Q, Lu G, et al. Single-Layer Semiconducting Nanosheets: High-Yield Preparation and Device Fabrication. Angew Chem Int Ed. 2011;50:11093-7.

[56] Chhowalla M, Shin HS, Eda G, Li L-J, Loh KP, Zhang H. The chemistry of two-dimensional layered transition metal dichalcogenide nanosheets. Nat Chem. 2013;5:263-75.

[57] Pandey K, Yadav P, Mukhopadhyay I. Electrochemical and electronic properties of flower-like MoS2 nanostructures in aqueous and ionic liquid media. RSC Adv. 2015;5:57943-9.

[58] Javed MS, Dai S, Wang M, Guo D, Chen L, Wang X, et al. High performance solid state flexible supercapacitor based on molybdenum sulfide hierarchical nanospheres. J Power Sources. 2015;285:63-9.

[59] Winchester A, Ghosh S, Feng S, Elias AL, Mallouk T, Terrones M, et al. Electrochemical Characterization of Liquid Phase Exfoliated Two-Dimensional Layers of Molybdenum Disulfide. ACS App Mater Interfaces. 2014;6:2125-30.

[60] Zhou X, Xu B, Lin Z, Shu D, Ma L. Hydrothermal Synthesis of Flower-Like MoS2 Nanospheres for Electrochemical Supercapacitors. J Nanosci Nanotech. 2014;14:7250-4.

[61] Huang K-J, Zhang J-Z, Shi G-W, Liu Y-M. Hydrothermal synthesis of molybdenum disulfide nanosheets as supercapacitors electrode material. Electrochimica Acta. 2014;132:397-403.

[62] Acerce M, Voiry D, Chhowalla M. Metallic 1T phase MoS2 nanosheets as supercapacitor electrode materials. Nat Nano. 2015;10:313-8.

[63] Qin X, Durbach S, Wu GT. Electrochemical characterization on RuO_2/carbon nanotubes composite electrodes for high energy density supercapacitors. Carbon. 2004;42:451-3.

[64] Gupta V, Miura N. Polyaniline/single-wall carbon nanotube (PANI/SWCNT) composites for high performance supercapacitors. Electrochimica Acta. 2006;52:1721-6.

[65] Zhang K, Zhang LL, Zhao XS, Wu J. Graphene/Polyaniline Nanofiber Composites as Supercapacitor Electrodes. Chemistry of Materials.22:1392-401.

[66] Wu Q, Xu Y, Yao Z, Liu A, Shi G. Supercapacitors Based on Flexible Graphene/Polyaniline Nanofiber Composite Films. ACS Nano.4:1963-70.

[67] Wang H, Hao Q, Yang X, Lu L, Wang X. Graphene oxide doped polyaniline for supercapacitors. Electrochemistry Communications. 2009;11:1158-61.

[68] Wang H, Hao Q, Yang X, Lu L, Wang X. Effect of Graphene Oxide on the Properties of Its Composite with Polyaniline. ACS Applied Materials & Interfaces.2:821-8.

[69] Qian T, Yu C, Wu S, Shen J. A facilely prepared polypyrrole-reduced graphene oxide composite with a crumpled surface for high performance supercapacitor electrodes. Journal of Materials Chemistry A.1:6539-42.

[70] de Oliveira HP, Sydlik SA, Swager TM. Supercapacitors from Free-Standing Polypyrrole/Graphene Nanocomposites. The Journal of Physical Chemistry C.117:10270-6.

[71] Chen S, Zhu J, Wang X. From Graphene to Metal Oxide Nanolamellas: A Phenomenon of Morphology Transmission. ACS Nano.4:6212-8.

[72] Shi G, Hanlumyuang Y, Liu Z, Gong Y, Gao W, Li B, et al. Boron Nitride–Graphene Nanocapacitor and the Origins of Anomalous Size-Dependent Increase of Capacitance. Nano Lett. 2014;14:1739-44.

[73] Cao X, Shi Y, Shi W, Lu G, Huang X, Yan Q, et al. Preparation of Novel 3D Graphene Networks for Supercapacitor Applications. Small.7:3163-8.

[74] Xia X, Tu J, Mai Y, Chen R, Wang X, Gu C, et al. Graphene Sheet/Porous NiO Hybrid Film for Supercapacitor Applications. Chemistry – A European Journal.17:10898-905.

1.2 SUPERCAPACITORS BASED ON NITROGEN-DOPED REDUCED GRAPHENE OXIDE AND BOROCARBONITRIDES

Summary*

Two-dimensional graphene exhibits fascinating electronic properties as exemplified by ballistic electronic conduction and occurrence of quantum Hall effect at room temperature. Electronic applications of graphene, however, get limited because of the band gap. It becomes necessary to tune the band gap by chemical modification or doping. Doping can modify the electronic structure of graphene significantly. We found an easy way of doping graphene with nitrogen by two different methods. We have obtained 7 wt. % of nitrogen content as found by with elemental analysis and X-ray photoelectron spectroscopy. The graphene samples generally had 2-4 layers estimated by atomic force microscopy and transmission electron microscopy. These N-doped RGO samples possess high surface areas and good supercapacitor properties. Two electrode measurements have been carried out both in aqueous (6 M KOH) and in ionic liquid media. Nitrogen-doped reduced graphene oxides exhibit satisfactory specific capacitance, the values reaching 126 F/g at a scan rate of 10 mV/s in aqueous medium.

Borocarbonitrides, $B_xC_yN_z$, are a new family of layered composites with a wide range of compositions, exhibiting electronic and other properties depending on the carbon content. Borocarbonitrides prepared by the urea route appear to be excellent supercapacitor electrode materials. Thus, $BC_{4.5}N$ exhibits a specific capacitance of 169 F/g at a scan rate of 10 mV/s in aqueous medium. In an ionic liquid medium, $BC_{4.5}N$ exhibit specific capacitance values 240 F/g at a scan rate of 5 mV/s. The ionic liquid enables a larger operating voltage range of 0.0–2.5 V compared to 0.0–1 V in aqueous medium.

*A Paper based on this work has been published in Solid State Commun. 2013, **175**, 43-50

1.2.1 Supercapacitors based on nitrogen-doped graphene

1.2.1.1 Introduction

Electrochemical capacitors find applications in many fields such as hybrid vehicles, mobile electronics and power supply devices due to their high power and energy density, long cycle life and cost effectiveness [1, 2]. Supercapacitors store and release electrical energy due to the formation of electrochemical double layers near the electrode surfaces or through fast Faradaic redox reactions [2]. Carbon-based supercapacitors showed excellent capacitance behaviour because of their high surface area and high electrical conductivity [3, 4]. Graphene, a single atomic layer of graphite exhibits various interesting physical properties with large surface areas and high chemical stability [5]. The main limitation of graphene is absence of band gap which is essential for making field-effect transistors and energy devices [6]. The electronic structure of graphene can be modified by electrochemical doping, chemical doping and doping through molecular charge transfer [7, 8]. Chemical substitution (doping) brings about significant changes in graphene [9]. Recent studies have shown that nitrogen- or boron-doped graphene have excellent supercapacitors properties [10, 11]. In particular, doping of graphene with nitrogen is of interest due to its structural closeness and electron configuration to carbon [12, 13]. The three valence electrons in nitrogen form strong bonds whereas the extra loan pair of electron improves the overall conductivity and enhances the electrochemical capacitance [9].

Different routes have been reported on the synthesis of nitrogen-doped graphene. Thus, graphene has been doped with nitrogen by interaction with ammonia. Nitrogen doped few-layer graphene can be synthesized by performing arc-discharge between two graphite electrodes in the presence of hydrogen, helium and ammonia or pyridine vapours [8]. The graphene obtained contain few-layers (~3–4 layers) with nitrogen content of 1–1.4 at.%. Dai and co-authors [14] reported 5 at.% nitrogen containing graphene by thermal annealing of graphene oxide (GO) with ammonia under different thermal conditions ranging from 300 to 1100 °C. The degree of doping depends upon the temperature and oxygen functionalities at graphene edges. Nitrogen-doped graphene can also be synthesized through chemical vapour deposition (CVD) or plasma conditions.

For example, Wei et al. [15] obtained ~9 at.% of nitrogen by CVD process using Cu film as catalyst on Si substrate in presence of methane, hydrogen, argon and ammonia at 800 °C. Nitrogen doped graphene prepared under nitrogen plasma conditions had a nitrogen content of 2.4 at.% [11]. Ball-milling can be efficiently used to produce nitrogen-doped graphene in large quantity by milling pristine graphite in the presence of ammonia (4.49% N) or nitrogen (14.84% N) [16]. Nitrogen-doped graphene is obtained by heating graphene oxide with melamine or urea as the nitrogen source at different temperatures [17]. In this procedure, graphene oxide is finely ground with melamine or urea at different mass proportions and heated at high temperatures. The extent of doping varies with the temperature as well as with the concentration of the nitrogen source.

Nitrogen-doped graphene can be synthesized at lower temperatures under hydrothermal or solvothermal conditions. Bao and co-workers [18] synthesized nitrogen-doped graphene containing 13 at.% by reacting tertachloromethane with lithium nitride. Long et al. [19] were able to dope up to 5 at.% nitrogen by reduction of GO with hydrazine hydrate and ammonia while the wet chemical reaction between dicyandiamide and GO gives 7.8 at.% [20]. The reaction of GO with urea gives 10.1 at.% after the reaction at 180 °C for 12 h [21]. Dai et al. reported a new approach to chemical exfoliation of graphite by grafting 4-aminobenzoic acid (ABA) on the edges of graphite via Friedel–Crafts acylation in poly(phosphoric acid) (PPA)/phosphorus pentoxide (P_2O_5) medium [22]. Selective synthesis of desired nitrogen type is a crucial part in nitrogen doped graphene [23]. Pyridinic- and pyrrolic-nitrogen-doped graphene can be prepared by the use of layered montmorillonite (MMT) as a quasi-closed flat nanoreactor. In a typical preparation, aniline is first intercalated into the layers of MMT, and in situ oxidation polymerization then performed. The composite is dehydrated at 120 °C and pyrolyzed at 900 °C under flowing N_2 for 3 h. MMT is etched off in a 40% HF solution.

1.2.1.2 Scope of the present investigations

Graphene has many possible applications in nanoelectronics, supercapacitors and lithium secondary batteries. Electronic applications of graphene, however, get limited because of the band gap. It becomes necessary to tune the band-gap by chemical

modification or doping. With this motivation, we have done nitrogenation of two different graphene using urea. We have examined X-ray photoelectron spectra (XPS) of the nitrogen doped graphene samples to understand the nature of nitrogen in the graphene matrix. These samples possess high surface areas. We have studied supercapacitor performance for these nitrogen doped reduced graphene (NRGO) samples and for purpose of comparison, we have carried out electrochemical measurements on nitrogenated graphene (NHG) obtained from graphene prepared by arc-discharge in hydrogen (HG).

1.2.1.3 Experimental section

Synthesis of Reduced Graphene oxide (RGO): Reduced graphene oxide (RGO) was prepared by two different methods starting with graphene oxide (GO) [24]. In a typical experiment, 15 ml of conc. sulfuric acid was taken in a round bottomed flask which was pre-cooled in an ice bath. To this, 300 mg of potassium nitrate (SD-fine chemicals) and 300 mg of graphite power (Alfa Aesar 99.9995 %) was added and stirred. Potassium permanganate (2 grams) was added slowly to the above mixture and the resulting product stirred for 30 min at 40 ^{o}C. The mixture was diluted with 30 mL of water and the temperature was raised to 80 ^{o}C, followed by addition of 4 mL of 30 % of hydrogen peroxide. The solution turned brown and the final product obtained was washed with de-ionized water and dried in vacuum at 50 ^{o}C for 12 h.

Synthesis of Few-layer graphene: Few-layer graphene (HG) was prepared by the arc evaporation of graphite in a water-cooled stainless steel chamber filled with a mixture of hydrogen (200 torr) and helium (500 torr) without using any catalyst [25]. In a typical experiment, a graphite rod (Alfa Aesar with 99.999% purity, 6 mm in diameter and 50 mm long) was used as the anode and another graphite rod (13 mm in diameter and 60 mm in length) was used as the cathode. The arc-discharge current was in the 100- 150 A range, with a maximum open circuit voltage of 60 V. The graphene obtained by this method i.e., arc evaporation of graphite contains 2-4 layers.

Synthesis of nitrogen-doped graphene: To prepare nitrogen-doped graphene samples, RGO or HG (30 mg) were dispersed in 50 mL absolute ethanol, to which urea (300 mg) was added. The mass ratio between the graphene sample and urea was 1:10. The

aqueous mixture was sonicated for 2 h, followed by evaporation of ethanol at 50 ^{o}C to give a grey powder. The powder was finely milled, made into a pellet, transferred to a quartz boat and heated to different temperatures ranging from 600 to 900 ^{o}C for 90 min in a nitrogen atmosphere. The products were re-dispersed in water and sonicated for 2 hours. After sonication, the product was centrifuged and washed several times with de-ionized water to remove residual species adsorbed on the surfaces. Nitrogen-doped RGO samples prepared from RGO I and RGO II are designated as NRGO I and NRGO II respectively. The temperature of the reaction is indicated in the sample as NRGO (I/II)-600,-700,-800,-900.

Characterization: Elemental analysis of the nitrogen-doped RGO samples was carried out using a Perkin-Elmer 2400 CHN analyzer. X-ray photoelectron spectra (XPS) of the nitrogen doped samples were recorded with an Omicron nanotechnology spectrometer. BET surface areas were measured with a Quanta Chrome Autosorb-1 instrument. Thermogravimetric analysis (TGA) of the samples was carried out in a flowing argon atmosphere or in air with a heating rate of 10 ^{o}C per minute using a Mettler-Toledo-TG-850 apparatus. Transmission electron microscope (TEM) images were recorded with a JEOL JEM 3010 instrument fitted with a Gatan CCD camera operating at an accelerating voltage of 80 kV. Raman spectra were recorded at different locations of the sample using Jobin Yvon LabRam HR spectrometer with 632 nm Ar laser. Atomic force microscope (AFM) measurements were performed using an Innova atomic force microscope.

Electrochemical measurements: For electrochemical measurements, a two-electrode system was employed. The electrochemical performance of nitrogen-doped graphene and RGO samples as well as borocarbonitrides was examined in 6 M KOH aqueous electrolyte as well as in an ionic liquid (tetraethylammonium tetrafluoroborate ($TEABF_4$, electrochemical grade >99%, Sigma Aldrich) in acetonitrile) without any binder or carbon additive. The graphene and BCN electrodes and supercapacitor cells were fabricated following Conway [1]. The mass of each electrode was 5 mg in the case of HG, BCN, and 8 mg in the case of RGO and nitrogen doped RGO samples. The geometrical area of each electrode is 1.3266 cm^2 and the sample loading was ~3.7707 mg/cm^2 for HG, BCN, and ~6.0331 mg/cm^2 for the RGO samples. For measurements in the ionic liquid, the electrochemical cells were fabricated in mBraun glove box maintaining oxygen and

moisture less than 0.1 ppm. The electrochemical performance of the graphene electrodes was determined by testing the cyclic voltammograms (CV) and constant current charge–discharge curves using PG262A potentiostat/galovanostat, (Technoscience Ltd, Bangalore, India).

Table 1. Nitrogen content in graphene and reduced graphene oxide[a]

Sample	Temperature (°C)	Nitrogen content (wt%)	SA_{BET}(m^2/g)
NHG	900	1.8	41
RGO I	900	–	312
NRGO I-900	900	2.5	348
NRGO I-800	800	3.8	405
NRGO I-700	700	5.9	458
NRGO I-600	600	8.5	600
NRGO II-900	900	4.5	527
NRGO II-800	800	2.5	411
NRGO II-700	700	2.3	420

[a]Weight ratio of graphene to urea in all the cases was 1:10

1.2.1.4 Results and discussion

In our synthesis of nitrogen-doped RGO, the reaction with urea was carried out at different temperatures between 600 and 900 °C by maintaining the graphene:urea (G:U) weight ratio at 1:10. The nitrogen content of the doped graphene samples as found by both XPS and elemental analysis was found to decrease with increase in reaction temperature (see Table 1). The NRGO I sample prepared at 600 °C had the highest nitrogen content of 8.5 wt. %. Table 1 also lists the surface areas of all the samples. We see that NRGO I prepared at 600 °C shows the highest surface area. The sample heated at 900 °C, on the other hand shows the highest surface areas amongst NRGO II, but smaller than that of NRGO I-600. Reaction at 900 °C yielded a nitrogen content of 2.5 wt. %. Reaction of pure graphene (HG) at 900 °C gave a nitrogen content of ~ 2 wt. % when the G:U ratio was 1:10. Reaction of RGO II with urea (G:U ratios of 1:10) at 900 °C gave 4.5 wt. % of nitrogen as found by with elemental analysis and XPS (Table 1). The presence oxygen functionalities in the samples appears to be responsible for the nitrogen content

rise in NRGO samples. In order to understand the nature of nitrogen in NRGO and NHG we have carried out a detailed study of the N (1s) region of the X-ray photoelectron spectra (XPS). In Figure 1(a & b), we show the N (1s) spectra of NRGO I-900 and NHG-900 respectively. The N 1s peak could be deconvoluted into three features with the peak at 398.2 eV corresponding to pyridinic nitrogen and that at 400.1 eV corresponding to pyrollic nitrogen (Scheme I). The peak at 401.8 eV corresponds to graphitic nitrogen. We see that the content of pyridinic nitrogen is higher than that of pyrollic nitrogen. In Figure 1(b), we show the N 1s spectra of NHG prepared at 900 ^{o}C (G:U of 1:10). The spectra was deconvoluted into three peaks 398.2, 400.1 and 401.7 eV due to pyridinic, pyrollic and graphitic nitrogens respectively. Pyrollic nitrogen content is higher in this sample.

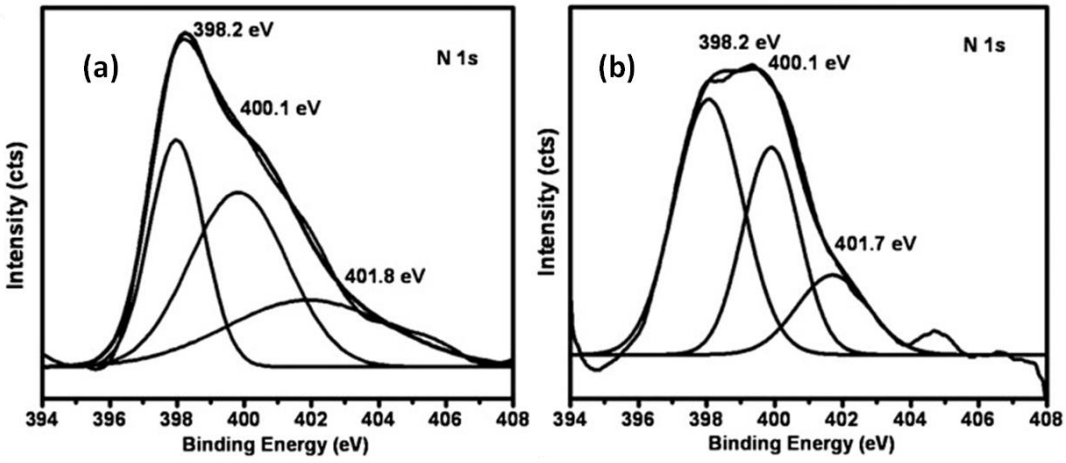

Figure 1. N 1s core level XP spectra of (a) NRGO I-900 °C and (b) NHG-900.

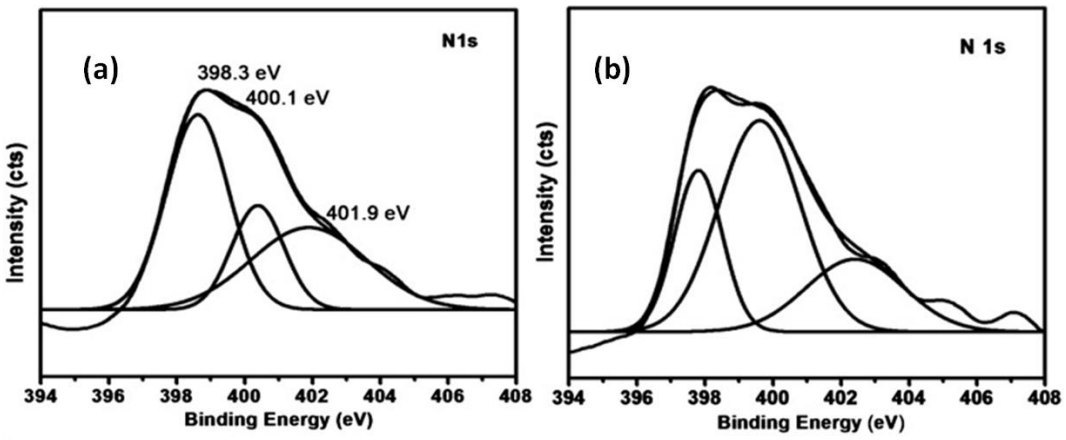

Figure 2 N 1s core level XP spectra of (a) NRGO II-900 and (b) NRGO II-800.

The N (1s) spectra of NRGO II-900 and NRGO II-800 are shown in Figure 2(a & b) respectively. Here also, the N 1s peak could also be deconvoluted into three features as described earlier. The peak at a binding energy of 398.3 eV corresponds to pyridinic nitrogen and the peak at 400.1 eV corresponds pyrollic nitrogen. The peak at 401.9 eV corresponds to graphitic nitrogen. We see the pyridinic nitrogen is maximum in NRGO II-900 and the pyrollic nitrogen is maximum in the sample prepared at 800 ^{o}C. The percentage of graphitic nitrogen is slightly greater in NRGO II-900 compared to NRGO II-800. NHG samples also shows a similar N 1s spectrum, although the lower intensities and different proportions of the various species.

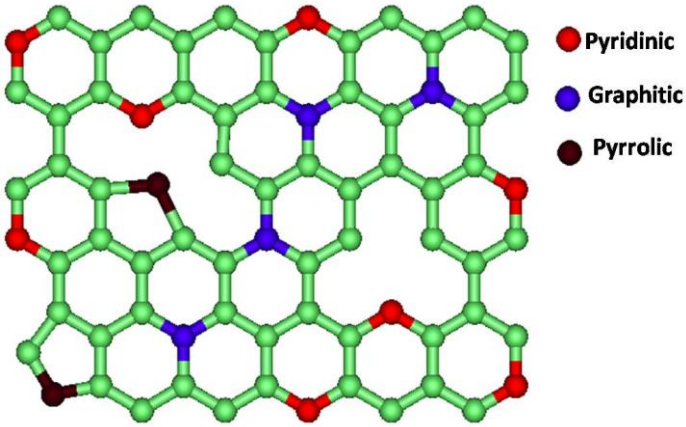

Scheme 1. Bonding of different nitrogens in N-doped graphene samples

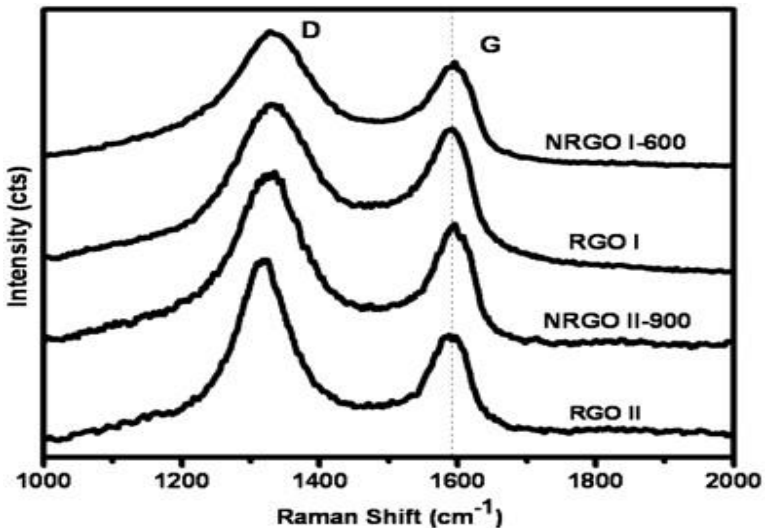

Figure 3. Raman spectra of RGO I, NRGO I-600, RGO II and NRGO II-900

In order to evaluate the degree of structural deformations of the graphene and nitrogen-doped graphene samples, Raman spectroscopy was carried out. The D band, at approximately 1340 cm^{-1} for RGO is disorder induced, attributable to structural defects and other disordered structures on the graphitic plane. The G-band, at approximately 1590 cm^{-1} of RGO is commonly observed for all graphitic structures. G-band can be attributed to the E_{2g} vibrational mode present in the sp^2 bonded graphitic carbons. The intensity ratio of D band to G band, namely the I_D/I_G ratio, provides the measurement for the amount of structural defects. In Figure 3, we show the Raman spectra of the RGO I, NRGO I-600, RGO II and NRGO II-900. The G-band in the nitrogen-doped graphene samples is shifted to higher frequencies by about 5–6 cm^{-1}. The D-band position is essentially insensitive to nitrogen content. The I_D/I_G ratio increases from 1.1 in RGO I to 1.4 in NRGO I-600. The G-band of NHG also shifts towards higher frequency relative to HG. The increase in the G-band frequency is around 5 cm^{-1}. HG shows G-band at 1570 cm^{-1} and the NHG show the G-band at 1575 cm^{-1}. There is no significant change in the I_D/I_G ratio.

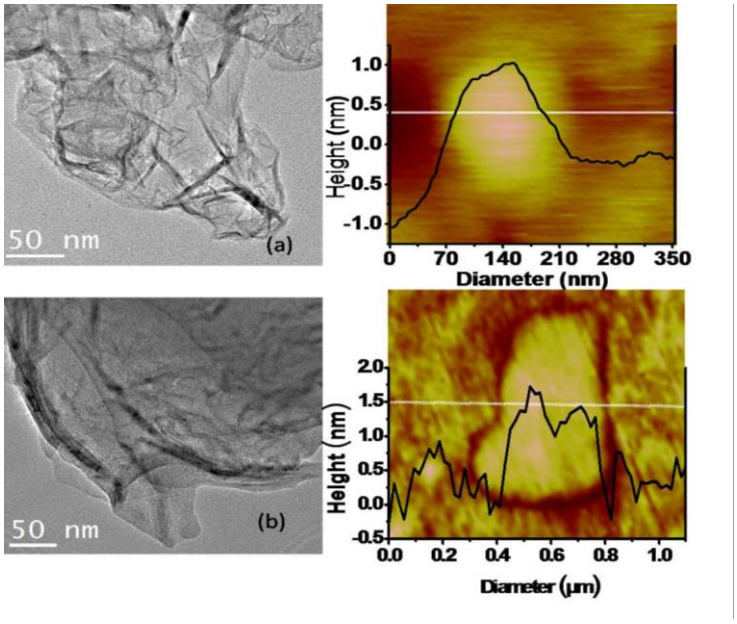

Figure 4. TEM images of (a) NHG and (b) NRGO II-900. AFM images of these samples are shown alongside.

We have shown typical TEM and AFM images of NRGO II-900 and NHG in Figure 4. The TEM image of NHG in Figure 4(a) reveals the presence of 2-4 layers, consistent

with the AFM image shown alongside. The TEM and the AFM images of N-RGO show that it has 4-5 layers. In Figure 5(a) we show the TGA curve of N-RGO (G:U of 1:10) samples prepared at 900 °C and 800 °C along with the TGA curve for RGO. In Figure 5(b), we show the TGA curve of NHG (G:U of 1:10) prepared at 900 °C. We notice a slight increase in the thermal stability of the nitrogen doped samples.

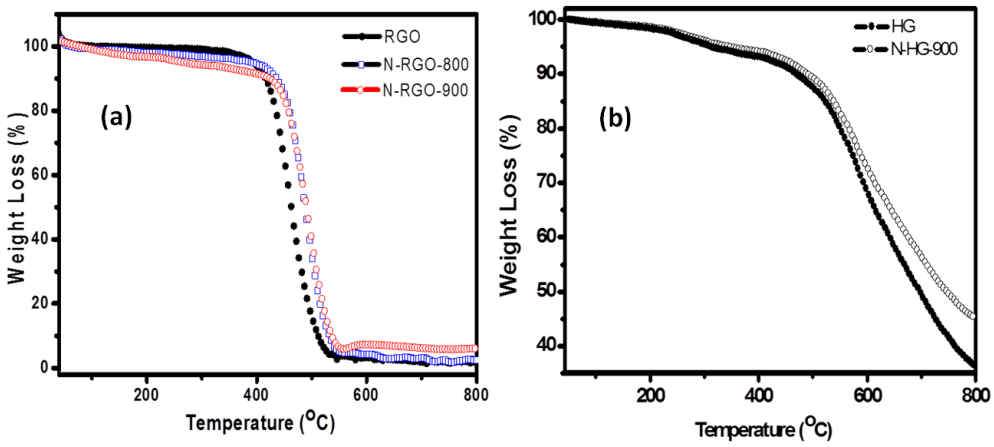

Figure 5. TGA curves of (a) RGO, NRGO II at 800 °C and 900 °C (b) HG and NHG at 900 °C.

Electrochemical performance: The electrochemical performance of the nitrogen-doped graphene and reduced graphene oxides (NHG, NRGO I and NRGO II) have been investigated in detail by means of CV, galvanostatic charge-discharge curves and electrochemical impedance spectroscopy (EIS), in comparison with measurements on the undoped graphene and RGO samples. In Figure 6(a), we show typical CV curves of RGO I and NRGO I (scan rate of 100 mV/s) for a sample loading of ~8 mg per electrode. The CV curve of RGO I shows Faradaic pseudocapacitance due the oxygen functionalities, but RGO I heated at 900 °C shows non-faradic behaviour because of the removal of most of the oxygen functionalities. There is a significant increase in the capacitance of the nitrogen-doped sample with increase in nitrogen content. We have got maximum capacitance 85 F/g at a scan rate of 100 mV/s for NRGO I-600 with a nitrogen content of 8.5 wt. %. The specific capacitance of the NRGO I-600 electrode under scan rates of 80, 40, 20 and 10 mV/ s are 89, 98, 110 and 126 F/g respectively. The galvanostatic charge-discharge curves of RGO I and NRGO I samples were measured at a potential window of 0-1 V at a current density of 60 mA/g and the results shown in Figure 6(b). The discharge

time increases with the increase in nitrogen content. The charge-discharge curves of the nitrogen-doped graphene samples are nearly symmetrical similar to those of ideal electrochemical double-layer capacitors. The specific capacitance values (at 60 mA/g) for RGO I and RGO I-900 are 24 and 30 F/g respectively while those of NRGO I-900, NRGO I-800, NRGO I-700 and NRGO I-600 are 48, 59, 71 and 84 F/g respectively.

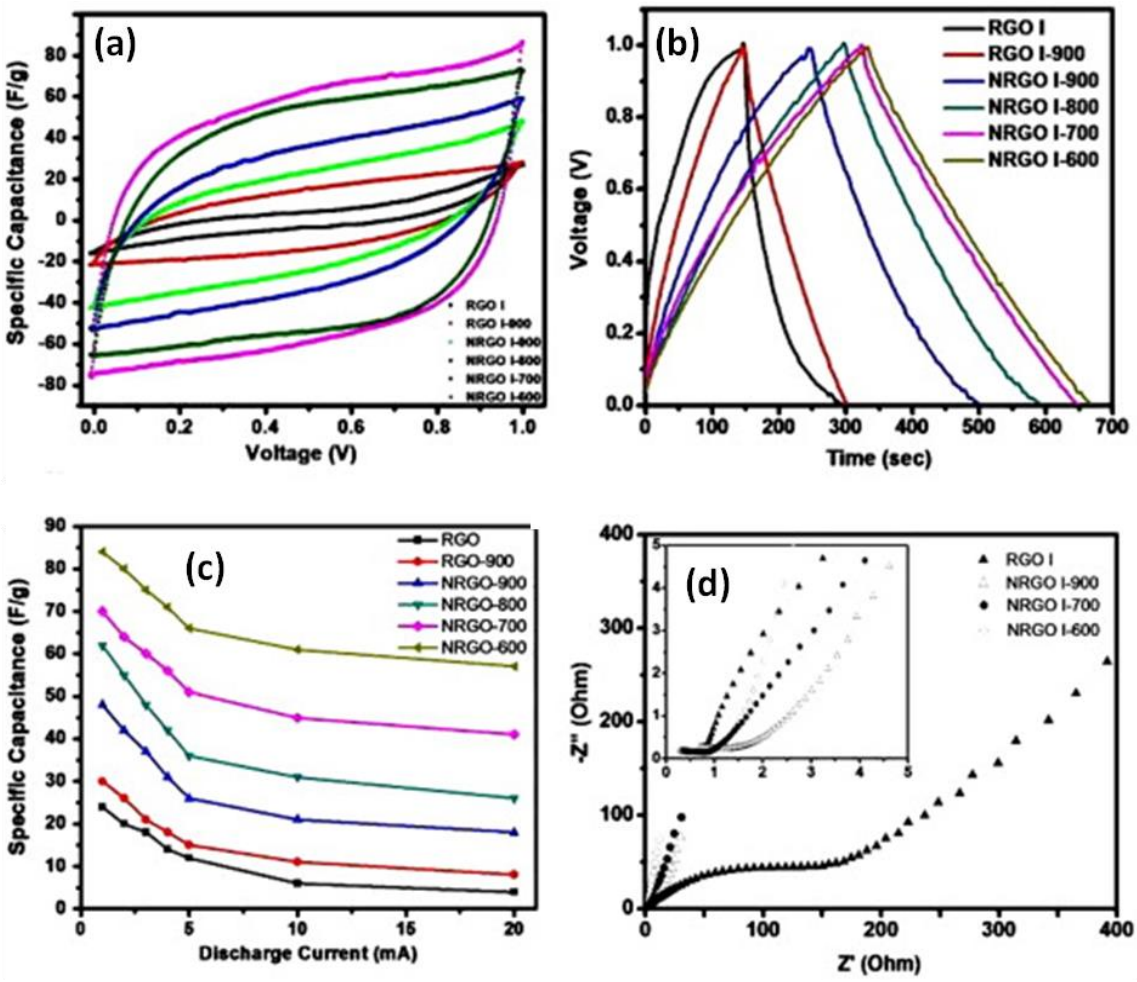

Figure 6. (a) Cyclic voltammograms of RGO I and NRGO I prepared at different temperatures (at scan rate 100 mV/s) (b) Galvanostatic charge/discharge curves for RGO I and NRGO I electrodes (at 60 mA/g) (c) Specific capacitance as a function of discharge current. (d) Nyquist curves of for RGO I and NRGO I electrodes.

Figure 6(c) shows the relationship between specific capacitance and discharge current. The specific capacitance decreases with increase in discharge current. In Figure 6(d), we present Nyquist plots where RGO I shows a charge transfer resistance at the

electrode/electrolyte interface while nitrogen-doped RGO I shows a vertical line in the low frequency region and the slope increase with increase in nitrogen content. The more the vertical curve is more closely does the electrochemical cell perform as an ideal capacitor. Magnified data of high frequency region is shown in the inset of Figure 6(d) reveals that N-doped RGO electrodes associated with less resistance than to undoped graphene. The high frequency region of the Nyquist plots show small equivalent series resistance (ESR), the value for RGO I being 0.70 ohm. The values for NRGO I-900, NRGO I-700, NRGO I-600 are 0.67, 0.37, 0.29 ohm respectively.

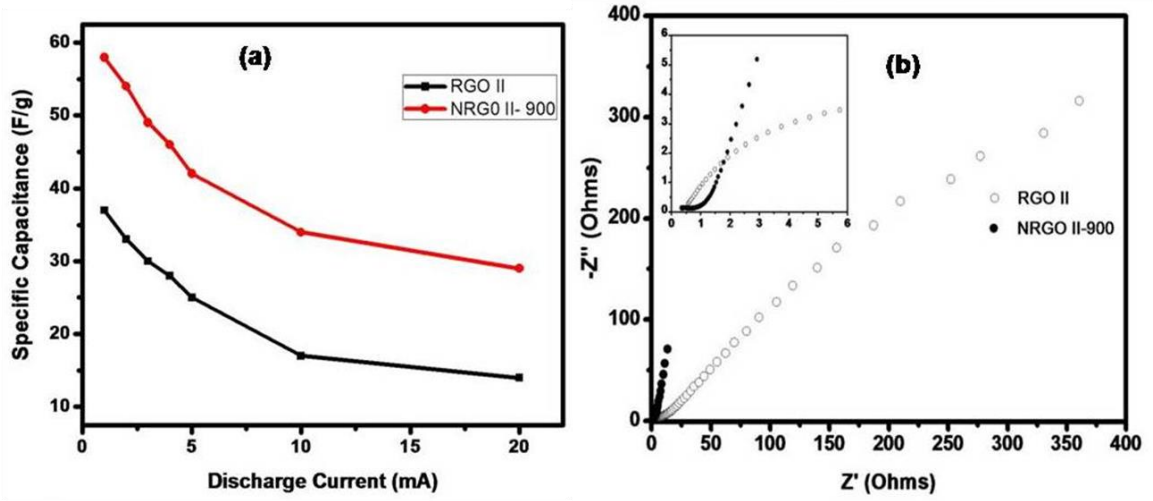

Figure 7. (a) Specific capacitance as a function of discharge current in aqueous media. (b) Nyquist curves of for RGO and NRGO II-900 electrodes.

The specific capacitance of RGO II also increases with nitrogen doping, the values being 37 F/g and 58 F/g for RGO II and NRGO II-900 respectively at a scan rate of 100 mV/s. NRGO II-800 and NRGO II-700 samples showed capacitance values of 49 F/g and 46 F/g respectively at 60 mA/g. Figure 7(a) shows the relationship between the specific capacitance and the discharge current. Specific capacitance decreases with increase in discharge current. The electrochemical impedance spectra are shown in Figure 7(b). NRGO II-900 has less charge transfer resistance compared to RGO II. Magnified EIS data of high frequency region are shown in the inset of Figure 7(b), the ESR value being 0.35 and 0.21 ohm for RGO I and NRGO II-900 respectively. We thus see that NRGO I-600 with the highest nitrogen content and surface area gives the best supercapacitor performance.

Amongst the NRGO II samples, the one prepared at 900 ^{o}C with the highest nitrogen content and surface area gives the best results. NRGO I-600 and NRGO II-900 show a capacitance of 14.1μF/cm^2 and 11.0 μF/cm^2 respectively. We studied the long-term cyclic stability of NRGO I-600 by repeating the galvanostatic charge/discharge test between 0 and 1 V at a current density of 0.5 A/g for 1000 cycles. After 1000 cycles, the capacitance decreased by 13 % of initial capacitance and exhibiting excellent cycle stability. We obtained a maximum energy density of 11.8 Wh/kg for NRGO II-600 at a current density of 60 mA/g.

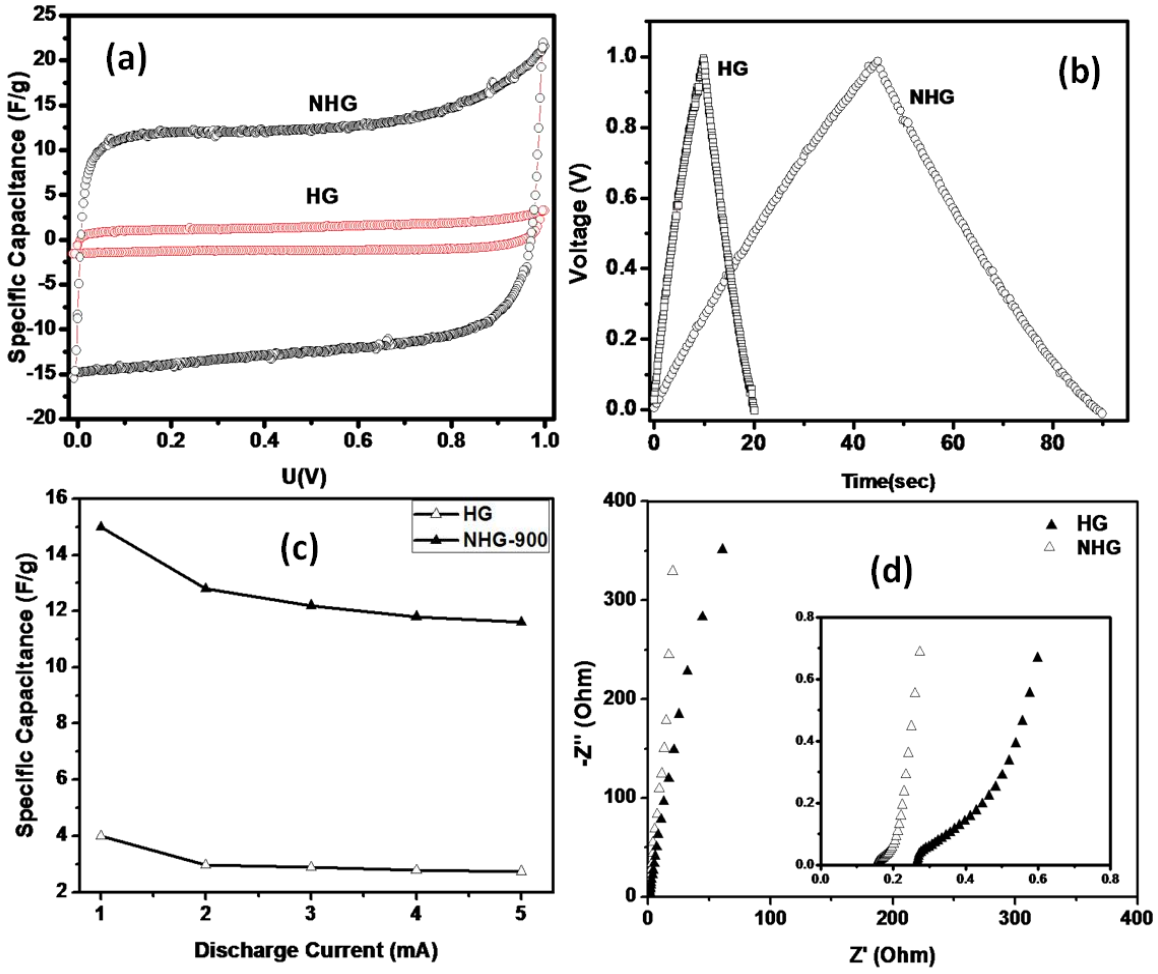

Figure 8. (a) Cyclic voltammograms of HG and NHG (at scan rate 100 mV/s) prepared at 900 ^{o}C (b) Charge/discharge curves (at 60 mA/g) for HG and NHG electrodes (c) Specific capacitance as a function of discharge current. (d) Nyquist curves of for HG and NHG electrodes

In Figure 8(a), we show the CV curves of HG and NHG-900 (scan rate of 100 mV/s) for a sample loading of ~8 mg per electrode in aqueous 6M KOH. The CV curve of NHG shows non- Faradaic behaviour because of the high carbon content and less defects. There is a significant increase in the capacitance of the nitrogen-doped sample when compared to undoped HG. The specific capacitance values are 2 F/g for HG and for NHG it is 14 F/g. The galvanostatic charge-discharge curves measured at 60 mA/g is shown in Figure 8(b). The specific capacitances of HG and NHG-900 are 4 F/g and 15 F/g respectively at current density of 100 mA/g from galvanostatic charge-discharge curves. Figure 8(c) shows the relationship between specific capacitance and discharge current. The specific capacitance decreases with increase in discharge current. The ESR values of HG and NHG is 0.27 and 0.15 ohm respectively as shown in Figure 8(d) and the inset shows the high frequency region.

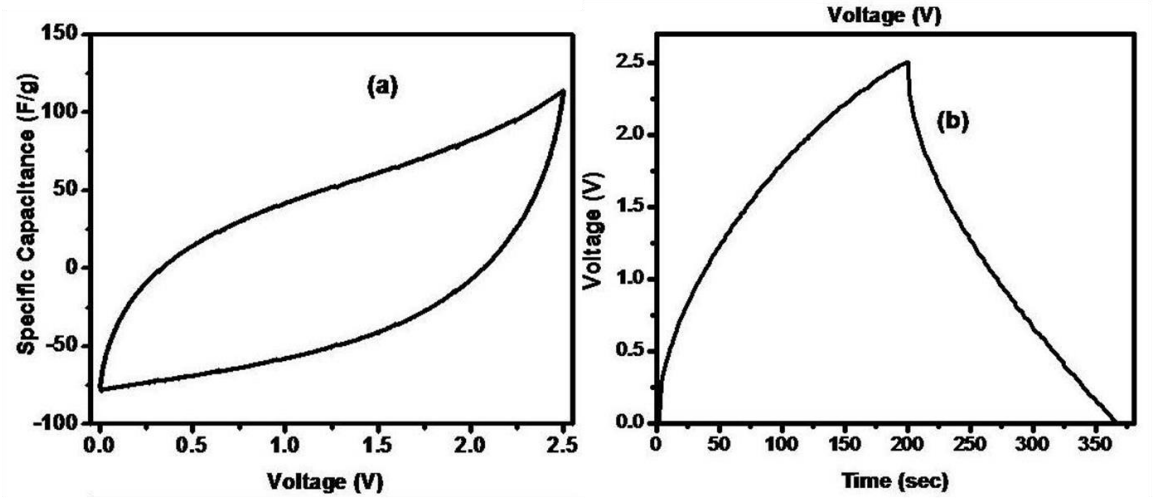

Figure 9. (a) Cyclic voltammogram of the NRGO I-600 in the ionic liquid $TEABF_4$ measured at 100 mV/s. (b) Galvanostatic charge-discharge of NRGO I-600 in $TEABF_4$ at 1 A/g.

We have carried out electrochemical measurements on NRGO I in the ionic liquid with a potential window of 0-2.5 V. Figure 9(a) shows the cyclic voltammogram of the NRGO I-600 in the ionic liquid $TEABF_4$ measured at 100 mV/s. The specific capacitance of the NRGO I-600 electrode under scan rates of 100, 80, 40, 20 and 5 mV/s are 99, 119, 128, 171 and 258 F/g respectively. Galvanostatic charge-discharge measurements on

NRGO I-600 made at a current density of 1 A/g, the specific capacitance was 249 F/g (Figure 9 (b)). The specific capacitance of NRGO I-600 in the ionic liquid was less than that in the aqueous electrolyte when the potential window was 0-1V. We obtained a maximum energy density of 34.5 Wh/kg for NRGO I-600 at a current density of 1 A/g. Comparison of our results on NRGO samples with those in the literature will be in order. Graphene in aqueous electrolytes are reported to show a specific capacitance in the range of 69-203 F/g [11, 21]. However, nitrogen-doped graphene has been found to show a specific capacitance of 56 F/g at a current density of 1 A/g in a two-electrode system [21]. Our results with NRGO I-600, therefore, appears to be better than or as good as literature values. We have obtained a specific capacitance of 59 F/g at a current density of 1 A/g in a two-electrode system. Based on cyclic voltammograms of graphene in ionic liquids, reported specific capacitance values are 72 and 106 F/g at 5 mV/s [4, 10]. Nitrogen doped graphene showed a specific capacitance of 248 F/g at 5 mV/s or 246 F/g at 1 A/g. The NRGO I-600 sample studied by us showed a specific capacitance of 257 F/g at 5 mV/s (249 F/g at 1 A/g).

1.2.2 Supercapacitors based on borocarbonitrides

1.2.2.1 Introduction

Graphene is known for its fascinating physical properties, such as quantum Hall effect and massless Dirac fermions, with potential applications in nanoelectronics and energy storage [5]. Single-layer graphene shows very high carrier mobility (~1.5 × 10^4 cm^2 V^{-1} s^{-1} at room temperature) [6]. In spite of this large carrier mobility, its gapless nature limits its performance as a versatile electronic material [9]. Borocarbonitrides with the general formula of $B_xC_yN_z$ constitute a new family of 2D materials, whose composition can be varied over a wide range [26]. These materials are generally nanoplatelets containing graphene and BN domains, possibly along with BCN rings. If the ratio of BN to carbon is 1:1 the composition would be BCN. Such $B_xC_yN_z$ species would therefore be comparable to the few-layer graphenes wherein the hexagonal networks are formed with B–C, B–N, C–N and C–C bonds but with no B–B or N–N bonds.

Borocarbonitrides have been generated by several means. These methods include chemical vapor deposition (CVD), pyrolysis of precursors or reaction of precursors in gas phase and solid state reaction of precursors [26]. Bartlett and co-workers [27] carried gas phase synthesis of $B_xC_yN_z$ by the reaction of CH_4 with ammonia and BCl_3 at 400-700 °C to obtain a composition of $B_{0.35}C_{0.30}N_{0.35}$ (BCN). A similar gas phase reaction using BBr_3, ammonia gas and 20% ethylene gas mixed with nitrogen as sources of boron, nitrogen and carbon gave $BC_{1.6}N$ containing domains of BN and graphene [28]. Pyrolysis of the BH_3–trimethylamine adduct is reported to yield $B_xC_yN_z$ nanotubes [29]. $B_xC_yN_z$ type materials have been prepared by the nitridation of boric acid and carbonization of saccharose in molten urea [30]. Urea gives NH_3 on heating and acts as a good nitrogen source.

1.2.2.2 Scope of the present investigation

Borocarbonitrides which have insulating BN and conducting graphite (or graphene) as limiting compositions, have many potential applications. The borocarbonitrides prepared for the purpose by the high-temperature reaction of carbon, boric acid and urea possess high surface areas and are likely to contain BCN rings as well as graphene and BN domains. We have carried out electrochemical supercapacitor measurements in aqueous KOH medium with an accessible voltage range 0-1 V, and in an ionic liquid medium in the voltage range of 0-2.5 V.

1.2.2.3 Experimental section

High surface area borocarbonitrides, $B_xC_yN_z$ were synthesized in the following manner. In a typical synthesis, 0.1 g H_3BO_3, 0.5 g activated charcoal and 2.4 g urea were taken in 50 mL water and sonicated for 15 min. Water was slowly evaporated at 80 ^oC to get thick slurry. The slurry was transferred to a quartz boat and heated at 900 ^oC for 10 h in nitrogen atmosphere followed by ammonia treatment at 930 ^oC for 3 hrs. We have prepared two borocarbonitrides samples with different compositions.

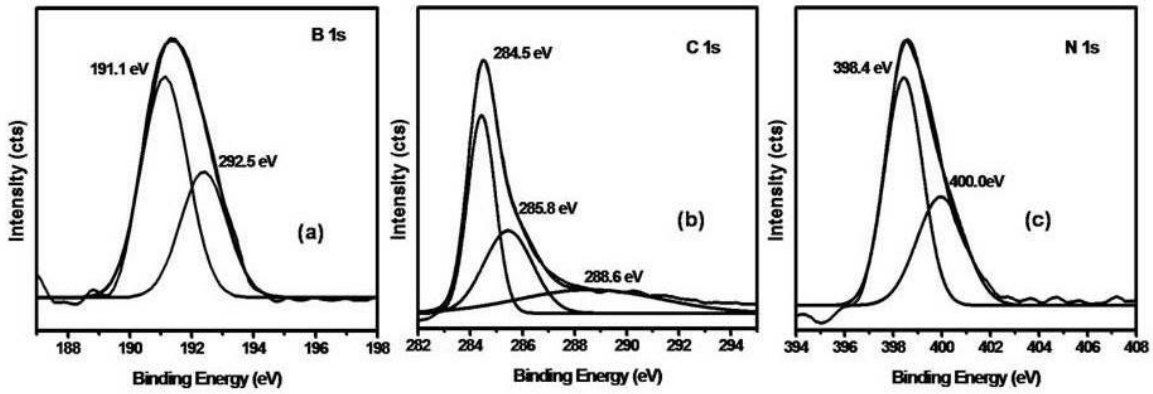

Figure 10. X-ray photoelectron spectra of $BC_{4.5}N$ in the (a) B 1s (b) C 1s and (c) N 1s regions.

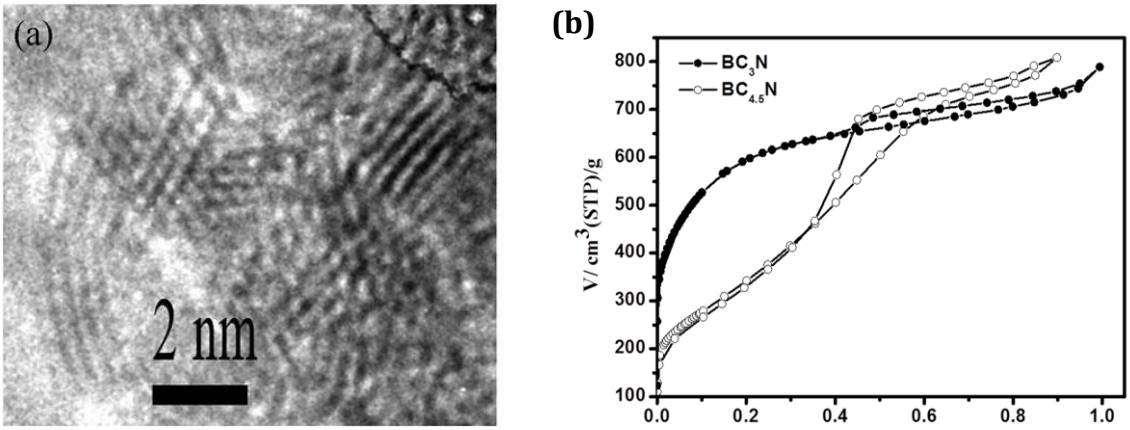

Figure 11. (a) HRTEM image and (b) BET surface area curves of BCN nanosheets

1.2.2.4 Results and discussion

We have prepared two different $B_xC_yN_z$ samples by the urea route. We have carried out XPS measurements on the samples to determine the compositions. The compositions of the two samples are found to be $BC_{4.5}N$ and BC_3N. In Figure 10, we show the XP spectrum of $BC_{4.5}N$. In The B 1s spectrum could be deconvoluted into two different features centered at 191.1 and 192.6 eV corresponding to B-N and B-C bonds respectively (Figure 10(a)). The C 1s feature could be can be deconvoluted into three peaks corresponding to C-B, C-C and C-N bonds at 284.5, 285.8 and 288.6 eV respectively (Figure 10 (b)). The N 1s feature could be deconvoluted into N-B and N-C contributions centered at 398.4 and 400.0 eV respectively as shown in Figure 10 (c) [23]. High resolution transmission

electron microscopy (HRTEM) images of BCN show the presence of 2–6 layers (Figure 11(a)) and the $BC_{4.5}N$ and BC_3N have BET surface areas 1280 and 1300 cm^2/g respectively (Figure 11(b)).

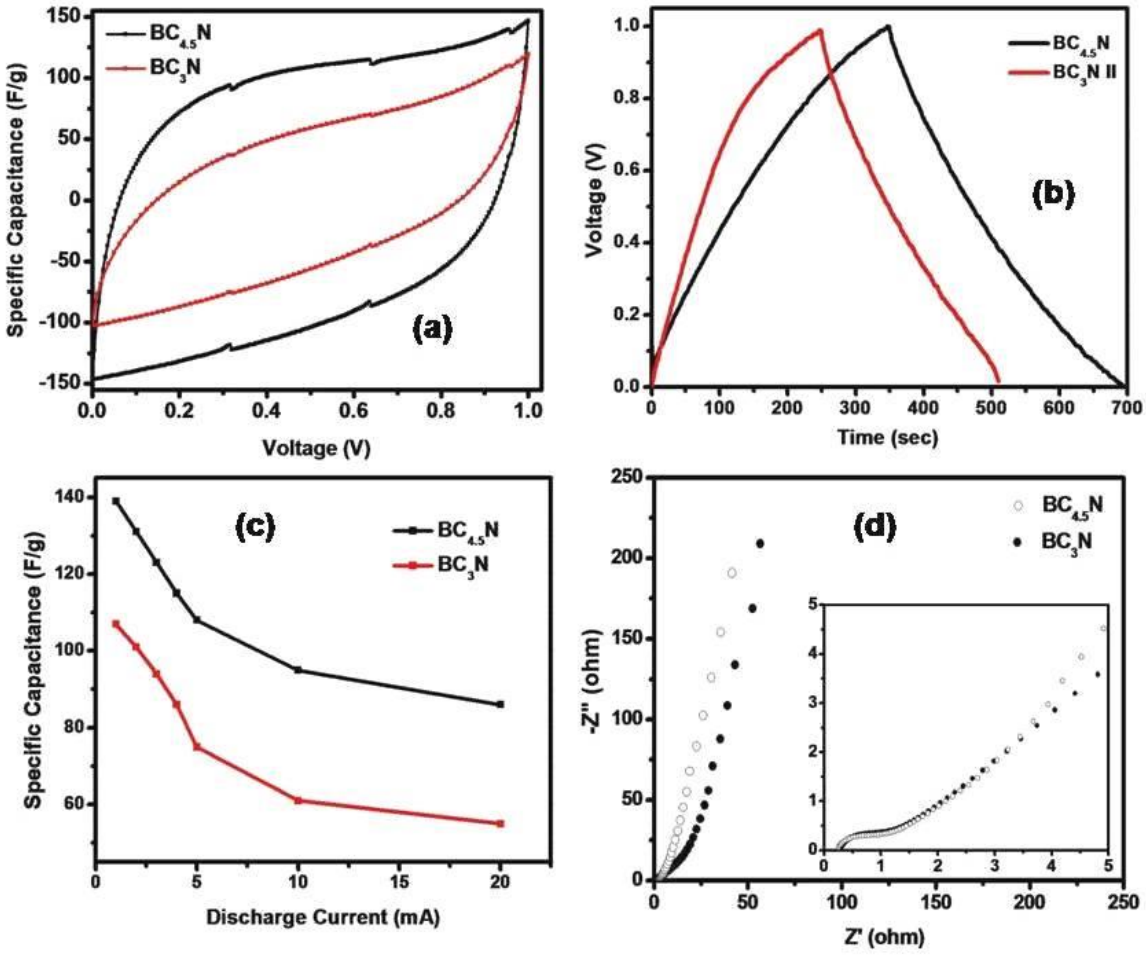

Figure 12. (a) Cyclic voltammograms of $BC_{4.5}N$ and BC_3N at a scan rate of 100 mV/s (b) Galvanostatic charge/discharge curves for $BC_{4.5}N$ and BC_3N electrodes at a current density of 100 mA/g (c) Specific capacitance as a function of discharge current. (d) Nyquist curves of for $BC_{4.5}N$ and BC_3N electrodes.

Figure 12(a) shows the cyclic voltammograms of $BC_{4.5}N$ and BC_3N recorded with a two-electrode system at 100 mV/s. The CV curves exhibit a rectangular shape at all scan rates. The specific capacitance of BCN electrodes decreases with the increase in the scan rate. The specific capacitance of $BC_{4.5}N$ at scan rates of 100, 80, 40, 20 and 10 mV/ s are 144, 149, 155, 161, 169 F/g respectively. The specific capacitance of BC_3N at scan rates of 100, 80, 40, 20 and 10 mV/ s are 102, 110, 119, 130, 138 F/g respectively. Galvanostatic charge-discharge curves of the BCN electrodes were measured at a current

density of 100 mA/g are shown in Figure 12(b). The value of specific capacitance decreases with the increase in the discharge current; for $BC_{4.5}N$ and BC_3N the values were, 140 and 109 F/g respectively at 100 mA/g (Figure 12(c)). We show the electrochemical impedance spectra in Figure 12(d). Both the BCN samples show ideal supercapacitor behaviour in the low frequency region. Magnified data in the high frequency region is shown in the inset of Figure 12(d). The equivalent series resistance of $BC_{4.5}N$ and BC_3N electrodes are 0.25 and 0.30 ohms respectively. We studied the long-term cyclic stability of $BC_{4.5}N$ by repeating the galvanostatic charge/discharge test between 0 and 1 V at a current density of 0.5 A/g for 1000 cycles. After 1000 cycles, the capacitance decreased by 9 % of the initial capacitance, thereby exhibiting excellent cycle stability better than NRGO I-600. We obtained a maximum energy density of 20.8 Wh/kg for $BC_{4.5}N$ at a current density of 100 mA/g.

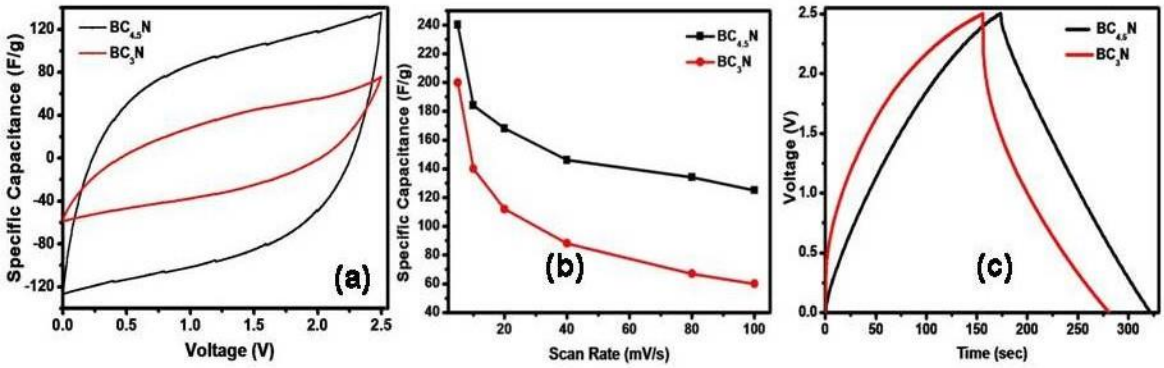

Figure 13. (a) Cyclic voltammograms of the $BC_{4.5}N$ and BC_3N in the ionic liquid, $TEABF_4$ measured at 100 mV/s. (b) Specific capacitance as a function of scan rate. (c) Galvanostatic charge-discharge of $BC_{4.5}N$ and BC_3N in $TEABF_4$ at 1 A/g.

We have carried out electrochemical measurements on the borocarbonitride electrodes in the ionic liquid with a potential window of 0-2.5 V. The specific capacitance of the $BC_{4.5}N$ and BC_3N electrodes are 125 and 60 F/g respectively at a scan rate of 100 mV/s (Figure 13(a)). The specific capacitance depends significantly on the scan rate and decreases as the scan rate increases (Figure 13(b)). Galvanostatic charge-discharge measurements on $BC_{4.5}N$ and BC_3N samples at a current density of 1 A/g, gave specific

capacitance values of 234 and 203 F/g in the ionic liquid (Figure 13(c)). We obtained a maximum energy density of 32.5 Wh/kg for $BC_{4.5}N$ at a current density of 1 A/g

1.2.3 Conclusions

In conclusion, N-doped graphenes were synthesized by heating graphene and urea at different temperatures. The nitrogen content in the graphene lattice can reach ~7 wt. % which can be tuned by changing the ratio of graphene and urea as well as at different temperatures. Oxygen-containing functional groups in RGO and amino-groups of urea are suggested to be essential to form C-N bonds and helps in greater doping. Nitrogen-doped reduced graphene oxide (specially NRGO I) is found to be a good electrode material for the use in supercapacitors. The value of specific capacitance is determined by the nitrogen content as well as the surface area. Borocarbonitrides appear to be even more suited for supercapacitor applications. The results obtained by us in aqueous medium and in an ionic liquid indicate that the latter can be conveniently used to have the advantage of a wider voltage range, without the loss of other desirable features.

References

[1] Conway BE. Transition from "Supercapacitor" to "Battery" Behavior in Electrochemical Energy Storage. J Electrochem Soc. 1991;138:1539-48.

[2] Conway BE. Similarities and Differences between Supercapacitors and Batteries for Storing Electrical Energy. Electrochemical Supercapacitors: Scientific Fundamentals and Technological Applications. Boston, MA: Springer US; 1999. p. 11-31.

[3] Zhu Y, Murali S, Stoller MD, Ganesh KJ, Cai W, Ferreira PJ, et al. Carbon-Based Supercapacitors Produced by Activation of Graphene. Science. 2011;332:1537-41.

[4] Vivekchand SRC, Rout CS, Subrahmanyam KS, Govindaraj A, Rao CNR. Graphene-based electrochemical supercapacitors. Journal of Chemical Sciences. 2008;120:9-13.

[5] Rao CNR, Sood AK, Subrahmanyam KS, Govindaraj A. Graphene: The New Two-Dimensional Nanomaterial. Angewandte Chemie International Edition. 2009;48:7752-77.

[6] Geim AK, Novoselov KS. The rise of graphene. Nat Mater. 2007;6:183-91.

[7] Das B, Voggu R, Rout CS, Rao CNR. Changes in the electronic structure and properties of graphene induced by molecular charge-transfer. Chem Comm. 2008:5155-7.

[8] Panchakarla LS, Subrahmanyam KS, Saha SK, Govindaraj A, Krishnamurthy HR, Waghmare UV, et al. Synthesis, Structure, and Properties of Boron- and Nitrogen-Doped Graphene. Adv Mater. 2009;21:4726-30.

[9] Wang H, Maiyalagan T, Wang X. Review on Recent Progress in Nitrogen-Doped Graphene: Synthesis, Characterization, and Its Potential Applications. ACS Catal. 2012;2:781-94.

[10] Wen Z, Wang X, Mao S, Bo Z, Kim H, Cui S, et al. Crumpled Nitrogen-Doped Graphene Nanosheets with Ultrahigh Pore Volume for High-Performance Supercapacitor. Adv Mater. 2012;24:5610-6.

[11] Jeong HM, Lee JW, Shin WH, Choi YJ, Shin HJ, Kang JK, et al. Nitrogen-Doped Graphene for High-Performance Ultracapacitors and the Importance of Nitrogen-Doped Sites at Basal Planes. Nano Lett. 2011;11:2472-7.

[12] Lai L, Potts JR, Zhan D, Wang L, Poh CK, Tang C, et al. Exploration of the active center structure of nitrogen-doped graphene-based catalysts for oxygen reduction reaction. Energy Environ Sci. 2012;5:7936-42.

[13] Qu L, Liu Y, Baek J-B, Dai L. Nitrogen-Doped Graphene as Efficient Metal-Free Electrocatalyst for Oxygen Reduction in Fuel Cells. ACS Nano. 2010;4:1321-6.

[14] Li X, Wang H, Robinson JT, Sanchez H, Diankov G, Dai H. Simultaneous Nitrogen Doping and Reduction of Graphene Oxide. J Am Chem Soc. 2009;131:15939-44.

[15] Wei D, Liu Y, Wang Y, Zhang H, Huang L, Yu G. Synthesis of N-Doped Graphene by Chemical Vapor Deposition and Its Electrical Properties. Nano Lett. 2009;9:1752-8.

[16] Jeon I-Y, Shin Y-R, Sohn G-J, Choi H-J, Bae S-Y, Mahmood J, et al. Edge-carboxylated graphene nanosheets via ball milling. Proc Natl Acad Sci U S A. 2012;109:5588-93.

[17] Mou Z, Chen X, Du Y, Wang X, Yang P, Wang S. Forming mechanism of nitrogen doped graphene prepared by thermal solid-state reaction of graphite oxide and urea. Appl Surf Sci. 2011;258:1704-10.

[18] Deng D, Pan X, Yu L, Cui Y, Jiang Y, Qi J, et al. Toward N-Doped Graphene via Solvothermal Synthesis. Chem Mater. 2011;23:1188-93.

[19] Long D, Li W, Ling L, Miyawaki J, Mochida I, Yoon S-H. Preparation of Nitrogen-Doped Graphene Sheets by a Combined Chemical and Hydrothermal Reduction of Graphene Oxide. Langmuir. 2010;26:16096-102.

[20] Zhang Y, Fugane K, Mori T, Niu L, Ye J. Wet chemical synthesis of nitrogen-doped graphene towards oxygen reduction electrocatalysts without high-temperature pyrolysis. J Mater Chem. 2012;22:6575-80.

[21] Sun L, Wang L, Tian C, Tan T, Xie Y, Shi K, et al. Nitrogen-doped graphene with high nitrogen level via a one-step hydrothermal reaction of graphene oxide with urea for superior capacitive energy storage. RSC Adv. 2012;2:4498-506.

[22] Choi E-K, Jeon I-Y, Bae S-Y, Lee H-J, Shin HS, Dai L, et al. High-yield exfoliation of three-dimensional graphite into two-dimensional graphene-like sheets. Chem Commun. 2010;46:6320-2.

[23] Ding W, Wei Z, Chen S, Qi X, Yang T, Hu J, et al. Space-Confinement-Induced Synthesis of Pyridinic- and Pyrrolic-Nitrogen-Doped Graphene for the Catalysis of Oxygen Reduction. Angew Chem Int Ed. 2013;52:11755-9.

[24] Marcano DC, Kosynkin DV, Berlin JM, Sinitskii A, Sun Z, Slesarev A, et al. Improved Synthesis of Graphene Oxide. ACS Nano. 2010;4:4806-14.

[25] Subrahmanyam KS, Panchakarla LS, Govindaraj A, Rao CNR. Simple Method of Preparing Graphene Flakes by an Arc-Discharge Method. J Phys Chem C. 2009;113:4257-9.

[26] Kumar N, Moses K, Pramoda K, Shirodkar SN, Mishra AK, Waghmare UV, et al. Borocarbonitrides, BxCyNz. J Mater Chem A. 2013;1:5806-21.

[27] Kaner RB, Kouvetakis J, Warble CE, Sattler ML, Bartlett N. Boron-carbon-nitrogen materials of graphite-like structure. Mater Res Bull. 1987;22:399-404.

[28] Kumar N, Raidongia K, Mishra AK, Waghmare UV, Sundaresan A, Rao CNR. Synthetic approaches to borocarbonitrides, BCxN (x=1–2). J Solid State Chem. 2011;184:2902-8.

[29] Sen R, Satishkumar BC, Govindaraj A, Harikumar KR, Raina G, Zhang J-P, et al. B–C–N, C–N and B–N nanotubes produced by the pyrolysis of precursor molecules over Co catalysts. Chem Phys Lett. 1998;287:671-6.

[30] Hubáček M, Sato T. Preparation and Properties of a Compound in the B-C-N System. J Solid State Chem. 1995;114:258-64.

1.3 EXTRAORDINARY SUPERCAPACITOR PERFORMANCE OF HEAVILY NITROGENATED GRAPHENE OXIDE OBTAINED BY MICROWAVE SYNTHESIS

Summary*

Although graphene have been successfully demonstrated for high-performance ultracapacitors, their capacitances need to be improved further for wider and more challenging applications. Herein, heavily nitrogenated graphene oxide (NGO) containing ~18 wt.% nitrogen, prepared by microwave synthesis with urea as the nitrogen source. The nitrogen content and species can be controlled by tuning the experimental parameters, including the mass ratio between urea and graphene oxide. NGO shows outstanding performance as a supercapacitor electrode material, with the specific capacitance going up to 461 F/g at 5 mV/s in aqueous electrolyte (6M KOH). The energy densities of the NGOs are remarkable, with the highest value of 44.4 Wh/kg at a current density of 0.3 A/g. The power densities are in the range of 852–10524 W/kg for NGO electrodes.

*A Paper based on this work has been published in J Mater Chem A, 2013, **1**, 7563

1.3.1 Introduction

Nitrogen-doped graphene is a important material due to properties such as the tuneable band-gap, and n-type semiconductivity [1]. Doping nitrogen into graphene not only opens the bandgap, but also opens up interesting electrochemical properties [2, 3]. Recent studies have shown N-doped graphene exhibits superior supercapacitor properties [4, 5]. This is due to the fact that nitrogen atoms in graphene can perform as active sites for adsorbing electrolyte ions and allow redox reactions. However, the nitrogen content of graphene cannot be infinitely doped because the high doping can lead to the formation of carbon nitride films which has extremely low electrical conductivity [6]. In addition, high doping may cause increasing defects which inevitably lead to the decline of the intrinsic features of graphene [6, 7].

Some methods to synthesize nitrogen doped graphene have been reported in literature, which includes nitrogen plasma treatment on graphene [4], arc-discharge between graphite electrodes in presence of ammonia [8], ammonolysis of graphene oxide under CVD conditions and hydrothermal treatment of graphene oxide and urea at different temperatures [9]. Lu et al prepared N-doped graphene sheets using 1,3,5-triazinemolecules as both carbon and nitrogen source [10]. Doping concentration increases with decrease in growth temperature. Shao et al [11] prepared N-doped graphene by exposing graphene to nitrogen plasma whereas Hu et al [12] prepared by thermal reduction of graphene oxide with ammonia hydroxide. N-doped graphene synthesized through thermal conversion of polyacrylonitrile thin film contain 2.7 at. % of nitrogen [13]. Du et al [14] reduced and doped graphene using ammonia solution. Electrothermal reaction of graphite oxide with NH_3 gave N-doped graphene with nitrogen content of 5 wt% [15]. Hydrothermal and solvothermal reactions have been used as effective approaches to fabricate N-doped graphene with a high nitrogen level [16, 17]. Yoon and co-workers [16] developed a hydrothermal process in the presence of hydrazine and ammonia. Bao et al [17] synthesized with a nitrogen level of up to 13 at% by a solvothermal reaction between tetrachloromethane and lithium nitride.

In general, nitrogen atoms could be bound together in four ways in graphene lattice [1]. The sp^2-hybridized carbons will hinder the nitrogen doping into graphene

lattice thus the quaternary-type nitrogen is difficult to form and often forms with lower nitrogen content [18]. Besides, the pyridinic nitrogen and **p**yrrolic nitrogen are easily formed on the graphene surface and also proven to be important electrochemical active sites [3]. Thus, the effective regulation of pyridinic, **p**yrrolic in graphene network with a well-defined pore structure is very important for accelerating application of carbon-based materials in energy storage fields. These nitrogen species also possess different structures and electronic distributions [8, 18]. As to different nitrogen species showing different functions, certain application tends to some main nitrogen species, which emphasizes the importance of selectively synthesizing nitrogen species. For example, the increase of pyridinic-N will be beneficial to improving electrocatalytic performance of ORR in fuel cells and supercapacitors [3, 11]. The effect of N doping types of graphene on supercapacitor performances has been previously investigated [19]. The redox reaction between **p**yrrolic and pyridine nitrogen atoms through Faraday processes increases the pseudocapacitance which contributes to the increase of the capacity of the supercapacitors. In addition, quaternary-type nitrogen will help to improve the wettability between the electrolyte and the electrode, thereby enhancing the capacitance. Moreover, quaternary-type nitrogen also increases the electronic conductivity and able to maintain a stable capacity during fast charging and discharging.

Microwave-assisted synthesis and processing represents a growing field in materials research and successfully entered the field of carbon nanomaterials [20]. By inducing temperatures of up to 1000 °C within just one minute microwave irradiation is a fascinating and promising tool for the preparation and modification of carbon materials [21]. Microwave heating is based on the interaction of matter with electromagnetic radiation. It is independent of the thermal conductivity of the surrounding materials and allows an instantaneous on/off switching of the heating. Due to fast heating rates, shorter treatment times are possible, which result in time and energy saving processes and might even suppress undesired side-reactions and enable new reaction pathways [22]. Transformation of solid materials, e.g., polymers or graphite into carbon nanomaterials, the exfoliation of graphite oxide (GO) to graphene, the cleavage of graphene, or the unzipping of CNTs to obtain C-dots or graphene ribbons have been reported earlier [20].

1.3.2 Scope of the present investigations

Carbon materials are common electrode materials for electrochemical capacitors. To improve their electrochemical performance, the introduction of a heteroatom, such as nitrogen has been reported as a promising approach. We have obtained heavily nitrogenated graphene with different N types and content using microwave synthesis with urea as the nitrogen source. In this process, urea release NH_3 that continually reacts with the oxygen functional groups of GO, which is favourable for doping of high-level nitrogen into graphene skeleton. Importantly, the nitrogen content and types could be tuned by controlling the experimental conditions, including the mass ratio between urea and GO. The highest nitrogen content in this approach could be up to 18 wt. %. Moreover, the synthesized N-doped graphene has surface area of 240 m^2/g. Most importantly, the NGO shows superior supercapacitors properties with an excellent capacitance, cycling stability and high power and energy density. In addition, urea used as nitrogen source is low-cost, nitrogen-enriched and easily available material.

1.3.3 Experimental

Synthesis of nitrogen doped graphene: Graphene oxide (GO), synthesized by the Hummer's method [23], was finely ground with different proportions of urea and the pelletized mixture heated in a microwave reactor (900 W) for 30 sec. The product was washed several times with deionized water and vacuum dried. In this method graphene oxide gets simultaneously reduced and doped with nitrogen. The products obtained with graphene:urea mass ratios of 1:0.5, 1:1 and 1:2 are designated as NGO-1, NGO-2 and NGO-3 respectively and the nitrogen content of these samples were 14.7, 18.2 and 17.5 wt. % respectively as found by elemental analysis. This nitrogen content is considerably higher than that in earlier reports.

Electrochemical measurements: For electrochemical measurements, a two-electrode system was employed. The electrochemical performance of nitrogen-doped graphene was examined in 6 M KOH aqueous electrolyte without any binder or carbon additive. The mass of each electrode was 2 mg. The electrochemical performance of the graphene electrodes was determined by testing the cyclic voltammograms (CV) and constant

current charge–discharge curves using PG262A potentiostat/galovanostat, (Technoscience Ltd, Bangalore, India).

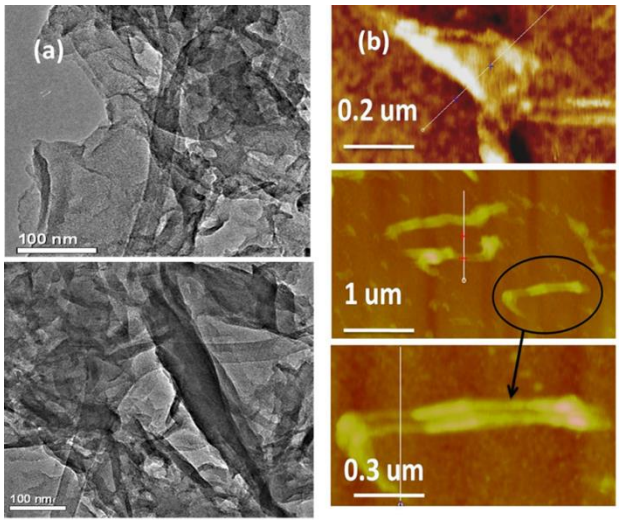

Figure 1. (a) TEM and (b) AFM images of NGO-3.

1.3.4 Results and discussion

Nitrogen-doped graphene synthesized by microwave method was investigated by transmission electron microscopy (TEM) and atomic force microscopy (AFM). We show typical TEM and AFM images in Figure 1(a) and (b) respectively. The images show that the graphene sheets appear like scrolls due to microwave treatment.

Table 1 XPS and Elemental analysis of nitrogen doped graphene oxide

Sample	Reaction time (sec)	Weight Ratio (G:U)	$S_{(BET)}$ (m^2/g)	N_{CHN} (wt. %)	N_{XPS} (at. %)	$N_{Pyridinic}$ (at. %)	$N_{Pyrrolic}$ (at. %)	$N_{Graphitic}$ (at. %)
NGO-1	30	1:0.5	195	14.7	13.2	2.3	7.1	3.8
NGO-2	30	1:1	210	18.2	15.6	2.6	9.3	3.7
NGO-3	30	1:2	235	17.5	15.3	2.6	7.2	5.5

NGO products derived from different mass ratio between urea and GO have been studied using XPS and CHN analyses. As a result, more nitrogen atoms (especially pyrrolic

and graphitic) could be doped into the graphene networks along with the increase of urea dose as shown in Table 1. In Figure 2, we show the N 1s spectra of a sample of nitrogenated graphene samples. The N 1s signal could be deconvoluted into three features with a peak at 398.7 eV corresponding to pyridinic nitrogen. The peak at 400.3 eV corresponds to pyrrolic nitrogen and the peak at 401.8 eV to graphitic nitrogen. Pyrrolic nitrogen is higher compared to the others in this sample. From the N (1s) spectra, the nitrogen contents of NGO-1,-2 and -3 were found to be 13.2, 15.6 and 15.3 at. % respectively (Table 1). We observed that if the reaction time exceeds 30 secs the nitrogen content decreases to less than 10 wt.%.

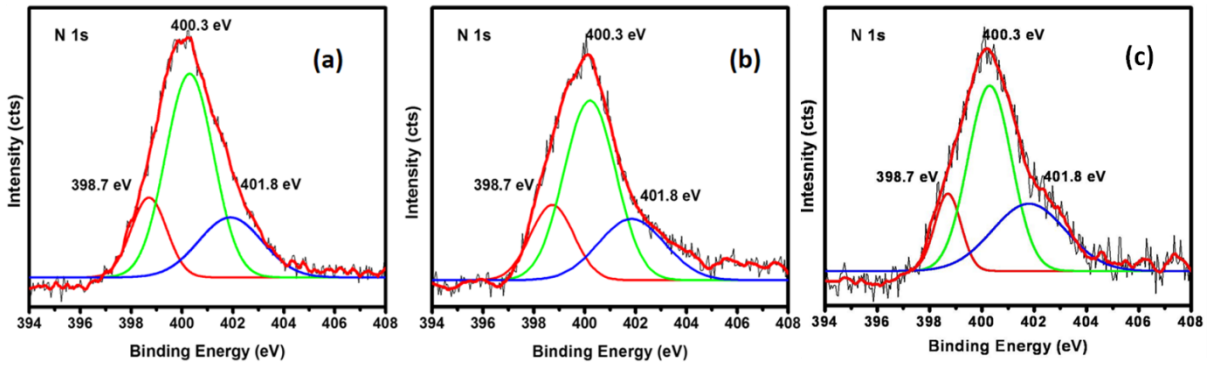

Figure 2. N 1s core level XP spectra of (a) NGO-1 (b) NGO-2 and (c) NGO-3

The NGO samples were characterized by Raman and infrared spectroscopy. Raman spectra show the G-band at 1602 cm^{-1}, shifted lower frequencies by about 10-12 cm^{-1} relative to GO. The I_D/I_D ratio of GO is 1.23 and it is slightly higher for NGOs. IR spectra show marked changes in the 1000-1700 cm^{-1} region, specially in the C-O stretching bands. The X-ray diffraction (XRD) patterns of the original GO and NGOs are displayed in Figure 3(a). The diffraction peak located at $2\theta = 11.3°$ is attributed to the (002) crystalline plane of GO. However, the peak at $2\theta = 11.3°$ entirely disappeared after hydrothermal reaction, and a broad diffraction peak around 26.1° of the graphite (002) plane was observed for the synthesized NGO samples, indicating the framework of the reduced sample was composed of few-layer stacked graphene nanosheets. We show typical N_2 adsorption-desorption isotherm of NGO-3 in Figure 3(b). The isotherm is of

type IV (IUPAC classification) suggesting that NGO-3 has porous characteristics. The surface areas of the three NGO samples are in the 200-240 m^2/g range.

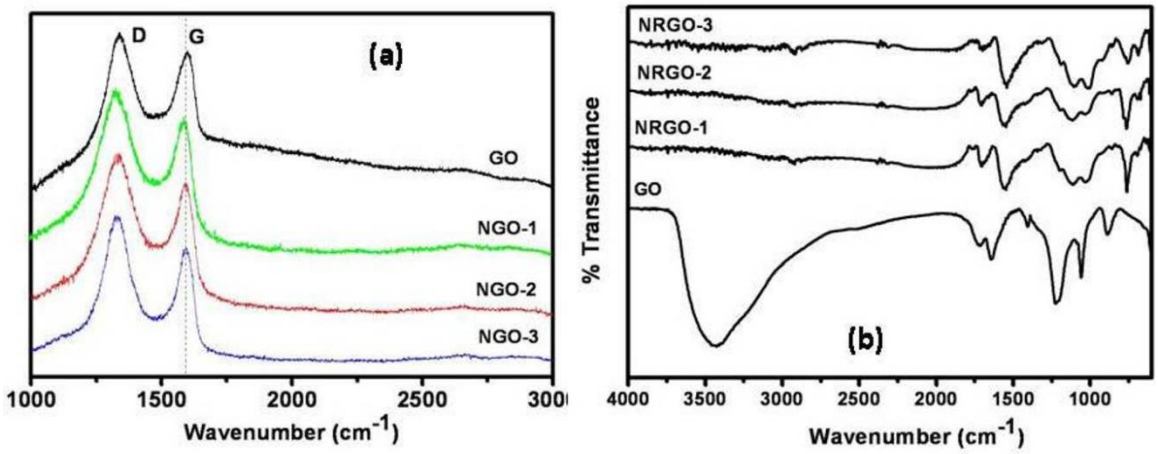

Figure 3. (a) Raman spectra (b) Infrared spectra of GO and nitrogen doped graphene oxide.

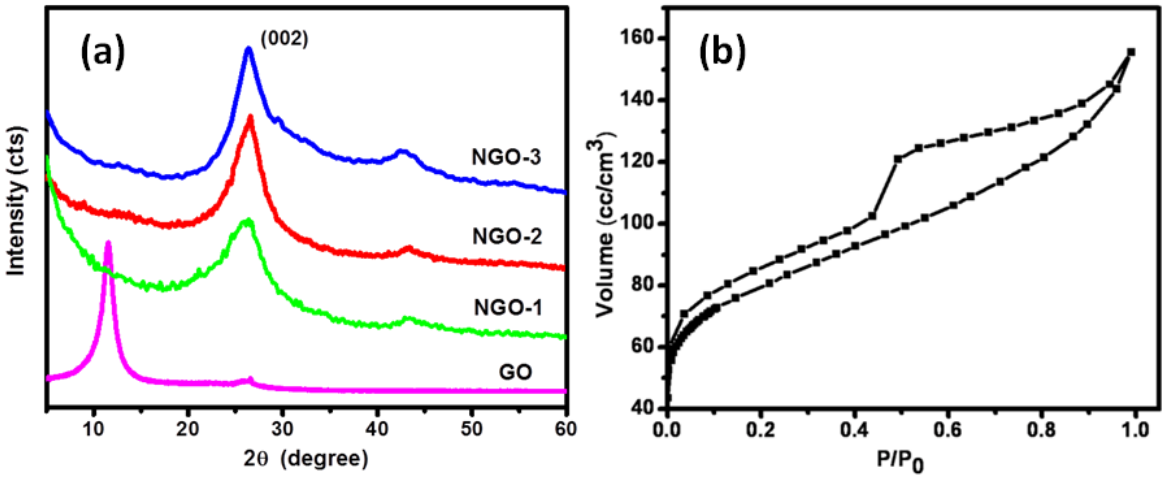

Figure 4. (a) XRD pattern of GO and NGOs (b) BET surface area of NGO-3

Electrochemical performance: The electrochemical performance of the nitrogen-doped graphene oxide (NGO) electrodes were investigated by means of cyclic voltammetry (CV), galvanostatic charge–discharge curves and electrochemical impedance spectroscopy (EIS) in 6 M KOH aqueous electrolyte without any binder or carbon additive. Cyclic voltammograms of the NGO samples measured at a scan rate of 20 mV/s for sample loading of ~2 mg per electrode are shown in Figure 5(a). The CV curves remain rectangular even at high scan rates indicating excellent charge storage characteristics, resembling those of an ideal supercapacitor. We have found a maximum

capacitance of 461 F/g at 5 mV/s in the case of NGO-3. The values of specific capacitance of the NGO-3 electrode under scan rates of 100, 80, 40, 20 and 10 mV/s are 338, 349, 380, 401 and 434 F/g respectively. The specific capacitance values of GO, NGO-1 and NGO-2 are 10, 438 and 442 F/g respectively at 5 mV/s. The galvanostatic charge–discharge curves of the NGO samples were measured at a potential window of 0–1 V at a current density of 0.5 A/g and shown in Figure 5(b). The discharge time of NGO-3 was longer compared to the other two materials at both high and low current densities. The galvanostatic charge-discharge curves of all the electrodes looks nearly symmetric, indicating that these materials have good electrochemical capacitive characteristics.

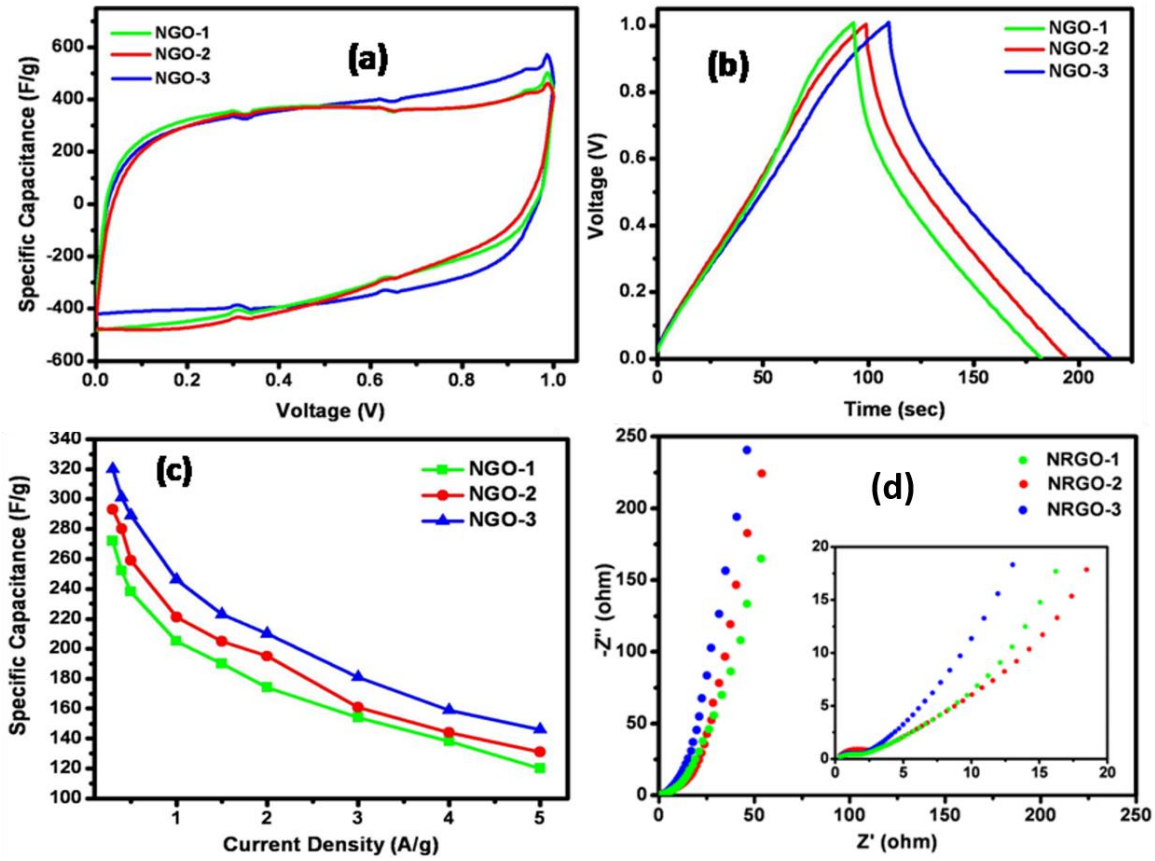

Figure 5. (a) Cyclic voltammograms of NGOs at a scan rate of 20 mV s^{-1}, (b) galvanostatic charge–discharge curves for NGO electrodes (at 0.5 mA g^{-1}) (c) specific capacitance as a function of discharge current (d) Nyquist curves for NGO electrodes.

The specific capacitance values derived from the discharging curves at different current densities are shown in Figure 5(c). We clearly see that the specific capacitance decreases with increase in current density for all the three materials. The specific

capacitance of NGO-3 is 320 F/g at 0.3 A/g and for NGO-1 and NGO-2 the values are 293 and 272 F/g respectively. Electrochemical impedance spectroscopy (EIS) is an important measurement to determine the performances of supercapacitors. Figure 5(d) shows Nyquist plots in the frequency range 100 kHz-0.01 Hz. These plots show excellent capacitive behavior, as indicated by the near vertical line over the low frequency ranges. It is well known that higher the slope value, faster is the formation of the electrical double layer. We clearly see that the slope of NGO-3 is greater than that for NGO-1 or NGO-2. The high frequency region is shown in the inset of Figure 5(d). We observe small charge transfer resistance (C_t) in these materials. Equivalent series resistances (ESR) of the samples are almost similar and the values are 0.35, 0.36 and 0.33 ohm for NGO-1, NGO-2 and NGO-3 respectively. ESR value follows the same trend as the graphitic nitrogen content.

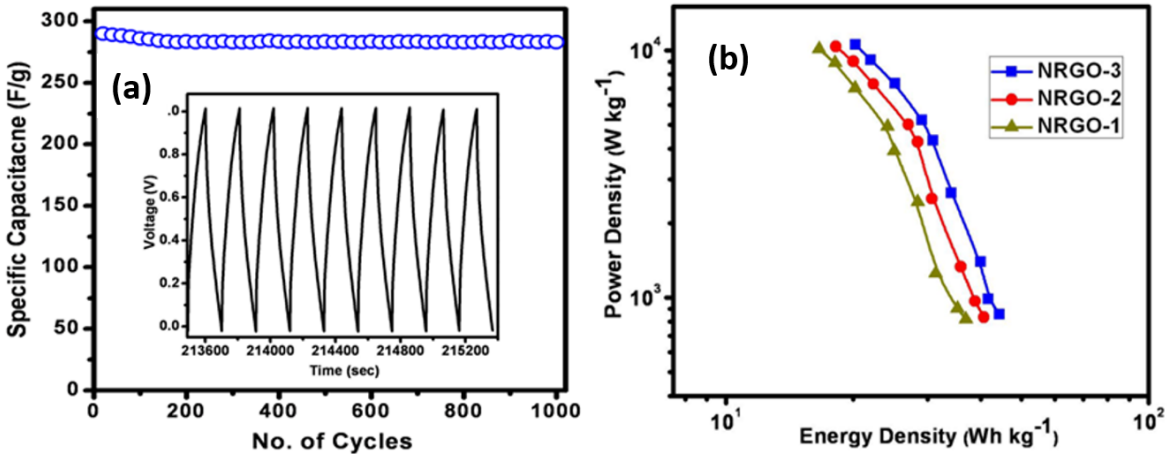

Figure 6. (a) Specific capacitance *versus* the cycle number of NGO-3 measured at a current density of 0.5 A/g within an operational window of 0.0–1 V (the inset shows the charge–discharge curves of the last few cycles for NGO-3). (b) Ragone plots of NGO based supercapacitors.

Cycling life is an important requirement for supercapacitor applications. Thus, we studied the cycling life tests for NGO-3 by repeating the galvanostatic charge-discharge between 0 and 1 V at a current density of 0.5 A/g for 1000 cycles (Figure 6(a)). NGO-3 showed a loss of only 2.7 % from the initial specific capacitance and showed good capacitance retention. The last few charge-discharge cycles looked almost similar when compared to the initial cycles (see Figure 6(a) inset) illustrating long-term cyclic stability. Energy and power densities are important factors for evaluating power applications of

electrochemical supercapacitors. Figure 6(d) shows the Ragone plots of all the nitrogen doped graphene oxide electrodes. The energy densities were calculated at various discharge current densities ranging from 0.3 to 5 A/g. The energy densities of the NGOs are remarkable, with NGO-3 showing the highest value of 44.4 Wh/kg at a current density of 0.3 A/g. NGO-1 and NGO-3 show energy densities of 40.7 and 36.9 Wh/kg respectively at a current density of 0.3 A/g. These values are higher than those reported earlier for other carbon-based supercapacitors. The power densities are in the range of 852–10524 W/kg for NGO-3 electrode.

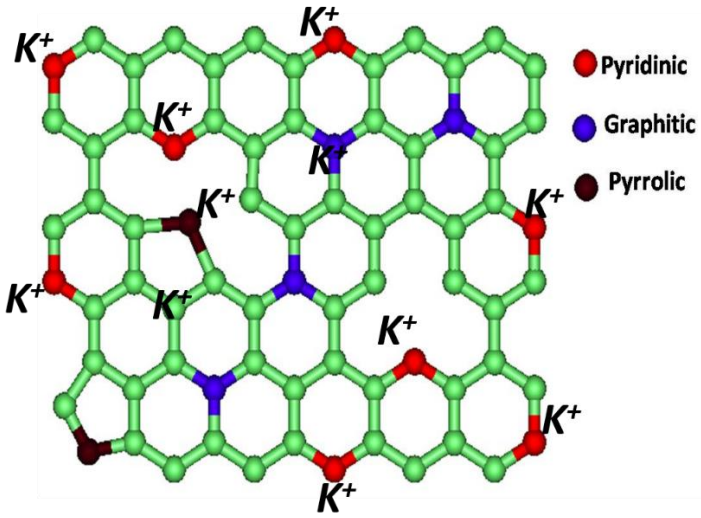

Figure 7. Scheme of the electrochemical reaction process of NGOs in 6M KOH

Based on the above experiment results, it can be assumed that the different type of nitrogen distributions result in the enhanced capacitance of NGOs in KOH electrolyte as shown in Figure 7. It is known that electrochemically active nitrogen atoms (pyridinic and pyrrolic) could easily control local electronic structures, which is beneficial to enhance the band between the N atoms and electrolyte ions of K^+ in the solution, resulting in plentiful K^+ ions accommodated on the electrode surface. At the same time, the larger number of H_2O around the K+ ions was also brought to the electrode surface. Besides, the graphitic-N atoms also play the role of enhancing capacitance by improving the conductivity of the materials, which is favourable to transport electrons in the electrode. It can be seen that the ESR of the NGOs materials improves in the order of NGO-3>NGO-1>NGO-2 indicating that the conductivity of NGO materials can be improved with the

increase in the graphitic-N atoms content. The specific capacitance value of NGO-3 is superior to that of NGO-2 and NGO-1, attributing to the fact that NGO-3 has abundant electrochemically active nitrogen groups (9.8 wt.%) raising the pseudocapacitance, and also has a suitable graphitic-N level (5.5 wt.%) which could change the electronic structure of the graphene nanosheets, leading to low-resistant pathways. However, the capacitance value of the NGO-2 is lower than that of NGO-3. It can be due to the slight increase in surface area of NGO-3, which is more crucial factor in enhancing the energy storage performance. Thus, the high total nitrogen content and the proper ratio among each type of nitrogen atom are very necessary for obtaining high electrochemical performance. It is deduced that the electrochemical properties of the as-prepared samples strongly depend on the nitrogen species due to the pyridinic-N and pyrrolic-N providing pseudo-capacitance by oxidation/reduction reaction, meanwhile the graphitic-N could enhance the conductivity of the materials, which is favourable for electron transfer through the NGO during the charge–discharge process.

1.3.5 Conclusions

In conclusion, an efficient method was developed for the fabrication of nitrogen doped graphene oxide with a high nitrogen content (~18 wt.%) using the microwave synthesis with urea as the nitrogen source. In this procedure, urea releases NH_3 for obtaining NGO with a high nitrogen content. Remarkably, the synthesized NGO-3 sample with both a high nitrogen level (17.5 wt.%) and a high surface area (235 m^2/g) shows excellent capacitance of 461 F/g at scan rate of 5 mV/s in 6 M KOH electrolyte, and also exhibited a good cyclic stability after 1000 cycles. Most importantly, the energy density of the NGOs are remarkable, with the highest value of 44.4 Wh/kg at a current density of 0.3 A/g. The power densities are in the range of 852–10524 W/kg for NGO electrodes by two-electrode symmetric capacitor tests. The outstanding performance of NGO is due to the high nitrogen doping content, proper ratio among each type of nitrogen atoms and the good surface area which can be provides the high pseudocapacitance and good electrical conductivity.

References

[1] Wang H, Maiyalagan T, Wang X. Review on Recent Progress in Nitrogen-Doped Graphene: Synthesis, Characterization, and Its Potential Applications. ACS Catal. 2012;2:781-94.

[2] Qu L, Liu Y, Baek J-B, Dai L. Nitrogen-Doped Graphene as Efficient Metal-Free Electrocatalyst for Oxygen Reduction in Fuel Cells. ACS Nano. 2010;4:1321-6.

[3] Lai L, Potts JR, Zhan D, Wang L, Poh CK, Tang C, et al. Exploration of the active center structure of nitrogen-doped graphene-based catalysts for oxygen reduction reaction. Energy Environ Sci. 2012;5:7936-42.

[4] Jeong HM, Lee JW, Shin WH, Choi YJ, Shin HJ, Kang JK, et al. Nitrogen-Doped Graphene for High-Performance Ultracapacitors and the Importance of Nitrogen-Doped Sites at Basal Planes. Nano Lett. 2011;11:2472-7.

[5] Wen Z, Wang X, Mao S, Bo Z, Kim H, Cui S, et al. Crumpled Nitrogen-Doped Graphene Nanosheets with Ultrahigh Pore Volume for High-Performance Supercapacitor. Adv Mater. 2012;24:5610-6.

[6] Cameron DC. Optical and electronic properties of carbon nitride. Surf Coat Tech. 2003;169–170:245-50.

[7] Wu J, Zhang D, Wang Y, Hou B. Electrocatalytic activity of nitrogen-doped graphene synthesized via a one-pot hydrothermal process towards oxygen reduction reaction. J Power Sources. 2013;227:185-90.

[8] Panchakarla LS, Subrahmanyam KS, Saha SK, Govindaraj A, Krishnamurthy HR, Waghmare UV, et al. Synthesis, Structure, and Properties of Boron- and Nitrogen-Doped Graphene. Adv Mater. 2009;21:4726-30.

[9] Li X, Wang H, Robinson JT, Sanchez H, Diankov G, Dai H. Simultaneous Nitrogen Doping and Reduction of Graphene Oxide. J Am Chem Soc. 2009;131:15939-44.

[10] Lu Y-F, Lo S-T, Lin J-C, Zhang W, Lu J-Y, Liu F-H, et al. Nitrogen-Doped Graphene Sheets Grown by Chemical Vapor Deposition: Synthesis and Influence of Nitrogen Impurities on Carrier Transport. ACS Nano. 2013;7:6522-32.

[11] Shao Y, Zhang S, Engelhard MH, Li G, Shao G, Wang Y, et al. Nitrogen-doped graphene and its electrochemical applications. J Mater Chem. 2010;20:7491-6.

[12] Hu T, Sun X, Sun H, Xin G, Shao D, Liu C, et al. Rapid synthesis of nitrogen-doped graphene for a lithium ion battery anode with excellent rate performance and super-long cyclic stability. Phys Chem Chem Phys. 2014;16:1060-6.

[13] Gao H, Guo L, Wang L, Wang Y. Synthesis of nitrogen-doped graphene from ployacrylonitrile. Materials Lett. 2013;109:182-5.

[14] Du X, Zhou C, Liu H-Y, Mai Y-W, Wang G. Facile chemical synthesis of nitrogen-doped graphene sheets and their electrochemical capacitance. J Power Sources. 2013;241:460-6.

[15] Wang X, Li X, Zhang L, Yoon Y, Weber PK, Wang H, et al. N-Doping of Graphene Through Electrothermal Reactions with Ammonia. Science. 2009;324:768-71.

[16] Long D, Li W, Ling L, Miyawaki J, Mochida I, Yoon S-H. Preparation of Nitrogen-Doped Graphene Sheets by a Combined Chemical and Hydrothermal Reduction of Graphene Oxide. Langmuir. 2010;26:16096-102.

[17] Deng D, Pan X, Yu L, Cui Y, Jiang Y, Qi J, et al. Toward N-Doped Graphene via Solvothermal Synthesis. Chem Mater. 2011;23:1188-93.

[18] Zheng B, Zheng WT, Zhang K, Wen QB, Zhu JQ, Meng SH, et al. First-principle study of nitrogen incorporation in amorphous carbon. Carbon. 2006;44:962-8.

[19] Sun L, Wang L, Tian C, Tan T, Xie Y, Shi K, et al. Nitrogen-doped graphene with high nitrogen level via a one-step hydrothermal reaction of graphene oxide with urea for superior capacitive energy storage. RSC Adv. 2012;2:4498-506.

[20] Schwenke AM, Hoeppener S, Schubert US. Synthesis and Modification of Carbon Nanomaterials utilizing Microwave Heating. Advanced Mater. 2015;27:4113-41.

[21] MacKenzie K, Dunens O, Harris AT. A review of carbon nanotube purification by microwave assisted acid digestion. Sep Purif Tech. 2009;66:209-22.

[22] Kappe CO, Dallinger D, Murphree SS. Microwave Synthesis - An Introduction. Practical Microwave Synthesis for Organic Chemists: Wiley-VCH Verlag GmbH & Co. KGaA; 2009. p. 1-9.

[23] Marcano DC, Kosynkin DV, Berlin JM, Sinitskii A, Sun Z, Slesarev A, et al. Improved Synthesis of Graphene Oxide. ACS Nano. 2010;4:4806-14.

1.4 SUPERCAPACITORS BASED ON COMPOSITES OF PANI WITH NANOSHEETS OF NITROGEN-DOPED RGO, $BC_{1.5}N$, MOS_2 AND WS_2

Summary*

Performance of supercapacitors based on 1:1 (by weight) composites of polyaniline (PANI) with nanosheets of nitrogenated reduced graphene oxide (NRGO), $BC_{1.5}N$, MoS_2 and WS_2 has been investigated in detail. The highest specific capacitance is found with the 1:1 NRGO-PANI composite, the value being 561 F/g at a current density of 0.2 A/g. All the 1:1 nanocomposites show good cyclability. Increasing the PANI content increases the specific capacitance and the highest value found being 715 F/g at a current density of 0.5 A/g in the case of the 1:6 NRGO-PANI composite. However, all the 1:6 composites show a marked decrease in specific capacitance with increase in current density. The energy density of 1:6 NRGO-PANI is ~25 Wh/Kg at 0.5 A/g and 1:1 NRGO-PANI is ~ 19 Wh/Kg at 0.2 A/g. NRGO-PANI composites clearly stand out as viable materials for practical applications.

*A Paper based on this work has been published in Nano Energy, 2015, **12**, 52-58

1.4.1 Introduction

Electrochemical supercapacitors have become promising energy storage devices and have attracted considerable attention owing to their wide applications in many fields, such as electric vehicles, portable electronic devices, memory back-up devices [1-3]. According to the different charge-storage mechanisms, they are basically divided into electrochemical double-layer capacitors (EDLCs) and pseudocapacitors [2]. The former capacitance arises from the high surface area electrodes (e.g. carbon nanomaterials) that store and release energy by charge separation at the interface between the electrode and electrolyte. The latter pseudocapacitance, relies on electrosorption and surface redox processes of electroactive species. Generally, EDLCs can achieve long electrochemical stability but with relatively low specific capacitance. In contrast, pseudocapacitors (e.g. conductive polymer composites) can supply a high specific capacitance but with poor cycle life, which limits their real applications in supercapacitors [4]. Therefore, there has been increasing interest in the preparation of supercapacitor electrode materials made from carbon nanomaterials and conductive polymer composites with high specific capacitance and long cycle stability by taking the advantage of EDLCs and pseudocapacitors [5].

Carbon nanomaterials such as activated carbon, carbon nanotubes and graphene have been used as electrode materials for supercapacitors owing to their large surface areas and good conductivity[5]. Among them, graphene, which consists of a sp^2-hybridized carbon atoms has many outstanding properties, such as high electrical conductivity, high specific area and low fabrication cost [4, 6, 7]. Hence, graphene is considered one of the best candidates for electrode materials. It shows good stability during charge–discharge process, but the specific capacitance (around 100 to 200 F g^{-1}) is limited by the stored energy mechanism, which mainly relies on the electric double-layer capacitance [6, 7]. Electronically conducting π-electrons polymers (ECPs) are promising electrode materials for supercapacitors because of their high specific capacitance, high conductivity, and ease of preparation. On the contrary, electrode materials for pseudocapacitors such as conducting polymers can provide high specific capacitance but have poor stability, which is based mainly on a faradic mechanism

[8]. Polypyrrole (PPy), polyaniline (PANI), and polythiophene (PT) as well as their derivatives are commonly used ECPs [9]. These polymers can be synthesized chemically or electrochemically. However, the main drawback of conducting polymers is their low stability [10]. Electro-reduction or electro-oxidation of a polymer generates a charge, which is balanced by oppositely charged counter ion entering or leaving the polymer film to maintain neutrality. Therefore, electrochemical charging and discharging irreversibly changes the structure of polymers due to swelling and shrinking. This problem can be solved by making composites with outstanding carbon material like graphene [11]. The resulting composites synergistically combine properties of graphene with high electrical conductivity and surface area.

To obtain good performance from electrode materials as supercapacitors with high specific capacitance and good stability, there as been effort to combine conducting polymers with graphene, such as graphene–polyaniline (PANI), graphene-polypyrrole, and graphene–polythiophene composites [11]. Among these conductive polymers, PANI is a promising active electrode material for pseudocapacitors, owing to its low cost, easy synthesis and high theoretical specific pseudocapacitance. Polyaniline (PANI) possesses high conductivity and chemical stability. Its electrochemical behaviour is complex due to the presence of several oxidation states of PANI including the fully reduced leucoemeraldine form, the intermediate emeraldine form, and the fully oxidized pernigraniline form. The specific capacity of PANI depends upon three parameters such as the preparation procedure used, morphology and thickness.

Graphene-PANI is considered one of the most important nanocomposites because of its high theoretical specific pseudocapacitance according to the multiple redox states of PANI [12]. The combination of graphene and PANI takes advantage of them to provide superior performance in supercapacitors. Chemically modified graphene and polyaniline nanofiber composites have been prepared by in situ polymerization of aniline monomer in the presence of graphene oxide under acid conditions [12]. The graphene oxide/PANI composites with different mass ratios were reduced to graphene using hydrazine followed by reoxidation and reprotonation of the reduced PANI to give the graphene/PANI nanocomposites. The BET surface areas of these composites were in the 4.3-20.2 m^2/g range and the highest specific capacitance achieved was 480 F g^{-1} at a

current density of 0.1 A/g. Cheng et al. [13] developed a freestanding and flexible graphene/polyaniline (GP/PANI) composite by an *in situ* anodic electropolymerization of polyaniline film on graphene paper. This composite electrode showed good tensile strength of 12.6 MPa and values of 233 F/g and 135 F/cm^3 for gravimetric and volumetric capacitances respectively. PANI sandwiched graphene layers prepared by mixed dispersion of chemically converted graphene (CCG) and polyaniline nanofibers (PANI-NFs) show high conductivity (44% higher than CCG (5.5102 S/m) and 10 times that of a PANI-NF film) [14]. Supercapacitor performance is excellent with a capacitance of 210 F g^{-1} at 0.3 A/g with energy density of ~ 19.2 Wh/Kg. Doping of PANI with graphene also shows good electrochemical performance with capacitance of 531 F/g [15]. Change in size of raw graphite flakes plays an important role in the electrochemical performance [16]. The specific capacitances are 746 F/g for 12500 mesh and 627 F/g for 500 mesh compared to PANI of 216 F/g at 0.200 A/g. Polyaniline-grafted reduced graphene oxide (PANI-*g*-rGO) composite synthesized using in-situ oxidative polymerization shows fibrillar morphology with a room-temperature electrical conductivity as high as 8.66 S cm^{-1} and a capacitance of 250 F/g with good cycling stability.

Ruoff et al. [17] have investigated the effect of graphene surface chemistry on the electrochemical performance of graphene/polyaniline composites as supercapacitor electrodes. Graphene oxide (G-O), chemically reduced G-O (RG-O), nitrogen-doped RG-O (N-RG-O), and amine-modified RG-O (NH_2-RG-O) were loaded with about 9 wt % of PANI. The NH_2-RG-O/PANI composite exhibited highest capacitance (420 F/g) and good cyclability when measured in a three-electrode system. Other than PANI, polypyrrole is a widely studied conducting polymer for energy storage devices. A polypyrrole-reduced graphite oxide core-shell composite fabricated through electrostatic interactions and π-π accumulation shows remarkable performance as a supercapacitor electrode material with a specific capacitance of 557 F g^{-1} at a current density of 0.5 A g^{-1} and retains a high value after 1000 charge–discharge processes [18]. Interfacial/*in-situ* oxidative polymerization of polypyrrole in the presence of functionalized graphene sheets produces high quality composites for supercapacitors [19]. Composites of polyaniline and graphene prepared by *in-situ* chemical polymerization of aniline show good supercapacitor properties with cyclic stability [20].

1.4.2 Scope of the present investigations

Of the various materials studied as supercapacitor electrodes, graphene, carbon nanotubes, certain metal oxides and conducting polymers have shown good results because of the high conductivity, surface area and pseudocapacitive properties [11]. Supercapacitors based on nitrogen-doped graphene and borocarbonitrides have shown remarkable supercapacitive performance in both aqueous and organic electrolytes with high cyclic stability, energy density and power density [21]. It has been shown recently that inorganic analogues of graphene based on layered inorganic materials such as MoS_2 and WS_2 possess useful properties of value to in electrochemistry, catalysis and other areas [22]. In the light of the above findings, we have investigated the performance of supercapacitors based on nanocomposites of PANI with a few important layered materials including few-layer MoS_2 and WS_2, borocarbonitrides ($B_xC_yN_z$) and nitrogen-doped reduced graphene oxide (NRGO). The choice of materials are based on the fact that they exhibit good conductivity and high surface area. The choice of N-doped RGO and BCN is because these materials by itself shows good supercapacitor performance. In all these nanocomposites of PANI, we have maintained a weight ratio of PANI to the other component at 1:1 and 1:6.

1.4.3 Experimental section

Synthesis of graphene oxide: A solution of graphene oxide (GO) was first prepared by following the modified Hummers method [23]. 70 mL conc. H_2SO_4 was added to a mixture of 3.0 g graphite flakes and 1.5 g $NaNO_3$, and the mixture was cooled in an ice bath. To this 9.0 g of $KMnO_4$ was added. The reaction was stirred for 30 min at room temperature, after which 150 mL water was added to the reaction mixture, followed by 300 mL of water and 10 mL 30% of H_2O_2. The solution turned brown yielding a solid product which was washed with deionized water and dried in vacuum at 50 °C for 12 h. To prepare reduced graphene oxide (RGO), 200 mg of GO was dispersed in 200 mL of deionized water, to which 7 mL of hydrazine hydrate was added. The mixture was refluxed for 12 h and the resulting product washed several times with deionized water, vacuum dried and then heated to 900 °C for 90 min in an argon atmosphere. The sample so obtained

consisted of 3-5 layers of RGO as determined by atomic force microscopy and other techniques.

Synthesis of nitrogen-doped reduced graphene: To prepare nitrogen-doped reduced graphene (NRGO), RGO (400 mg) was dispersed in 50 mL absolute ethanol, to which urea (2 gram) was added. The mass ratio between the RGO and urea was 1:5. The aqueous mixture was sonicated for 2 h, followed by evaporation of ethanol at 50 °C to give a grey powder. The powder was finely milled, pelletized and transferred to a quartz boat. It was then heated to 900 °C for 90 min in a nitrogen atmosphere. The product was dispersed in water and sonicated for 2 h. After sonication, the product was centrifuged and washed several times with deionized water to remove residual species adsorbed on the surfaces. The sample so obtained consisted of 3-5 layers of NRGO. The nitrogen content of NRGO as determined by elemental analysis was 5.4 wt. %.

Synthesis of molybdenum sulfide: MoS_2 nanosheets were prepared by hydrothermal method. A mixture of 0.3 g $(NH_4)_6Mo_7O_{24}.6H_2O$ (ammonium heptamolybdate) and 0.2 g NH_2CSNH_2 (thiourea) was dissolved in 17 mL distilled water and solution heated in a oven at 200°C for 72 hours in a stainless steel autoclave. The product was washed and dried. The nanosheets so obtained consisted of 3-7 layers. To prepare WS_2 nanosheets, 100 mg of tungstic acid was finely ground with 5 grams of thiourea and heated to 600 ^oC for 5 h. The product consisted of 4-7 layers of WS_2.

Synthesis of borocarbonitride: High surface area borocarbonitride was synthesized as follows [24]. In a typical synthesis, 0.1 g H_3BO_3, 0.5 g activated charcoal and 2.4 g urea were taken in 50 mL water and sonicated for 15 min. Water was slowly evaporated at 80 °C to get thick slurry. The slurry was transferred to a quartz boat and heated at 900 °C for 10 h in nitrogen atmosphere followed by ammonia treatment at 930 °C for 3 h. The composition of the material was found to be $BC_{1.5}N$ from X-ray photoelectron spectroscopy. The material consisted of 4-8 layers. For simplicity the sample is designated as BCN in the text. The surface areas of the NRGO, MoS_2, WS_2 and $BC_{1.5}N$ are 324, 35, 21 and 1350 m^2/g respectively.

Synthesis of polyaniline: Polyaniline (PANI) was prepared as follows. Vacuum distilled aniline (0.5 g) was dissolved in 10 mL of 1 M HCl aqueous solution and kept in an ice bath. To this solution ammonium peroxydisulfate (2.5 g) dissolved in 10 mL of 1 M HCl was

added rapidly under vigorous sonication at 4 ^oC. The obtained product was washed thoroughly and kept for drying at 50 ^oC.

Synthesis of polyaniline composites: To prepare the 1:1 polyaniline composites, 25 mg NRGO, MoS_2, WS_2 or BCN was dispersed in 5 ml 1 M HCl. To this solution, 25 µL of distilled aniline was added and kept in an ice bath. Ammonium peroxydisulfate (0.8 g,) dissolved in 5 mL of 1 M HCl was added rapidly into the reaction mixture under vigorous sonication at 4 ^oC. The obtained product was washed thoroughly and kept for drying at 50 ^oC.

To prepare the 1:6 polyaniline composites, 25 mg NRGO, MoS_2, WS_2 or BCN was dispersed in 5 ml 1 M HCl. 150 µL of distilled aniline was added to the dispersion and the mixture kept in an ice bath. Ammonium peroxydisulfate (1.5 g,) dissolved in 5 mL of 1 M HCl was added rapidly into the aniline solution under vigorous sonication at 4 ^oC. The product was washed thoroughly and kept for drying at 50 ^oC. All the nanocomposites were investigated by transmission as well as scanning electron microscopy, Raman and infrared spectroscopy and thermogravimetric analysis. Four-point probe measurements were carried out to obtain conductivities of the samples. Typically, 15 mg a composite was pressed under 5 ton at room temperature and the pellets placed under probes for conductivity measurements.

Electrochemical measurements: Supercapacitor measurements were performed on an PGSTAT 262A (Techno Science Instruments) electrochemical workstation in 2 M H_2SO4 aqueous electrolyte solutions under three-electrode assembly with a catalyst coated glassy carbon (GC) electrode as the working electrode with a large-area Pt foil and Ag/AgCl as counter and reference electrodes respectively. The working electrode was fabricated by dispersing 3 mg of sample in 1 mL ethanol-water mixture (1:1) from that 10 µL was drop casted on glassy carbon electrode followed by 10 µL of 0.05 wt.% nafion solution was used as binder. The electrodes were dried in air at 60 ^oC for 30 min.

1.4.4 Results and discussion

The morphology and microstructures of the 1:1 PANI-composites were investigated by transmission electron microscopy (TEM). Figures 1 (a) and (b) show the TEM images of NRGO and flower-like MoS_2 which were the starting materials while Figures 1 (c) and (d)

show the TEM images of the MoS_2-PANI and NRGO-PANI composites respectively. We see that PANI is homogeneously deposited on the surfaces of the MoS_2 and nitrogen-doped graphene nanosheets. The composites still maintain the layered nature without aggregation.

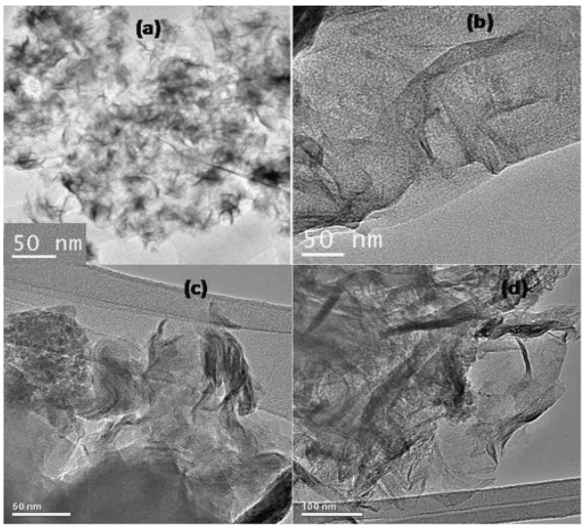

Figure 1. TEM image of (a) nanosheets of MoS_2 and (b) NRGO and of (c) MoS_2-PANI (d) NRGO-PANI 1:1 nanocomposites.

The composites with BCN and WS_2 showed similar features. Figure 2(a) shows the infrared spectra of PANI and it composites with NRGO, MoS_2, WS_2 and BCN. The bands in the 1600-1500 cm^{-1} region arise from the aromatic C-H stretching mode and the bands at 1473 and 1445 cm^{-1} are due to the C=N stretching modes. The bands in the 1300-1200 cm^{-1} region are due to C-N stretching as in primary aromatic amines and the bands between 1000 and 1150 cm^{-1} arise from C-H bending vibrations. The bands below 1000 cm^{-1} are characteristic of monosubstituted benzenes. In Figure 2(b), we present the Raman spectra of PANI and it composites with NRGO, MoS_2, WS_2 and BCN. The band at 1336 cm^{-1} corresponds to the D band and that at 1573 cm^{-1} to the G band of NRGO. NRGO-PANI shows two bands at 1500 and 1491 cm^{-1} due to C=C stretching and C=N stretching vibrations respectively of the quinonoid ring and a band at 1258 cm^{-1} due to C-N bond stretching. The band at 1160 cm^{-1} is attributed to the C-H bending vibration of the benzenoid ring. MoS_2 and WS_2-PANI composites also show their corresponding E^1_{2g} and A_{1g} bands along with PANI bands.

Thermogravimetric analysis (TGA) curves of PANI and NRGO-PANI composites are given in Figure 3. The NRGO-PANI composites (1:1 and 1:6) show breaks at the

corresponding composition indicative of the PANI contents and show good stability between 400-600 ^oC. The decomposition of PANI is clearly seen by a weight loss around 250^oC and in the 400-600 ^oC region due to the decomposition of the amine and other functional groups in the composites. Electrical conductivity data are listed in Table 1. We can see that NRGO-PANI (1:1) composite shows conductivity of 196.4 S/m which is higher than that of the pristine PANI. This enhancement in conductivity is attributed to the π-π stacking between the NRGO and PANI. MoS_2, WS_2 and $BC_{1.5}N$ composites also show increased conductivity. Further increase in PANI concentration increases the conductivity of NRGO to 211.2 S/m. The same is true of the other composites as well. NRGO, MoS_2, WS_2 and $BC_{1.5}N$ show conductivities of 145.3, 11.2, 4.5 and 8.1 S/m respectively.

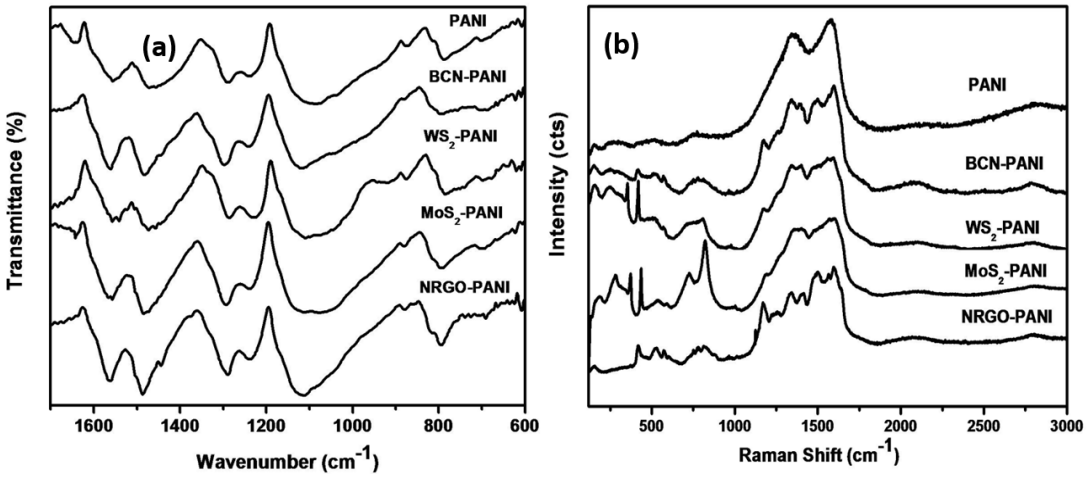

Figure 2. (a) Infrared spectra and (b) Raman spectra of PANI and 1:1 nanocomposites with NRGO, MoS_2, WS_2 and BCN.

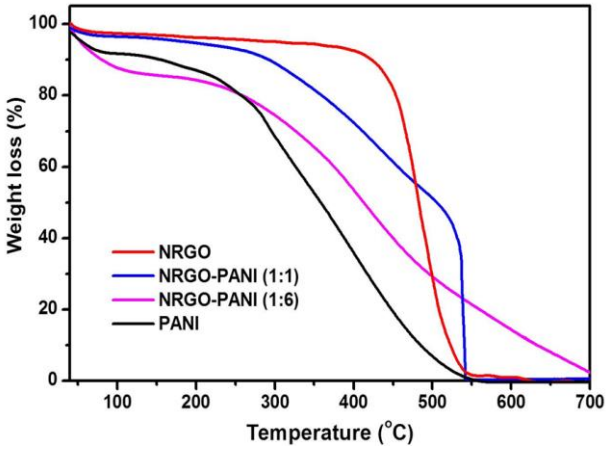

Figure 3. Thermogravimetric curves of PANI, NRGO and nanocomposites of PANI with NRGO

Table 1. Values of specific capacitance (F/g) of nanocomposites based on PANI

Material	Conductivity (S/m) (1:1)	Specific Capacitance at 0.2 A/g (1:1)	Conductivity (S/m) (1:6)	Specific Capacitance at 0.5 A/g (1:6)
PANI	45.3	210	45.3	165
NRGO-PANI	196.4	561	211.2	715
MoS_2-PANI	108.6	417	124.4	567
WS_2-PANI	52.1	382	65.7	441
BCN-PANI	62.6	340	79.3	395

Electrochemical performance: Electrochemical performance of the PANI nanocomposites was investigated by means of cyclic voltammetry (CV), galvanostatic charge-discharge curves and electrochemical impedance spectroscopy (EIS) in 2 M H_2SO_4 aqueous electrolyte. Cyclic voltammograms of PANI, NRGO, MoS_2, WS_2, BCN and its composites are measured at different scan rates (5-100 mV/s) and the CV curves measured at 40 mV/s are shown in Figure 5(a). Cyclic voltammograms show two pairs of redox peaks corresponding to reversible charge-discharge behaviour and pseudocapacitance characteristic of PANI. The pair of peaks Q_1/Q_2 are attributed to the redox transition of PANI between leucoemeraldine and emeraldine and the pair of peaks Q_3/Q_4 are attributed to the emeraldine–pernigraniline transformation. The increase in the integrated area of the CV loop indicates much higher capacitance for the composites than the pure PANI. NRGO-PANI composite shows the highest peak current of all the composites. The cyclic voltammograms of NRGO-PANI measured at different scan rates shown in Figure 5(b), clearly reveal that the peak current increases the increase in scan rates.

The galvanostatic charge-discharge curves of PANI, NRGO, MoS_2, WS_2, BCN and its composites were measured in a potential window of -0.2-0.8 V *vs* Ag/AgCl (2M KCl). Figure 5(c) shows charge-discharge curves measured at a current of 0.2 A/g. The discharging curve of the NRGO-PANI shows two voltage stages in the ranges of 0.8 to 0.4

V and 0.4 to -2.0 V, respectively. The former stage with a relatively short discharging duration is ascribed to electrical double layer (EDL) capacitance while the latter stage with a much longer discharging duration is associated with the combination of EDL and Faradaic capacitances of NRGO and PANI. The other composites also show a similar behavior. Figure 5(d) show the variation of specific capacitance at different current densities. The specific capacitance values decreases slightly as the current density increases, generally stabilizing above 1 A/g. The capacitance values of the PANI, NRGO, MoS_2, WS_2, $BC_{1.5}N$ are 210, 110, 60, 55 and 85 respectively. The specific capacitances of the composites are listed in Table 1. The highest capacitance is found with NRGO-PANI, the value being 561 F/g at 0.2 A/g. This composite also exhibits high conductivity.

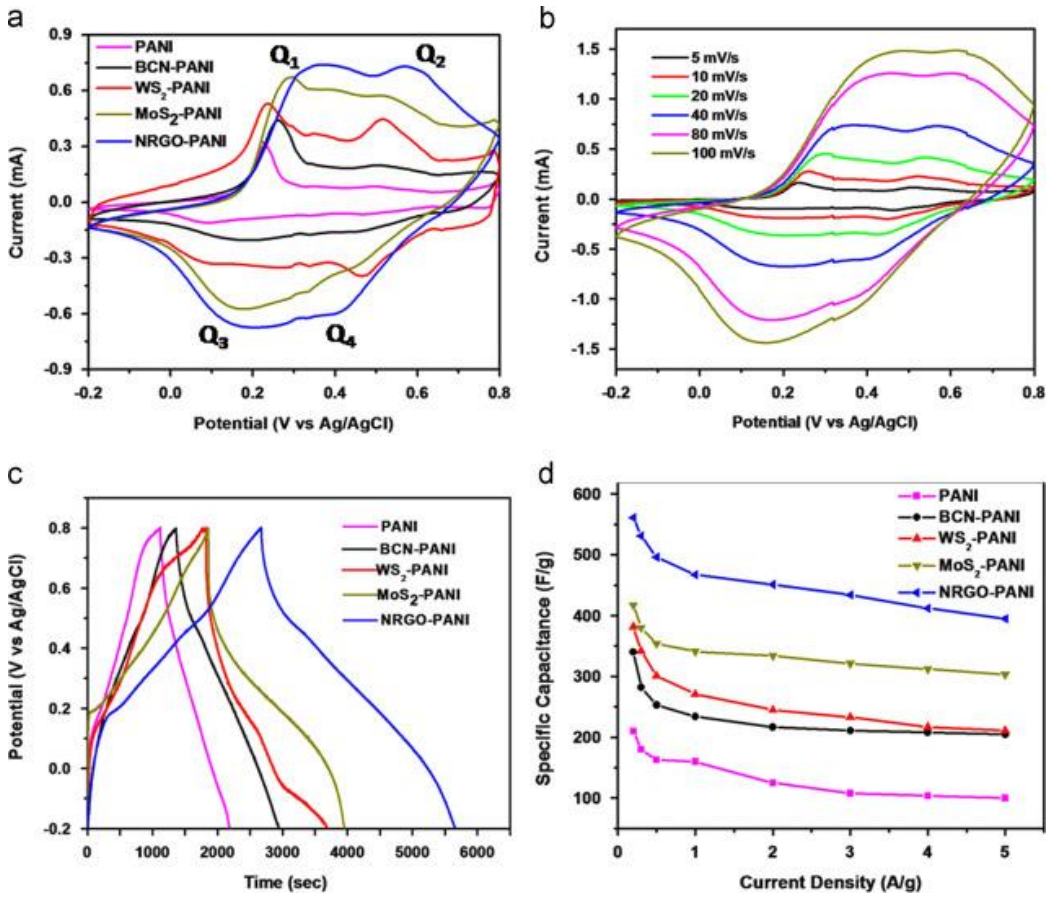

Figure 4. Cyclic voltammograms of PANI and 1:1 nanocomposites with NRGO, MoS_2, WS_2 and BCN at 40 mV/s. (b) Cyclic voltammograms of NRGO-PANI at different scan rates (c) Galvanostatic charge discharge curves of PANI and the 1:1 nanocomposites with NRGO, MoS_2, WS_2 and BCN at a current density of 0.2 A/g (d) Specific capacitance of PANI and 1:1 nanocomposites with NRGO, MoS_2, WS_2 and BCN at different current densities.

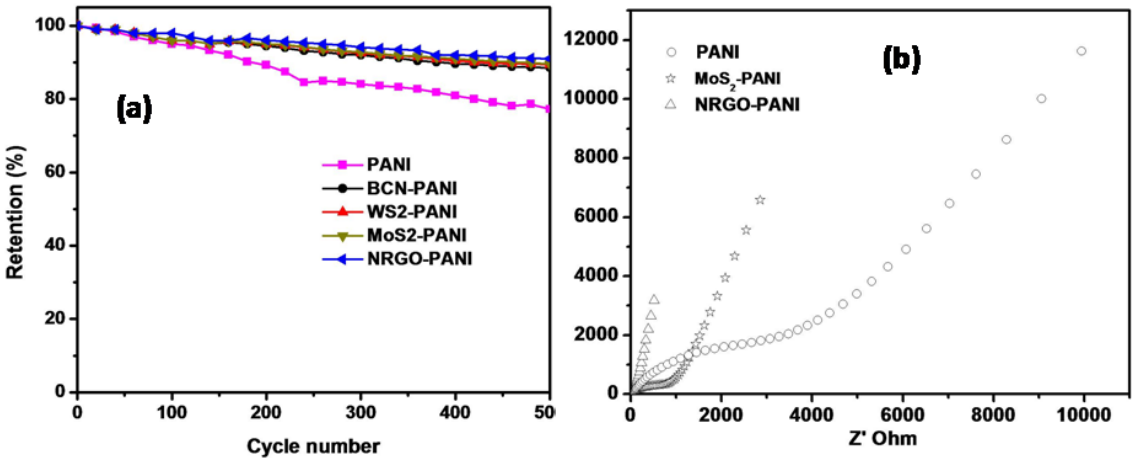

Figure 5. (a) Cyclic stability of PANI and the 1:1 nanocomposites with NRGO, MoS_2, WS_2 and BCN at a current density of 2 A/g. (b) Nyquist plots of PANI, BCN-PANI and NRGO-PANI.

Cyclic stability and electrochemical impedance measurements are necessary to understand the performance of supercapacitors. Cyclic stability tests for PANI and its composites were carried out by repeating the galvanostatic charge-discharge between -0.2 and 0.8 V at a current density of 2 A/g for 500 cycles as shown in Figure 6 (a). Composite showed almost similar capacitance loss in which NRGO-PANI showed the lowest loss of ~8% from the initial specific capacitance, indicating good capacitance retention the PANI. Figure 6 (b) shows the Nyquist plots of PANI, NRGO-PANI and MoS2-PANI. The plots show excellent capacitive behavior of NRGO-PANI and MoS_2-PANI as indicated by the near vertical line at the lower frequency range whereas PANI shows huge transfer resistance which is minimal in the composites.

We have hitherto discussed composites of PANI with NRGO, MoS_2, WS_2 and BCN where the weight ratio of PANI to the other material was 1:1. We have also prepared composites with higher PANI content, the weight ratio being 1:6. Cyclic voltammograms of NRGO, MoS_2, WS_2, BCN and its composites are measured at 20 mV/s are shown in Figure 6(a). Figure 6(b) shows charge-discharge curves measured at a current of 1 A/g. The discharging curve of the NRGO-PANI shows two voltage stages in the ranges as like 1:1 composite. We have obtained specific capacitance values of 715, 567, 441 and 395 F/g with 1:6 NRGO-PANI, MoS_2-PANI, WS_2-PANI and BCN-PANI nanocomposites respectively at a current density of 0.5 A/g (Figure 7 (a)). The 1:6 composites, however,

exhibit a fairly marked decrease in the specific capacitance as the current density increases. In Figure 7 (b), we show Ragone plots for the NRGO-PANI composites. The highest energy density obtained is ~ 25 Wh/Kg for the 1:6 NRGO-PANI nanocomposite. The corresponding value for the 1:1 composite is ~ 19 Wh/Kg.

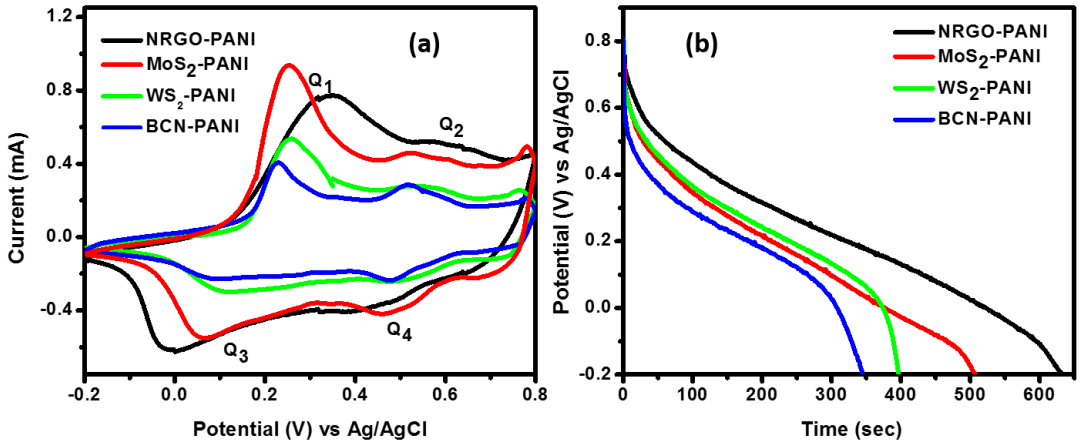

Figure 6. Cyclic voltammograms of PANI and 1:6 nanocomposites with NRGO, MoS_2, WS_2 and BCN at 20 mV/s. (b) Galvanostatic charge discharge curves of (1:6) PANI nanocomposites with NRGO, MoS_2, WS_2 and BCN at a current density of 1 A/g.

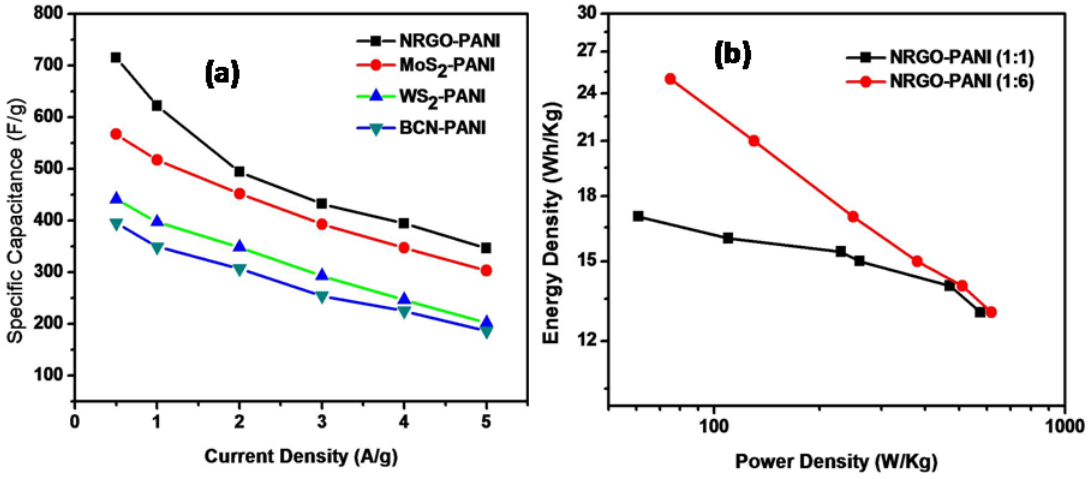

Figure 7 (a) Specific capacitance 1:6 PANI nanocomposites with NRGO, MoS_2, WS_2 and BCN at different current densities (b) Ragone plots of 1:1 and 1:6 NRGO-PANI nanocomposites.

The higher specific capacitance of NRGO-PANI composites compared with that of NRGO can be ascribed to the π-π stacking and pseudocapacitance from the PANI in the

composite which increases the electrical conductivity. The specific capacitance and the stability of the electrode based on NRGO-PANI (1:1) are much greater than those of PANI and the other composites. NRGO-PANI (1:6) composite shows excellent supercapacitor performance but the stability of the composites decreases at higher current density because of the excessive PANI which makes it unstable higher current densities. In addition, the behavior at high current density can related with the porosity of the material, and the ease with which ions to reach the available electrochemical surface area. The synergy works well only at a particular concentration of PANI and NRGO.

1.4.5 Conclusions

In conclusion, the present study shows that 1:1 (by weight) nanocomposites of PANI with MoS_2, WS_2, $BC_{1.5}N$ and nitrogen-doped RGO exhibit good performance characteristics in supercapacitor applications. The performance of NRGO-PANI is best in terms of specific capacitance and energy density. For stable operation at high current densities it is best to keep the relative proportions of PANI and NRGO at 1:1, since at high of PANI content, the specific capacitance decreases at high current densities.

References

[1] Conway BE. Similarities and Differences between Supercapacitors and Batteries for Storing Electrical Energy. Electrochemical Supercapacitors: Scientific Fundamentals and Technological Applications. Boston, MA: Springer US; 1999. p. 11-31.

[2] Conway BE. Transition from "Supercapacitor" to "Battery" Behavior in Electrochemical Energy Storage. J Electrochem Soc. 1991;138:1539-48.

[3] Kötz R, Carlen M. Principles and applications of electrochemical capacitors. Electrochimica Acta. 2000;45:2483-98.

[4] Zhu Y, Murali S, Stoller MD, Ganesh KJ, Cai W, Ferreira PJ, et al. Carbon-Based Supercapacitors Produced by Activation of Graphene. Science. 2011;332:1537-41.

[5] Zhang LL, Zhao XS. Carbon-based materials as supercapacitor electrodes. Chem Soc Rev. 2009;38:2520-31.

[6] Vivekchand SRC, Rout CS, Subrahmanyam KS, Govindaraj A, Rao CNR. Graphene-based electrochemical supercapacitors. J Chem Sci 2008;120:9-13.

[7] Stoller MD, Park S, Zhu Y, An J, Ruoff RS. Graphene-Based Ultracapacitors. Nano Lett. 2008;8:3498-502.

[8] Ryu KS, Lee Y, Han K-S, Park YJ, Kang MG, Park N-G, et al. Electrochemical supercapacitor based on polyaniline doped with lithium salt and active carbon electrodes. Solid State Ionics. 2004;175:765-8.

[9] Sivaraman P, Rath SK, Hande VR, Thakur AP, Patri M, Samui AB. All-solid-supercapacitor based on polyaniline and sulfonated polymers. Synth Met. 2006;156:1057-64.

[10] Brožová L, Holler P, Kovářová J, Stejskal J, Trchová M. The stability of polyaniline in strongly alkaline or acidic aqueous media. Polym Degrad Stab. 2008;93:592-600.

[11] Frackowiak E. Electrode Materials with Pseudocapacitive Properties. Supercapacitors: Wiley-VCH Verlag GmbH & Co. KGaA; 2013. p. 207-37.

[12] Zhang K, Zhang LL, Zhao XS, Wu J. Graphene/Polyaniline Nanofiber Composites as Supercapacitor Electrodes. Chem Mater. 2010;22:1392-401.

[13] Wang D-W, Li F, Zhao J, Ren W, Chen Z-G, Tan J, et al. Fabrication of Graphene/Polyaniline Composite Paper via In Situ Anodic Electropolymerization for High-Performance Flexible Electrode. ACS Nano. 2009;3:1745-52.

[14] Wu Q, Xu Y, Yao Z, Liu A, Shi G. Supercapacitors Based on Flexible Graphene/Polyaniline Nanofiber Composite Films. ACS Nano.4:1963-70.

[15] Wang H, Hao Q, Yang X, Lu L, Wang X. Graphene oxide doped polyaniline for supercapacitors. Electrochemistry Commun. 2009;11:1158-61.

[16] Wang H, Hao Q, Yang X, Lu L, Wang X. Effect of Graphene Oxide on the Properties of Its Composite with Polyaniline. ACS Applied Materials & Interfaces.2:821-8.

[17] Gopinadhan K, Shin YJ, Jalil R, Venkatesan T, Geim AK, Neto AHC, et al. Extremely large magnetoresistance in few-layer graphene/boron-nitride heterostructures. Nat Commun. 2015;6: 8337.

[18] Qian T, Yu C, Wu S, Shen J. A facilely prepared polypyrrole-reduced graphene oxide composite with a crumpled surface for high performance supercapacitor electrodes. J Mater Chem A.1:6539-42.

[19] de Oliveira HP, Sydlik SA, Swager TM. Supercapacitors from Free-Standing Polypyrrole/Graphene Nanocomposites. J Phys Chem C.117:10270-6.

[20] Shulga YM, Baskakov SA, Smirnov VA, Shulga NY, Belay KG, Gutsev GL. Graphene oxide films as separators of polyaniline-based supercapacitors. J Power Sources. 2014;245:33-6.

[21] Gopalakrishnan K, Moses K, Govindaraj A, Rao CNR. Supercapacitors based on nitrogen-doped reduced graphene oxide and borocarbonitrides. Solid State Commun. 2013;175–176:43-50.

[22] Rao CNR, Maitra U, Waghmare UV. Extraordinary attributes of 2-dimensional MoS2 nanosheets. Chem Phys Lett. 2014;609:172-83.

[23] Marcano DC, Kosynkin DV, Berlin JM, Sinitskii A, Sun Z, Slesarev A, et al. Improved Synthesis of Graphene Oxide. ACS Nano. 2010;4:4806-14.

[24] Kumar N, Moses K, Pramoda K, Shirodkar SN, Mishra AK, Waghmare UV, et al. Borocarbonitrides, BxCyNz. J Mater Chem A. 2013;1:5806-21.

1.5 REMARKABLE PERFORMANCE OF MOS_2-RGO NANOCOMPOSITES AS SUPERCAPACITORS

Summary*

Considering the desirable attributes of the nanosheets of MoS_2 and reduced graphene oxide (RGO), we have prepared composites of the two and investigated their use in supercapacitors. The best results are obtained with the MoS_2:RGO (1:2) composite which exhibits a specific capacitance of 416 F g^{-1} at 5 mV/s. The excellent performance of the MoS_2-RGO (1:2) composite is attributed to the combined effect of good electrical conductivity of RGO, and unique surface properties of MoS_2 as well as of RGO. The study shows how there a common factor determines good supercapacitor performance.

*A Paper based on this work has been published in Nanomater. Energy, 2015, **4**, 9-17

1.5.1 Introduction

MoS_2 and related layered metal chalcogenides have been found to exhibit extraordinary properties which are not only of academic interest, but may have potential applications [1, 2]. Being a typical layered transition metal sulfide, it is composed of three atomic layers (S-Mo-S) stacked together and bonded through van der Waals interactions. This versatility is attributed to its 2D structure, which is analogous to graphene [2]. Thus, few layer MoS_2, being used as an industrial catalyst for hydrodesulfurization reaction [3], exhibits excellent catalytic properties for electrochemical and photochemical hydrogen evolution reaction [4-6]. MoS_2 is one of the first transition metal dichacogenides used as an electrode material in Li-ion batteries and has since been employed as a high energy and high current density electrode material [7, 8]. MoS_2 can potentially store charge by intersheet and intrasheet double-layers over individual atomic MoS_2 layers and faradaic charge transfer processes on the Mo center because this atom exhibits several oxidation states, similar to ruthenium [9]. Accordingly, nanoforms of MoS_2 have been used in supercapacitors [10, 11]. Ajayan et al have fabricated film-based micro-supercapacitors via spray painting of MoS_2 nanosheets and subsequent laser patterning [9]. This MoS_2-based micro-supercapacitor exhibits good electrochemical performance for energy storage in aqueous electrolytes, with a high area capacitance of 8 mF cm^{-2} (volumetric capacitance of 178 F/cm^3) and excellent cyclic performance. Chemically exfoliated nanosheets of MoS_2 containing a high concentration of the metallic 1T phase shown capacitance values ranging from ~400 to ~700 F cm^{-3} in a variety of aqueous electrolytes [12].

There are few methods of synthesis of MoS_2 in the literature [1, 2, 6]. Micromechanical cleavage MoS_2 using the scotch tape technique yields single and few-layered flakes on Si/SiO_2 substrates [13]. Physical methods like ultra-sonication in solvents as well as exfoliation using lasers also produce single and few-layer MoS_2 [14, 15]. Hydrothermal reduction of MoO_3 by KSCN yields few layer to MoS_2 [16] whereas chemical vapour deposition of MoO_3 thin films in H_2, sulfur vapour yields thin films of MoS_2 on Cu substrates [17]. Decomposition of molybdic acid–thiourea mixtures in N_2 [16] or of ammonium thiomolybdate in sulfur produces few-layer MoS_2 [17]. Li

intercalation of MoS_2 using *n*-butyl lithium can be used to prepare dispersions of single layered materials [18, 19].

MoS_2 sheets provide a large surface area for double-layer charge storage but shows low specific capacitance due to the low conductivity of the MoS_2 molybdenite phase. To enhance the supercapacitor properties of MoS_2, it is necessary to increase the available surface area for storing charge as well as the efficiency of electron transport to the electrode. Composites of graphene with MoS_2 and WS_2 have proven to show enhanced performance in Li ion batteries, wherein graphene provides the higher surface-area as well as greater electrical conductivity. Using graphene as a substrate for MoS_2 layers can also facilitate electron transport through MoS_2 nanostructures, which provides an easier and faster ion diffusion between MoS_2 layers/electrolytes and produces high specific capacitance values. MoS_2 is deposited on reduced graphene oxide by microwave heating shows capacitance of 148 F/g at 10 mV/s [20]. MoS_2-graphene composite is synthesized by a modified l-cysteine-assisted solution-phase method exhibits good supercapacitor properties showing a capacitance of 243 F/g at 1 A/g.

1.5.2 Scope of the present investigations

Two-dimensional materials such as graphene and molybdenum disulfide show excellent charge storing capability due to their high surface area and versatile electronic structure. Making composites MoS_2 with graphene will lead to interesting synergistic properties. We would expect to observe better charge storage properties if MoS_2 flakes could be grown almost vertically on graphene sheets. This would not only increase the available surface area for charge storage but also the electrical conductivity of the chalcogenide. We have investigated the supercapacitor performance of composites formed by few-layer MoS_2 with reduced graphene oxide (RGO) where in the composition of the composites was varied over a wide range (MoS_2:RGO, weight ratios of 1:3. 1:2 and 2:1).

1.5.3 Experimental section

Preparation of graphene oxide: GO solution was prepared following the modified Hummers method. 70 mL conc. H_2SO_4 was added to a mixture of 3.0 g graphite flakes and

1.5 g $NaNO_3$, and the mixture was cooled in an ice bath. To this 9.0 g of $KMnO_4$ was added. The reaction was stirred for 30 min at room temperature, after which 150 mL water was added. Additional water (420 mL) and 10 mL 30% H_2O_2 were added and the reaction stirred overnight.

Preparation of MoS_2 nanosheets: MoS_2 was prepared by hydrothermal method. Mixture of 0.3 g $(NH_4)_6Mo_7O_24.6H_2O$ (ammonium heptamolybdate) and 0.2 g NH_2CSNH_2 (thiourea) was dissolved in 17 mL distilled water. The solution was heated in a oven at 200°C for 72 hours in a stainless steel autoclave. The product was washed and dried. The nanosheets consisted of 3-7 layers.

Preparation of MoS_2-RGO composites: MoS_2-RGO composites were synthesized by the hydrothermal method. Different compositions were prepared by varying the weight of $(NH_4)_6Mo_7O_{24}.6H_2O$. First, 1.5 mL of 20mg/mL GO solution was ultrasonicated with 15 mL distilled water for half an hour. To this, 'x' g of $(NH_4)_6Mo_7O_{24}.6H_2O$ and 0.5 g of NH_2CSNH_2 were added and stirred for an hour. The mixture was heated in a oven at 200°C for 24 hours in a stainless steel autoclave. The product was washed and dried. Under the conditions of experiments GO gets reduced to RGO. RGO had 3-5 layers on average.

Electrochemical measurements*:* Supercapacitor measurements were performed on an PGSTAT 262A (Techno Science Instruments) electrochemical workstation in 1 M H_2SO4 aqueous electrolyte solutions under three-electrode assembly with a catalyst coated glassy carbon (GC) electrode as the working electrode (WE) with a large-area Pt foil and Ag/AgCl as counter and reference electrodes respectively. The working electrode was fabricated by dispersing 3 mg of sample in 1 mL ethanol-water mixture (1:1) from that 10 µL was drop casted on glassy carbon electrode followed by 10 µL of 0.05 wt.% nafion solution was used as binder. The electrodes were dried in air at 60 ^oC for 30 mins.

1.5.4 Results and Discussion

In Figures 1 (a) and (b) we show FESEM and TEM images of the MoS_2-RGO nanocomposites respectively. The TEM image shows flower-like MoS_2 nanosheets deposited on graphene sheets. High resolution TEM image is shown in Figure 1(c) shows the lattice spacing of the perpendicularly growing sheets to be similar to that of interlayer

distance between two MoS_2 layers. The Raman spectra of given in Figure 1(d) show the G-band of RGO at 1584 cm^{-1} and the D-band at 1329 cm^{-1}. MoS_2-RGO (1:2) and the other nanocomposites show the G-band 1594 cm^{-1} and D- band at 1350 cm^{-1}. There are significant shifts in the peak positions of RGO after the addition of MoS_2, indicating that there is interaction between MoS_2 and RGO. The characteristic bands due to the E^1_{2g} and A_{1g} modes of MoS_2 are clearly seen in the MoS_2-RGO (1:2) composite. Figure 2 shows the XRD patterns of MoS2, RGO, MoS2-RGO (1:2) and MoS_2-RGO (2:1) composites. Figure 2(a) shows the XRD pattern of MoS_2 with (002), (100) and (110) diffraction planes which indicates that the MoS_2 is of amorphous nature. RGO shows appearance of the (002) plane at ~28°, which shows that the graphite oxide is reduced to form RGO as shown in Figure 29(b). MoS_2-RGO composites show XRD patterns corresponding to both MoS_2 and RGO, which confirms that MoS_2 is grown on graphene.

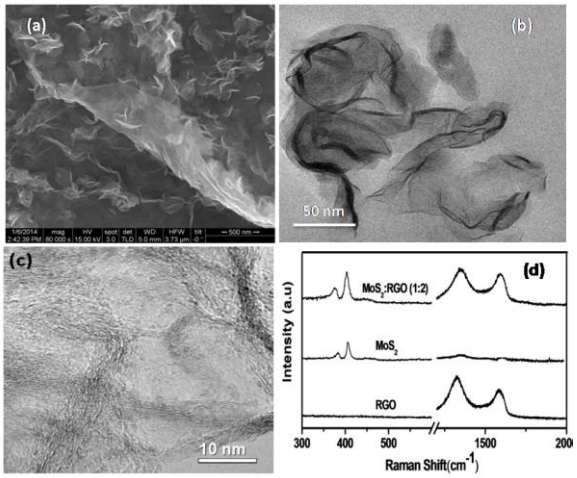

Figure 1. (a) FESEM, (b) TEM and (c) HRTEM image MoS_2-RGO (1:2) and (d) Raman spectra of MoS_2, RGO and MoS_2-RGO (1:2)

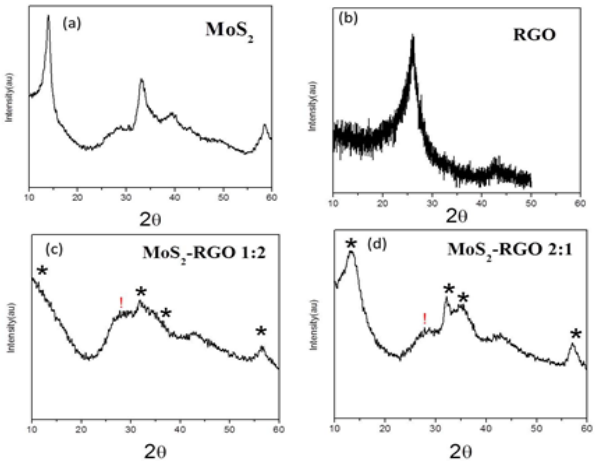

Figure 2. XRD of (a) MoS_2, (b) RGO, (c) MoS_2-RGO 1:2 and (d) MoS_2-RGO 2:1 prepared by hydrothermal method. Symbols in (c) and (d) represent reflections due to ∗ = MoS_2, and ! = RGO.

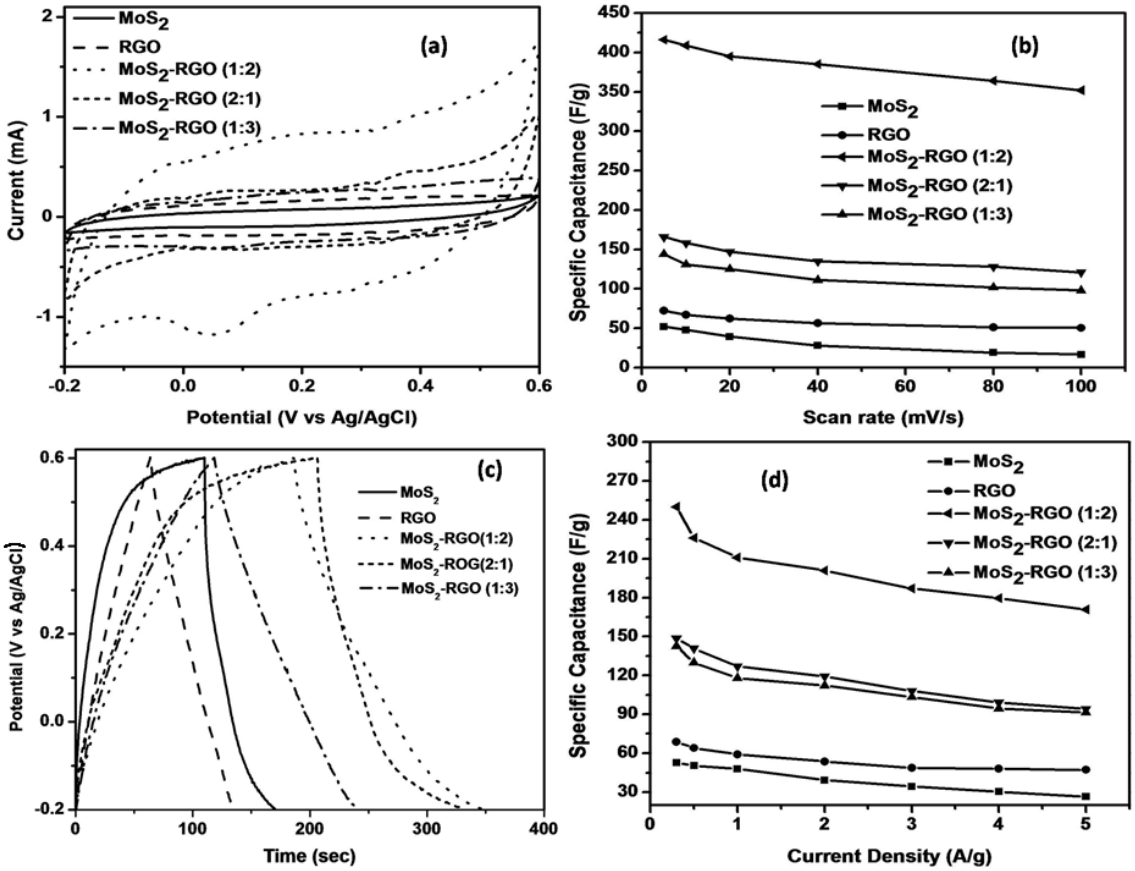

Figure 3. (a) Cyclic voltammograms of MoS_2, RGO and MoS_2-RGO nanocomposites at 100 mV s^{-1}. (b) Specific capacitance of MoS_2, RGO and MoS_2-RGO nanocomposites at different scan rates. (c) Galvanostatic charge discharge curves of MoS_2, RGO and MoS_2-RGO nanocomposites at a current density of 1 A g^{-1} (d) Specific capacitance of MoS_2, RGO and MoS_2-RGO nanocomposites at different current densities.

Electrochemical performance: The electrochemical performance of the MoS_2-RGO nanocomposites was investigated by means of cyclic voltammetry (CV), galvanostatic charge-discharge curves and electrochemical impedance spectroscopy (EIS) in 1 M H_2SO_4 aqueous electrolyte. Cyclic voltammograms of MoS_2, RGO and MoS_2-RGO composites are measured at different scan rates (5-100 mV/s) and the CV curves measured at 100 mV/s are shown in Figure 3(a). The CV curves MoS_2-RGO nanocomposites shows quasi-rectangular CV curves with small humps due to redox process. This quasi-rectangular CV curves indicates excellent charge storage capability of MoS_2-RGO nanocomposites which resembles those of an ideal supercapacitor. We have obtained a maximum capacitance of 416 $Fg^{-1}$with MoS_2-RGO (1:2) at a scan rate of 5 mV/s. It is smaller on either side of this composition as found in the 2:1 and 1:3 composites. When the scan rate increases, the

current increases while the capacitance decreases as shown in Figure 3(b). The MoS_2-RGO (1:2) composite exhibits the best results. The galvanostatic charge-discharge curves of MoS_2, RGO and MoS_2-RGO composites were measured in a potential window of -0.2-0.6 V *vs* Ag/AgCl (2M KCl). Figure 2 (c) shows the charge-discharge curves measured at a current of 1 A g^{-1}. The discharge time of MoS_2-RGO (1:2) was significantly longer than the other composites and the curves look nearly symmetrical indicating remarkable charge storing ability of this composite. The calculated specific capacitance of this composite is 249 F/g when measured at 0.3 A/g. The specific capacitance of MoS_2, RGO and MoS_2-RGO composites obtained at different current densities are shown in Figure 3 (d). It can be clearly seen that the capacitance decreases with the increasing current density. The maximum capacitance obtained for MoS_2, RGO and the MoS_2-RGO composites are shown in the bar diagram in Figure (4).

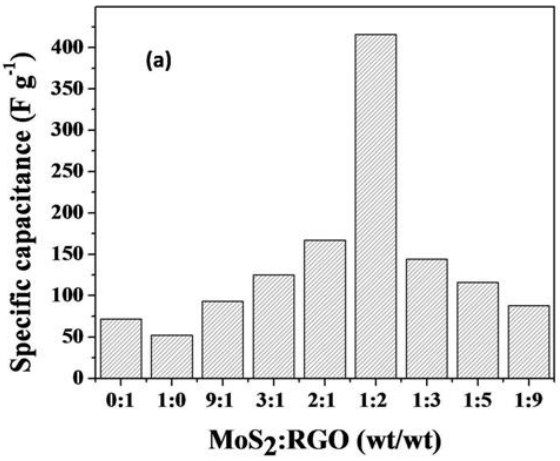

Figure 4. Dependence of specific capacitance with MoS_2-RGO weight ratio at scan rate of 5 mV/s

Cyclic stability and electrochemical impedance measurements are the very important measurements to understand the performances of supercapacitors. Figure 5(a) shows the Nyquist of MoS_2 and MoS_2-RGO (1:2). The plots show the capacitive behaviour of MoS_2-RGO (1:2) as indicated by the near vertical line at the lower frequency range. The high frequency region is shown in the inset of Figure 5(a). The equivalent series resistances (ESRs) of MoS_2 21.6 ohm and for MoS_2-RGO (1:2) it was 18.8 ohm indicating that the conductivity of MoS_2 got increased after the addition of RGO and also the capacitance. Cyclic stability tests for MoS_2-RGO (1:2) were carried out by repeating

the galvanostatic charge-discharge between -0.2 and 0.6 V at a current density of 2 A g^{-1} for 1000 cycles as shown in Figure 5(b). This composite shows a loss of 6.4% from the initial specific capacitance, indicating good capacitance retention. The last few cycles are also given in Figure 5(b). The energy density obtained was 79.68 Wh Kg^{-1} at 0.3 A/g for MoS_2-RGO (1:2) composite. The increase in the supercapacitive performance of MoS_2 and RGO in the 1:2 composite is attributed to a synergistic effect between RGO and MoS_2.

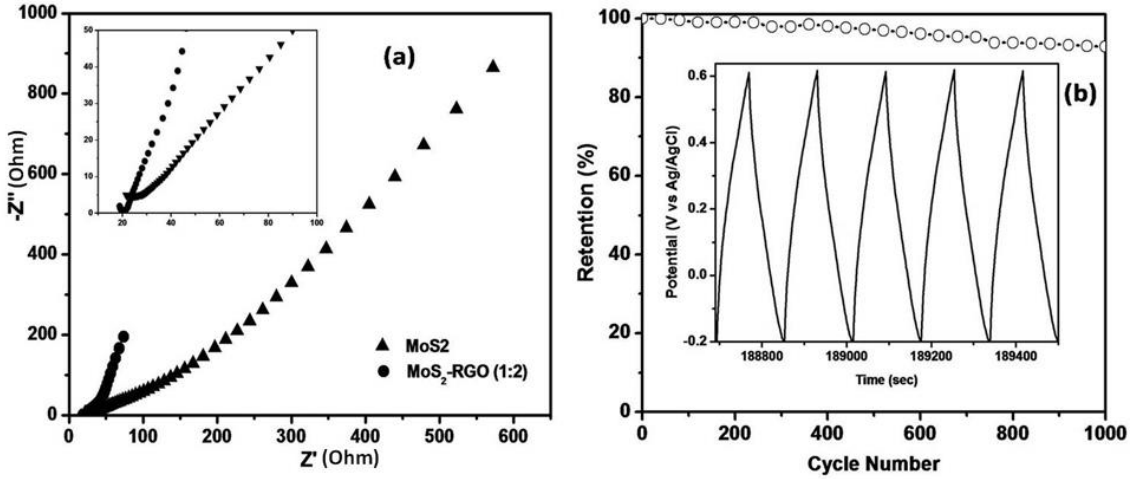

Figure 5 (a) Nyquist plots of MoS_2 and MoS_2-RGO (1:2). Inset shows the higher frequency region. (b) Cyclic stability of MoS_2-RGO (1:2) at current density of 2 A/g. Boxed figure gives cyclic stability over a large number of cycles.

1.5.6 Conclusions

The present study demonstrates synergy in the properties of the MoS_2-RGO composites with the 1:2 composite exhibiting excellent capacitance for possible use in the supercapacitors. Good electronic conductivity of RGO and the surface properties of both MoS_2 and RGO in the composites appear to be the factors responsible for good specific capacitance.

References

[1] Rao CNR, Ramakrishna Matte HSS, Maitra U. Graphene Analogues of Inorganic Layered Materials. Angew Chem Int Ed. 2013;52:13162-85.

[2] Rao CNR, Maitra U, Waghmare UV. Extraordinary attributes of 2-dimensional MoS2 nanosheets. Chem Phys Lett. 2014;609:172-83.

[3] Rao BG, Matte HSSR, Chaturbedy P, Rao CNR. Hydrodesulfurization of Thiophene over Few-Layer MoS2 Covered with Cobalt and Nickel Nanoparticles. ChemPlusChem. 2013;78:419-22.

[4] Hinnemann B, Moses PG, Bonde J, Jørgensen KP, Nielsen JH, Horch S, et al. Biomimetic Hydrogen Evolution: MoS2 Nanoparticles as Catalyst for Hydrogen Evolution. J Am Chem Soc. 2005;127:5308-9.

[5] Jaramillo TF, Jørgensen KP, Bonde J, Nielsen JH, Horch S, Chorkendorff I. Identification of Active Edge Sites for Electrochemical H2 Evolution from MoS2 Nanocatalysts. Science. 2007;317:100-2.

[6] Maitra U, Gupta U, De M, Datta R, Govindaraj A, Rao CNR. Highly Effective Visible-Light-Induced H2 Generation by Single-Layer 1T-MoS2 and a Nanocomposite of Few-Layer 2H-MoS2 with Heavily Nitrogenated Graphene. Angew Chem Int Ed. 2013;52:13057-61.

[7] Haering RR, Stiles JAR, Brandt K. Lithium molybdenum disulphide battery cathode. US 06/071,395: Google Patents; 1980.

[8] Stephenson T, Li Z, Olsen B, Mitlin D. Lithium ion battery applications of molybdenum disulfide (MoS2) nanocomposites. Energy Environ Sci. 2014;7:209-31.

[9] Cao L, Yang S, Gao W, Liu Z, Gong Y, Ma L, et al. Direct Laser-Patterned Micro-Supercapacitors from Paintable MoS2 Films. Small. 2013;9:2905-10.

[10] Soon JM, Loh KP. Electrochemical Double-Layer Capacitance of MoS2 Nanowall Films. Electrochem Solid-State Lett. 2007;10:A250-A4.

[11] Ramadoss A, Kim T, Kim G-S, Kim SJ. Enhanced activity of a hydrothermally synthesized mesoporous MoS2 nanostructure for high performance supercapacitor applications. New J Chem. 2014;38:2379-85.

[12] Acerce M, Voiry D, Chhowalla M. Metallic 1T phase MoS2 nanosheets as supercapacitor electrode materials. Nat Nano. 2015;10:313-8.

[13] Late DJ, Liu B, Matte HSSR, Rao CNR, Dravid VP. Rapid Characterization of Ultrathin Layers of Chalcogenides on SiO2/Si Substrates. Adv Funct Mater. 2012;22:1894-905.

[14] Matte HSSR, Maitra U, Kumar P, Govinda Rao B, Pramoda K, Rao CNR. Synthesis, Characterization, and Properties of Few-layer Metal Dichalcogenides and their Nanocomposites with Noble Metal Particles, Polyaniline, and Reduced Graphene Oxide. Z anorg allg Chem. 2012;638:2617-24.

[15] Castellanos-Gomez A, Barkelid M, Goossens AM, Calado VE, van der Zant HSJ, Steele GA. Laser-Thinning of MoS2: On Demand Generation of a Single-Layer Semiconductor. Nano Lett. 2012;12:3187-92.

[16] Ramakrishna Matte HSS, Gomathi A, Manna AK, Late DJ, Datta R, Pati SK, et al. MoS2 and WS2 Analogues of Graphene. Angew Chem Internat Ed. 2010;49:4059-62.

[17] Zhan Y, Liu Z, Najmaei S, Ajayan PM, Lou J. Large-Area Vapor-Phase Growth and Characterization of MoS2 Atomic Layers on a SiO2 Substrate. Small. 2012;8:966-71.

[18] Joensen P, Crozier ED, Alberding N, Frindt RF. A study of single-layer and restacked MoS2 by X-ray diffraction and X-ray absorption spectroscopy. J Phys C: Solid State Phys. 1987;20:4043.

[19] Chhowalla M, Shin HS, Eda G, Li L-J, Loh KP, Zhang H. The chemistry of two-dimensional layered transition metal dichalcogenide nanosheets. Nat Chem. 2013;5:263-75.

[20] da Silveira Firmiano EG, Rabelo AC, Dalmaschio CJ, Pinheiro AN, Pereira EC, Schreiner WH, et al. Supercapacitor Electrodes Obtained by Directly Bonding 2D MoS2 on Reduced Graphene Oxide. Adv Energy Mater. 2014;4:1301380.

1.6 BN-GRAPHENE COMPOSITES GENERATED BY COVALENT CROSS-LINKING WITH ORGANIC LINKERS

Summary*

Composites of boron nitride (BN) and carboxylated graphene are prepared using covalent cross-linking employing the carbodiimide reaction. The $BN_{1-x}G_x$ ($x \approx 0.25$, 0.5, and 0.75) obtained are characterized using a variety of spectroscopic techniques. The composites show composition-dependent electrical resistivity, the resistivity decreases with increase in graphene content. The composites exhibit microporosity and the $x \approx 0.75$ composite especially exhibits satisfactory performance with high stability as an electrode in supercapacitors.

*A Paper based on this work has been published in Adv. Funct. Mater, 2015, **25**, 5910.

1.6.1 Introduction

Hexagonal boron nitride (h-BN) is a layered insulator while graphene is a layered conductor [1-3]. Although h-BN nanosheets and graphene are isoelectronic with the same layered structure, there are essential differences in the chemistry and properties of BN nanosheets [2]. Composites of BN and graphene are expected to be materials of great interest and there have been efforts to study ternary borocarbonitrides [4, 5]. $B_xC_yN_z$ with varying carbon content, prepared by different methods [5]. By varying the C content optical, electrical and other functional properties of the borocarbonitrides can be tuned. There has also been effort to deposit BN sheets over graphene and vice versa [6]. Numerous applications of these two nanomaterials have been reported in the recent literature such as field effect transistors, photoresponse devices, supercapacitors, Li battery and as oxygen reduction reaction catalysts in fuel cells [5].

Theoretical calculations show that there is a band-gap change in the graphene/BN heterostructure with change in BN concentration [1]. Monte Carlo simulations, predict the formation of BN domains in graphene to generate BCNs. Kumar et al [5] have examined various configurations of the borocarbonitride, $C_4B_2N_2$, with a hexagonal supercell containing a random distribution of B, C and N atoms. The energetic stability of the bonds are in the order, B-N > C-C > C-N > C-B > B-B > N-N. The band gap of graphene can be tuned by varying the BN concentration. Banerjee and Pati [7] have used density functional theory to study the carrier mobility of BCN. Carbon-rich compositions (BCN and BC_4N) are metallic whereas the BN predominant compositions ($B_{2.5}CN_{2.5}$) are semiconducting with high hole mobility ($\sim 10^6$ $cm^2/V.s$) compare to BCN ($\sim 10^4$ $cm^2/V.s$) and BC_4N ($\sim 10^5$ $cm^2/V.s$). A Monte-Carlo simulated annealing process has been employed to investigate electronic and structural properties of BCN over a wide doping range [8]. For a given BN doping concentration, the doping-induced band gap can vary from 2.08 up to 10.42%. Kaloni et al [9] used density functional theory to compare the electronic properties of BN-doped graphene mono-layer, bi-layer, tri-layer, and multi-layer. Doping concentrations are between 12.5% and 75% and the obtained band gaps are from 0.02 eV to 2.43 eV. The effect of doping of B and N in graphene has been studied by first-principles electronic structure calculation [10]. BN domains seem to be more

likely to form in BCN. Effects of geometric shape and size of BCN superlattices have been studied [11]. The band gap increases with increase in BN concentration. A study of BN-doping in graphene has shown that the bandgap to be dependent on BN concentration [12].

In case of FETs, graphene shows conducting behavior whereas the h-BN showing no conductivity (sheet resistance R_{sheet} >400 TΩ) [13]. The mobilities of graphene/h-BN heterostructure are in the range of ~190 to 2,000 cm^2/V.s. Graphene encapsulated by boron nitride is reported to show a carrier mobility up to 80,000 cm^{-2}/V.s at room temperature [14]. The FET of a BCN (40 at.% C) show ambipolar semiconducting behavior [6]. The electron and hole mobilities of BCN devices are in the range of 5-20 cm^2/V.s. Shiue et al [14] have demonstrated photo-detector based on a hybrid graphene/BN. The detector has been tested using 250 fs pulses at 1800 nm. Supercapacitors based on B,N-doped graphene show good performance. The supercapacitors shows a specific capacitance of 62 F/g [15]. Nanostructured graphene-BN composites show enhanced electrical conductivity and supercapacitor performance (824 F/g) [16]. BN/graphene synthesized by liquid-phase exfoliation show a specific capacitance of 140 F/g [17]. Shi et al [18] have fabricated the thinnest nanocapacitor electrode consisting of h-BN and graphene with different layers of h-BN ranging from bulk to 2 layers. The electrode with thickness of 0.8 nm (h-BN=2 layers) shows a capacitance of ~12 pF. BCN performs as an catalyst for ORR compared to undoped graphene or B-graphene and N-graphene electrodes [19].

There are few methods of synthesis of graphene/BN heterostructure. Levendorf et al [13] obtained graphene-BN lateral heterojunctions on Cu foils using methane, diborane ammonia under CVD conditions. Here, domains of BN and graphene are next to one another to form continuous sheets across the heterojunctions. Ci et al [6] have made atomic sheets of BCN with a wide range of composition by the decomposition of methane and ammonia-borane precursors on Cu substrates at 1000 ^oC for 40 min. BN and graphene layers were deposited one over the other. Atomic layers of graphene/BN are grown on Cu under CVD conditions at 1000 ^oC for 20 min [20]. Low-pressure chemical vapor deposition yields BCN at 1050 ^oC using CH_4 and ammonia borane vapor in an argon atmosphere [21]. Different BN concentrations are obtained by heating ammonia borane

from 70-110 ^{o}C. Hexagonal graphene/BN nanosheets have been prepared by atmospheric pressure CVD by using CH_4 mixed with argon and ammonia borane on Cu foil at 1057 ^{o}C [22]. Conversion of graphene to BCN has been made by heating boric acid powder in a flow of NH_3 and Ar gas for 2 h at 1000 ^{o}C [23]. Zhang et al [24] have grown graphene/BN vertical heterostructures by annealing Ni(C)/(B,N)/Ni samples in a vacuum furnace in the 900-1050 ^{o}C range.

BN and graphene sheets can be stacked by mixing dispersions or by the use of the liquid-liquid interface [25]. Boron nitride powder is sonicated in isopropyl alcohol while graphite powder dissolved in dimethylformamide and supernatants were collected [26]. These supernatants are mixed under sonication for 2h to form hybrids of BN with graphene. Graphene/BN hybrid structures can be obtained by exfoliation in liquid-phase. Graphite and BN were added to a mixture (conc. H_2SO_4 and HNO_3) to obtain a hybrid compound. This compound is subjected to thermal treatment to yield an expanded hybrid structure which is sonicated in dimethylformamide.

1.6.2 Scope of the present investigations

Graphene/BN heterostructure shows excellent transfer characteristics and excellent electrochemical properties [5]. We have been interested in preparing hybrid composites of BN and graphene with different compositions by covalent cross-linking using organic linkers. We have recently used covalent cross-linking to prepare assemblies of single-walled carbon nanotubes as well as graphene [27]. Graphene–BN composites prepared by covalent cross-linking would be expected to possess properties different from those obtained by depositing BN and grapheme sheets on each other. We have prepared $BN_{1-x}G_x$ composites with varying graphene content (x = 0-1) and studied their electrical properties. Another property that we have investigated relates to the use in supercapacitors. It may be noted that graphene doped with nitrogen as well as borocarbonitrides show good supercapacitive characteristic.

1.6.3 Experimental Section

Synthesis of $BN_{1-x}G_x$ composites:* Amine functionalized few-layer BN (~ 1–4 layers) was prepared by mixing boric acid and urea in 1:48 molar ratio and heating in high purity

*carried out by Mr. Ram Kumar

ammonia atmosphere at 900 °C for 5h. Graphite oxide (GO) was synthesized using modified Hummers method {Marcano, 2010 #94}. GO was placed in an alumina boat inside a quartz tube and inserted in the heating zone of furnace at 1050 °C under constant N_2 flow to obtain the exfoliated graphene (EG). Carboxylate functionalized graphene was obtained by microwave irradiation. In a typical batch 200 mg EG was placed in 125 ml microwave reactor, 8 ml conc. HNO_3, 8 ml conc. H_2SO_4, 64 ml deionized H_2O was added and irradiated with microwave for 10 min at 450 W followed by heating in an oven at 100 °C for 12 h. Obtained product was filtered using 0.45 μm PTFE membrane, washed with copious amount of water to remove excess acid and dried at 100 °C.

Three different composites $BN_{1-x}G_x$ (x ≈ 0.25, 0.5 and 0.75) were obtained by varying the ratio of BN with respect to carboxylated graphene. In a Schlenck flask 150 mg of BN and carboxylated graphene was mixed in appropriate ratio, purged with N_2, sealed using septum and 35 ml DMF was added. In the uniform dispersion *N*-(3-Dimethylaminopropyl)-*N'*-ethylcarbodiimidehydrochloride (EDC.HCl) 80 mg, 1-Hydroxybenzotriazole (HOBt) 80 mg and *N,N*-Diisopropylethylamine (DIPEA) 1.2 ml was added under constant stirring and allowed for 48 h. Nitrogen atmosphere was maintained during the reaction. Obtained product was filtered using 0.45 μm PTFE membrane, washed with copious amount of DMF and water. The solid product was further washed with methanol in a Soxhlet extractor for 48 h and dried at 100 °C under vacuum. Further, $BN_{1-x}G_x$ samples were annealed at 300 °C in N_2 atmosphere for 6 h and IR spectra was recorded to monitor the loss of amide bond between BN and graphene.

Electrochemical Measurements: Supercapacitor measurements were performed on PGSTAT 262 A (Techno Science Instruments) electrochemical workstation in 2 M H_2SO_4 aqueous electrolyte. Three-electrode assembly was used with a catalyst coated glassy carbon (GC) electrode as the working electrode (WE), large-area Pt foil and Ag/AgCl as counter and reference electrodes respectively. The working electrode was fabricated by dispersing 3 mg of sample in 1 mL ethanol-water mixture (1:1) and dropcasting 10 μL on glassy carbon electrode followed by 10 μL of 0.05 wt.% nafion solution as binder. The electrodes were dried at 60 °C. Cyclic voltammetry (CV) measurements were carried out at different scan rates from 2 to 100 mV/s. Electrochemical impedance spectroscopy (EIS) measurements were studied by applying an AC voltage with 10 mV amplitude in

the frequency range from 0.1 Hz to 100 kHz. A galvanostatic charge–discharge (GCD) test was also conducted at different current densities

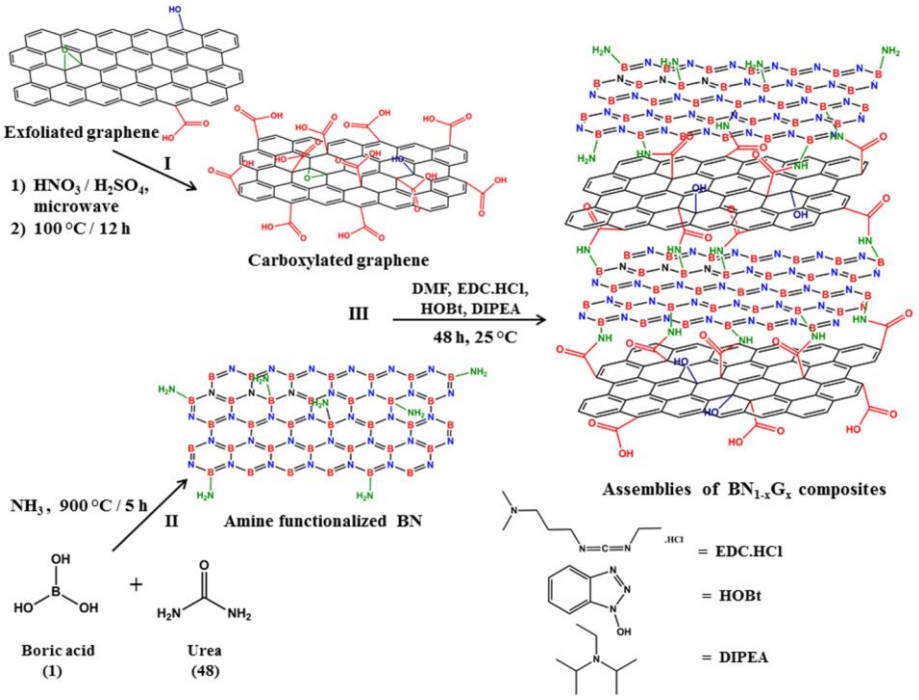

Scheme 1. Schematic representation of the synthesis of covalently cross-linked assemblies of BN and graphene using EDC coupling. (I) Synthesis of carboxylated graphene; (II) synthesis of amine functionalized few-layer BN; (III) Synthesis of assemblies of $BN_{1-x}G_x$ composites by amide bond cross-linking using EDC coupling.

1.6.4 Results and Discussion

Scheme 1 shows the steps involved in the synthesis of the amide bond cross-linked assemblies of BN and graphene ($BN_{1-x}G_x$, x ≈ 0.25, 0.5, 0.75). Carboxylate functionalized graphene (G) obtained by microwave irradiation of graphene in a HNO_3/H_2SO_4 mixture, was reacted with amine–functionalized few-layer BN (~1 – 4 layers) prepared by heating boric acid and urea in 1:48 molar ratio in an ammonia atmosphere. We have employed the carbodiimide method to link BN and G with amide bond, by using EDC {1-ethyl-3-(3-dimethylaminopropyl) carbodiimide)} as the reagent. The advantage of EDC coupling over $SOCl_2$ - based activation is that no HCl is liberated and urea obtained as a by-product is water soluble. Three different compositions of the $BN_{1-x}G_x$ composites (x ≈ 0.25, 0.5, 0.75) were obtained by varying the ratio of BN with respect to graphene.

We have examined the $BN_{1-x}G_x$ composites using electron microscopy. Figure 1 shows typical electron microscope images of few-layer BN, carboxylated graphene and $BN_{0.5}G_{0.5}$. Transmission electron microscope (TEM) images of few-layer BN and carboxylated graphene show wrinkled transparent sheets. TEM images of the $BN_{1-x}G_x$ composites show layer by layer self-assembly of the component sheet structures. The layer by layer self-assembly of graphene and BN is facilitated by amide bond formation between the amine group on the BN sheets and the carboxylate groups on the graphene sheets. Elemental mapping of the $BN_{1-x}G_x$ using energy-dispersive X-ray spectroscopy (EDAX) shows uniform distribution of B, N and C confirming homogeneous nature of the composite (Figures 2).

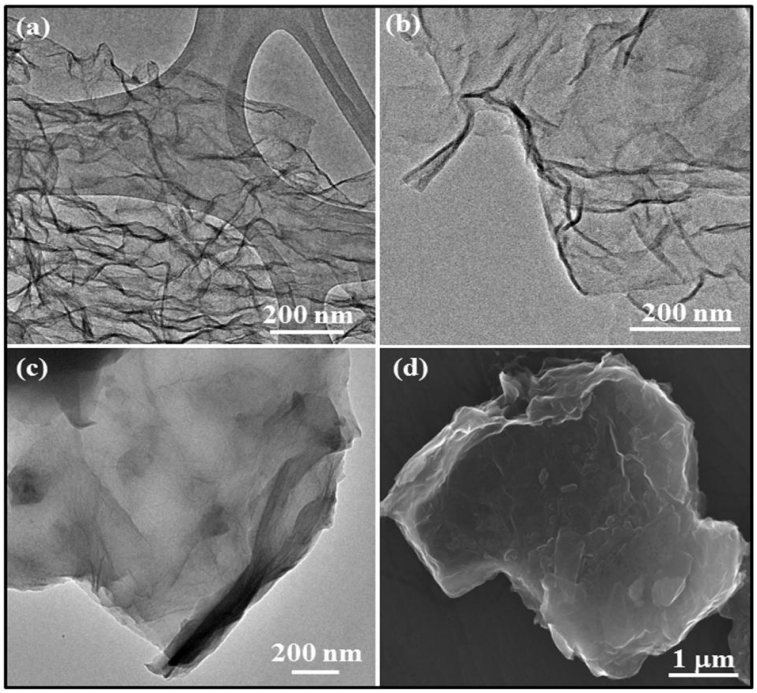

Figure 1. TEM images of (a) few-layer BN, (b) carboxylated graphene, (c) and (d) TEM and SEM images of $BN_{0.5}G_{0.5}$.

The electron energy loss spectrum (EELS) of $BN_{0.5}G_{0.5}$ displayed in Figure 3 shows the K shell ionization edges of B, C, N and O. The K shell ionization edge at 192.6 eV is due to the transition of B 1s electron to the π^* antibonding orbitals, associated with planar bonding and sp^2 hybridization of boron in BN. The peak at 200, 204.8, 207.5 and 216 eV

are due to 1s → σ* transition of boron in BN. The broad feature around 234 eV is extended energy-loss fine structure (EXELFS) due to the backscattering from nearest neighbors. The C K shell ionization edge have bands at 286, 296, and 324 eV corresponding to 1s → π*, 1s → σ* and EXELFS feature respectively. The nitrogen EEL spectrum have peaks at 402.5 eV due to 1s → π* whereas peaks at 409 and 416 eV are due to 1s → σ* transitions. Band at 439 eV is EXELFS feature due to backscattering from nearest neighbors. The O K shell ionization is also observed at 541 eV with no distinct feature as observed in ionization edge of B, C and N indicating the absence of periodicity in the distribution of oxygen containing functional groups in the composite.

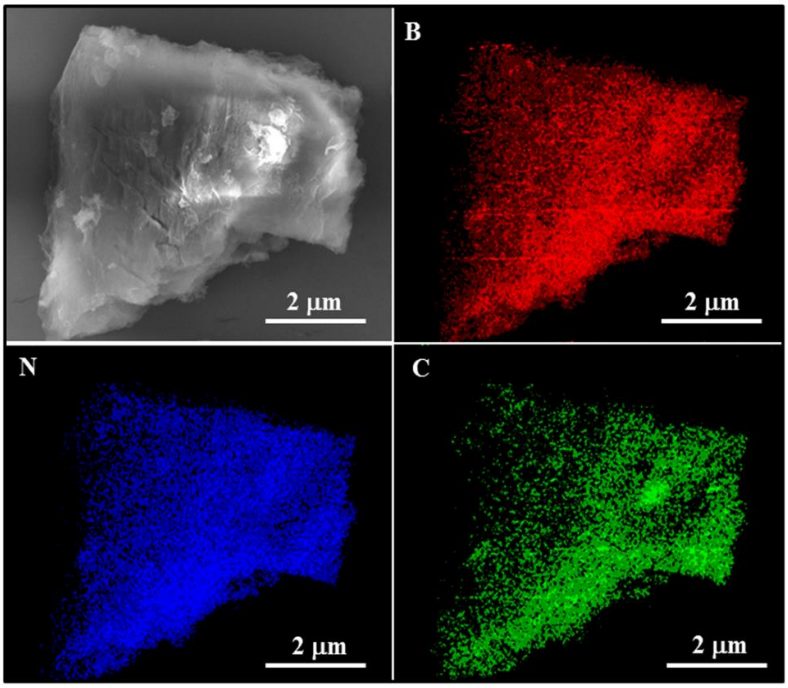

Figure 2. Elemental mapping of $BN_{0.5}G_{0.5}$. B (red), N (blue) and C (green).

Core level X-ray photoelectron spectra (XPS) of $BN_{0.5}G_{0.5}$ are shown in Figure 4. The B 1s core level has main peak at 190.7 eV corresponding to B–N bonding along with two minor contributions at 188.8 eV and 192.7 eV due to interaction of B with C and O of graphene basal plane. The N 1s core level has signal at 398 eV due to bonding with B. The peak at 400.5 eV is due to N of amide groups on the BN basal plane. The carboxylate functionalization of graphene involves HNO_3/H_2SO_4 treatment which introduces minor

concentration of other oxygen functionalities such as epoxide and hydroxyl groups. This is reflected as additional broadness of the C 1s spectrum. Peak at 284.6 and 288 eV are due to sp^2 aromatic C domains and amide bond C. Peak at 286.4 eV have contributions from sp^3 C along with minor concentration of epoxide and hydroxyl groups which we were not able to deconvolute. Unreacted carboxylate group is reflected as minor contribution at 289 eV. C 1s core level spectrum also shows signals at 284.6 and 288 eV due to grapheme (sp^2) and amide carbons.

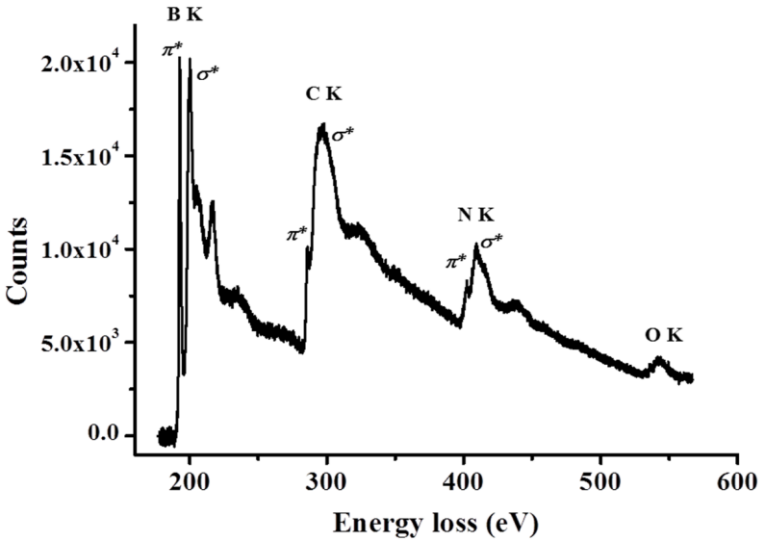

Figure 3. Electron energy loss spectrum (EELS) of $BN_{0.5}G_{0.5}$ composite.

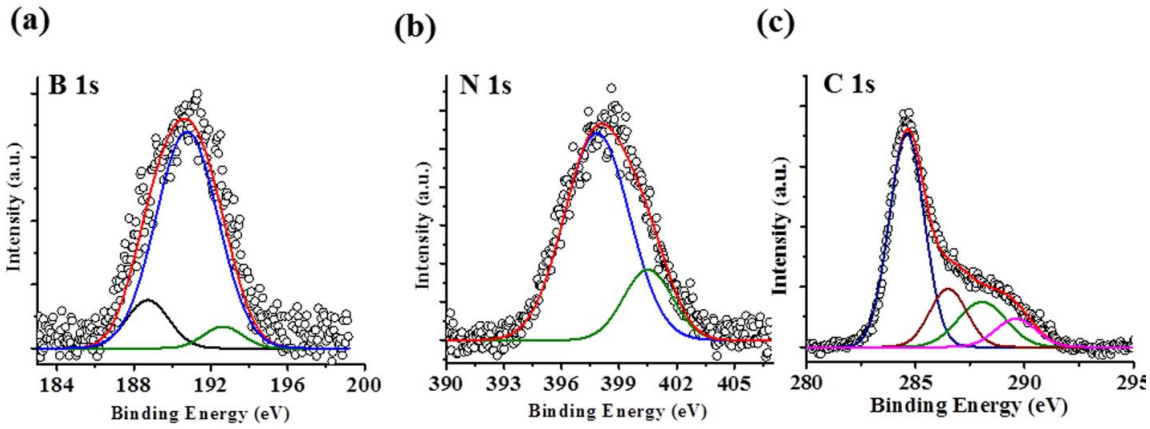

Figure 4. X-ray photoelectron spectrum of $BN_{0.5}G_{0.5}$ composite (a) B 1s, (b) N 1s, (c) C 1s.

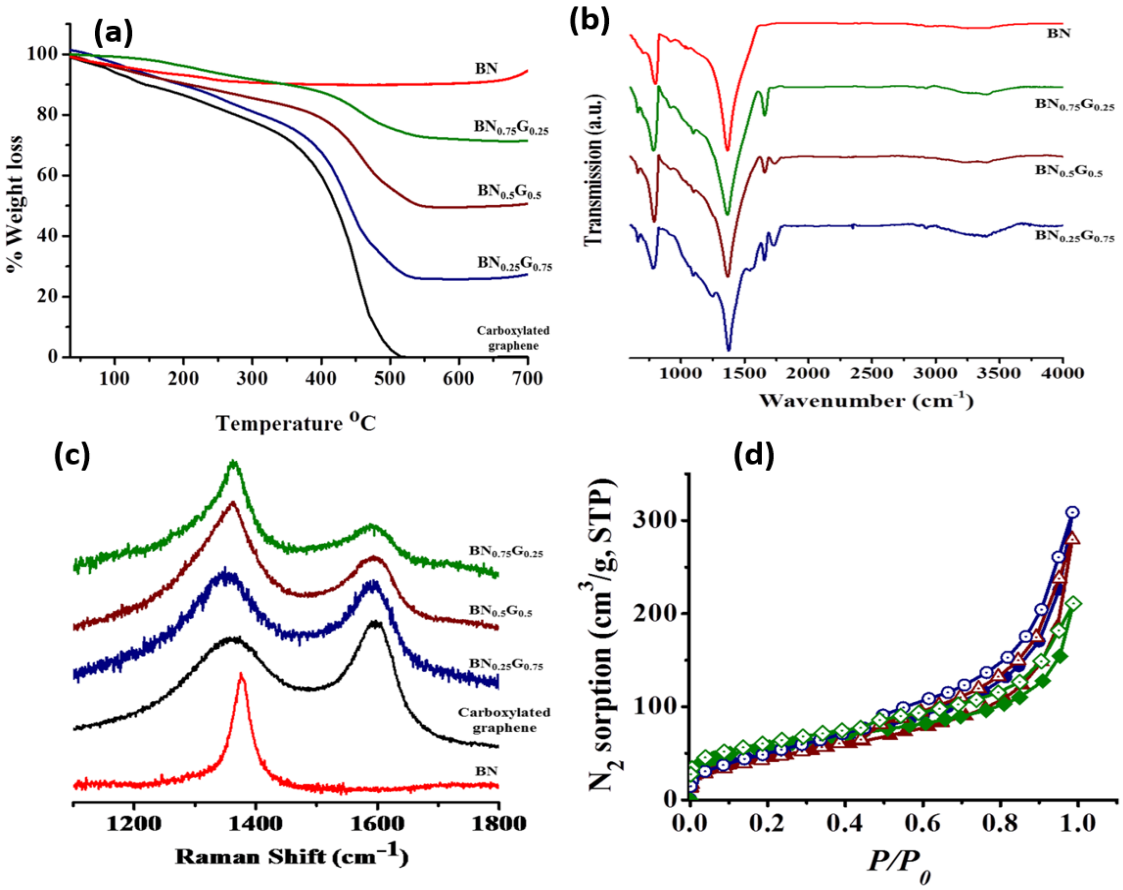

Figure 5. (a) Thermogravimetric analysis (b) Infra-red spectra (c) Raman spectra and (d) Nitrogen adsorption-desorption curves of carboxylated graphene (black), $BN_{0.25}G_{0.75}$ (blue), $BN_{0.5}G_{0.5}$ (wine), $BN_{0.75}G_{0.25}$ (olive) and BN (red) in oxygen atmosphere.

Thermogravimetric analysis was carried out in oxygen atmosphere to determine the compositions of the composites (Figure 5(a)). Few-layer BN has high thermal stability with no weight loss in the 500-700 °C range. The TGA profile of carboxylated graphene shows complete combustion in the 400-500 °C temperature range. The BN content in the composites can be determined from the residual weight in this temperature range. The residual weight for $BN_{0.25}G_{0.75}$, $BN_{0.5}G_{0.5}$, and $BN_{0.75}G_{0.25}$ are 24, 49.5, and 72% respectively which match with the stated compositions. The infrared spectrum of few-layer BN shows two strong and broad bands at 800 and 1367 cm^{-1} corresponding to the out-of-plane B–N–B bending mode (A_{2u}) and the in-plane B–N transverse optical mode (E_{1u}) respectively (Figure 5(b)). IR spectra of $BN_{1-x}G_x$ composites have bands at 1653 and

1724 cm^{-1} due to the amide bond between graphene and BN nanosheets and remaining carboxylate group on the graphene basal plane. As the amount of BN in the composites increases the relative intensity of the 1653 cm^{-1} amide band increases, $BN_{0.75}G_{0.25}$ showing an almost negligible intensity of the 1724 cm^{-1} band. The weak band around 1250 cm^{-1} of the composites is associated with the oxygen functional groups on graphene and disappears on heating at 300 °C. The Raman spectrum of few-layer BN has a relatively narrow (~35 cm^{-1}) band at 1375 cm^{-1} corresponding to the E_{2g} mode of BN (Figure 5(c)). Carboxylated graphene shows the characteristic D and G bands at 1359 and 1593 cm^{-1} with line widths of 165 and 75 cm^{-1} respectively. Raman spectra of composites have features of both BN as well as graphene. As the BN content increases in the $BN_{1-x}G_x$ composites, the spectrum shows dominating BN feature and decrease in G-band intensity. Surface area and porosity of the $BN_{1-x}G_x$ composites were obtained by N_2 sorption at 77 K (Figure 5(d)). The Brunauer-Emmet-Teller (BET) surface areas of $BN_{0.25}G_{0.75}$, $BN_{0.5}G_{0.5}$ and $BN_{0.75}G_{0.25}$ are 183, 171 and 197 m^2/g respectively. The sorption profiles show type H4 hysteresis loop associated with narrow slit-like pores, with type-I isotherm character in the low pressure region indicative of microporosity according to IUPAC classification. Slit-like micropores are created due to cross-linking and stacking of BN and graphene sheets. Carboxylated graphene has a BET surface area of 38 m^2/g with type-IV mesoporous sorption profile due to agglomeration of graphene sheets. Few–layer BN has type-II microporous sorption profile with BET surface area of 452 m^2/g.

Electrical resistivity data of the $BN_{1-x}G_x$ composites are shown in Figure 6. The $BN_{1-x}G_x$ composites show typical semiconducting behaviour with the resistance decreasing on increasing the temperature. The resistivity of the composites is least in the case of $BN_{0.25}G_{0.75}$ and increases on increasing the BN content. This is expected since BN is a known large band gap insulator. This interesting variable resistivity suggests the possible use of different $BN_{1-x}G_x$ composites for various applications. The resistivity of $BN_{0.5}G_{0.5}$ decreases significantly on annealing at 300 °C (see inset of Figure 6) due to the loss of the amide linkers. Presence of a slit-like microporous network in the $BN_{1-x}G_x$ composites prompted us to investigate the performance of $BN_{1-x}G_x$ as supercapacitor electrode materials.

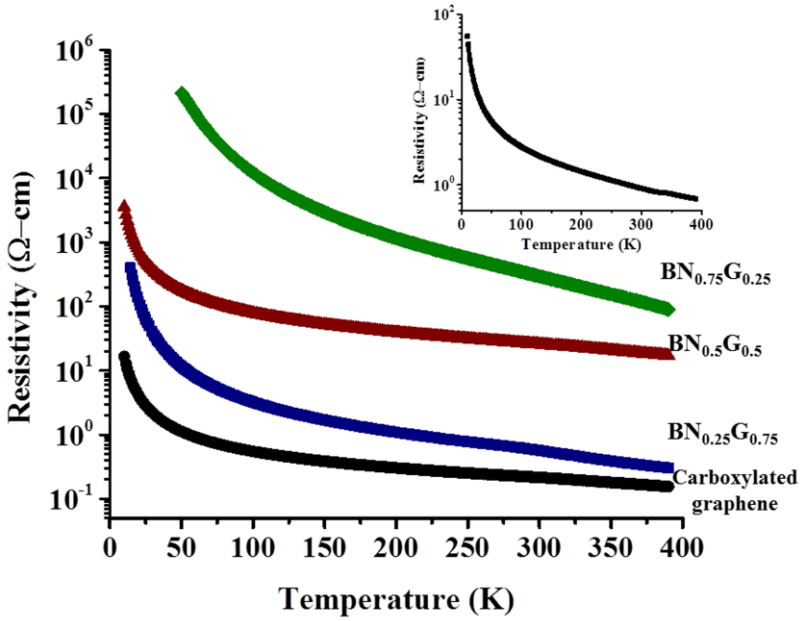

Figure 6. Temperature dependence of resistivity in $BN_{1-x}G_x$ composites with varying BN content measured using four probe method. Carboxylated graphene (black circle), $BN_{0.25}G_{0.75}$ (blue square), $BN_{0.5}G_{0.5}$ (wine triangle) and $BN_{0.75}G_{0.25}$ (olive diamond). **(Inset)** Temperature dependent resistivity of $BN_{0.5}G_{0.5}$ on annealing at 300 °C in nitrogen atmosphere.

Electrochemical performance: Electrochemical performance of the $BN_{1-x}G_x$ composites was investigated by means of cyclic voltammetry (CV), galvanostatic charge-discharge curves and electrochemical impedance spectroscopy (EIS) in 2 M H_2SO_4 electrolyte. Cyclic voltammograms of carboxylated graphene, $BN_{0.25}G_{0.75}$, $BN_{0.5}G_{0.5}$ and $BN_{0.75}G_{0.25}$ are measured at different scan rates (2–100 mV/s) at a voltage window of -0.2-0.6 V. The CV curves measured at 40 mV/s are shown in Figure 7(a). The CV curves show a rectangular feature even at higher scan rates which indicates that these materials are good charge storage supercapacitor electrodes. We have found a maximum capacitance of 217 F/g at a scan rate of 2 mV/s in the case of $BN_{0.25}G_{0.75}$. The specific capacitance values of carboxylated graphene, $BN_{0.5}G_{0.5}$ and $BN_{0.75}G_{0.25}$ are 89, 180, 92 F/g respectively at 2 mV/s. The galvanostatic charge-discharge curves of the BNG samples were measured in a voltage window of -0.2-0.6 V at a different current densities. Figure 7(b) shows the charge-discharge curves of carboxylated graphene and $BN_{1-x}G_x$ composites measured at 1 A/g. The discharge time of $BN_{0.25}G_{0.75}$ was longer when compared to carboxylated graphene and other two composites. The charge-discharge curves looks symmetric for the $BN_{1-x}G_x$ composites resembling those of ideal capacitors. The specific capacitance

values decreases with increase in the current density as shown in Figure 7(c). The specific capacitance of carboxylated graphene, $BN_{0.25}G_{0.75}$, $BN_{0.5}G_{0.5}$ and $BN_{0.75}G_{0.25}$ are 87, 238, 204 and 116 F/g respectively at 0.3 A/g. The increase in specific capacitance of $BN_{1-x}G_x$ with respect to carboxylated graphene is attributed to enhancement in the surface area along with slit-like microporous channels created in the composite due to covalent cross-linking. We have studied the cycling stability for $BN_{0.25}G_{0.75}$ by charge-discharge experiment between -0.2 and 0.6 V at a current density of 1 A g^{-1} for 1000 cycles. $BN_{0.25}G_{0.75}$ showed a loss of only ~ 2 % from the initial specific capacitance with excellent stability and capacitance retention (Figure 7(d)). BN has exceptionally high chemical and thermal stability, its presence in the conductive graphene matrix provides synergistic interactions with high electrochemical stability.

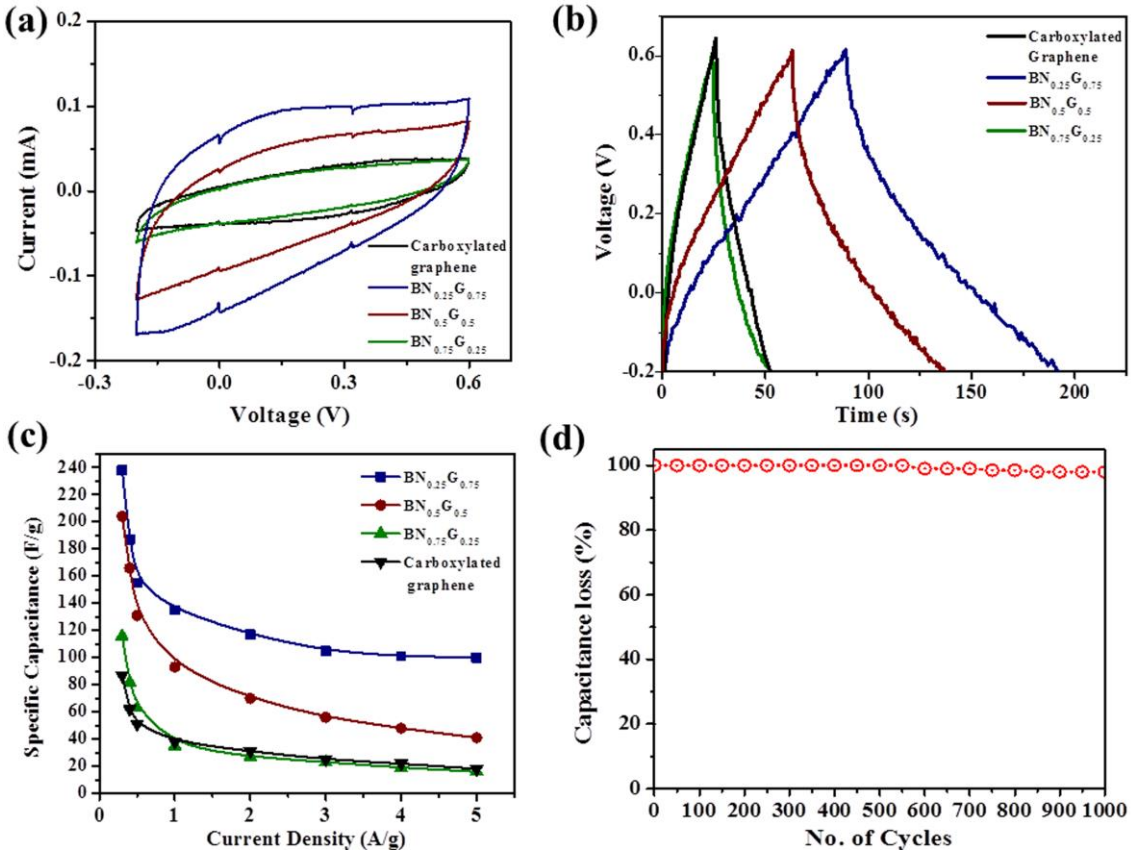

Figure 7. (a) Cyclic voltammograms of carboxylated graphene and $BN_{1-x}G_x$ electrodes at a scan rate of 40 mV/s; (b) galvanostatic charge-discharge curves for carboxylated graphene and $BN_{1-x}G_x$ electrodes (at 1 A/g) and (c) specific capacitance as a function of discharge current. (d) % capacitance loss *versus* the cycle number of $BN_{0.25}G_{0.75}$ measured at a current density of 1 A/g within an operational window of -0.2-0.6 V.

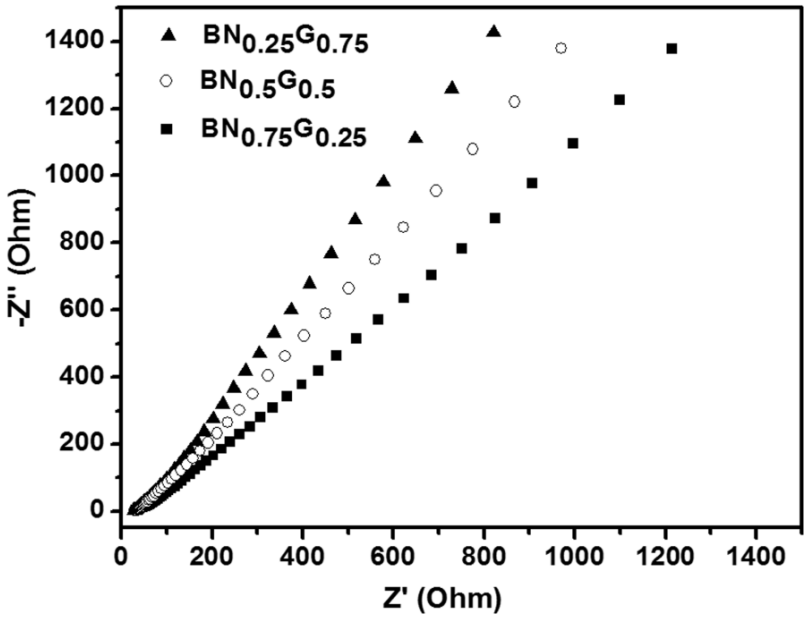

Figure 8. Nyquist curves for $BN_{1-x}G_x$ electrodes.

We show the Nyquist plots in the frequency range 100 kHz–0.01 Hz in Figure 8. These plots show excellent capacitive behavior of $BN_{1-x}G_x$ composites which is indicated by the near vertical line over the lower frequency range. The charge transfer resistance (C_t) in $BN_{0.25}G_{0.75}$, $BN_{0.5}G_{0.5}$ and $BN_{0.75}G_{0.25}$ is small and the equivalent series resistances (ESRs) are 26.75, 29.09 and 45.33 Ω respectively. It is interesting that the specific capacitance increases with increasing graphene content going up to ~ 200 F/g for $BN_{0.25}G_{0.75}$ and $BN_{0.5}G_{0.5}$. It is noteworthy that the resistivity decreases in the same order although the surface area remains nearly constant.

1.6.5 Conclusions

In conclusion, we have successfully prepared composites of BN and graphene with different compositions by covalent cross–linking with amide bonds by using EDC coupling. The composites exhibit tunable resistivity depending on the composition. The composites, especially $BN_{0.25}G_{0.75}$, show microporosity and satisfactory performance with high stability as supercapacitor electrode material.The results in this study demonstrate that covalent cross-linking can be used as a strategy to generate novel composites with useful properties.

References

[1] Xu B, Lu YH, Feng YP, Lin JY. Density functional theory study of BN-doped graphene superlattice: Role of geometrical shape and size. Journal of Applied Physics. 2010;108:073711.

[2] Nag A, Raidongia K, Hembram KPSS, Datta R, Waghmare UV, Rao CNR. Graphene Analogues of BN: Novel Synthesis and Properties. ACS Nano. 2010;4:1539-44.

[3] Pakdel A, Bando Y, Golberg D. Nano boron nitride flatland. Chem Soc Rev. 2014;43:934-59.

[4] Song L, Liu Z, Reddy ALM, Narayanan NT, Taha-Tijerina J, Peng J, et al. Binary and Ternary Atomic Layers Built from Carbon, Boron, and Nitrogen. Advan Mater. 2012;24:4878-95.

[5] Kumar N, Moses K, Pramoda K, Shirodkar SN, Mishra AK, Waghmare UV, et al. Borocarbonitrides, BxCyNz. J Mater Chem A. 2013;1:5806-21.

[6] Ci L, Song L, Jin C, Jariwala D, Wu D, Li Y, et al. Atomic layers of hybridized boron nitride and graphene domains. Nat Mater. 2010;9:430-5.

[7] Banerjee S, Pati SK. Criticality of surface topology for charge-carrier transport characteristics in two-dimensional borocarbonitrides: design principles for an efficient electronic material. Nanoscale. 2014;6:13430-4.

[8] Nascimento R, Martins JdR, Batista RJC, Chacham H. Band Gaps of BN-Doped Graphene: Fluctuations, Trends, and Bounds. The Journal of Physical Chemistry C. 2015;119:5055-61.

[9] Kaloni TP, Joshi RP, Adhikari NP, Schwingenschlögl U. Band gap tunning in BN-doped graphene systems with high carrier mobility. App Phys Lett. 2014;104:073116.

[10] Rani P, Jindal VK. Stability and electronic properties of isomers of B/N co-doped graphene. Applied Nanoscience. 2013;4:989-96.

[11] Fan X, Shen Z, Liu AQ, Kuo J-L. Band gap opening of graphene by doping small boron nitride domains. Nanoscale. 2012;4:2157-65.

[12] Loh GC, Pandey R. A graphene-boron nitride lateral heterostructure - a first-principles study of its growth, electronic properties, and chemical topology. J Mater Chem C. 2015;3:5918-32.

[13] Levendorf MP, Kim C-J, Brown L, Huang PY, Havener RW, Muller DA, et al. Graphene and boron nitride lateral heterostructures for atomically thin circuitry. Nature. 2012;488:627-32.

[14] Shiue R-J, Gao Y, Wang Y, Peng C, Robertson AD, Efetov DK, et al. High-Responsivity Graphene–Boron Nitride Photodetector and Autocorrelator in a Silicon Photonic Integrated Circuit. Nano Lett. 2015;15:7288-93.

[15] Wu Z-S, Winter A, Chen L, Sun Y, Turchanin A, Feng X, et al. Three-Dimensional Nitrogen and Boron Co-doped Graphene for High-Performance All-Solid-State Supercapacitors. Advanced Materials. 2012;24:5130-5.

[16] Saha S, Jana M, Khanra P, Samanta P, Koo H, Murmu NC, et al. Band Gap Engineering of Boron Nitride by Graphene and Its Application as Positive Electrode Material in Asymmetric Supercapacitor Device. ACS Applied Materials & Interfaces. 2015;7:14211-22.

[17] Gao T, Gong L-j, Wang Z, Yang Z-k, Pan W, He L, et al. Boron nitride/reduced graphene oxide nanocomposites as supercapacitors electrodes. Materials Letters. 2015;159:54-7.

[18] Shi G, Hanlumyuang Y, Liu Z, Gong Y, Gao W, Li B, et al. Boron Nitride–Graphene Nanocapacitor and the Origins of Anomalous Size-Dependent Increase of Capacitance. Nano Lett. 2014;14:1739-44.

[19] Xue Y, Yu D, Dai L, Wang R, Li D, Roy A, et al. Three-dimensional B,N-doped graphene foam as a metal-free catalyst for oxygen reduction reaction. Physical Chemistry Chemical Physics. 2013;15:12220-6.

[20] Liu Z, Song L, Zhao S, Huang J, Ma L, Zhang J, et al. Direct Growth of Graphene/Hexagonal Boron Nitride Stacked Layers. Nano Letters. 2011;11:2032-7.

[21] Chang C-K, Kataria S, Kuo C-C, Ganguly A, Wang B-Y, Hwang J-Y, et al. Band Gap Engineering of Chemical Vapor Deposited Graphene by in Situ BN Doping. ACS Nano. 2013;7:1333-41.

[22] Han GH, Rodríguez-Manzo JA, Lee C-W, Kybert NJ, Lerner MB, Qi ZJ, et al. Continuous Growth of Hexagonal Graphene and Boron Nitride In-Plane Heterostructures by Atmospheric Pressure Chemical Vapor Deposition. ACS Nano. 2013;7:10129-38.

[23] Gong Y, Shi G, Zhang Z, Zhou W, Jung J, Gao W, et al. Direct chemical conversion of graphene to boron- and nitrogen- and carbon-containing atomic layers. Nat Commun. 2014;5:3193.

[24] Zhang C, Zhao S, Jin C, Koh AL, Zhou Y, Xu W, et al. Direct growth of large-area graphene and boron nitride heterostructures by a co-segregation method. Nat Commun. 2015;6:6519.

[25] Chaturbedy P, Matte HSSR, Voggu R, Govindaraj A, Rao CNR. Self-assembly of C60, SWNTs and few-layer graphene and their binary composites at the organic–aqueous interface. Journal of Colloid and Interface Science. 2011;360:249-55.

[26] Gao G, Gao W, Cannuccia E, Taha-Tijerina J, Balicas L, Mathkar A, et al. Artificially Stacked Atomic Layers: Toward New van der Waals Solids. Nano Letters. 2012;12:3518-25.

[27] Kumar R, Rao CNR. Assemblies of single-walled carbon nanotubes generated by covalent cross-linking with organic linkers. J Mater Chem A. 2015;3:6747-50.

PART 2

OXYGEN REDUCTION REACTION CATALYSTS BASED ON GRAPHENE, BOROCARBONITRIDES AND OTHER 2D MATERIALS

"In this part we examine the use of graphene, borocarbonitrides and other 2D materials for the oxygen reduction reaction in fuel cells. The results are quite encouraging."

PART 2

OXYGEN REDUCTION REACTION CATALYSTS BASED ON GRAPHENE, BOROCARBONITRIDES AND OTHER 2D MATERIALS

2.1 Brief overview

2.1.1 Introduction

The rising global energy crisis and the environmental impact of traditional energy resources impose serious challenges to humans and the environment [1]. According to recent studies, the world primary energy consumption is expected to grow by more than 30% from 2013 to 2030 and have indicated that the reserve for the natural fuel resources will near an end within the next 50 years [2]. One of the promising renewable energy technology to replace the fossil fuels and to resolve the rising demand is the fuel cell technology, especially polymer electrolyte membrane fuel cell (PEMFC), which provides clean and sustainable power [3]. Fuel cells are popular because of their high energy conversion efficiency, high power density, and environmental friendly [4]. Fuel cells are electrochemical devices which generate electricity by reducing oxygen electrochemically and oxidizing the fuel into water as the only by-product [5]. Despite the advantages, making PEM fuel cells are still costly and a majority of the cost comes from the use of platinum as the catalyst in the electrodes. Platinum (Pt) has been regarded as the best oxygen reduction reaction (ORR) catalyst but limited availability and the high cost has made barrier for the commercialization [6]. In addition to the cost, Pt-based electrodes also suffer from stability and CO poisoning issues. To overcome this limitation, low-cost catalysts with higher activity and durability for ORR should be developed.

2.1.2 Polymer electrolyte membrane fuel cell

Polymer electrolyte membrane **f**uel cells are electrochemical devices that produce electrical energy from the chemical energy of a fuel and oxygen [5]. Where, most common fuel used is hydrogen or methanol. The process is an electrochemical reaction similar to

a battery, but unlike batteries, fuel cells do not store the energy within the chemicals internally [7]. Instead, fuel cells use a continuous supply of fuel from an external storage tank. The basic principle of hydrogen fuel cell is illustrated in Figure 1. The core of fuel cell consists of an electrolyte and two electrodes [8]. At the anode, a fuel such as hydrogen is being oxidized while at the cathode, oxygen is reduced. The produced protons pass through a proton-conducting electrolyte whereas the electrons are directed through an external circuit powering an attached device and leading to the cathode to reduce oxygen. At the cathode, the protons are combined with oxygen to produce water. The type of electrolyte used determines the operating temperature and in turn operating temperature determines the catalyst. At the open circuit, the voltage of a hydrogen-oxygen fuel cell is 1.23 V at 298 K but under load conditions, the cell voltage is between 0.5 and 1 V.

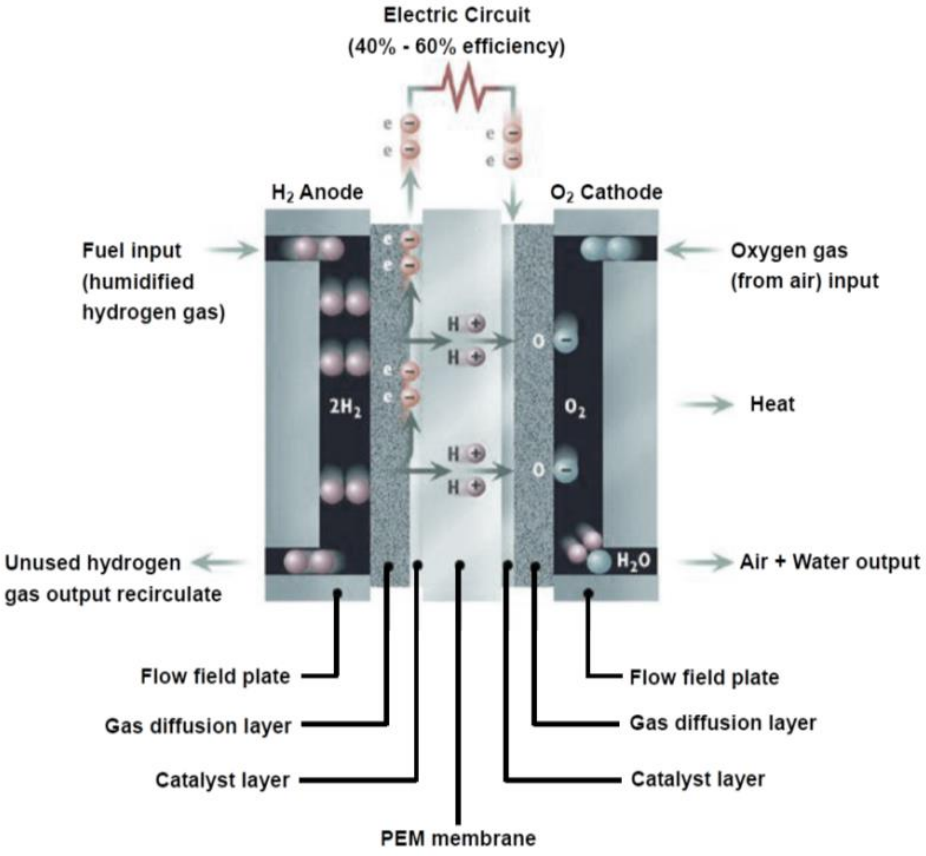

Figure 1. Schematic of the operating principle of a hydrogen-based PEMFC [9].

Fuel cell operation depends not only on hydrogen oxidation at the anode but also on oxygen reduction at the cathode. This reaction is a kinetically slow process, which dominates the overall performance of a fuel cell [10]. The ORR can proceed through two ways. One is a direct four-electron pathway, in which O_2 is reduced directly to water without involvement of hydrogen peroxide, $O_2 + 4H^+ + 4e^- \rightarrow 2H_2O$. The other is a less efficient two-step two-electron pathway in which hydrogen peroxide is formed as an intermediate, $O_2 + 2H^+ + 2e^- \rightarrow H_2O_2$. To achieve a high efficiency fuel cell, the four-electron pathway is expected to occur. Because the ORR process is very slow in nature, catalysts must be used to facilitate the four-electron pathway to boost the efficiency of fuel cells. Thus, oxygen reduction reaction plays a very significant role in limiting the operating efficiency of the fuel cell and is also very dependent on high precious metal (e.g. Pt, Pt-Pd, and Pt-Ru) loading in the catalyst layer [11]. Improving the efficiency of the oxygen reduction reaction while lowering the precious metal loading is critical to commercialization of fuel cell technology for transportation applications. Thus, there are reports on metal-free carbon based ORR catalysts, which have shown excellent catalytic activity, stability and moreover it is cost-effective [12]. Recently, it has been demonstrated that vertically aligned nitrogen-containing carbon nanotubes (N-CNTs) and nitrogen-doped graphene sheets (N-graphene), reduced graphene oxide/platinum supported electrocatalysts (Pt/RGO), borocarbonitrides and transition metal chalcogenides show a much better electrocatalytic activity with long-term operation stability and CO poisoning than platinum electrodes [12].

2.1.3 Carbon based ORR catalysts

2.1.3.1 Carbon nanotubes

Since the discovery of carbon nanotubes (CNTs), it have shown excellent applications in nanoelectronics and in energy devices due to its high electrical conductivity and good surface area [13, 14]. Thus, carbon nanotubes have been used as a support in heterogeneous catalysis especially in liquid-phase reactions [15]. In addition, carbon nanotubes have been utilized as catalyst supports to reduce Pt loading and improve long-term stability in fuel cell applications [16]. Doping CNTs with nitrogen greatly improves the ORR activity compared to that of pristine CNT but activity is poor compared to

platinum-based materials [17]. Gong et al. [18] have synthesized vertically aligned nitrogen-doped carbon nanotube arrays with better electrocatalytic activity and long-term stability compared to Pt/C in alkaline conditions. It has been demonstrated that nitrogen in the carbon lattice is essential to obtain non-noble metallic-based catalytic sites. Aligned nitrogen-doped carbon nanotubes with bamboo-like structure synthesized via thermal chemical vapour deposition using melamine and urea have shown superior ORR performance in terms of limiting current density and number of electrons transferred [19]. Nagaiah et al [20] have synthesized NCNTs by treating oxidized CNTs with ammonia. NCNTs treated at 800 °C have shown improved activity for oxygen reduction as compared with commercially available Pt/C catalysts. The improved catalytic activity of NCNT is be attributed to two different active sites in the form of pyridinic and pyrrolic nitrogen.

2.1.3.2 Graphene

2.1.3.2.1 Doped graphene

Unlike carbon nanotube, graphene is an atom-thick planar sheet of sp^2-bonded carbon atoms in a honeycomb crystal lattice [21, 22]. Graphene is known for its exceptional properties including high current density, ballistic transport, chemical inertness, high thermal conductivity and optical transmittance [23, 24]. Electrical characterization has shown a remarkably high electron mobility at room temperature with reported values up to 15000 $cm^2/V.s$ [23]. This exceptional electrical property of graphene have attracted applications in nanoelectronics, sensors and energy devices [25]. Graphene has a high surface area and for the same reason it has shown excellent supercapacitor properties [26, 27]. In addition, graphene have shown enhanced catalytic activity in ORR equal to that of platinum with low fuel crossover, low cost and good durability [28]. Introduction of nitrogen in the graphene network enhances the ORR activity due to increase in the electron density of states near the Fermi level like in carbon nanotubes [29, 30]. Since the nitrogen in N-doped graphene is an n-type dopant it can donate electrons to the neighbouring π-orbital of conjugated carbon which in turn provide an electron to the π*-orbital in the oxygen molecule and thus facilitating the splitting [31].

Dai and co-workers [32] propose a 4-electron pathway in alkaline solutions for nitrogen doped graphene, which shows a higher current density and good amperometric response for ORR compared to the commercial platinum-carbon catalyst. It also showed good tolerance against carbon monoxide with an operation stability of more than 200,000 cycles. Nitrogen plasma treated graphene exhibits much higher electrocatalytic activity toward oxygen reduction than graphene under alkaline conditions [33]. The ORR overpotential is significantly decreased in N-graphene thereby increasing its electrocatalytic activity of graphene towards ORR with a lower initial electrocatalytic activity than Pt/C, but much higher durability than Pt/C. In addition to the ORR ability, nitrogen doped graphene also used as carbon support for platinum [34]. The N-doped graphene with superior electron mobility than undoped graphene acts as a good support for Pt and improves the ORR ability [35]. The defects and the edges produced due to nitrogen doping can act as good anchoring sites for the platinum nanoparticles. The enhancement in the ORR activity is attributed to the pyridinic and pyrrolic nitrogens which increase the reactivity of the neighbouring carbon atoms. The Pt-Au/N-graphene nanocomposites exhibit good electrocatalytic activity and stability towards the methanol oxidation reaction [36]. These electrochemical characteristics are unique from those of graphene nanocomposites and commercially available Pt/C catalysts, indicating that the alloying effect of Pt-Au and its synergistic interaction with the N-graphene sheet to give raise to the enhanced activity [102]. Selectively synthesized pyridinic- and pyrrolic-nitrogen-doped graphene show excellent oxygen reduction reactivity [37]. Although platinum based electrocatalyst showed enhanced ORR activity, the unaffordable cost hinders the usage of Pt in fuel cells. There are a few reports based on non-precious transition metals (iron, cobalt etc.,) used as cathode catalyst in fuel cells [38, 39]. Composites of N-doped graphene with transition metal oxides shows significant enhancement in the electrocatalytic activity. Dai et al. [40] report cobalt oxide-nitrogen doped graphene oxide (Co_3O_4/N-RGO) based bi-functional catalysts for the ORR and oxygen evolution reaction (OER). These catalysts showed positive onset potential and higher cathodic currents when compared to cobalt oxide (Co_3O_4) and nitrogen-doped reduced graphene (N-RGO). The electron transfer was ~3.9 for Co3O4/RGO and ~4 for Co3O4/N-RGO in alkaline solutions. It's noteworthy that, the composites of the spinel

manganese cobalt oxide ($MnCo_2O_4$) with N-RGO showed improved catalytic activity than Co_3O_4/N-RGO composites [41]. The average electron transfer was ~3.9 for the $MnCo_2O_4$/N-RGO hybrid.

Boron-doped graphene (BG) shows good electrocatalytic activity towards oxygen reduction reaction in alkaline conditions similar to the performance of Pt catalysts. In addition, the non-metallic BG catalyst shows long-term stability and good CO tolerance superior to that of Pt-based catalysts [42]. Edge-sulfurized graphene nanoplatelets (4.94 at. % S) can be prepared by ball-milling graphite in the presence of sulfur (S_8). It shows excellent electrocatalytic activity for ORR in alkaline medium [43]. It also shows better tolerance to methanol crossover/CO poisoning effects compared to pristine graphite or commercial Pt/C electrocatalysts.

2.1.4 Borocarbonitrides

Borocarbonitrides, $B_xC_yN_z$, constitute a new family of layered two-dimensional materials containing graphene and BN domains or more complex materials possessing B–C and C–N bonds besides B–N and C–C bonds [44]. Properties of these materials depend on the composition, and the method of synthesis, wherein one can traverse from the insulating end (BN) to the conducting end (graphene). The borocarbonitrides exhibit some interesting electronic [45] and gas adsorption properties [46]. They also exhibit excellent characteristics for supercapacitor applications [44]. Borocarbonitrides of tunable B/N co-doping levels performed as efficient ORR electrocatalysts simply by thermal annealing GO in the presence of boric acid and ammonia [47]. The stoichiometries being of $B_{38}C_{28}N_{34}$, $B_7C_{87}N_6$ and $B_{12}C_{77}N_{11}$ out of which $B_{12}C_{77}N_{11}$ showed superior catalytic activity than other two materials. The ORR activity is very low for $B_{38}C_{28}N_{34}$ which is probably due to its low conductivity associated with the low carbon content. In contrast, $B_{12}C_{77}N_{11}$ shows an onset potential close to that of the commercial Pt/C catalyst, indicating an excellent ORR catalytic activity induced by the synergetic effect through co-doping with N and B. In addition, it showed higher selectivity toward ORR and better methanol tolerance than the commercial Pt/C electrocatalyst. The electron transfer number n of ORR on this BCN graphene electrocatalyst is close to 4, as determined by the rotating ring disk electrode. Composition dependent ORR activity has been studied in

few-layer borocarbonitrides [48]. The study shows a 4e- process with the onset of potential and half-wave potentials close to those found with a commercial Pt/C catalyst. Three-dimensional B,N-doped graphene foam (BN-GF) performed as excellent metal free catalyst for ORR [49]. Compared to un-doped GF and B-GF or N-GF electrodes, the BN-GF electrode showed significantly improved electrocatalytic activity towards ORR in terms of both the onset/peak potentials and the peak current. The synergetic effect associated with the B- and N-co-doping makes the 3D BN-GF electrode to be most active among all of the electrodes and even slightly better than the Pt/C electrode in terms of the reduction in peak current. This is because both N and B atoms can act as active sites for ORR through charge transfer with neighbouring C atoms but also interaction between adjacent N and B atoms could reduce the bandgap energy to further facilitate the ORR performance of the BN-GF electrode.

2.1.5 MoS_2

Molybdenum disulfide (MoS_2) has been receiving much research attention due to its novel functionalities and its suitability for a wide range of electronic and optoelectronic applications [50]. MoS_2, has been reported to show catalytic activity towards the electrochemical and photochemical hydrogen-evolution reaction [51, 52]. MoS_2 nanoparticles supported on gold nanoparticle films follow a four-electron pathway for the oxygen reduction reaction in alkaline media with an onset potential of −0.10 V against the saturated calomel electrode [53]. These films exhibit superior stability and better electrocatalytic performance than commercial Pt/C. MoS_2 particles with different size distributions prepared by simple ultrasonication of bulk MoS_2 showed significantly improved catalytic activity toward the ORR. It is found that a decrease in particle size increases the catalytic activity [54].Composites of MoS_2 with nitrogen doped graphene show good ORR activity [55]. MoS_2/nitrogen doped graphene (NG) hybrid composites obtained through loading MoS_2 sheets onto NG through ultrasonication, exhibit improved electrocatalytic activity for ORR with dominant 4 electron pathway in alkaline solutions. The synergistic effects along with exposed edges and increase conductivity make the MoS_2/NG composites highly competitive ORR catalysts. Phosphorus doped-ultrathin MoS_2 nanosheets synthesized via thermolytical process enhanced the ORR

activity with four-electron selectivity and also seven-fold current increase in both onset and half-wave potentials than that of un-doped MoS_2 [56]. The reason for this is that the less electronegative of phosphorus atoms in the plane of MoS_2 nanosheets are polarized by the surrounding sulfur atoms with larger electronegativity, endowing the phosphorus atoms with more positive charge than the sulfur. MoS_2 nanodots embedded 3-D porous frameworks of N-doped graphene show good activity towards oxygen reduction reaction in basic media [57]. This is because the MoS_2 nanodots have an abundance of exposed edge sites with good accessibility to oxygen molecules and also nitrogen-doped graphene played an important role in providing good conductivity, a large surface area and porous structure, which facilitated the electron and mass transfer.

2.1.6 Characterization techniques

Electrochemical measurements are performed in an O_2-saturated aqueou 0.1 M potassium hydroxide (KOH) solution (Ag/AgCl reference electrode). Rotating disc electrode (RDE) measurements were carried out with a system from Beckman Instruments by coupling with a galvanostat/potentiostat. The number of electrons transferred per oxygen molecule from the electrodes can be calculated by using the Koutechy-Levich (K-L) equation:

$$1/I = 1/i_k + 1/i_d$$

$$1/i = -1/(nFkC_o) - 1/(0.62\, nFD_o^{2/3}\gamma^{-1/6}C_o\omega^{1/2})$$

Here, I denotes the measured current densities at the respective potentials, while i_k and i_d represent kinetic and diffusion current densities respectively and n gives the overall number of electrons transferred per O_2 molecule. F is the Faraday constant (96485 C mol^{-1}), C_o the bulk concentration of O_2 (1.2×10^{-6} mol mL^{-1}), k the electron transfer rate constant, D_o the O_2 diffusion coefficient (1.73×10^{-5} cm^2 s^{-1}) in 0.1 M KOH, γ kinematic viscosity (0.0109 cm^2 s^{-1}) and ω the rotation speed of the electrode. The number of electrons transferred, n, is obtained by calculating the slope of i^{-1} *vs* ω^{-1} plot.

The *ik* values can be calculated by the following equation.

$$i_k=(i \times i_d)/(i_d - i)$$

where i_k is the kinetic current density, i_d is the measured diffusion limited current density, and i is the measured current density

References

[1] The Ethics of Global Climate Change. Cambridge: Cambridge University Press; 2011.

[2] World energy demand and economic outlook. International Energy Outlook 2016 Report Number: DOE/EIA-0484(2016).

[3] Dresselhaus MS, Thomas IL. Alternative energy technologies. Nature. 2001;414:332-7.

[4] Steele BCH. Materials for electrochemical energy conversion and storage systems. Ceramics International. 1993;19:269-77.

[5] Srinivasan S, Krishnan L, Marozzi C. FUEL CELL PRINCIPLES. Fuel Cells: From Fundamentals to Applications. Boston, MA: Springer US; 2006. p. 189-233.

[6] Abbas MA, Bang JH. Rising Again: Opportunities and Challenges for Platinum-Free Electrocatalysts. Chem Mater. 2015;27:7218-35.

[7] Scott K, Shukla AK. Polymer electrolyte membrane fuel cells: Principles and advances. Rev Environ Sci Biotechnol. 2004;3:273-80.

[8] Kraytsberg A, Ein-Eli Y. Review of Advanced Materials for Proton Exchange Membrane Fuel Cells. Energy & Fuels. 2014;28:7303-30.

[9] Pinterest. https://in.pinterest.com/pin/480337116478162386/.

[10] Zhang L, Xia Z. Mechanisms of Oxygen Reduction Reaction on Nitrogen-Doped Graphene for Fuel Cells. J Phys Chem C. 2011;115:11170-6.

[11] Lee Y-W, Cha S, Park K-W, Sohn JI, Kim JM. High Performance Electrocatalysts Based on Pt Nanoarchitecture for Fuel Cell Applications. J Nanomater. 2015;2015:20.

[12] Dai L, Xue Y, Qu L, Choi H-J, Baek J-B. Metal-Free Catalysts for Oxygen Reduction Reaction. Chem Rev. 2015;115:4823-92.

[13] Iijima S. Helical microtubules of graphitic carbon. Nature. 1991;354:56-8.

[14] Yuchi C, Haitian C, Hui G, Jia L, Bilu L, Chongwu Z. Review of carbon nanotube nanoelectronics and macroelectronics. Semicond Sci Tech. 2014;29:073001.

[15] Oosthuizen RS, Nyamori VO. Carbon Nanotubes as Supports for Palladium and Bimetallic Catalysts for Use in Hydrogenation Reactions. Platinum Metals Rev. 2011;55:154-69.

[16] Niu JJ, Wang JN. Activated carbon nanotubes-supported catalyst in fuel cells. Electrochimica Acta. 2008;53:8058-63.

[17] Chen Z, Higgins D, Tao H, Hsu RS, Chen Z. Highly Active Nitrogen-Doped Carbon Nanotubes for Oxygen Reduction Reaction in Fuel Cell Applications. J Phys Chem C. 2009;113:21008-13.
[18] Gong K, Du F, Xia Z, Durstock M, Dai L. Nitrogen-Doped Carbon Nanotube Arrays with High Electrocatalytic Activity for Oxygen Reduction. Science. 2009;323:760-4.
[19] Xiong C, Wei Z, Hu B, Chen S, Li L, Guo L, et al. Nitrogen-doped carbon nanotubes as catalysts for oxygen reduction reaction. J Power Sources. 2012;215:216-20.
[20] Nagaiah TC, Kundu S, Bron M, Muhler M, Schuhmann W. Nitrogen-doped carbon nanotubes as a cathode catalyst for the oxygen reduction reaction in alkaline medium. Electrochem Commun. 2010;12:338-41.
[21] Rao CNR, Sood AK, Subrahmanyam KS, Govindaraj A. Graphene: The New Two-Dimensional Nanomaterial. Angewandte Chemie International Edition. 2009;48:7752-77.
[22] Geim AK, Novoselov KS. The rise of graphene. Nat Mater. 2007;6:183-91.
[23] Novoselov KS, Geim AK, Morozov SV, Jiang D, Zhang Y, Dubonos SV, et al. Electric Field Effect in Atomically Thin Carbon Films. Science. 2004;306:666-9.
[24] Choi W, Lahiri I, Seelaboyina R, Kang YS. Synthesis of Graphene and Its Applications: A Review. Critical Reviews in Solid State and Materials Sciences. 2010;35:52-71.
[25] Huang Y, Liang J, Chen Y. An Overview of the Applications of Graphene-Based Materials in Supercapacitors. Small. 2012;8:1805-34.
[26] Vivekchand SRC, Rout CS, Subrahmanyam KS, Govindaraj A, Rao CNR. Graphene-based electrochemical supercapacitors. Journal of Chemical Sciences. 2008;120:9-13.
[27] Stoller MD, Park S, Zhu Y, An J, Ruoff RS. Graphene-Based Ultracapacitors. Nano Lett. 2008;8:3498-502.
[28] Pumera M. Graphene-based nanomaterials and their electrochemistry. Chem Soc Rev. 2010;39:4146-57.
[29] Rao CNR, Gopalakrishnan K, Govindaraj A. Synthesis, properties and applications of graphene doped with boron, nitrogen and other elements. Nano Today. 2014;9:324-43.

[30] Wang H, Maiyalagan T, Wang X. Review on Recent Progress in Nitrogen-Doped Graphene: Synthesis, Characterization, and Its Potential Applications. ACS Catal. 2012;2:781-94.
[31] Wang X, Sun G, Routh P, Kim D-H, Huang W, Chen P. Heteroatom-doped graphene materials: syntheses, properties and applications. Chem Soc Rev. 2014;43:7067-98.
[32] Qu L, Liu Y, Baek J-B, Dai L. Nitrogen-Doped Graphene as Efficient Metal-Free Electrocatalyst for Oxygen Reduction in Fuel Cells. ACS Nano. 2010;4:1321-6.
[33] Shao Y, Zhang S, Engelhard MH, Li G, Shao G, Wang Y, et al. Nitrogen-doped graphene and its electrochemical applications. J Mater Chem. 2010;20:7491-6.
[34] Ma J, Habrioux A, Luo Y, Ramos-Sanchez G, Calvillo L, Granozzi G, et al. Electronic interaction between platinum nanoparticles and nitrogen-doped reduced graphene oxide: effect on the oxygen reduction reaction. J Mater Chem A. 2015;3:11891-904.
[35] Imran Jafri R, Rajalakshmi N, Ramaprabhu S. Nitrogen doped graphene nanoplatelets as catalyst support for oxygen reduction reaction in proton exchange membrane fuel cell. J Mater Chem. 2010;20:7114-7.
[36] Yang G, Li Y, Rana RK, Zhu J-J. Pt-Au/nitrogen-doped graphene nanocomposites for enhanced electrochemical activities. J Mater Chem A. 2013;1:1754-62.
[37] Ding W, Wei Z, Chen S, Qi X, Yang T, Hu J, et al. Space-Confinement-Induced Synthesis of Pyridinic- and Pyrrolic-Nitrogen-Doped Graphene for the Catalysis of Oxygen Reduction. Angew Chem Int Ed. 2013;52:11755-9.
[38] Wu G, More KL, Johnston CM, Zelenay P. High-Performance Electrocatalysts for Oxygen Reduction Derived from Polyaniline, Iron, and Cobalt. Science. 2011;332:443-7.
[39] Peng H, Mo Z, Liao S, Liang H, Yang L, Luo F, et al. High Performance Fe- and N-Doped Carbon Catalyst with Graphene Structure for Oxygen Reduction. Sci Reports. 2013;3:1765.
[40] Liang Y, Li Y, Wang H, Zhou J, Wang J, Regier T, et al. Co3O4 nanocrystals on graphene as a synergistic catalyst for oxygen reduction reaction. Nat Mater. 2011;10:780-6.
[41] Liang Y, Wang H, Zhou J, Li Y, Wang J, Regier T, et al. Covalent Hybrid of Spinel Manganese–Cobalt Oxide and Graphene as Advanced Oxygen Reduction Electrocatalysts. J Am Chem Soc. 2012;134:3517-23.

[42] Sheng Z-H, Gao H-L, Bao W-J, Wang F-B, Xia X-H. Synthesis of boron doped graphene for oxygen reduction reaction in fuel cells. Journal of Materials Chemistry. 2012;22:390-5.
[43] Jeon I-Y, Zhang S, Zhang L, Choi H-J, Seo J-M, Xia Z, et al. Edge-Selectively Sulfurized Graphene Nanoplatelets as Efficient Metal-Free Electrocatalysts for Oxygen Reduction Reaction: The Electron Spin Effect. Adv Mater. 2013;25:6138-45.
[44] Kumar N, Moses K, Pramoda K, Shirodkar SN, Mishra AK, Waghmare UV, et al. Borocarbonitrides, BxCyNz. J Mater Chem A. 2013;1:5806-21.
[45] Kota M, Sharmila NS, Waghmare UV, Rao CNR. Composition-dependent photoluminescence and electronic structure of 2-dimensional borocarbonitrides. Materials Research Express. 2014;1:025603.
[46] Kumar N, Subrahmanyam KS, Chaturbedy P, Raidongia K, Govindaraj A, Hembram KPSS, et al. Remarkable Uptake of CO2 and CH4 by Graphene-Like Borocarbonitrides, BxCyNz. ChemSusChem. 2011;4:1662-70.
[47] Wang S, Zhang L, Xia Z, Roy A, Chang DW, Baek J-B, et al. BCN Graphene as Efficient Metal-Free Electrocatalyst for the Oxygen Reduction Reaction. Angewandte Chemie International Edition. 2012;51:4209-12.
[48] Moses K, Kiran V, Sampath S, Rao CNR. Few-Layer Borocarbonitride Nanosheets: Platinum-Free Catalyst for the Oxygen Reduction Reaction. Chemistry – An Asian Journal. 2014;9:838-43.
[49] Xue Y, Yu D, Dai L, Wang R, Li D, Roy A, et al. Three-dimensional B,N-doped graphene foam as a metal-free catalyst for oxygen reduction reaction. Physical Chemistry Chemical Physics. 2013;15:12220-6.
[50] Rao CNR, Ramakrishna Matte HSS, Maitra U. Graphene Analogues of Inorganic Layered Materials. Angew Chem Int Ed. 2013;52:13162-85.
[51] Maitra U, Gupta U, De M, Datta R, Govindaraj A, Rao CNR. Highly Effective Visible-Light-Induced H2 Generation by Single-Layer 1T-MoS2 and a Nanocomposite of Few-Layer 2H-MoS2 with Heavily Nitrogenated Graphene. Angew Chem Int Ed. 2013;52:13057-61.
[52] Rao CNR, Maitra U, Waghmare UV. Extraordinary attributes of 2-dimensional MoS2 nanosheets. Chem Phys Lett. 2014;609:172-83.

[53] Wang T, Zhuo J, Chen Y, Du K, Papakonstantinou P, Zhu Z, et al. Synergistic Catalytic Effect of MoS2 Nanoparticles Supported on Gold Nanoparticle Films for a Highly Efficient Oxygen Reduction Reaction. ChemCatChem. 2014;6:1877-81.
[54] Wang T, Gao D, Zhuo J, Zhu Z, Papakonstantinou P, Li Y, et al. Size-Dependent Enhancement of Electrocatalytic Oxygen-Reduction and Hydrogen-Evolution Performance of MoS2 Particles. Chem Euro J. 2013;19:11939-48.
[55] Zhao K, Gu W, Zhao L, Zhang C, Peng W, Xian Y. MoS2/Nitrogen-doped graphene as efficient electrocatalyst for oxygen reduction reaction. Electrochimica Acta. 2015;169:142-9.
[56] Huang H, Feng X, Du C, Song W. High-quality phosphorus-doped MoS2 ultrathin nanosheets with amenable ORR catalytic activity. Chem Commun. 2015;51:7903-6.
[57] Du C, Huang H, Feng X, Wu S, Song W. Confining MoS2 nanodots in 3D porous nitrogen-doped graphene with amendable ORR performance. J Mater Chem A. 2015;3:7616-22.

2.2 REMARKABLE PERFORMANCE OF HEAVILY NITROGENATED GRAPHENE IN THE OXYGEN REDUCTION REACTION OF FUEL CELLS IN ALKALINE MEDIUM

Summary*

Graphene and other 2D materials have been used as catalysts in the oxygen reduction reaction (ORR) in fuel cells with a few limitations in terms of the onset potential and number of electrons transferred per oxygen molecule. We find that heavily nitrogenated graphene with a nitrogen content of 14-18 wt.% and a high proportion of pyrrolic nitrogen, prepared under microwave irradiation, shows excellent activity towards ORR comparable to platinum, with the transferred electron number of 4.

*A Paper based on this work has been published in Mater. Res. Express, 2015, **2**, 095503.

2.2.1 Introduction

The oxygen reduction reaction *(*ORR*)* is an important process occurring at the cathode in proton exchange membrane fuel cells and developing an efficient and cheap electrocatalyst remains a problem [1, 2]. The common catalyst used in ORR is platinum but it is desirable to replace it with a cheaper and more easily available material. In addition, there are problems due to the diffusion of fuel molecules into the electrodes and poisoning due to carbon monoxide [3]. There are a few reports in the literature on catalysts based on non-precious transition metals such as iron and cobalt [4]. Nitrogen-doped carbon materials such carbon nanotubes, carbon nonofibers and graphene with nitrogen content of 5 wt.% or less are known to show improved ORR catalytic activity in addition to low fuel crossover, low cost and good durability [5-7]. Doping carbon materials with nitrogen effectively tunes the electronic structure and related properties [8, 9]. Of the N-doped carbon materials, nitrogen-doped graphene stands out because of its unique 2D layered structure, high electrical conductivity and good electron-donor ability, making it an excellent candidate as a ORR electrocatalyst [10, 11] as well as excellent supercapacitor electrodes [12-14]. Since the nitrogen in N-doped graphene is an n-type dopant, it can donate electrons to the neighbouring π-orbital of the conjugated carbon, in turn providing an electron to the π*-orbital of oxygen to facilitate its splitting [15]. Clearly, it is important to prepare graphene with high nitrogen content to explore its beneficial effect in ORR.

Several methods have been employed for the synthesis of nitrogenated graphene in the literature [8]. Arc-discharge between graphite electrodes in the presence of ammonia permits doping of 1 at.% nitrogen into the graphene lattice [16]. While 5 at.% of nitrogen could be substituted by ammonolysis of graphene oxide under chemical vapor deposition (CVD) conditions [17]. N-doped graphene films on Cu substrate were synthesized by chemical vapour deposition technique using hexane and acetonitrile precursor at 950 °C in Ar/H_2 flow (N content is 9 at.%) [18]. Nitrogen-doped graphene on a Pt(111) surface yields 4.0 at. % at 500 ^oC [19] whereas chemical vapour deposition of 1,3,5-triazine on Cu metal catalyst gives 2-6 at.% of nitrogen content [20]. Nitrogen-doped graphene on Cu foils by plasma-enhanced chemical vapour deposition at 950 ^oC

gives 1.1 at.% of nitrogen [21]. Treating monoethanolamine at 1100 ^{o}C for 12 min gives few-layer nitrogen-doped graphene with nitrogen content of 2.9 at.% [22].

Recently, the hydrothermal method has been used as an effective approach to fabricate graphene and nitrogen-doped graphene [8]. Various nitrogen sources have also been reported so far for the use in hydrothermal method such as pyrrole [23], ammonia/organic amines [24] and hydrazine hydrate . Amino acids containing multiple functional groups (–NH2, –COOH and other functional groups) have also been used in the synthesis [25]. Chen et al. employed L-cysteine as a reductant to prepare reduced graphene oxide nanosheets at room temperature [26]. One-step hydrothermal approach using hexamethylenetetramine as single carbon and nitrogen to produce N-graphene with unique structure and high surface area [27].

2.2.3 Scope of the present investigations

Nitrogen doped graphenes have shown enhanced electrocatalytic activity in ORR for fuel cell [28]. The nitrogen atoms in graphene can be pyrrolic, pyridinic or graphitic and there are reports showing superior activity of pyrrolic and pyridinic nitrogens in promoting ORR in nitrogen-doped graphene. Enhanced ORR activity from selectively synthesized pyridinic- and pyrrolic-nitrogen-doped graphene has been reported [29]. We have prepared graphene heavily doped with nitrogen, containing more of pyrrolic nitrogens by employing microwave synthesis using urea as the nitrogen source. By this means we have been able to obtain a nitrogen content of 14 to 18 wt. % in the graphene lattice. The heavily nitrogenated graphene samples show outstanding ORR activity in alkaline media.

2.2.3 Experimental section

Synthesis of NG: Graphene oxide (GO), synthesized by the Hummer's method [30], was finely ground with different proportions of urea (graphene:urea mass ratios of 1:0.5, 1:1 and 1:2) and pressed into pellets. The pelletized mixture was heated in a microwave reactor (900 W, 2.4 GHz) for 30 s. The product was washed several times with deionized water and dried. Samples of nitrogen-doped graphene (NG), NG-1, NG-2 and NG-3, had nitrogen contents of 14.7, 17.5 and 18.2 wt.% respectively based on elemental analysis. Reduced graphene oxide (RGO) was synthesized by reducing GO with 10 mL of hydrazine

hydrate for 12 h.

Electrochemical Measurements: A standard three-electrode cell with a Pt plate as the counter electrode was employed for the electrochemical study. For the oxygen reduction reaction, the catalyst was prepared by dispersing the catalyst (5 mg) in 1 mL mixture of ethanol and water in the presence of 0.05 wt.% Nafion. From this solution, 4 µL catalyst ink was drop casted on a glassy carbon electrode (GCE) (3mm diameter). The commercial Pt-loaded carbon catalyst (Pt/C 40% on Vulcan XC, Sainergy Fuel cell India Ltd.) was used for comparison. 1 mg mL^{-1} Pt/C dispersion in isopropanol was prepared using ultrasonication. From this 10 µL was drop casted on GCE using micro syringe. Electrochemical measurements were performed in an O_2-saturated aqueous 0.1 M potassium hydroxide (KOH) solution (Ag/AgCl reference electrode). Rotating disc electrode (RDE) measurements were carried out with a system from Beckman Instruments by coupling with a galvanostat/potentiostat (Technoscience, Bangalore).

Table 1. Elemental analysis and XPS data on nitrogen doped graphene oxide.

Sample	N_{CHN} (wt.%)	N_{XPS} (at. %)	$N_{Pyridinic}$ (at.%)	$N_{Pyrrolic}$ (at.%)	$N_{Graphitic}$ (at.%)
NG-1	14.7	13.2	2.3	7.1	3.8
NG-2	17.5	15.3	2.6	7.2	5.5
NG-3	18.2	15.6	2.6	9.3	3.7

2.2.4 Results and discussion

Of the different proportions of heavily nitrogenated graphene obtained by microwave synthesis, NG-3 prepared with 1:2 weight ratio of GO and urea had the highest nitrogen content of 18.2 wt%, while NG-1 and -2 had nitrogen content of 14.7 and 17.5 wt.% respectively (Table 1). The surface areas of the samples were in the 195-235 m^2/g range. In order to understand the nature of nitrogen in NG we have carried out a detailed study of the N (1s) region in the X-ray photoelectron

spectra. In Figure 1, we show the N (1s) spectrum of NG-1 and -3. The N 1s signal could be deconvoluted into three features with the signal at ~398.2 eV corresponding to pyridinic nitrogen and those that at ~400.1 eV and 401.8 eV corresponding to pyrrolic and graphitic nitrogens respectively. We see that the content of pyrrolic nitrogen is higher than that of pyridinic and graphitic nitrogen in all the 3 samples. From the N (1s) spectra, the nitrogen contents of NG-1, -2 and -3 were found to be 13.2, 15.3 and 15.6 at. % respectively (Table 1). In Figure 2(a), we show a TEM image of a NG sample. The image shows that graphene gets crumpled under microwave treatment. The Raman spectrum shows the G-band at 1602 cm^{-1}, shifted to lower frequencies by about 10-12 cm^{-1} relative to GO. The I_D/I_G ratio of 1.23 in GO increases in NG samples as can be seen from Figure 2(b). X-ray diffraction patterns of GO shows the peak (002) reflection at 10.8° corresponding to an interlayer spacing of 0.742 nm. This peak disappears after microwave treatment with urea due to the removal of oxygen functional groups. Instead, a broad diffraction peak centred at 25.4° (d_{002} of ~0.365 nm) is observed in the NG samples indicating stacked few-layer graphene nanosheets.

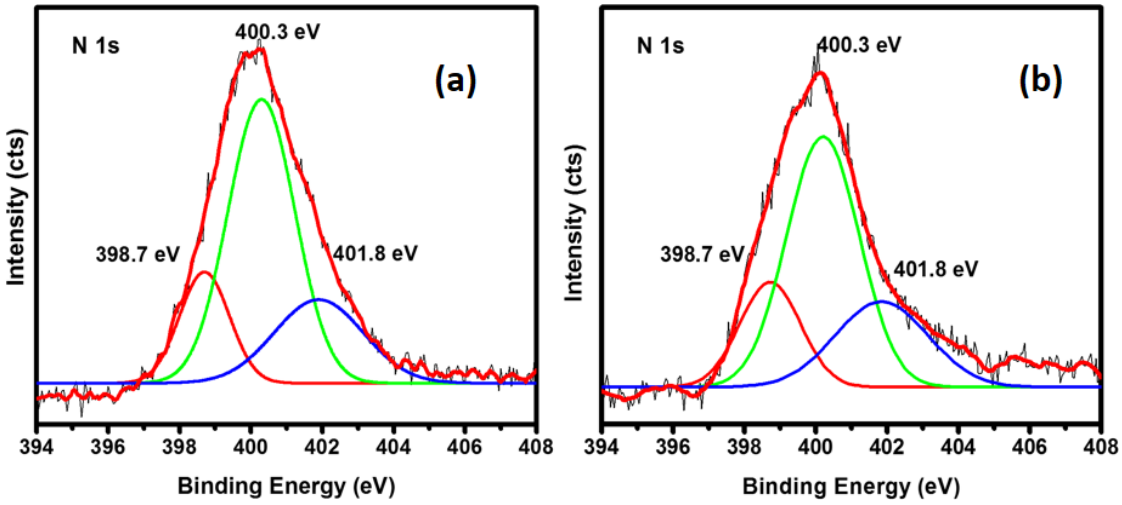

Figure 1. N 1s core level XP spectra of (a) NG-1 and (b) NG-3

Figure 3 shows theromogravimetric curves of GO and NG samples. Nitrogen doped graphene oxides show increase in thermal stability. TGA curve of GO shows

three major steps of weight loss starting from 110, 120–170 and 170-280 ^{o}C which were attributed to the removal of adsorbed water, the decomposition of the oxygen functionalities and the decomposition of stable oxygen functional groups present in the materials, respectively. Compared with the GO, NGs exhibit no significant weight loss in the range of 170-280 ^{o}C, indicating that efficient removal of oxygen functional groups occurs during the microwave treatment.

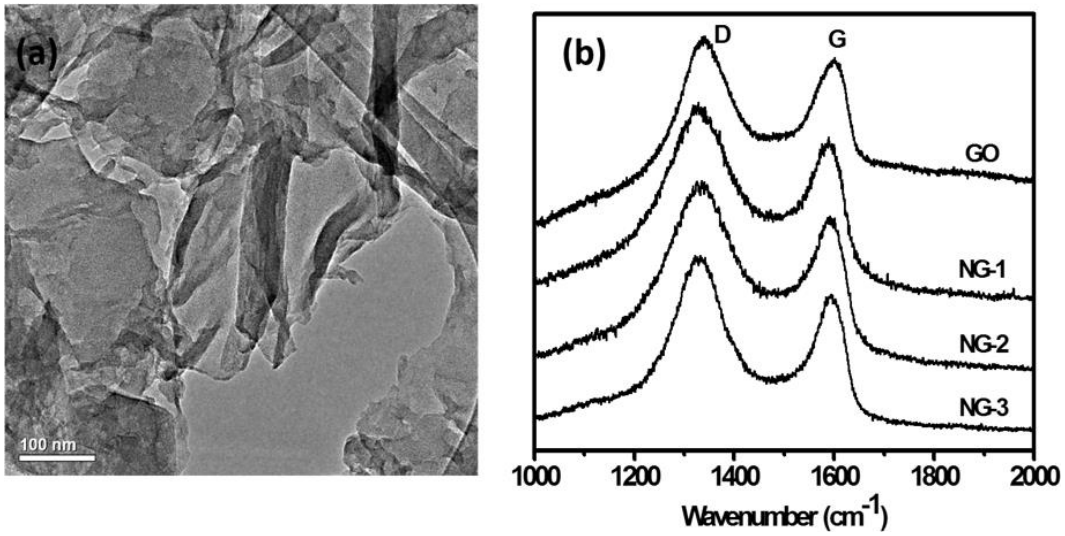

Figure 2. (a) TEM image of NG-3 (b) Raman spectra of GO and NG samples

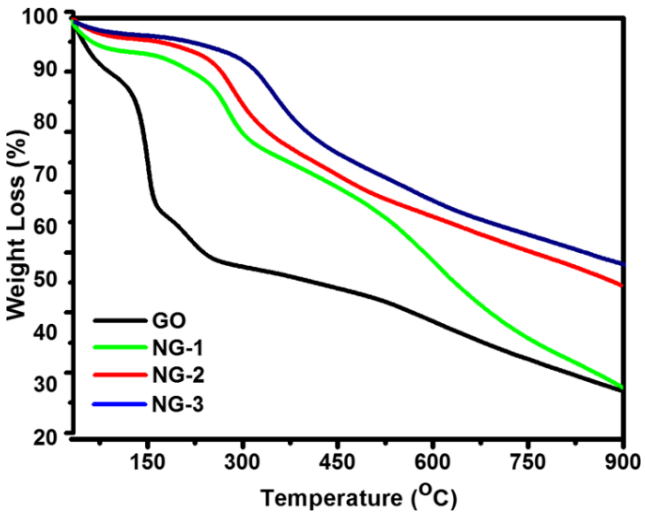

Figure 3. Thermogravimetric curves of GO and NG samples

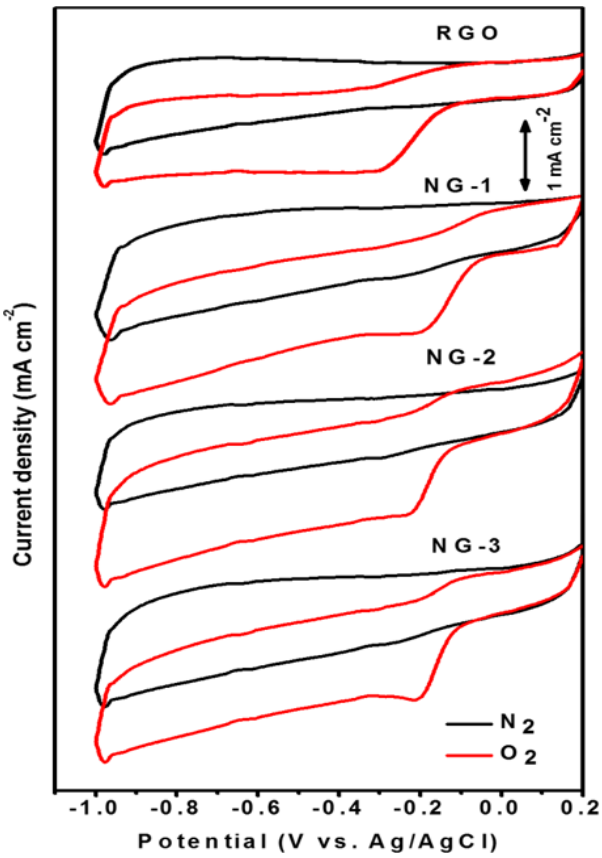

Figure 4. Cyclic volatammetry curves of RGO and NGs in nitrogen or oxygen saturated 0.1 M KOH with a scan rate of 5 mV/s.

Electrocatalytic activity of RGO, NG-1, NG-2 and NG-3 in ORR was first examined by cyclic voltammetry (CV) at a slow scanning rate of 5 mV/s in O_2-saturated and N_2-saturated 0.1 M KOH electrolytes in a conventional three-electrode system, as shown in Figure 4. The NG catalysts show a pure capacitive current background in the N_2-saturated electrolyte and relatively broad cathodic peaks ranging from -0.2 to -0.25 V *vs.* Ag/AgCl in the O_2-saturated electrolyte, indicating a good O_2 reduction property. In addition, to evaluate the electrocatalytic activity of NGs, linear-sweep voltammetry (LSV) of NGs at a rotation speed of 1600 rpm was also measured in the O_2-saturated 0.1 M KOH solution on a RDE, and this is shown in Figure 5(a). NG samples exhibit much higher current density compared to Pt/C or RGO, representing an enhanced activity for ORR. The onset potential of RGO is around -0.2 V, slightly shifting to -0.07 V in nitrogen-doped samples. This positive shift indicates that the nitrogen

in the graphene reduce the ORR overpotential, thus enhancing the catalytic activity. NG-3 shows a much more positive onset potential than that of NG-1 or NG-2 and is closer to that of platinum. This observation shows that the activity of NG-3 is outstanding.

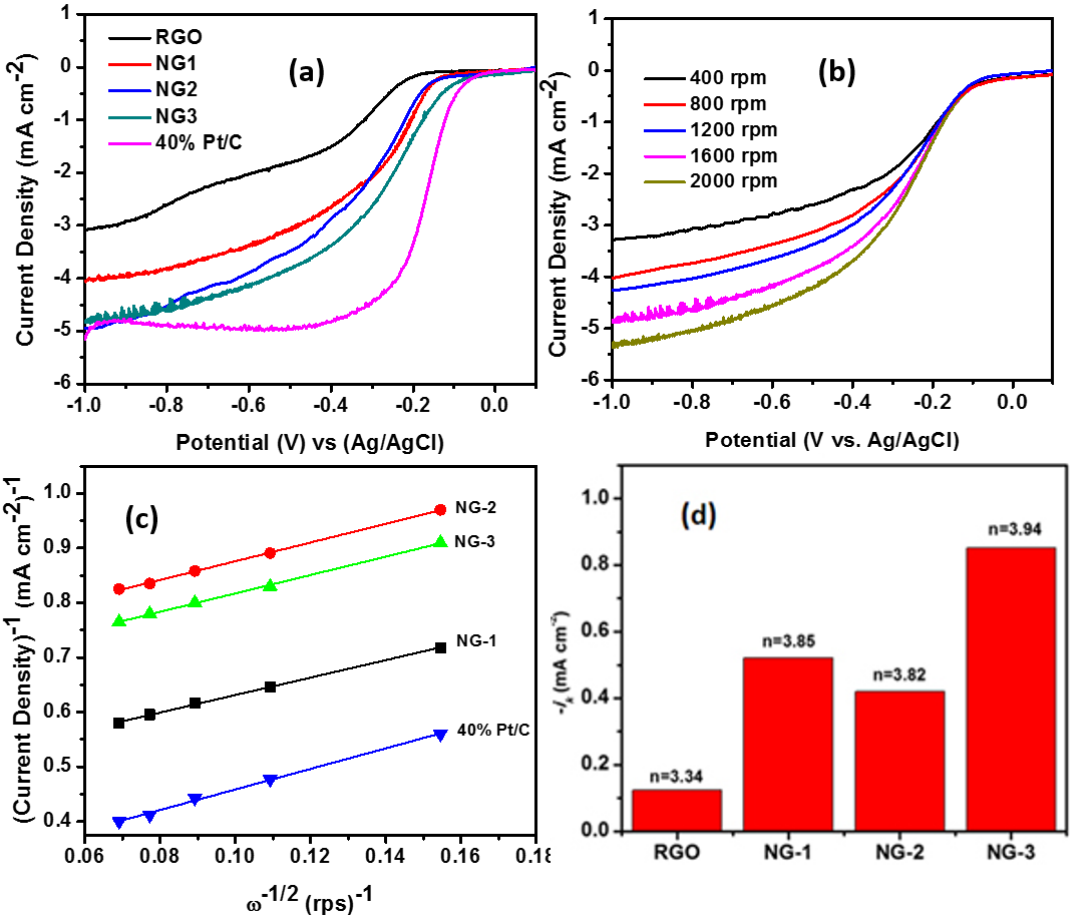

Figure 5. (a) LSV curves of 40% Pt/Vulcan X and NG samples in oxygen saturated 0.1 M KOH with a scan rate of 5 mV s^{-1} and a rotation rate of 1600 rpm (b) RDE measurement of NG-3 in oxygen saturated 0.1 M KOH with a scan rate of 5 mV/s (c) Koutecky–Levich plots obtained at -0.2 V. (d) Variation of kinetic-limiting current density (i_k) at -0.2 V for RGO and NG samples.

Furthermore, a set of LSV curves for ORR based on the NG-3 catalyst recorded 400-2400 rpm, as shown in Figure 5(b). It is also seen that the measured current density increased with the increase in rotation speed, since the diffusion distance shortens at higher rotation rates. Koutecky–Levich plots (i^{-1} versus $\omega^{-1/2}$) were

obtained from the polarization curves at a potential of -0.2 V *vs.* Ag/AgCl for all the catalysts, as shown in Figure 5(c). The transferred electron number (n) per O_2 from the slopes of Koutecky–Levich plots was calculated to be ~4 (-0.2 *vs.* Ag/AgCl) for all the NG samples, while in RGO it is only ~3.34. We have achieved an electron transfer of 4 at lower potentials (i.e. at (-0.2 *vs.* Ag/AgCl). This is considered to be due to the high nitrogen content in graphene. The *n* and kinetic current density (*ik*) values of RGO and NG are shown in Figure 5(d). The i*k* values of RGO, NG-1, NG-2, NG-3 and Pt/C are -0.1, -0.5, -0.4, -0.8 and -1.2 mA cm^{-2}, respectively at -0.2 *vs.* Ag/AgCl. NG-3 shows higher i_k values than graphene samples but lower than that of Pt/C. The increase in the ORR activity of NG samples can be attributed to the pyrrolic nitrogens present, on which the oxygen molecules can be activated and reduced. The graphitic nitrogens transfer an electron from the adjacent carbon to the nitrogen atoms and the nitrogen atoms donate back electrons to adjacent C_{pz} orbitals; the donation and back-donation process facilitates O_2dissociation. The pyridinic nitrogen located at the graphene edges also activates the oxygen dissociation through direct bonding with the lone electron pair of nitrogen. The increase in the ORR activity of NG samples can be attributed to the pyrrolic nitrogens present.

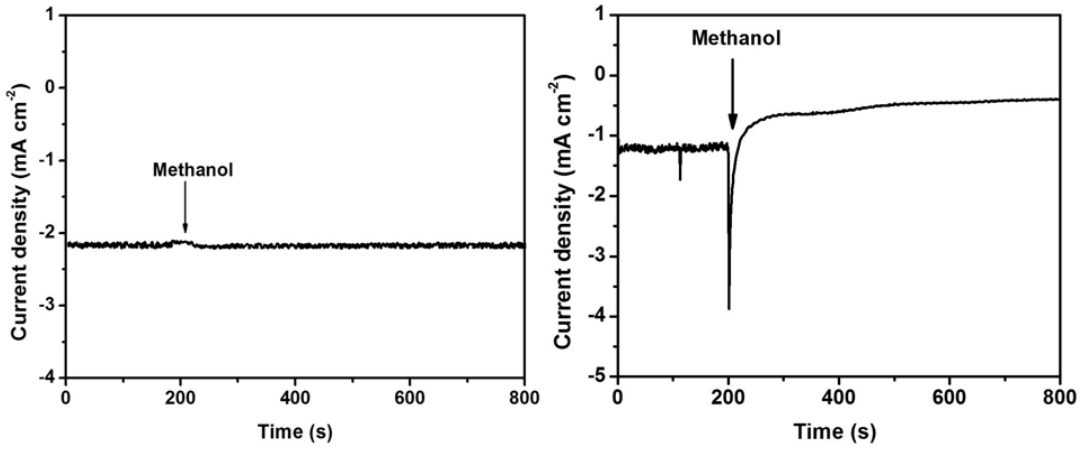

Fig. 6 Current (*i*) vs time (*t*) chronoamperometric response of (a) NG-3 and (b) 40% Pt/C electrodes in 0.1 M KOH (at -0.15 V) and 0.3 M methanol.

Figure 6 is the current density (i) vs time (t) chronoamperometric response of NG-3 as well as 40% Pt/C in presence of 0.3 M methanol. As shown in Figure 6 (a) NG-3 shows strong and stable amperometric response in presence of methanol whereas, a 50% decrease in current appears at the Pt/C electrode upon the addition of methanol (Figure 6 (b)). This clearly demonstrates that NG possesses high stability towards ORR in the presence of methanol.

2.2.5 Conclusions

The present study shows heavily nitrogenated graphenes to be far superior ORR catalysts in terms of the onset potential and the number of electron transferred per oxygen molecule. The performance of the heavily nitrogenated graphenes is as good as platinum. The reason behind the good performance is of these nitrogenated graphene samples is ascribed to the high proportion of pyrrolic nitrogens in the graphene lattice.

References

[1] Darling RM, Meyers JP. Kinetic Model of Platinum Dissolution in PEMFCs. J Electrochem Soc. 2003;150:A1523-A7.

[2] GreeleyJ, Stephens IEL, Bondarenko AS, Johansson TP, Hansen HA, Jaramillo TF, et al. Alloys of platinum and early transition metals as oxygen reduction electrocatalysts. Nat Chem. 2009;1:552-6.

[3] Pillay D, Johannes MD, Garsany Y, Swider-Lyons KE. Poisoning of Pt3Co Electrodes: A Combined Experimental and DFT Study. J Phys Chem C. 2010;114:7822-30.

[4] Dathar GKP, Shelton WA, Xu Y. Trends in the Catalytic Activity of Transition Metals for the Oxygen Reduction Reaction by Lithium. J Phys Chem Lett. 2012;3:891-5.

[5] Du Z, Wang S, Kong C, Deng Q, Wang G, Liang C, et al. Microwave plasma synthesized nitrogen-doped carbon nanotubes for oxygen reduction. J Solid State Electrochem. 2015:1-9.

[6] Dorjgotov A, Ok J, Jeon Y, Yoon S-H, Shul Y. Nitrogen-doped ordered porous carbon catalyst for oxygen reduction reaction in proton exchange membrane fuel cells. J Solid State Electrochem. 2013;17:2567-77.

[7] Zhao Y, Zhou Y, Xiong B, Wang J, Chen X, O'Hayre R, et al. Facile single-step preparation of Pt/N-graphene catalysts with improved methanol electrooxidation activity. J Solid State Electrochem. 2013;17:1089-98.

[8] Rao CNR, Gopalakrishnan K, Govindaraj A. Synthesis, properties and applications of graphene doped with boron, nitrogen and other elements. Nano Today. 2014;9:324-43.

[9] Srivastava D, Susi T, Borghei M, Kari L. Dissociation of oxygen on pristine and nitrogen-doped carbon nanotubes: a spin-polarized density functional study. RSC Adv. 2014;4:15225-35.

[10] Soin N, Roy S, Sharma S, Thundat T, McLaughlin J. Electrochemical and oxygen reduction properties of pristine and nitrogen-doped few layered graphene nanoflakes (FLGs). J Solid State Electrochem. 2013;17:2139-49.

[11] Yasuda S, Yu L, Kim J, Murakoshi K. Selective nitrogen doping in graphene for oxygen reduction reactions. Chem Commun. 2013;49:9627-9.

[12] Zheng B, Chen T-W, Xiao F-N, Bao W-J, Xia X-H. KOH-activated nitrogen-doped graphene by means of thermal annealing for supercapacitor. J Solid State Electrochem. 2013;17:1809-14.

[13] Gopalakrishnan K, Govindaraj A, Rao CNR. Extraordinary supercapacitor performance of heavily nitrogenated graphene oxide obtained by microwave synthesis. J Mater Chem A. 2013;1:7563-5.

[14] Gopalakrishnan K, Moses K, Govindaraj A, Rao CNR. Supercapacitors based on nitrogen-doped reduced graphene oxide and borocarbonitrides. Solid State Commun. 2013;175–176:43-50.

[15] Shao Y, Zhang S, Engelhard MH, Li G, Shao G, Wang Y, et al. Nitrogen-doped graphene and its electrochemical applications. Journal of Materials Chemistry. 2010;20:7491-6.

[16] Panchakarla LS, Subrahmanyam KS, Saha SK, Govindaraj A, Krishnamurthy HR, Waghmare UV, et al. Synthesis, Structure, and Properties of Boron- and Nitrogen-Doped Graphene. Adv Mater. 2009;21:4726-30.

[17] Wang X, Li X, Zhang L, Yoon Y, Weber PK, Wang H, et al. N-Doping of Graphene Through Electrothermal Reactions with Ammonia. Science. 2009;324:768-71.

[18] Reddy ALM, Srivastava A, Gowda SR, Gullapalli H, Dubey M, Ajayan PM. Synthesis Of Nitrogen-Doped Graphene Films For Lithium Battery Application. ACS Nano. 2010;4:6337-42.

[19] Imamura G, Saiki K. Synthesis of Nitrogen-Doped Graphene on Pt(111) by Chemical Vapor Deposition. J Phys Chem C. 2011;115:10000-5.

[20] Lu Y-F, Lo S-T, Lin J-C, Zhang W, Lu J-Y, Liu F-H, et al. Nitrogen-Doped Graphene Sheets Grown by Chemical Vapor Deposition: Synthesis and Influence of Nitrogen Impurities on Carrier Transport. ACS Nano. 2013;7:6522-32.

[21] Tomo-o T, Koichiro S. Synthesis of Nitrogen-Doped Graphene by Plasma-Enhanced Chemical Vapor Deposition. Jap J Appl Phys. 2012;51:055101.

[22] Bao JF, Kishi N, Soga T. Synthesis of nitrogen-doped graphene by the thermal chemical vapor deposition method from a single liquid precursor. Mater Lett. 2014;117:199-203.

[23] Zhao Y, Hu C, Hu Y, Cheng H, Shi G, Qu L. A Versatile, Ultralight, Nitrogen-Doped Graphene Framework. Angew Chem Int Ed. 2012;51:11371-5.

[24] Long D, Li W, Ling L, Miyawaki J, Mochida I, Yoon S-H. Preparation of Nitrogen-Doped Graphene Sheets by a Combined Chemical and Hydrothermal Reduction of Graphene Oxide. Langmuir. 2010;26:16096-102.

[25] Jia. Hydrothermal synthesis of nitrogen-doped graphene hydrogels using amino acids with different acidities as doping agents. J Mater Chem A. 2014;2: 8352-61.

[26] Dezhi C, Lidong L, Lin G. An environment-friendly preparation of reduced graphene oxide nanosheets via amino acid. Nanotech. 2011;22:325601.

[27] Xing Z, Ju Z, Zhao Y, Wan J, Zhu Y, Qiang Y, et al. One-pot hydrothermal synthesis of Nitrogen-doped graphene as high-performance anode materials for lithium ion batteries. Sci Rep. 2016;6:26146.

[28] Wang H, Maiyalagan T, Wang X. Review on Recent Progress in Nitrogen-Doped Graphene: Synthesis, Characterization, and Its Potential Applications. ACS Catal. 2012;2:781-94.

[29] Ding W, Wei Z, Chen S, Qi X, Yang T, Hu J, et al. Space-Confinement-Induced Synthesis of Pyridinic- and Pyrrolic-Nitrogen-Doped Graphene for the Catalysis of Oxygen Reduction. Angew Chem Int Ed. 2013;52:11755-9.

[30] Marcano DC, Kosynkin DV, Berlin JM, Sinitskii A, Sun Z, Slesarev A, et al. Improved Synthesis of Graphene Oxide. ACS Nano. 2010;4:4806-14.

2.3 BN-GRAPHENE COMPOSITES GENERATED BY COVALENT CROSS-LINKING AS OXYGEN REDUCTION REACTION CATALYST IN FUEL CELLS

Summary*

We have prepared composites of BN and carboxylated graphene, $BN_{1-x}G_x$, by covalent cross-linking employing the carbodiimide reaction. $BN_{1-x}G_x$ ($x \approx 0.25$, 0.5 and 0.75) so obtained have been characterized. The $x \approx 0.75$ composite is found to be a good electrocatalyst for the oxygen reduction reaction in fuel cells.

*A Paper based on this work has been published in Adv. Funct. Mater, 2015, **25**, 5910.

2.3.1 Introduction

Graphene, the two-dimensional sheet of sp^2 carbons, has received great attention due to its novel properties, optical properties with potential applications in nanoelectronics and energy storage [1, 2]. Electronic devices based on graphene are of interest due to its high carrier mobility and ballistic transport properties [3, 4]. Field effect transistors (FETs) based on graphene as well as photoresponse properties of graphene have been studied [5, 6]. The main limitation of graphene is absence of band gap essential for transistor and photo response properties. Recent studies have shown chemical doping of graphene with nitrogen and other hetero atoms alter the electronic and electrochemical properties [7, 8]. Theoretical calculations have shown that random doping of graphene with boron or nitrogen can open a small gap in the Dirac points [9]. There are a few reports on the synthesis of B, N-doped graphene with different doping levels [7, 10]. Thus, B, N-doped graphene films have been synthesized using a thermal catalytic CVD method [11-13]. Kumar et al [14] describe a general method of preparing borocarbonitrides, $B_xC_yN_z$, of different compositions starting with mixtures of activated carbon, boric acid and urea. These materials are generally nanoplatelets containing graphene and BN domains, possibly along with BCN rings. If the ratio of BN to carbon is 1:1 the composition would be BCN. $B_xC_yN_z$ compositions contain hexagonal networks of B–C, B–N, C–N and C–C bonds but no B–B or N–N bonds.

On the other hand, lateral integration of graphene and hexagonal boron nitride permits the intricate design of a hybrid heterostructure in which the electronic characteristics can be tuned as required for a particular application [14]. Hexagonal BN is a 2D analogue of graphene which is composed of alternating B and N atoms in a honeycomb lattice with a bandgap of 5.9 eV [15]. In recent studies, theoretical calculations predicted that bandgap can opened in h-BN and graphene heterostructures with a relatively high carrier mobility in the range of 10^3–10^5 $cm^2/V.s$ [16]. In addition to electrical properties, BN-graphene heterostructures have shown supercapacitor properties [17] but there are no literature on their application as oxygen reduction catalyst.

The heterostructures of graphene and h-BN can be formed by mechanical overlap,

chemical vapour deposition (CVD), or controlled continuous growth [18]. Ajayan et al. [19] reported the one-batch growth of BCN hybrids on Cu foils using methane and ammonia borane simultaneously as precursors for graphene and h-BN growth respectively. Park et al. [20] developed a patterned regrowth approach to synthesize monolayer in-plane BN-G heterostructures. Similar patterned regrowth method has been used by Ajayan et al [21] to grow lateral monolayer BN-G heterostructures and also reported a topological substitution reaction to convert graphene to h-BNC layers on Cu foils [22]. Johnson et al. [23] used two-step continuous growth method to achieve lateral BN-G films on Cu substrates without involvement of photolithography. In addition to patterned regrowth techniques, graphene and boron nitride heterostructures have been grown epitaxially [24, 25]. All these synthetic efforts helps to study the interfacial properties of BN-graphene heterostructures and provide great prospects for exploring their applications in graphene-based electronics.

2.3.2 Scope of the present investigations

Graphene-BN heterostructues have shown intersting electronic properties and interfacial properties. Its electrochemical properties such as charge storing ability or electrocatlytic actvitiy were not studied in the literature. For this purpose, we have prepared covalently linked $BN_{1-x}G_x$ composites with varying graphene content (x = 0-1) and studied their electrocatlytic activity in oxygen reduction reaction (ORR) for fuel cells.

2.3.3 Experimental section

Synthesis of $BN_{1-x}G_x$ composites:* Amine functionalized few-layer BN (~ 1–4 layers) was prepared by mixing boric acid and urea in 1:48 molar ratio and heating in high purity ammonia atmosphere at 900 °C for 5h [15]. Graphite oxide (GO) was synthesized using modified Hummers method [26] and exfoliated at 1050 °C under constant N_2. Carboxylic acid functionalized graphene was obtained by treating EG in conc. HNO_3 + H_2SO_4 mixture under microwave. Obtained product was filtered and washed with deionized water to remove excess acid and dried at 100 °C.

Three different composites $BN_{1-x}G_x$ (x ≈ 0.25, 0.5 and 0.75) were obtained by varying the ratio of BN with respect to carboxylated graphene. We have employed the carbodiimide

*carried out by Mr. Ram Kumar

method to link BN and G with amide bond, by using EDC {1-ethyl-3-(3-dimethylaminopropyl) carbodiimide)} as the reagent. Nitrogen atmosphere was maintained during the reaction. Obtained product was filtered using 0.45 μm PTFE membrane, washed with copious amount of DMF and water.

2.3.4 Results and discussion

We have synthesized $BN_{1-x}G_x$ composites by linking covalently BN and graphene with amide bond, by using EDC {1-ethyl-3-(3-dimethylaminopropyl) carbodiimide)} as the reagent. Figure 1 shows the transmission electron microscopy images of $BN_{1-x}G_x$ composites. The energy dispersive spectroscopic mapping is shown in Figure 2 which shows the presence of boron, nitrogen and graphene.

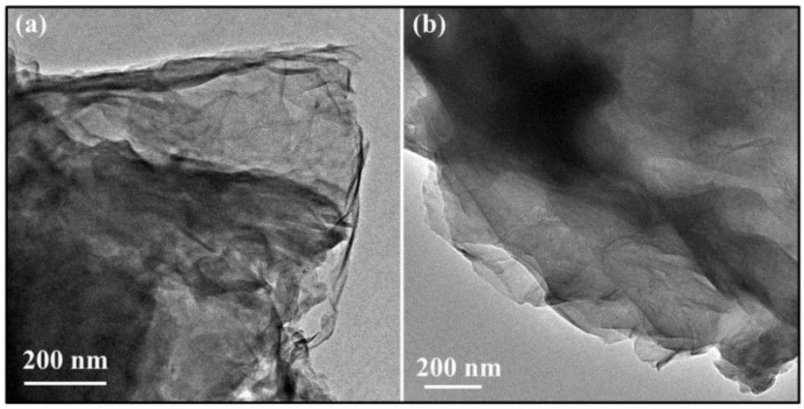

Figure 1. TEM image of **(a)** $BN_{0.25}G_{0.75}$, **(b)** $BN_{0.75}G_{0.25}$ composites.

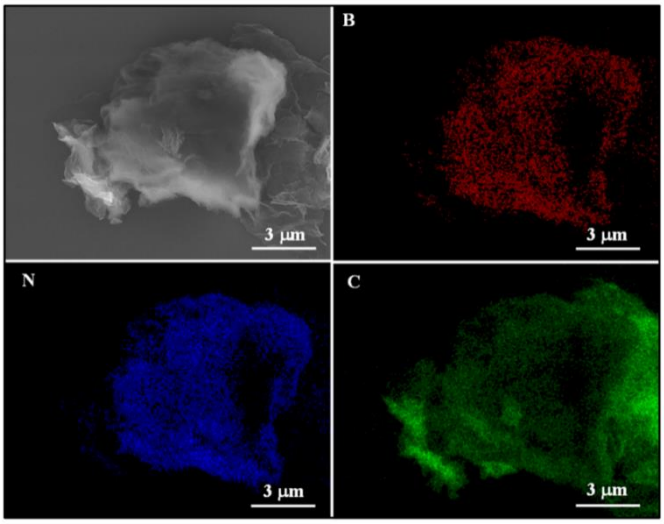

Figure 2. Elemental mapping of $BN_{0.25}G_{0.75}$ composite. B (red), N (blue) and C (green).

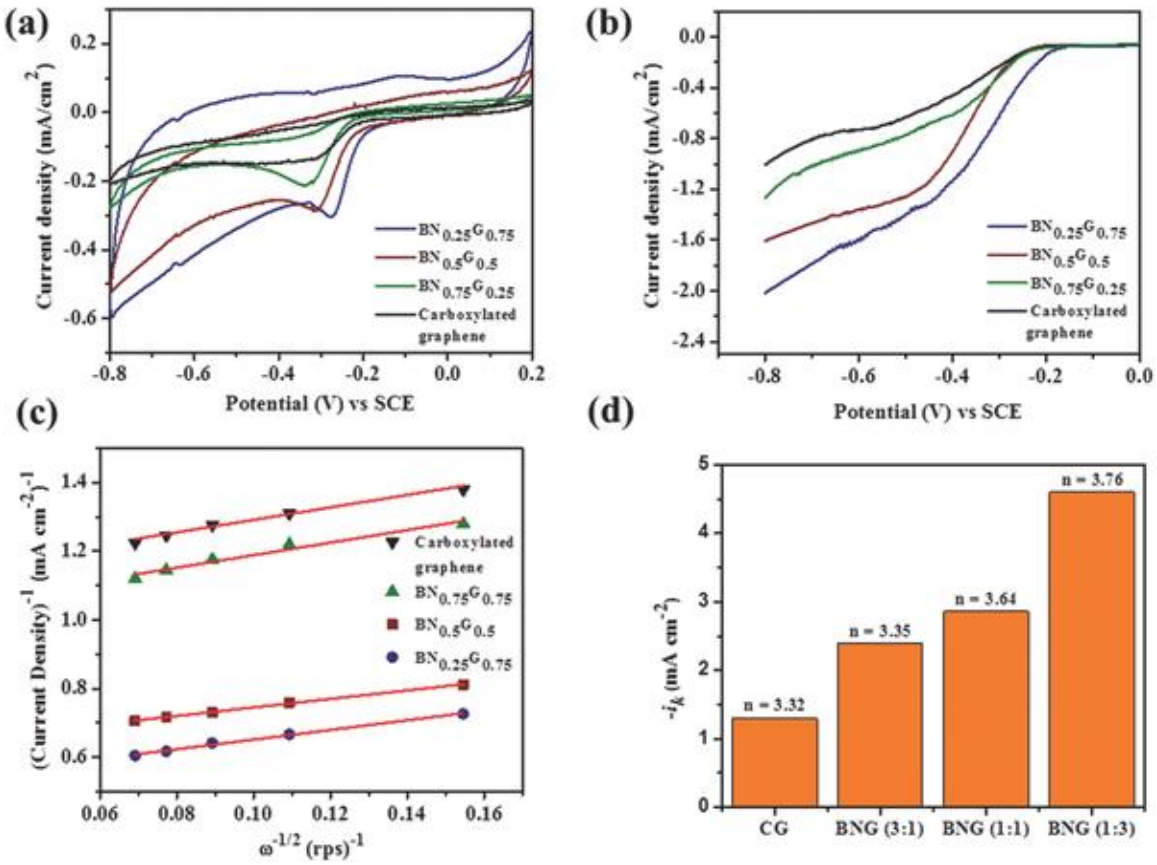

Figure 3. (a) Cyclic voltammetry curves of carboxylated graphene and $BN_{1-x}G_x$ composites in oxygen saturated 0.1 m KOH with a scan rate of 5 mV/s. (b) LSV curves of EG and $BN_{1-x}G_x$ composites in oxygen saturated 0.1 m KOH with a scan rate of 5 mV/s and a rotation rate of 1600 rpm. (c) Koutecky–Levich plots obtained at −0.6 V versus SCE, and (d) variation of kinetic current density (i_k) at −0.4 V versus SCE for EG and $BN_{1-x}G_x$ composites. Aqueous 0.1 m KOH solution used as electrolyte.

Oxygen reduction reaction: We have investigated the electrocatalytic activity of carboxylated graphene and $BN_{1-x}G_x$ composites in the ORR by CV at a slow scan rate of 5 mV s^{-1} in O_2-saturated and N_2-saturated 0.1 m KOH electrolytes, using a conventional three-electrode system (Figure 3(a)). The $BN_{1-x}G_x$ composites show cathodic peaks ranging from −0.25 to −0.35 V versus standard calomel electrode (SCE) in an O_2-saturated electrolyte, indicating a good O_2 reduction property whereas carboxylated graphene does not show a prominent reduction peak. This shows that addition of BN to graphene assists the reduction of oxygen. Linear-sweep voltammetry (LSV) of carboxylated graphene and $BN_{1-x}G_x$ composites at a rotation speed of 1600 rpm is displayed in Figure 3(b). The $BN_{1-x}G_x$ composites exhibit higher current density on

addition of graphene to BN representing an enhanced activity for ORR. $BN_{0.25}G_{0.75}$ shows a more positive onset potential than $BN_{0.5}G_{0.5}$, $BN_{0.75}G_{0.25}$, and carboxylated graphene. The Koutecky–Levich plots (i^{-1} vs $\omega^{-1/2}$) were obtained from the polarization curves at a potential of −0.6 V versus SCE for all the catalysts as shown in Figure 3(c). The transferred electron number (n) per O_2 calculated from the slopes of Koutecky–Levich plots ranges from 3.3 to 3.8. $BN_{0.25}G_{0.75}$ shows electron transfer of 3.8 per oxygen molecule. The kinetic current density (i_k) values at −0.4 V versus SCE of $BN_{0.25}G_{0.75}$ is −4.6 mA cm^{-2} which is higher than $BN_{0.5}G_{0.5}$, $BN_{0.75}G_{0.25}$, and carboxylated graphene which showed −2.9, −2.4, and −1.3 mA cm^{-2}, respectively (Figure 3(d)). The present study demonstrates that addition of a small amount of BN to the graphene matrix enhances the ORR activity significantly.

2.3.5 Conclusions

In conclusion, BN-G composites have been successfully synthesized by carbodiimide reaction. These composites exhibits good electrocatalytic activity in ORR when compared to graphene and BN itself. The electron transfer being very close to 3.8.

References

[1] Geim AK, Novoselov KS. The rise of graphene. Nat Mater. 2007;6:183-91.

[2] Rao CNR, Sood AK, Subrahmanyam KS, Govindaraj A. Graphene: The New Two-Dimensional Nanomaterial. Angewandte Chemie International Edition. 2009;48:7752-77.

[3] Novoselov KS, Geim AK, Morozov SV, Jiang D, Zhang Y, Dubonos SV, et al. Electric Field Effect in Atomically Thin Carbon Films. Science. 2004;306:666-9.

[4] Mayorov AS, Gorbachev RV, Morozov SV, Britnell L, Jalil R, Ponomarenko LA, et al. Micrometer-Scale Ballistic Transport in Encapsulated Graphene at Room Temperature. Nano Lett. 2011;11:2396-9.

[5] Late DJ, Ghosh A, Subrahmanyam KS, Panchakarla LS, Krupanidhi SB, Rao CNR. Characteristics of field-effect transistors based on undoped and B- and N-doped few-layer graphenes. Solid State Commun. 2010;150:734-8.

[6] Iqbal MZ, Siddique S, Iqbal MW, Eom J. Formation of p-n junction with stable p-doping in graphene field effect transistors using deep UV irradiation. J Mater Chem C. 2013;1:3078-83.

[7] Rao CNR, Gopalakrishnan K, Govindaraj A. Synthesis, properties and applications of graphene doped with boron, nitrogen and other elements. Nano Today. 2014;9:324-43.

[8] Kota M, Sharmila NS, Waghmare UV, Rao CNR. Composition-dependent photoluminescence and electronic structure of 2-dimensional borocarbonitrides. Materials Research Express. 2014;1:025603.

[9] Fan X, Shen Z, Liu AQ, Kuo J-L. Band gap opening of graphene by doping small boron nitride domains. Nanoscale. 2012;4:2157-65.

[10] Zhu J, He C, Li Y, Kang S, Shen PK. One-step synthesis of boron and nitrogen-dual-self-doped graphene sheets as non-metal catalysts for oxygen reduction reaction. J Mater Chem A. 2013;1:14700-5.

[11] Wu T, Shen H, Sun L, Cheng B, Liu B, Shen J. Nitrogen and boron doped monolayer graphene by chemical vapor deposition using polystyrene, urea and boric acid. New J Chem. 2012;36:1385-91.

[12] Bepete G, Voiry D, Chhowalla M, Chiguvare Z, Coville NJ. Incorporation of small BN domains in graphene during CVD using methane, boric acid and nitrogen gas. Nanoscale. 2013;5:6552-7.

[13] Zheng Y, Jiao Y, Ge L, Jaroniec M, Qiao SZ. Two-Step Boron and Nitrogen Doping in Graphene for Enhanced Synergistic Catalysis. Angew Chem Inter Ed. 2013;52:3110-6.

[14] Kumar N, Moses K, Pramoda K, Shirodkar SN, Mishra AK, Waghmare UV, et al. Borocarbonitrides, BxCyNz. J Mater Chem A. 2013;1:5806-21.

[15] Nag A, Raidongia K, Hembram KPSS, Datta R, Waghmare UV, Rao CNR. Graphene Analogues of BN: Novel Synthesis and Properties. ACS Nano. 2010;4:1539-44.

[16] Xu B, Lu YH, Feng YP, Lin JY. Density functional theory study of BN-doped graphene superlattice: Role of geometrical shape and size. Journal of Applied Physics. 2010;108:073711.

[17] Saha S, Jana M, Khanra P, Samanta P, Koo H, Murmu NC, et al. Band Gap Engineering of Boron Nitride by Graphene and Its Application as Positive Electrode Material in Asymmetric Supercapacitor Device. ACS Applied Materials & Interfaces. 2015;7:14211-22.

[18] Li Q, Liu M, Zhang Y, Liu Z. Hexagonal Boron Nitride–Graphene Heterostructures: Synthesis and Interfacial Properties. Small. 2016;12:32-50.

[19] Ci L, Song L, Jin C, Jariwala D, Wu D, Li Y, et al. Atomic layers of hybridized boron nitride and graphene domains. Nat Mater. 2010;9:430-5.

[20] Levendorf MP, Kim C-J, Brown L, Huang PY, Havener RW, Muller DA, et al. Graphene and boron nitride lateral heterostructures for atomically thin circuitry. Nature. 2012;488:627-32.

[21] Liu Z, Ma L, Shi G, Zhou W, Gong Y, Lei S, et al. In-plane heterostructures of graphene and hexagonal boron nitride with controlled domain sizes. Nat Nano. 2013;8:119-24.

[22] Gong Y, Shi G, Zhang Z, Zhou W, Jung J, Gao W, et al. Direct chemical conversion of graphene to boron- and nitrogen- and carbon-containing atomic layers. Nat Commun. 2014;5:3193.

[23] Han GH, Rodríguez-Manzo JA, Lee C-W, Kybert NJ, Lerner MB, Qi ZJ, et al. Continuous Growth of Hexagonal Graphene and Boron Nitride In-Plane Heterostructures by Atmospheric Pressure Chemical Vapor Deposition. ACS Nano. 2013;7:10129-38.

[24] Liu L, Park J, Siegel DA, McCarty KF, Clark KW, Deng W, et al. Heteroepitaxial Growth of Two-Dimensional Hexagonal Boron Nitride Templated by Graphene Edges. Science. 2014;343:163-7.

[25] Sutter P, Huang Y, Sutter E. Nanoscale Integration of Two-Dimensional Materials by Lateral Heteroepitaxy. Nano Lett. 2014;14:4846-51.

[26] Marcano DC, Kosynkin DV, Berlin JM, Sinitskii A, Sun Z, Slesarev A, et al. Improved Synthesis of Graphene Oxide. ACS Nano. 2010;4:4806-14.

PART 3

PHYSICO-CHEMICAL STUDIES BASED ON CHEMICALLY DOPED GRAPHENES

"In this part, results of physico-chemical studies on doped graphene are presented. Boron- and nitrogen-doped graphene show interesting selectivity in photocatalytic properties in their composites with TiO2. They also show different interactions with donor and acceptor molecules."

PART 3

PHYSICO-CHEMICAL STUDIES BASED ON CHEMICALLY DOPED GRAPHENES

3.1 SELECTIVITY IN THE PHOTOCATALYTIC PROPERTIES OF THE COMPOSITES OF TiO_2 NANOPARTICLES WITH B- AND N-DOPED GRAPHENES

Summary*

In this chapter, we show the selectivity in the photocatalytic properties of TiO_2- graphene composites with boron and nitrogen doped graphenes. These TiO_2-graphene composites also show an excellent enhancement in the photocatalytic activity. We have chosen two different dyes, methylene blue (MB) and rhodamine B (RB) for the photocatalytic studies. These dyes show selectivity towards the nitrogen-doped and boron doped graphenes. Methylene blue being a good electron donor and has a low ionization energy interacts strongly with electron-deficient boron-doped graphene resulting in fast degradation of the dye. On the other hand, RB which is not such a good electron donor and has higher ionization energy interacts strongly with electron-rich nitrogen-doped graphene causing a faster degradation of the dye. Raman spectroscopy was used to understand the interaction between the dye molecules and the graphene composites. The electronic structure of graphene plays an important role in the selectivity as well as the enhancement of the photocatalytic activity.

* A paper based on this work has been published in *Chem. Phys. Lett.* 2011, **511**, 304-308

3.1.1 Introduction

As an important semiconducting material, titanium dioxide (TiO_2) has been studied and widely applied in photocatalysis due to its excellent photoelectrochemical properties, including in energy conversion [1, 2], photocatalysis involving photodegradation of organic contaminants [3] and it is widely used as a pigment, in sunscreens, paints, ointments and toothpaste [4]. The capability to utilize TiO_2 for these purposes arises from the enhanced reactivity of nanoparticulate TiO_2 compared to that of the bulk material and also it is nontoxic, easy to be made, inexpensive and chemically stable. Moreover, TiO_2 nanoparticles in the 10-50 nm range take on unusual properties and can be used in various applications, such as self-cleaning window glass, air and water purification systems. TiO_2 is a wide band-gap semiconductor and researchers are looking at it as a substitute for silicon to make solar power cells, as well as battery storage media.

In 1972, Fujishima and Honda [5] discovered that water can be split, *i.e.*, simultaneously oxidized to oxygen and reduced to hydrogen, when a bias potential is applied to an "*illuminated*" TiO_2 single crystal electrode. This remarkable discovery marked the onset of photo induced redox reactions on semiconductor surfaces. It was soon realized that such redox processes could be utilized for environmental cleanup applications, when Frank and Bard [6] in 1977, showed the photocatalytic oxidation of CN^- and SO_3^- using different semiconductor materials like TiO_2, ZnO, CdS, Fe_2O_3 and WO_3. This was followed by the demonstration of the TiO_2 catalyzed photodegradation of chlorinated organic compounds by Ollis [7] and the Pt-loaded-TiO_2 catalyzed photochemical sterilization of microorganisms by Matsunaga et al. [8] in the early 1980s. Later, O'Regan and Gratzel [9] showed the first high-efficiency solar cell based on dye-sensitized colloidal TiO_2 films for photovoltaic power generation.

Naturally occurring TiO_2 has three polymorphs, *i.e.* anatase, brookite, and rutile [10]. Although all three types of polymorphs are expressed using the same chemical formula (TiO_2), their crystal structures are different. Rutile is thermodynamically the most stable phase than anatase phase. Both of these phases show photocatalytic activity whereas the brookite phase does not. Despite the fact that the band gap values are 3.0 eV for the rutile and 3.2 eV for the anatase phases, both absorb only UV rays. Such characteristics of the rutile phase seem more suitable for use as a photocatalyst because

the rutile phase can absorb light of a wider range. However, the anatase phase exhibits higher photocatalytic activity [11]. The most prominent reasons are attributed to the difference in the energy structure between the two phase types and the surface area. In both phases, the position of the valence band is deep, and the resulting positive holes show sufficient oxidative power. Usually, the anatase crystal phase forms at lower temperatures, showing higher surface areas compared to the rutile phase. A larger surface area with a constant surface density of adsorbents leads to faster surface photocatalytic reaction rates. In this sense, the higher the specific surface area, the higher the photocatalytic activity that one can expect. Therefore, the anatase phase exhibits higher overall photocatalytic activity compared to the rutile phase. High temperature treatment usually improves the crystallinity of TiO_2 nanomaterials, which can induce the aggregation of small nanoparticles and decrease the surface area. Therefore, it is very difficult to predict the photocatalytic activities from the physical properties of TiO_2 nanomaterials.

Graphene is one of the most exciting material [12, 13] and continues to receive significant attention due to its promising applications such as nanoelectronics, supercapacitors [14] and more. Graphene has been used as a two-dimensional photocatalyst support in photocatalysis. Exfoliated graphene sheets have a theoretical surface area of ~2600 m^2/g, making graphene highly attractive as a high-surface area 2D photocatalyst support. The application of graphene in combination with TiO_2 therefore presents the opportunity to enhance photocatalytic activity. The newly developed graphene-TiO_2 nanocomposites are based on the use of graphene oxide (GO), derived by chemical oxidation of graphene. Zhang et al [15] have hydrothermally synthesized GO-TiO_2 composite and assessed photocatalytic activity via the degradation of methylene blue. Photocatalytic activity was found to be higher than that of TiO_2 alone, or CNT-TiO_2 composites with the same carbon content. The enhancement was ascribed to the two-dimensional planar graphene structure favouring dye absorption, and suppressed electron–hole recombination due to the high electrical conductivity. Enhancement was also attributed to extension of light absorption to longer wavelengths in the visible range due to the high transparency and band-gap narrowing resulting from the presence of Ti–O–C bonds.

3.1.2 Scope of the present investigations

Selective photocatalysis is an interesting field with potential applications in organics separation as well as selective degradation. Most studies of the TiO_2-graphene composites have concentrated on electron transfer between TiO_2 and graphene oxide or graphene although there are indications that the electronic structure of the nanocarbons may play a crucial role in the photocatalysis. We considered it important to examine the nature of interaction of graphene with TiO_2 as well as with adsorbed molecules to understand the photocatalytic properties. Since the electronic properties of graphene can be conveniently tuned chemically by doping with nitrogen and boron, thereby changing the effective band gap of the composites, we have investigated the photocatalytic properties of TiO_2 by using chemically doped graphenes as supports. With this purpose, we have studied the interaction of TiO_2 nanoparticles with B- and N-doped graphenes and also the interaction of the graphenes with two dye molecules possessing widely different electron-donating abilities or ionization energies. The molecules investigated are methylene blue (I) and rhodamine B (II), the former with a very low ionization energy of 5.3 eV. Rhodamine B has an ionization energy of 6.7 eV. It was felt that the study would show whether the photodegradation of these dye molecule by the TiO_2-graphene composites depends on the electronic properties of graphene.

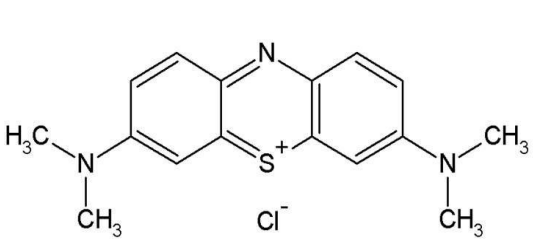

I

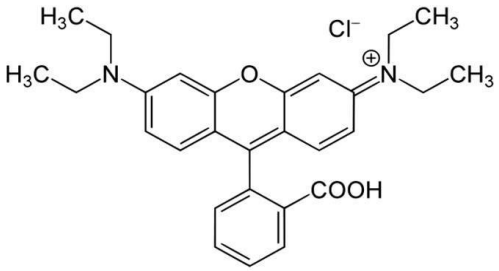

II

3.1.3 Experimental Section

Synthesis of graphene and doped graphenes: Graphene with 2-4 layers (HG) was prepared by arc-discharge in the presence of hydrogen (200 Torr) and helium (500 Torr)

[16]. Boron-doped graphene (BG) was prepared by carrying out the arc-discharge using boron-packed graphite electrodes (3 at. % Boron) in the presence of H_2 (200 Torr) and He (500 Torr) [17].Nitrogen-doped graphene (NG) was prepared by carrying out arc-discharge of graphite in the presence of H_2 (200 Torr), He (200 Torr), and NH_3 (300 Torr).

Acidification of graphene and doped graphene: 2 mg of graphene was added to a mixture of 1.6 mL of conc. sulphuric acid, 1.6 mL conc. nitric acid and 3.5 mL of distilled water. The mixture was sonicated for 10 min and transferred to a teflon lined autoclave and treated under microwave irradiation at 600 W for 20 min. The graphene samples so obtained were washed several times with distilled water to remove excess acid.

Synthesis of TiO_2 nanoparticles: TiO_2 nanoparticles were prepared as follows. In a typical reaction, a solution of ethanol (25 mL) and water (2.5 mL) was heated to 80 °C with constant stirring. A mixture of 0.18 mL titanium orthobutoxide and 0.045 ml H_2SO_4 in 5 mL ethanol was added to the above solution. The resulting mixture was kept stirring at 80 ^oC for 12 h. The reaction mixture was then cooled down to room temperature and the solid was collected by centrifugation and washed with distilled water. In the second step of the synthesis, the washed solid was dispersed in water/DMF (12 mL/0.3 mL). The suspension was transferred to a 25 mL teflon-lined stainless steel autoclave for hydrothermal reaction at 180 °C for 16 h. The final product was collected by centrifugation and washed with distilled water. The nanoparticles were examined by electron microscopy.

Synthesis of TiO_2-Graphene nanocomposites: Composites of TiO_2 with undoped graphene (TG), with N-doped graphene (TNG) and with B-doped graphene (TBG) were prepared by the procedure described by Dai et al [18]. In a typical reaction, 1.8 mg of acidified graphene (same for doped graphene) was dispersed in EtOH/water (25 mL/2.5 mL) mixture. The suspension was heated to 80 °C with stirring. Mixture of 0.18 mL titanium orthobutoxide and 0.045 mL of H_2SO_4 in 5 mL ethanol was added to above solution. The resulting mixture was kept stirring at 80 ^oC for 12 h. The reaction mixture was cooled to room temperature, the solid collected by centrifugation and washed with distilled water. In the second step of the synthesis, the washed solid was dispersed in water/DMF (12 mL/0.3 mL). The suspension was transferred to a 25 mL teflon-lined

stainless steel autoclave for hydrothermal treatment at 180 °C for 16 h. The final composite material was collected by centrifugation and washed with distilled water.

Photocatalytic study: Photodegradation kinetics were studied as follows. In a typical kinetic study, 4 mg of photocatalyst (TiO_2, TG, TNG and TBG) was suspended in 10 mL of 0.015 mmol/L aqueous solution of rhodamine B (RB) or methylene blue (MB). The resulting suspension was sonicated for 10 min followed by 10 min stirring to allow sufficient mixing. Under constant stirring conditions, the mixture RB (or MB) with the photocatalyst was irradiated with a 120 W high pressure mercury lamp which was positioned 30 cm away from the quartz vessel (see Figure 1). Samples were collected after regular intervals and the changes in concentration of the organic dye were monitored by measuring UV-Vis absorption spectra. The collected samples were centrifuged for 5 min to remove the TiO_2 or TiO_2-graphene composites before UV-Vis measurements. The peak maximum of rhodamine B (at 553 nm) was used to determine dye concentration. Photodegradation of methylene blue was conducted in a similar way by using 10 mL portions of a 0.015 mmol/L aqueous solution of methylene blue and 4 mg suspension of TiO_2 and other composite materials. The absorption maximum of methylene blue was at 655 nm.

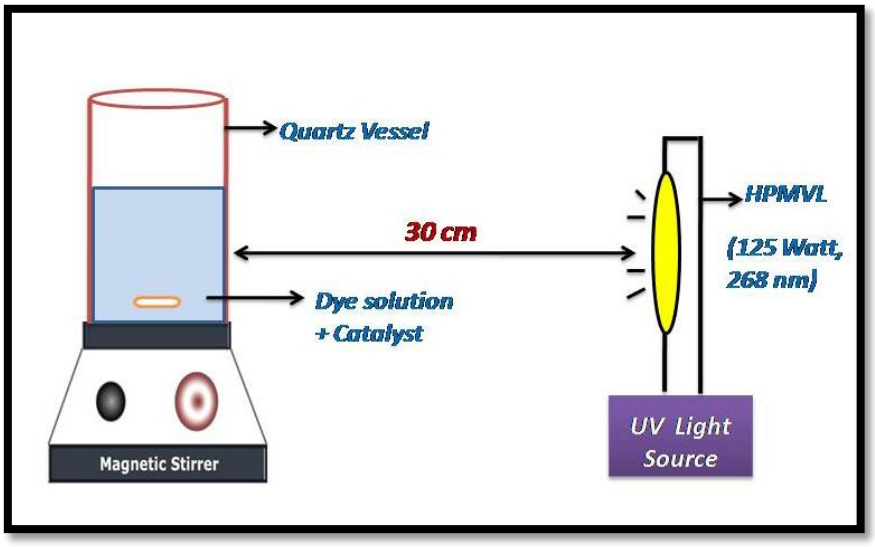

Figure 1. Design of the photocatalytic reactor used for photocatalytic study

3.1.4 Results and Discussion

A typical FESEM image of the as-synthesized TiO_2 nanoparticles and TiO_2-graphene composites is shown in Figure 2. It can be observed from the SEM image that the graphene sheets are covered with TiO_2 nanoparticles. The TEM images also present the morphology of the composites, wherein the graphene sheets are decorated with TiO_2 particles. The TiO_2 particles exhibit a narrow size distribution with an average size of 15 nm. The good distribution of TiO_2 particles on graphene will benefit the photocatalysis.

The X-Ray diffraction pattern of the TiO_2 nanoparticles could be indexed on the anatase structure (a=3.7852Å, c= 9.5139Å, JCPDS 21-1272). The TiO_2 nanoparticles in the composite with graphene also had the anatase structure with presented peak intensities (101), (004), (105), and (211) (see Figure 3).

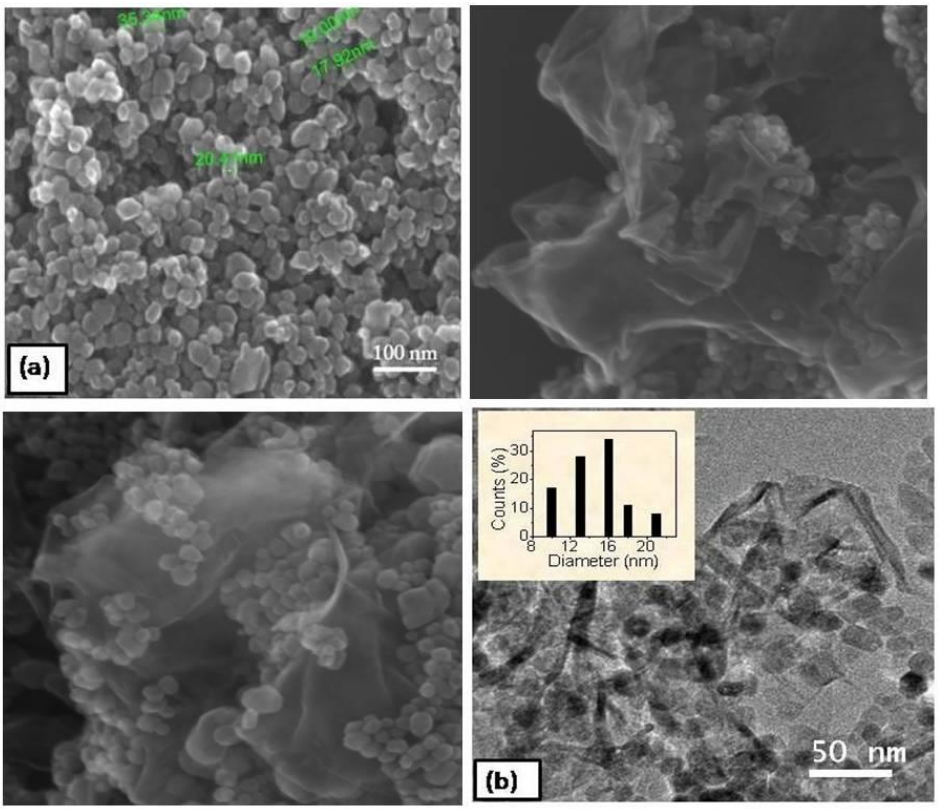

Figure 2. (a) FESEM images of TiO_2, TG and TBG and (b) TEM image of TG composite.

Raman spectroscopy is known to be a sensitive tool for characterizing TiO_2, graphene and its interaction with other molecules. The anatase phase of TiO_2 was

evidenced from Raman spectroscopy. We show the typical Raman spectra of TiO_2 and TiO_2-graphene composites in Figure 4(a). We observed four peaks at the low frequency region for both TiO_2 and TiO_2-graphene composites and are assigned to the E_{1g} (149 cm^{-1}), B_{1g} (398 cm^{-1}), A_{1g} (516 cm^{-1}) and E_g (637 cm^{-1}) modes of anatase phase respectively.

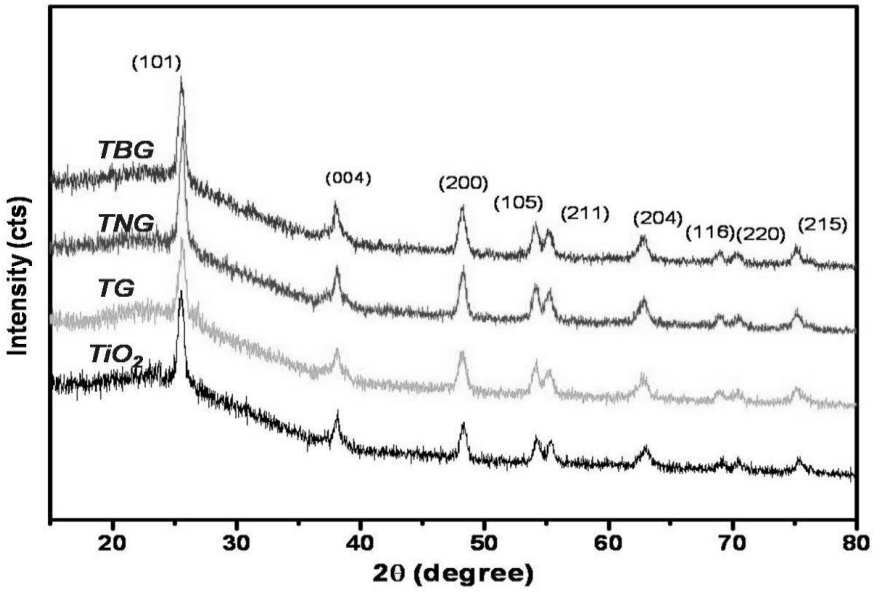

Figure 3. XRD patterns of (a) TiO_2 (b) TG (c) TNG (d) TBG.

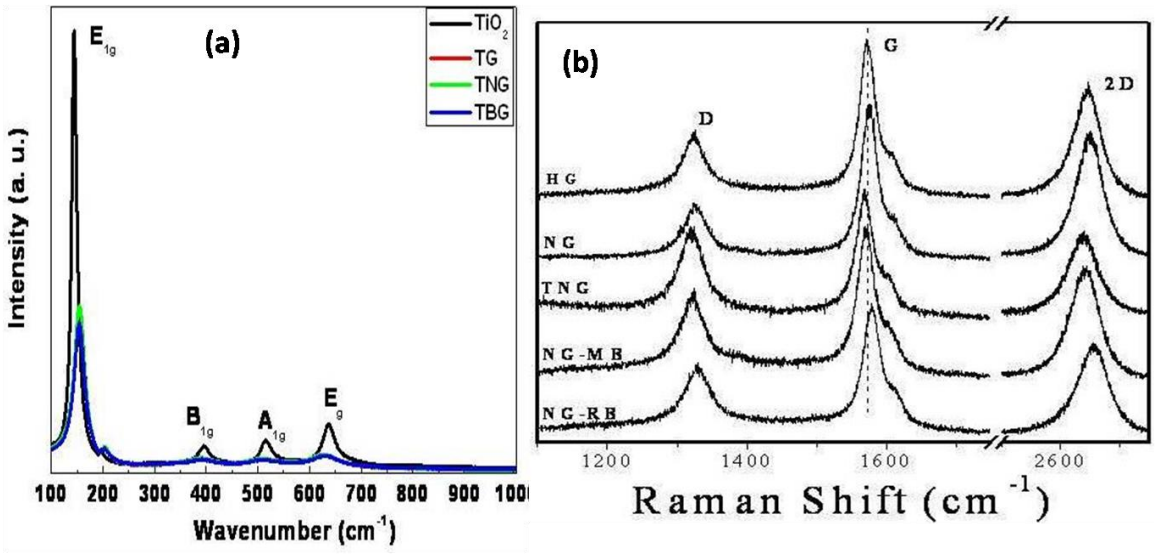

Figure 4 (a) Raman spectra for TiO_2 nanoparticles with pure and doped graphenes (b) Raman Spectra of G, NG, TNG, NG-MB and NG-RB.

Table 1. Raman data of the graphenes, TiO_2-graphene composites and graphene-dye adducts.

Sample	G Band (cm^{-1})	2D Band (cm^{-1})	I_{2D}/I_G
HG	1572	2645	0.73
TG	1569	2640	0.55
NG	1574	2649	0.66
TNG	1569	2638	0.66
BG	1581	2647	0.10
TBG	1574	2641	0.15
G-RB	1570	2643	0.70
NG-RB	1580	2663	0.70
BG-RB	1583	2652	0.09
G-MB	1573	2646	0.61
NG-MB	1571	2443	0.76
BG-MB	1587	2614	0.17

The Raman G-band, characteristic of the sp^2 carbon network, and the defect-related 2D band are especially useful in examining effects of doping and charge-transfer interactions. In Figure 4(b), we show typical Raman spectra and list the important Raman results in Table 1. Some interesting conclusions can be drawn regarding the interaction of graphene with TiO_2 and with the dye molecules on the basis of the changes in the Raman G and 2D bands. The effect of doping graphene with boron and nitrogen is to shift the Raman G-band slightly to a higher frequency. The ratio of the intensity of the 2D band with respect to that of the G-band, I_{2D}/I_G, decreases on B- and N-doping. On depositing TiO_2 nanoparticles on the graphene samples, the G-band frequency decreases in both the doped and the undoped cases (see Table 1). The I_{2D}/I_G ratio remains around the same value or decreases slightly in the composites. Interaction of rhodamine B (RB) and methylene blue (MB) with the graphene samples causes interesting changes in the G band (see Figure 4(b) and Table 1).

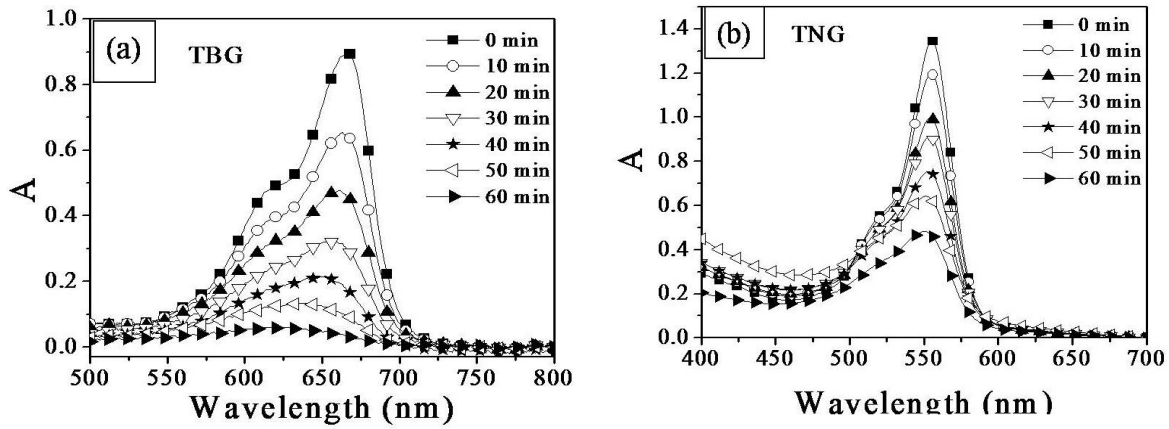

Figure 5. Changes in absorption spectra of (a) methylene blue and (b) rhodamine B deposited on TBG and TNG, respectively, on irradiation.

The most important observation with regard to the interaction of the dye with graphene from this study is that there is a substantial increase in the G-band frequency of N-doped graphene (NG) on interaction with RB, with the changes in the G-bands of HG and BG being marginal. In the case of MB, the largest shift in the G-band frequency is found in the case of B-doped graphene (BG). We also observe significant changes in the 2D band. Thus, the frequency of the 2D band of NG increases on interaction with RB whereas changes in the case of HG and BG are marginal. The 2D band frequency of BG decreases on interaction with MB and the changes in the HG and NG are marginal. These shifts in the G and 2D bands are significant, whereas methylene blue which is a good electron donor with low ionization energy interacts more with the p-type graphene, BG. On the other hand, Rhodamine B with a higher ionization energy interacts strongly with the n-type graphene, NG. Photocatalytic activities of pure TiO_2 and of the composites of TiO_2 with HG, BG and NG were investigated in the case of rhodamine B and methylene blue by making use of the changes in electronic absorption spectra of the dyes with respect to time.

In Figure 5 (a,b), we show typical changes in the absorbance of the dyes on irradiation with respect to time. Photodegradation of these dyes appears to follow the Langmuir-Hinshelwood reaction kinetics, which predicts an exponential decrease in the concentration of the dye molecule as a function of time. We have examined the change in the concentration (C/C_0) of the dyes with reaction time. In Figure 6(a), we show the time

variation of C/C_0 of methylene blue. We notice that the degradation rate varies as TBG > TNG > TG > TiO_2. In Figure 7(a), we show the time variation of C/C_0 of rhodamine B. The degradation rate varies as TNG > TBG > TG > TiO_2.

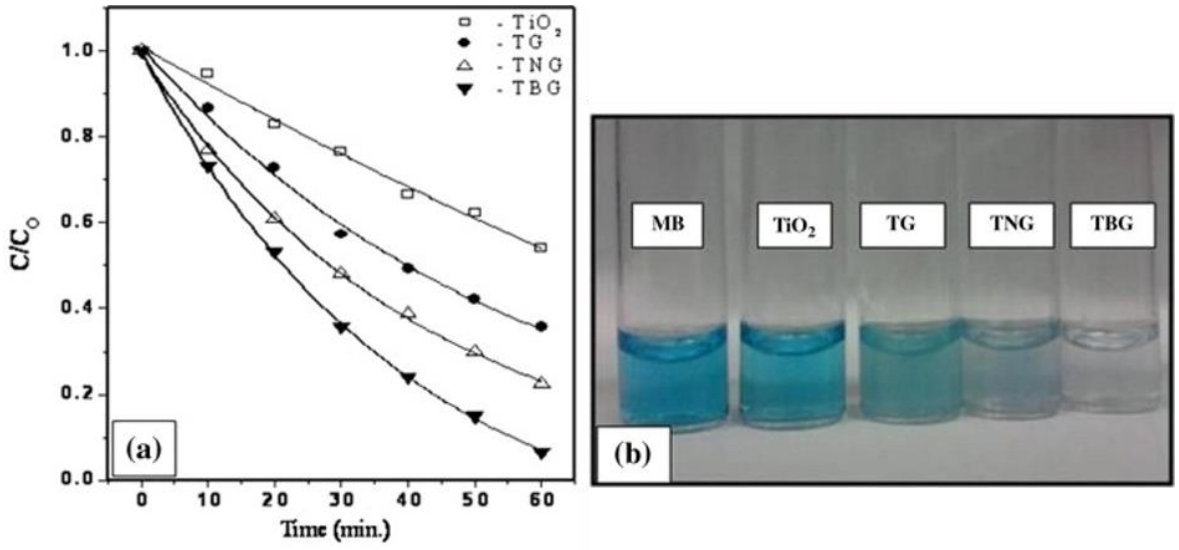

Figure 6. (a) Photocatalytic degradation of methylene blue monitored as the variation of normalized concentration with the irradiation time in the presence of TiO_2, TG, TNG and TBG. (b) Photographs showing color variation after 1 h.

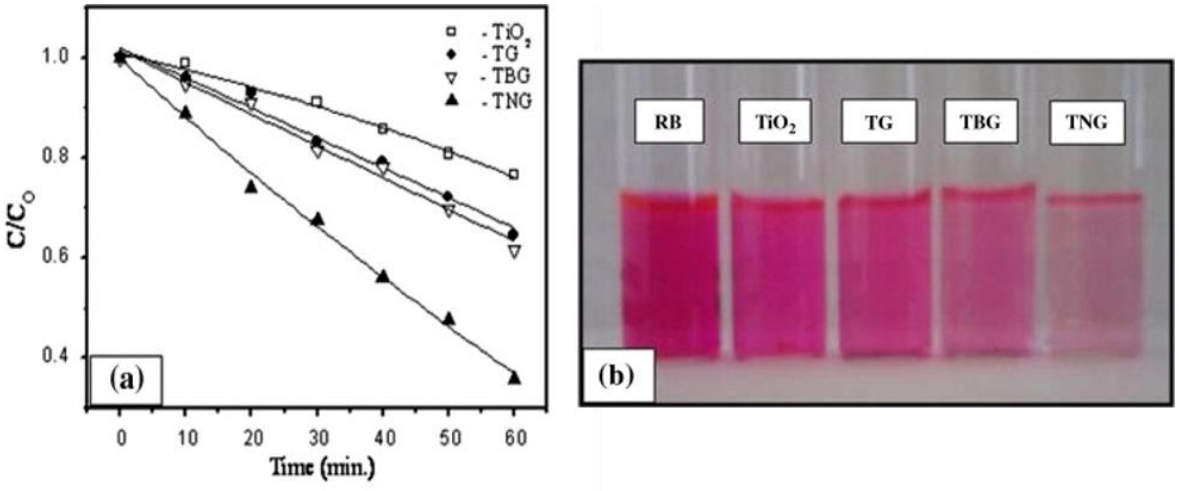

Figure 7. (a) Photocatalytic degradation of rhodamine B monitored as the variation of normalized concentration with the irradiation time in the presence of TiO_2, TG, TBG and TNG. (b) Photographs showing color variation after 1 h.

We have shown the photographs of the dye solutions after 1h of irradiation in Figure 6(b) and 7(b). The photographs clearly show how TBG is more effective with MB and TNG with RB. Electron-poor TBG is selective in the degradation of MB because of the higher electron-donating ability of this dye. Similarly, electron-rich TNG is selective in the degradation of RB which is not a good electron donor. The effectiveness TBG in the photodegradation of MB can be understood on the basis of the strong interaction between the two as inferred from Raman spectra. The same is true for the effectiveness of TNG in the case of RB.

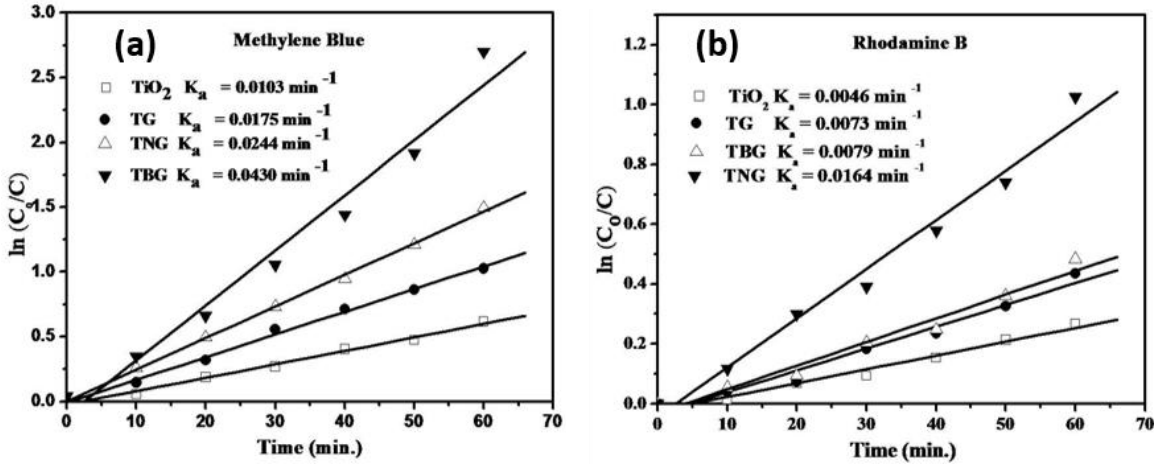

Figure 8. ln(C_0/C) versus irradiation time for TiO_2 and its composites with graphene for (a) Methylene blue and (b) Rhodamine B

The kinetics of the degradation reaction are fitted to a pseudo first order reaction at low dye concentrations: $\ln(C_0/C) = k_a t$, where k_a is the apparent rate constant, C_0 is the initial concentration of the reactant. Under the conditions of the experiments we used here, the initial concentration of methylene blue, C_0, is 0.015 mmol/L, which is very small. The $\ln(C_0/C)$ vs t curves for TiO_2 and its composites with graphene for methylene blue and rhodamine B are plotted in Figure 8 (a) and (b) respectively. The linearity of the curves indicates that the kinetics for the photocatalytic decomposition of MB and RB follows a pseudo first order rate. The rate constant of TiO_2 is smaller when compare to its graphene composites. In methylene blue case, the values of k_a for the TiO_2, TG, TNG, TBG are 0.010, 0.018, 0.024, 0.043 min^{-1} respectively. The value of k_a for the TBG is found to be more than four times that of TiO_2. In rhodamine B case, the value of k_a for the TiO_2,

TG, TNG, TBG are 0.005, 0.0073, 0.016, 0.008 min^{-1} respectively. The value of k_a for the TNG is found to be nearly three times that of TiO_2.

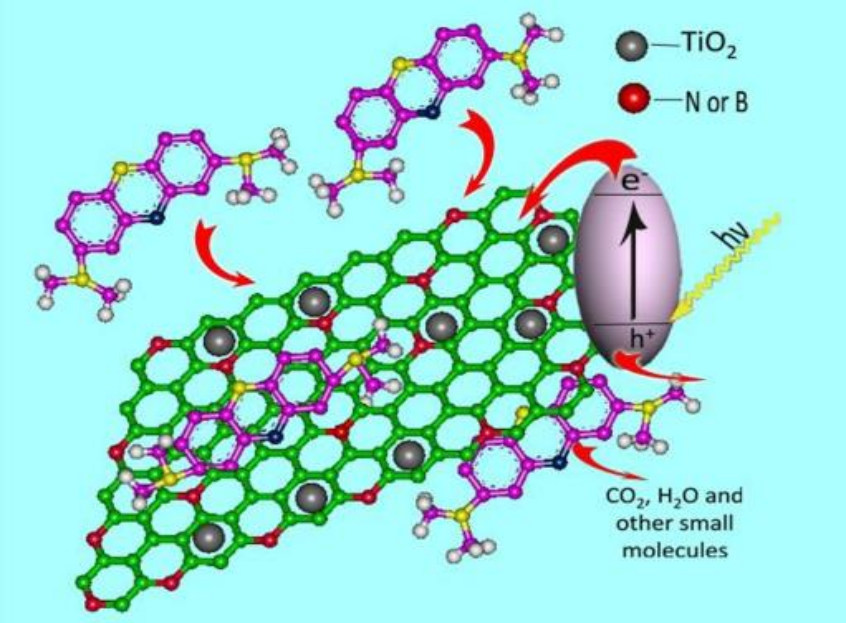

Scheme I. Structure of TiO_2- doped graphene and tentative processes of the photodegradation of methylene blue (MB) over TiO_2- doped graphene

3.1.5 Conclusions

The present study clearly establishes selectivity in the interaction of dyes with chemically doped graphenes and the photodegradation of the dyes catalyzed by the TiO_2 nanoparticles present on the graphene surface. The mechanism is likely to involve the photoexcitation of electrons in the TiO_2 nanoparticles followed by their transfer to graphene (see Scheme I). The adsorbed dye molecules interact with graphene using π-π and charge transfer interaction. Accordingly, a dye which is a good electron donor (MB in present case) interacts more strongly with hole-doped graphene (BG), while a dye which is a poorer electron donor interacts more strongly with electron-doped graphene (NG). This selective interaction is reflected in the photodegradation kinetics as well, since photodegradation occurs through the electrons transferred to graphene from TiO_2. The electronic structure of graphene, therefore, plays a significant role in the photodegradation kinetics.

References

[1] Bard AJ. Design of semiconductor photoelectrochemical systems for solar energy conversion. J Phys Chem. 1982;86:172-7.

[2] Kalyanasundaram K, Grätzel M, Pelizzetti E. Interfacial electron transfer in colloidal metal and semiconductor dispersions and photodecomposition of water. Coord Chem Rev. 1986;69:57-125.

[3] Turchi CS, Ollis DF. Photocatalytic degradation of organic water contaminants: Mechanisms involving hydroxyl radical attack. J Catalysis. 1990;122:178-92.

[4] Pfaff G, Reynders P. Angle-Dependent Optical Effects Deriving from Submicron Structures of Films and Pigments. Chem Rev. 1999;99:1963-82.

[5] Fujishima A, Honda K. Electrochemical Photolysis of Water at a Semiconductor Electrode. Nature. 1972;238:37-8.

[6] Frank SN, Bard AJ. Heterogeneous photocatalytic oxidation of cyanide and sulfite in aqueous solutions at semiconductor powders. J Phys Chem. 1977;81:1484-8.

[7] Pruden AL, Ollis DF. Photoassisted heterogeneous catalysis: The degradation of trichloroethylene in water. J Catalysis. 1983;82:404-17.

[8] Matsunaga T, Tomoda R, Nakajima T, Wake H. Photoelectrochemical sterilization of microbial cells by semiconductor powders. FEMS Microbio Lett. 1985;29:211-4.

[9] O'Regan B, Gratzel M. A low-cost, high-efficiency solar cell based on dye-sensitized colloidal TiO2 films. Nature. 1991;353:737-40.

[10] Diebold U. The surface science of titanium dioxide. Surf Sci Rep. 2003;48:53-229.

[11] Herrmann J-M. Heterogeneous photocatalysis: state of the art and present applications In honor of Pr. R.L. Burwell Jr. (1912–2003), Former Head of Ipatieff Laboratories, Northwestern University, Evanston (Ill). Top Cat. 2005;34:49-65.

[12] Rao CNR, Sood AK, Subrahmanyam KS, Govindaraj A. Graphene: The New Two-Dimensional Nanomaterial. Angewandte Chemie International Edition. 2009;48:7752-77.

[13] Geim AK, Novoselov KS. The rise of graphene. Nat Mater. 2007;6:183-91.

[14] Vivekchand SRC, Rout CS, Subrahmanyam KS, Govindaraj A, Rao CNR. Graphene-based electrochemical supercapacitors. Journal of Chemical Sciences. 2008;120:9-13.

[15] Zhang H, Lv X, Li Y, Wang Y, Li J. P25-Graphene Composite as a High Performance Photocatalyst. ACS Nano. 2010;4:380-6.

[16] Subrahmanyam KS, Panchakarla LS, Govindaraj A, Rao CNR. Simple Method of Preparing Graphene Flakes by an Arc-Discharge Method. J Phys Chem C. 2009;113:4257-9.

[17] Panchakarla LS, Subrahmanyam KS, Saha SK, Govindaraj A, Krishnamurthy HR, Waghmare UV, et al. Synthesis, Structure, and Properties of Boron- and Nitrogen-Doped Graphene. Adv Mater. 2009;21:4726-30.

[18] Liang Y, Wang H, Sanchez Casalongue H, Chen Z, Dai H. TiO2 nanocrystals grown on graphene as advanced photocatalytic hybrid materials. Nano Res. 2010;3:701-5.

3.2 A RAMAN STUDY OF THE INTERACTION OF ELECTRON-DONOR AND -ACCEPTOR MOLECULES WITH CHEMICALLY DOPED GRAPHENE

Summary*

Effect of interaction of tetracyanoethylene (TCNE) and tetrathiafulvalene (TTF) with boron- and nitrogen-doped graphene has been investigated by Raman spectroscopy. The G- and 2D bands of boron- and nitrogen-doped graphenes in the Raman spectra show significantly different changes on interaction with electron-donor and -acceptor molecules. Thus, tetracyanoethylene (TCNE) and tetrathiafulvalene (TTF) have different effects on the Raman spectra of boron- and nitrogen-doped graphenes. The changes in the Raman spectra brought about by electron-donor and -acceptor molecules can be understood in general terms on the basis of molecular charge transfer.

*A Paper based on this work has been published in J Mol. Struct. 2012, **1023**, 2-6.

3.2.1 Introduction

Graphene, the mother of all graphitic materials exhibits a number of exciting physical properties, previously not observed at nanoscale [1, 2]. In particular, the band structure of graphene exhibits two intersecting bands at two in-equivalent K points in the reciprocal space, and its low energy excitations are massless Dirac fermions near these K points because of the linear energy momentum dispersion relationship [3]. This results in very high electron mobility in graphene, which can be further improved significantly, even up to $\sim 10^5$ $cm^2/V.s$ [4]. Electron or hole transport in field-effect devices based on graphene can be controlled by an external electric field [4]. Park et al [5] demonstrated theoretically that the chiral massless Dirac fermions of graphene propagate anisotropically in a periodic potential, which suggests the possibility of building graphene based electronic circuits . Graphene-based devices can be expected to have many advantages over silicon-based devices [2]. However, precise control of the carrier type and concentration in graphene is not easy. Up to now, most of the graphene samples were either deposited on a SiO_2 surface or grown on a SiC surface, and these epitaxial graphenes are usually electron doped by the substrate [6]. To control the n-type carrier concentration in the graphene, alkali metal atoms have been deposited on graphene [7]. The single, open-shell NO_2 molecule is found to be a strong acceptor, whereas its equilibrium gaseous state N_2O_4 acts as a weak dopant and does not result in any significant doping effect [8]. Thus, it is desirable and crucial to develop new method to precisely control the carrier type and concentration in graphene for further development of graphene-based nanoelectronics.

Raman spectroscopy has emerged as an effective probe to characterize graphene sample in terms of the number of layers and their quality [9, 10]. Single-layer graphene shows the well-known G-band characteristic of the sp^2 carbon network around 1580 cm^{-1}. The D band around 1350 cm^{-1} and D' band around 1620 cm^{-1} are defect induced. The 2D band at $\sim$2680 cm^{-1} differs in single and few-layer graphene and can be understood on the basis of the double resonance Raman process involving different electronic dispersion. The 2D band can be employed to determine the number of layers in few-layer graphene. By combining Raman experiments with *in-situ* transport measurements of

graphene in field-effect transistor geometry, it has been shown that the G-modes of single- and bi-layer graphenes blue shift on doping with electron as well as holes. On the other hand, the 2D band blue-shifts on hole doping whereas it red shifts on doping with electrons [11, 12]. The relative intensity of the 2D band is quite sensitive to doping. Theoretical calculations based on time-dependent perturbation theory have been employed to explain the observed shifts of the G-band. Comparison between theory and experiment, however, is not entirely satisfactory at high doping levels ($>1x10^{13}/cm^2$) and the disagreement is greater for the 2D band.

Graphene is near nearly semi-metal, whose extreme physical strength and electron mobility at room temperature result from extensive electron conjugation and delocalization [13]. Charge-transfer to and from adsorbed species can shift the graphene Fermi level by a large fraction of an electron volt [14]. Such adsorption-induced chemical doping adjusts the Fermi level without introducing substitutional impurities, or basal plane reactions, that interrupt the conjugated network. Adsorption induced chemical doping may well become an important aspect of future graphene technologies [15]. In graphene, consisting of only a few-layers, chemical doping can result from both surface adsorption and intercalation between layers. Organic molecules containing aromatic π-systems can be used to solubilize and modify the electronic structure of graphene. Charge-transfer with coronene tetracarboxylate (CT) has been exploited recently to solubilize graphene sheets [16]. It is shown that the CT molecules help to exfoliated few-layer graphene and selectively solubilize single- and double- layer graphenes. Graphene quenches the fluorescence of aromatic molecules, probably due to the electron transfer, feature of possible use in photovoltaics. Charge-transfer from fluorescent molecules to graphene has been utilized in visualization of graphene sheets by fluorescence microscopy [17] and in the use of graphene as a substrate for resonance Raman spectroscopy [18]. This chapter describes our efforts towards understanding the effect of electron-donor and acceptor molecules on the electronic structure of doped graphenes.

3.2.2 Scope of the present investigations

Nanocarbons are receiving great attention in the last few years due to their fascinating properties. Among the nanocarbons, graphene have emerged as frontier areas of research, specially because of the novel electronic properties. The electronic structure of graphene can be modified by electrochemical doping, chemical doping and doping through molecular charge transfer. Doping holes and electrons in graphene affects the Raman spectra markedly [19]. The Raman G-band which corresponds to the tangential mode is highly sensitive to changes in the electronic structure of graphene. The G-band has been shown to stiffen and soften on interaction with electron-acceptor and electron-donor molecules respectively. The intensity and position of the Raman 2D band are also sensitive to doping. Recent studies have demonstrated that electron-donating molecules such as tetrathiafulvalene (TTF) and electron-withdrawing molecules such as tetracynoethylene (TCNE) bring about significant changes in the Raman spectra of graphene due to charge-transfer effects. Since the interaction of electron-donating molecules corresponds to electron-doping while interaction with electron-withdrawing molecules corresponds to hole doping, we considered it important to investigate the effect of electron-donor and electron-acceptor molecules on the Raman spectra of boron- and nitrogen-doped graphene which correspond to p- and n-type graphene respectively.

3.2.3 Experimental section

Synthesis of few-layer graphene: Few-layer graphene (HG) was prepared by the arc evaporation of graphite in a water-cooled stainless steel chamber filled with a mixture of hydrogen (200 Torr) and helium (500 Torr) without using any catalyst [20]. In a typical experiment, a graphite rod (Alfa Aesar with 99.999% purity, 6 mm in diameter and 50 mm long) was used as the anode and another graphite rod (13 mm in diameter and 60 mm in length) was used as the cathode. The discharge current was in the 100-150 A range, with a maximum open circuit voltage of 60 V. The graphene obtained by this method contains 2-4 layers.

Synthesis of doped graphenes: Boron-doped graphene (BG) was prepared by carrying out the arc-discharge using boron-packed graphite electrodes (3 at. % Boron) in the

presence of H_2 (200 Torr) and He (500 Torr) [21]. Nitrogen-doped graphene (NG) was prepared by carrying out arc-discharge of graphite in the presence of H_2 (200 Torr), He (200 Torr), and NH_3 (300 Torr) [21]. The boron and nitrogen contents in the doped graphene samples were approximately 3 and 1 at. % respectively as estimated by X-ray photoelectron spectroscopy and electron energy loss spectroscopy. The number of layers of the doped graphene samples was 2-4 as determined by atomic force microscopy.

3.2.4 Results and Discussion

We have prepared boron-doped graphene (BG) by arc-discharge between two graphite electrodes was carried out where one of the electrodes was filled with elemental boron. The B-doped graphene sample so obtained also contained 2–4 layers [21]. We prepared nitrogen-doped (NG) graphene with 2–4 layers by carrying out arc discharge in the presence of H_2 + ammonia [21]. The samples were characterized Raman spectroscopy (Figure 1a), transmission electron microscopy and atomic force microscopy (Figure 1b) as described in the literature[21].

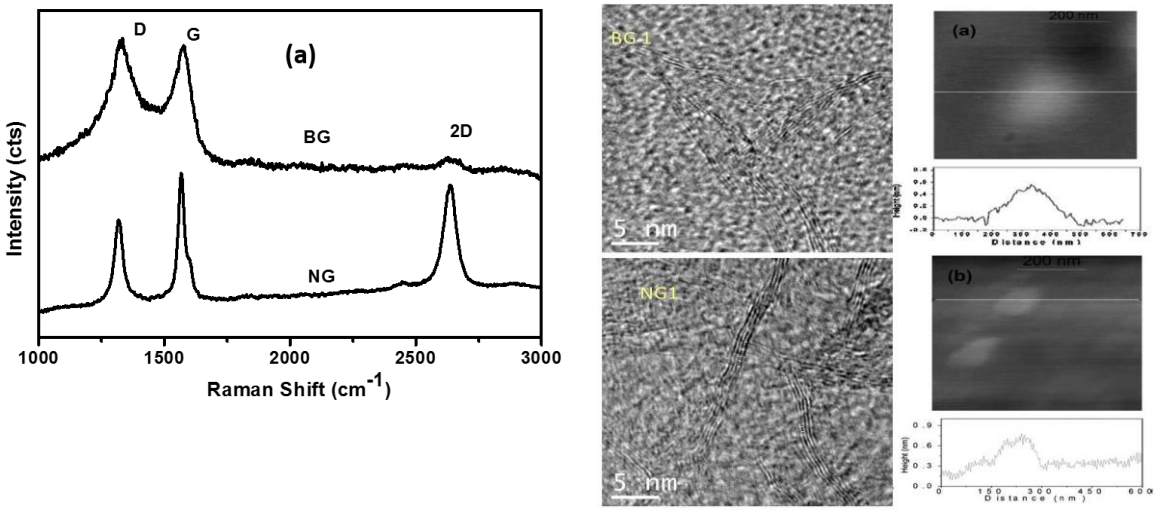

Figure 1. (a) Raman spectra of boron-doped (BG) and nitrogen-doped graphene (NG) (b) TEM images of boron- doped graphene (BG) and nitrogen-doped graphene (NG). AFM images of these samples are shown alongside

In Figure 2(a) we show the effect of interaction of TCNE and TTF on the Raman G-band of undoped graphene. The G-band is not affected in the absence of dopants. In Figure 2(b), we plot the shifts of the G-band on interaction of TCNE and TTF with

undoped graphene. We see that TCNE causes greater shift of the G-band than TTF though in the opposite direction. The stiffening of BG is slightly smaller than in pure graphene.

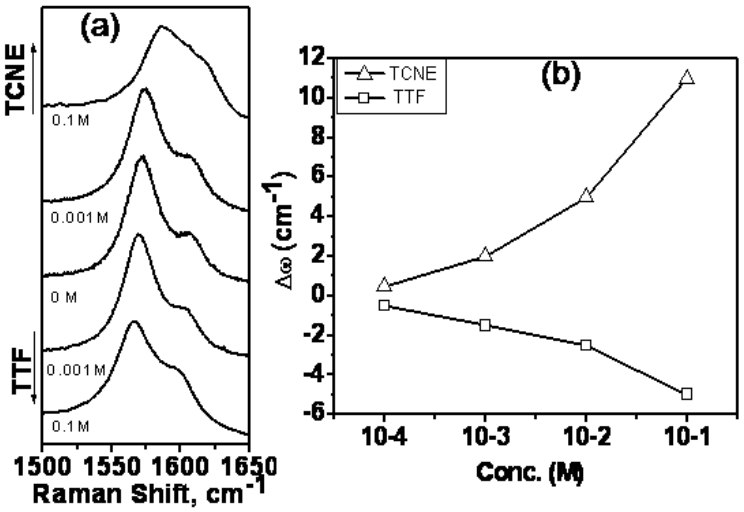

Figure 2. (a) Raman G-band of undoped graphene caused by interaction with TCNE and TTF (b) plots of the G-band shifts against concentrations of TCNE and TTF.

In Figure 3 we show typical Raman spectra of NG and BG and the effect of TCNE and TTF on the Raman bands. BG shows the Raman G-band at 1581 cm^{-1} and the 2D band at 2636 cm^{-1}. NG shows the G-band at 1574 cm^{-1} and the 2D band at 2648 cm^{-1}. We first examine the interaction of BG with TTF and TCNE.

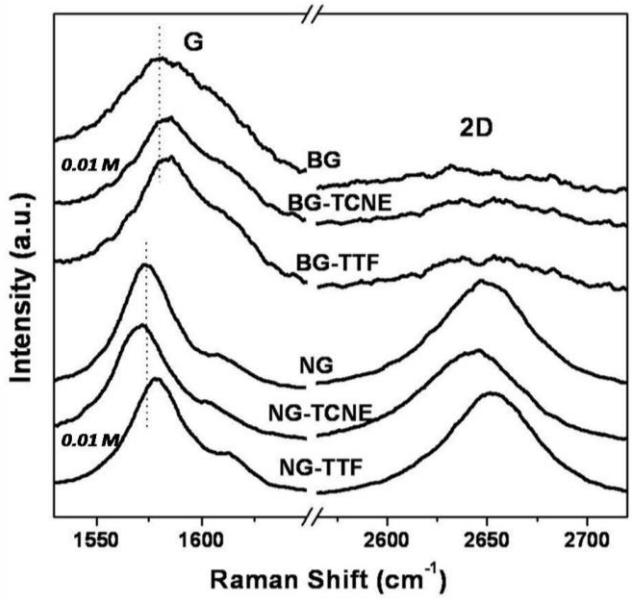

Figure 3. Raman spectra of NG and BG and the effect of TCNE and TTF on the Raman G and 2D bands

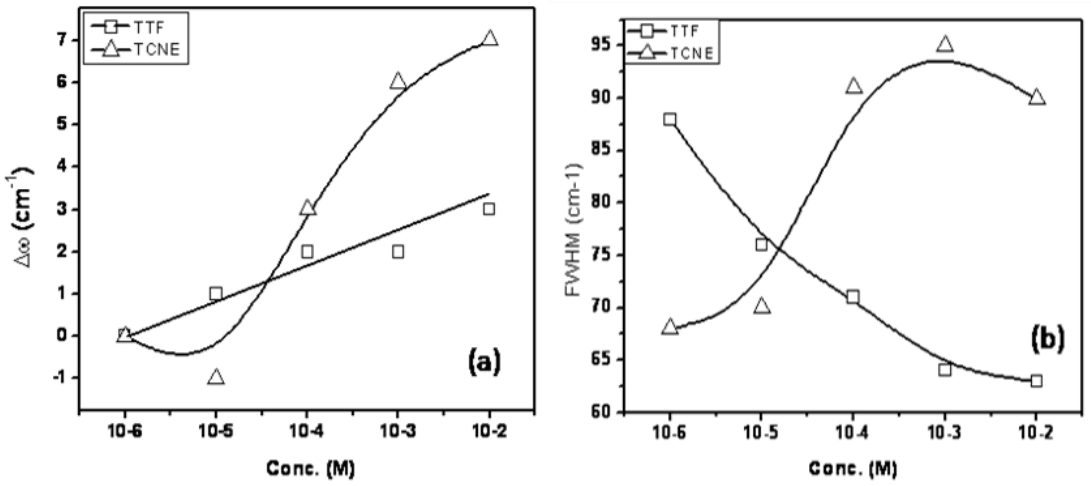

Figure 4. (a) Raman shifts of the G-band of BG on interaction with varying concentrations of TTF and TCNE. (b) Change in the FWHM of G-band with the concentration of TTF and TCNE. The curves are drawn as guides to the eye.

In Figure 4(a) we show the effect of concentration of TTF and TCNE on the Raman G-band of BG. We observe a significant shift of the G-band to higher frequencies on interaction with TCNE. Doping holes through interaction with TCNE stiffens the G-band significantly in the case of B-doped graphene just as in the case of undoped graphene. Since TTF donates electrons, the G-band shift is negligible. In Figure 4(b), we show the variation of the full-width at half maximum (FWHM) of the G-band on interaction with TTF and TCNE with BG. We see that the FWHM increases with the increase in the concentration of TCNE while there is decrease in FWHM with increase in TTF concentration. Thus, the concentration dependence of the FWHM shows opposite trends in the case of electron-donor and -acceptor molecules.

In Figure 5(a) we show the effect of concentration of TTF and TCNE on the 2D band position of BG. There is greater softening of the 2D band in the case of TTF compared to that found with TCNE. In Figure 5(b), we plot the ratio of the intensity of the 2D band with respect to that of the G-band, I_{2D}/I_{G}, as a function of concentration of TTF and TCNE. It is well documented that I_{2D}/I_{G} ratio is sensitive to doping [11]. TCNE has negligible effect on the I_{2D}/I_{G} ratio while there is a measurable decrease at moderate concentrations of TTF.

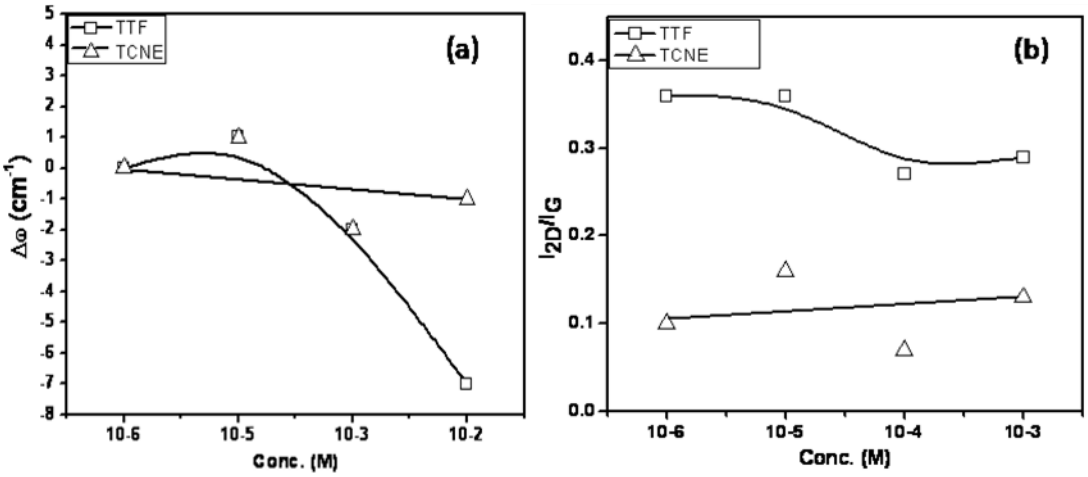

Figure 5. (a) Raman shifts of the 2D band of BG on interaction with varying concentrations of TTF and TCNE. (b) Ratio of the relative intensities of the 2D and G-bands with varying the concentration of TTF and TCNE. The curves are drawn as guides to the eye.

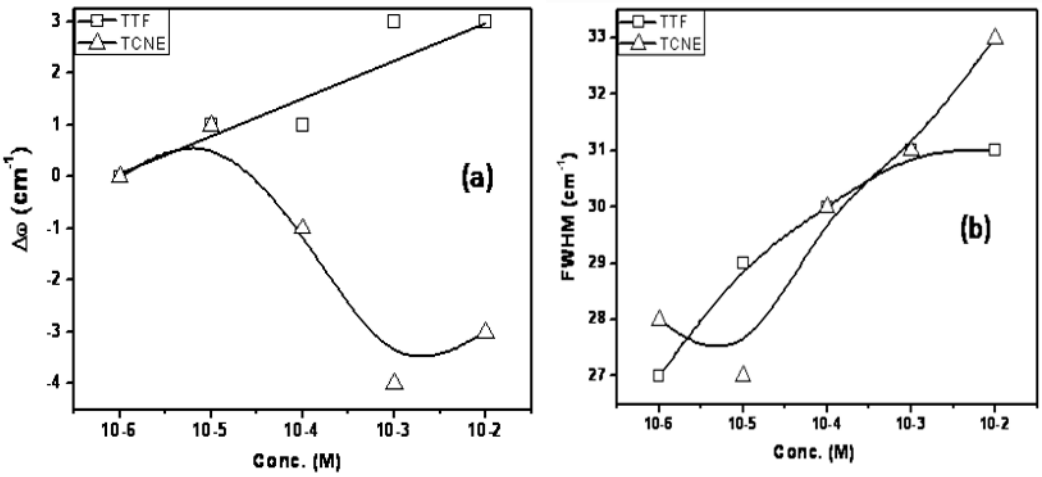

Figure 6. (a) Raman shifts of the G-band of NG on interaction with varying concentrations of TTF and TCNE. (b) Change in the FWHM of the G-band with the concentration of TTF and TCNE. The curves are drawn as guides to the eye.

In Figure 6(a) we show the variation of the G-band position of NG on interaction with TTF and TCNE. The G-band softens on interaction with TCNE and stiffens in the case of TTF. It is significant that TTF and TCNE shows opposite trends of the shifts of G-band. Undoped graphene shows stiffening of the G-band with TCNE and softening with TTF. This behavior of NG with TCNE is exactly opposite to that of BG. This is understandable since NG is electron doped while BG is hole doped. The FWHM of the G-band increases on

interaction with both TTF and TCNE as shown in Figure 6(b), the effect of TCNE being slightly larger. The 2D band of NG shows opposite trends of the shifts on interaction with TTF and TCNE, the directions being similar to those of the G-band as shown in Figure 7 (a). The I_{2D}/I_G ratio decreases sharply on interaction with these molecules (Figure 7 (b)).

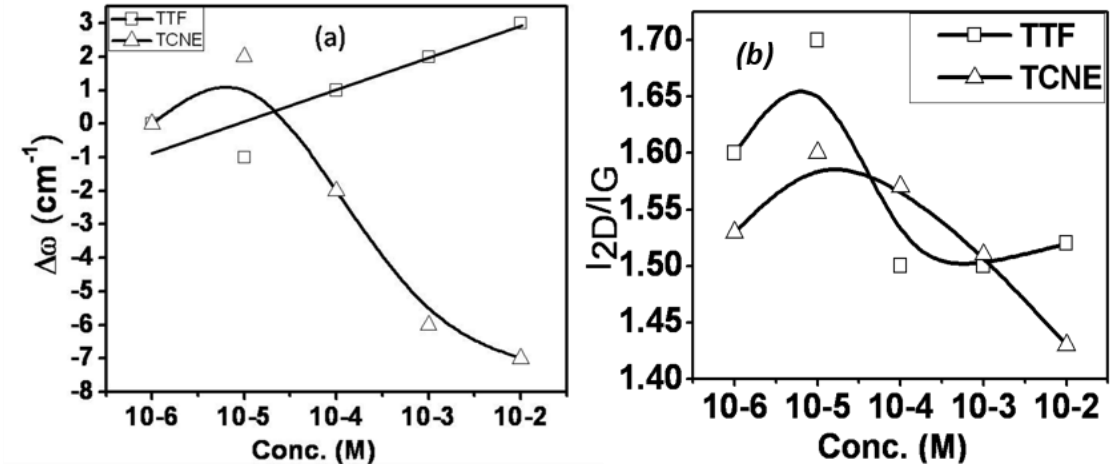

Figure 7 (a) Raman shifts of the 2D band of NG on interaction with TTF and TCNE. (b)The ratio of the relative intensities of the 2D and G-bands with varying the concentrations of TTF and TCNE. The curves are drawn as guides to the eye.

It is noteworthy that B- and N-doped graphenes show differences in the Raman spectral changes on interaction with electron-donor and -acceptor molecules. Thus, BG shows a much greater stiffening of the G-band on interaction with TCNE compared to TTF. The change in the FWHM value is in opposite directions. NG shows softening of the G-band with TCNE and slight stiffening with TTF. The FWHM values, however, show similar changes. The 2D band softens significantly on interaction of BG with TTF and a negligible change with TCNE. NG, on the other hand, shows significant softening of the G-band with TCNE and a little stiffening with TTF. The 2D band of NG becomes somewhat narrower on interaction with TTF and TCNE. That BG and NG show distinctly different Raman shifts due to molecular charge-transfer with donor and acceptor molecules is consistent with the fact that these graphenes have p-type and n-type character respectively. It is gratifying that Raman spectroscopy is such a fine probe to monitor minor changes in the electronic structure of the lightly doped graphenes, brought about

by molecular charge-transfer (see Scheme I). A complete understanding of the nature of charge-transfer induced changes in the Raman spectra requires theoretical study.

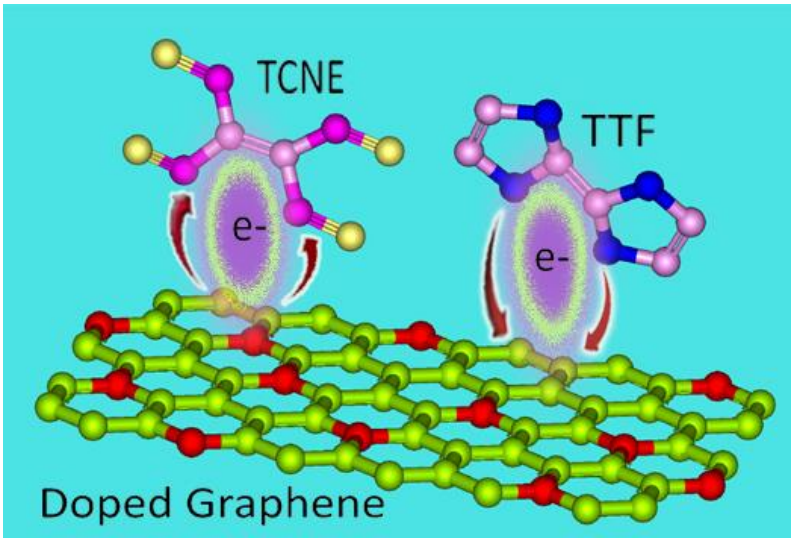

Scheme I. Interaction of electron-donor (TTF) and -acceptor molecule (TTF) with chemically doped graphene.

The changes in the Raman spectra of chemically doped graphenes observed on interaction with electron donor and acceptor molecules reflect the changes in the electronic structure on electron-phonon interaction. The G-band is a doubly degenerate phonon mode (E_g) of the sp^2 carbon network and stiffening of this band arises from the non-adiabatic removal of Kohn anomaly at Γ-point. Broadening of the G-band occurs due to the absence of blockage of the decay channels of the phonons into electron-hole pairs. Changes in the Raman spectrum by molecular doping would involve local structural changes and inhomogeneities arising from the interaction of the adsorbed molecules and randomness in the position, in addition to the changes in the Fermi energy caused by the charge transfer. These different channels of interaction of the donor and acceptor molecules can have effects on the G-band frequency of graphene that are opposite in sign, which is further effected by chemical doping of graphene. It is clear that interaction of electron donating molecules such as TTF (n-type doping) is weaker than that of electron accepting molecules such as TCNE (p-type doping). Thus, TCNE would have greater effect on the G-band frequency as reflected in a larger shift in the Fermi energy. Dynamical

corrections to the G-band frequency dominate in this case, compensating the effects of opposite sign arising from any changes in structure. Such effects due to adsorbed molecules are further influenced by chemical doping of graphene. One, would, therefore, expect differences in the effects of molecular charge transfer between N- and B- doped graphenes.

3.2.5 Conclusions

The present study demonstrates that Raman spectra of chemically doped graphenes are sensitive to molecular charge-transfer with electron-donor and acceptor molecules. Not only do nitrogen- and boron-doped graphenes exhibit different changes in the Raman spectra on interaction with these molecules, but also the donor and acceptor molecules themselves have different effects on the Raman spectra of both n- and p-type graphenes.

References

[1] Rao CNR, Sood AK, Subrahmanyam KS, Govindaraj A. Graphene: The New Two-Dimensional Nanomaterial. Angewandte Chemie International Edition. 2009;48:7752-77.

[2] Geim AK, Novoselov KS. The rise of graphene. Nat Mater. 2007;6:183-91.

[3] Lu YH, Chen W, Feng YP, He PM. Tuning the Electronic Structure of Graphene by an Organic Molecule. J Phys Chem B. 2009;113:2-5.

[4] Novoselov KS, Geim AK, Morozov SV, Jiang D, Zhang Y, Dubonos SV, et al. Electric Field Effect in Atomically Thin Carbon Films. Science. 2004;306:666-9.

[5] Park C-H, Yang L, Son Y-W, Cohen ML, Louie SG. Anisotropic behaviours of massless Dirac fermions in graphene under periodic potentials. Nat Phys. 2008;4:213-7.

[6] Zhou SY, Gweon GH, Fedorov AV, First PN, de Heer WA, Lee DH, et al. Substrate-induced bandgap opening in epitaxial graphene. Nat Mater. 2007;6:770-5.

[7] Chen JH, Jang C, Adam S, Fuhrer MS, Williams ED, Ishigami M. Charged-impurity scattering in graphene. Nat Phys. 2008;4:377-81.

[8] Wehling TO, Novoselov KS, Morozov SV, Vdovin EE, Katsnelson MI, Geim AK, et al. Molecular Doping of Graphene. Nano Lett. 2008;8:173-7.

[9] Ferrari AC, Meyer JC, Scardaci V, Casiraghi C, Lazzeri M, Mauri F, et al. Raman Spectrum of Graphene and Graphene Layers. Phys Rev Lett. 2006;97:187401.

[10] Gupta A, Chen G, Joshi P, Tadigadapa S, Eklund. Raman Scattering from High-Frequency Phonons in Supported n-Graphene Layer Films. Nano Lett. 2006;6:2667-73.

[11] DasA, PisanaS, ChakrabortyB, PiscanecS, Saha SK, Waghmare UV, et al. Monitoring dopants by Raman scattering in an electrochemically top-gated graphene transistor. Nat Nano. 2008;3:210-5.

[12] Das A, Chakraborty B, Piscanec S, Pisana S, Sood AK, Ferrari AC. Phonon renormalization in doped bilayer graphene. Phys Rev B. 2009;79:155417.

[13] Lee C, Wei X, Kysar JW, Hone J. Measurement of the Elastic Properties and Intrinsic Strength of Monolayer Graphene. Science. 2008;321:385-8.

[14] Wang X, Li X, Zhang L, Yoon Y, Weber PK, Wang H, et al. N-Doping of Graphene Through Electrothermal Reactions with Ammonia. Science. 2009;324:768-71.

[15] Rakesh V, Barun D, Chandra Sekhar R, Rao CNR. Effects of charge transfer interaction of graphene with electron donor and acceptor molecules examined using Raman spectroscopy and cognate techniques. J Phys Cond Mat. 2008;20:472204.

[16] Ghosh A, Rao KV, George SJ, Rao CNR. Noncovalent Functionalization, Exfoliation, and Solubilization of Graphene in Water by Employing a Fluorescent Coronene Carboxylate. Chem Euro J. 2010;16:2700-4.

[17] Kim J, Cote LJ, Kim F, Huang J. Visualizing Graphene Based Sheets by Fluorescence Quenching Microscopy. J Am Chem Soc. 2010;132:260-7.

[18] Xie L, Ling X, Fang Y, Zhang J, Liu Z. Graphene as a Substrate To Suppress Fluorescence in Resonance Raman Spectroscopy. J Am Chem Soc. 2009;131:9890-1.

[19] Das B, Voggu R, Rout CS, Rao CNR. Changes in the electronic structure and properties of graphene induced by molecular charge-transfer. Chem Comm. 2008:5155-7.

[20] Subrahmanyam KS, Panchakarla LS, Govindaraj A, Rao CNR. Simple Method of Preparing Graphene Flakes by an Arc-Discharge Method. J Phys Chem C. 2009;113:4257-9.

[21] Panchakarla LS, Subrahmanyam KS, Saha SK, Govindaraj A, Krishnamurthy HR, Waghmare UV, et al. Synthesis, Structure, and Properties of Boron- and Nitrogen-Doped Graphene. Adv Mater. 2009;21:4726-30.

PART 4

REVERSIBLE CHEMICAL STORAGE OF HALOGENS IN FEW-LAYER GRAPHENE

"Graphene is shown to be good chemical storage material for halogens."

PART 4

REVERSIBLE CHEMICAL STORAGE OF HALOGENS IN FEW-LAYER GRAPHENE

Summary*

Few-layer graphene can be chlorinated up to 56 wt. % by irradiation with UV light in liquid chlorine medium. Spectroscopic studies reveal the presence of sp^3 C-Cl bonds in the chlorinated graphenes. They, however, decompose readily on heating to 500 °C or on irradiation with UV or laser radiation releasing all the chlorine. Laser-induced dechlorination of graphene showed appreciable photothermal effects. Similarly, we could brominate few-layer graphene up to 25 wt. % wherein the sp^3 C-Br bond dissociates on heating to 500 ^oC giving out bromine. The present study shows the possible use of few-layer graphene for chemical storage of halogens.

* A paper based on this work has been published in *RSC Adv.* 2012, **2**, 1605-1608 and *Macromol. Chem. Phys.* 2012, **213**, 1146–1163

4.1.1 Introduction

Halogens are notable as being the only group in the periodic table (Group 17) in which the elements exist in all three states of matter at room temperature. In ascending order of size, the halogens are fluorine, chlorine, bromine, iodine and astatine [1]. All of the halogens exist as diatomic molecules when pure elements. Fluorine and chlorine are gaseous and more toxic than other halogens and are stored in containers with great complexity and these containers may burst when exposed to elevated temperatures. Fluorine and chlorine can react with and corrode some forms of rubber and metal coatings. Fluorine is problematic, as the element will react with most other materials. Even storage materials like glass can react with fluorine and create dangerous results. Bromine is a liquid at standard temperature and pressure, and so storage and transport doesn't involve the same level of hazard as the gaseous halogens. Iodine is a solid at standard conditions and less dangerous than the other halogens and storing is very easy. Astatine is a solid and is considered the rarest substance in Earth. There is only a tiny amount in existence, unlike the other four halogens that are produced in much larger quantities due to their large applications.

Chlorine will combine directly with almost all other elements. Large amounts are used yearly for making chlorinated organic compounds, bleaches, and inorganic compounds. Organic compounds, ones which have a skeleton of carbon atoms bonded to each other, can contain halogen atoms connected to the carbon atoms. Low molecular weight organic chlorine compounds are liquids and are good solvents for many purposes. They dissolve starting materials for chemical reactions, and are effective for cleaning such different items as computer parts and clothing (dry cleaning). These uses are now being phased out because of problems that the compounds cause in Earth's atmosphere.

Halogens have variety of applications; chlorine containing organic polymers are also widely employed. Polymers are large molecules made of many small units that hook together. One is polyvinyl chloride (PVC), from which plastic tubings and many other plastic products are made. Neoprene is a synthetic rubber made with another chlorine-

containing polymer. Neoprene is resistant to the effects of heat, oxidation, and oils, and so is widely used in automobile parts.

Many medicines are organic molecules containing chlorine, and additional chlorine compounds form intermediate steps in the synthesis of a variety of others. Most crop protection chemicals, herbicides, pesticides, and fungicides have chlorine in them. Freon refrigerants are chlorofluorocarbons (CFCs). These perform well because they are volatile, that is they evaporate easily, but they are not flammable. Freon 12, one of the most common, is CCl_2F_2 two chlorine atoms and two fluorine atoms bonded to a carbon atom.

Chlorine is part of several compounds, such as the insecticide DDT, that are soluble in fats and oils rather than in water. These compounds tend to accumulate in the fatty tissues of biological organisms. Some of these compounds are carcinogens, substances that cause cancer. DDT and other pesticides, polychlorinated biphenyls (PCBs), and dioxins are substances that are no longer manufactured. However, they are still present in the environment, and disposal of materials containing these compounds is a problem.

The next heaviest element in the halogen family is bromine, named from a Greek word for stink, because of its strong and disagreeable odour. It was first isolated as an element in 1826. Bromine is a reddish-brown liquid that vaporizes easily. The vapours are irritating to the eyes and throat. Elemental bromine is made by oxidation, removal of electrons from bromide ions in brine. Brines in Arkansas and Michigan are fairly rich in bromide. Other worldwide sources are the Dead Sea and ocean water. There are a variety of applications for bromine compounds. The major use at one time was in ethylene dibromide, an additive in leaded gasoline. This need has declined with the phase-out of leaded fuel. Several brominated organic compounds have wide utilization as pesticides or disinfectants. Currently, the largest volume organic bromine product is methyl bromide, a fumigant. Some medicines contain bromine, as do some dyes. Halons, or halogenated carbon compounds, have been utilized as flame retardants. The most effective compound containing bromine, for example, halon 1301 is $CBrF_3$. Inorganic bromine compounds function in water sanitation and silver bromide is used in photographic film. Bromine also appears in quartz-halide light bulbs.

Storage of halogens: Though halogens have a variety of applications storing is a major issue. Since chlorine is a harmful gas, it must be stored in a sealed container. Chlorine gas which is gaseous at ordinary temperatures, generally stored in a special cylinder. For the purpose of overcoming storing difficulty, methods other than the techniques for directly liquefying the halogen are being researched. Heretofore, there has been used one method in which the halogen is converted into a complex compound with an amine and is stored in a liquid state [2], and another method (a hydrate method) in which has been cooled to several degrees centigrade or less and is stored in the form of a solid hydrate such as $Cl_2.6H_2O$ or $Br_2.10H_2O$ [3]. These methods involve reactions such as complexing reactions and hydrating reactions, and thus in these cases, to form and decompose a complex or hydrate heat energy corresponding to the heat of each reaction mush be eliminated from the system. As for the hydrate method, the halogen cannot be stored securely, unless solid hydrate continuously maintained in a cold state during the storage.

Antimony pentachloride **is** used as a storage material for chlorine chemically. It is prepared by passing chlorine gas into molten antimony trichloride.

$$SbCl_3 + Cl_2 \rightarrow SbCl_5$$

It liberates chlorine when heated to 300 ^oC.

$$SbCl_5 \rightarrow SbCl_3 + Cl_2\uparrow$$

Even phosphorous pentachloride also used as storage material for chlorine.

Graphene, a new storage material: Single and few few-layer graphene attracted attention as promising storage media [4]. Graphene is a lightweight, chemically stable and exhibits attractive physico-chemical properties for hydrogen adsorption. Theoretical studies regarding chemically modified graphene suggest that it can absorb up to 8 wt. % of hydrogen, which is close to the objectives of the US Department of Energy for hydrogen storage (9 wt% by 2015). For practical use as a storage medium, hydrogen should be released when needed, possibly without heating the device to high temperatures (several hundred centigrade).

Recently, Rao et al [4] showed that Birch-reduction of few-layer graphene gives rise to hydrogenated graphene containing up to 5 wt. % of hydrogen. Interestingly, hydrogenated graphene decomposes on heating up to 500 ^oC or on laser irradiation,

releasing all the hydrogen. This result demonstrates that the sp^3 C-H bond of hydrogenated graphene can be considered to act as a reversible chemical storage of hydrogen. Reversible fluorination of graphene has also been reported by Zhu et al [5].

4.1.2 Scope of the present investigations

Storage of chlorine in high pressure cylinders and tanks is well known. It will be interesting if there is an alternative way of storing chlorine. They are few ways of storing halogens like hydrate method or by making complexes with amines. These methods have their own demerits. Recently, graphene, a noble material has found to be a good candidate for storing hydrogen. Interestingly, hydrogenated graphene decomposes on heating up to 500 ^oC or on laser irradiation, releasing all the hydrogen. This shows that the sp^3 C-H bond of hydrogenated graphene can be considered to act as a reversible chemical storage of hydrogen. In the light of this observation, we felt that it would be of interest to carry out chlorination of graphene and examine the nature of the chlorinated product. It would be interesting to explore whether chlorinated graphene decomposes on heating or on laser irradiation. When excimer laser is irradiated upon chlorinated graphene the C-Cl bond is cleaved to give back graphene. Such photoinitiated chemical transformations are exothermic in nature and therefore release heat. Such heat can be measure from the rise of temperature of the solution. We have therefore carried out chlorination of graphene and examined the stability of the chlorinated product. We have also carried out a similar study on the bromination of graphene.

4.1.3 Experimental section

Synthesis of Few-layer graphene: Few-layer graphene (G) was prepared by the arc evaporation of graphite in a water-cooled stainless steel chamber filled with a mixture of hydrogen (200 Torr) and helium (500 Torr) without using any catalyst [6]. In a typical experiment, a graphite rod (Alfa Aesar with 99.999% purity, 6 mm in diameter and 50 mm long) was used as the anode and another graphite rod (13 mm in diameter and 60 mm in length) was used as the cathode. The arc-discharge current (during the

evaporation of anode) was in the 100-150 A range, with a maximum open circuit voltage of 60 V. The graphene obtained by this method contains 2-4 layers.

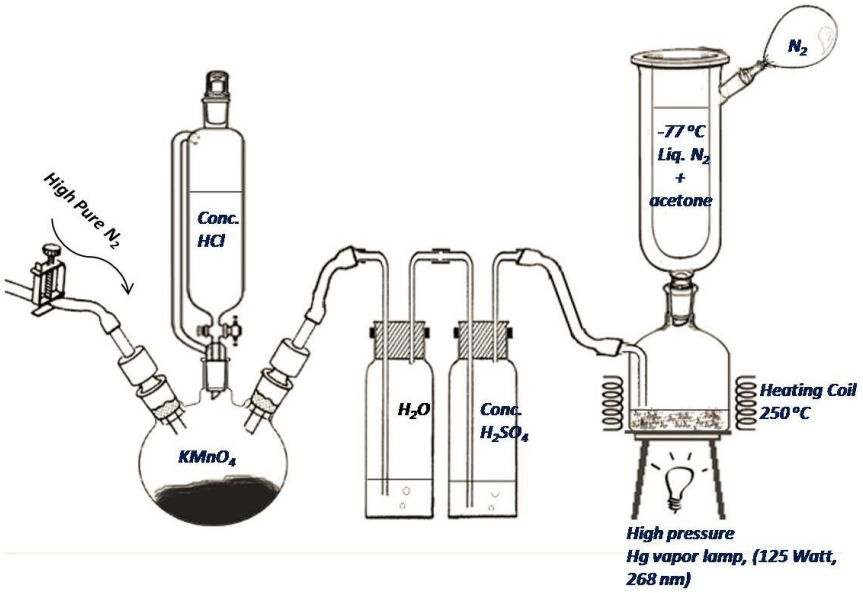

Figure 1. Experimental setup used for chlorination of graphene

Synthesis of chlorinated graphene (G-Cl): Graphene (15 mg) was taken in 30 mL of carbon tetrachloride (spectroscopic grade) and sonicated for 20 min using an ultrasonicator. The suspension obtained was transferred to a 500 mL quartz vessel which was fitted with a condenser maintained at -77 ^{o}C. The reaction chamber was purged with high pure nitrogen (99.9999%) for 30 min and chlorine gas was passed through the chamber. The gaseous chlorine condensed in the quartz vessel (see Figure 1). The quartz vessel containing around 20 mL of liquid chlorine was heated to 250 ^{o}C with simultaneous irradiation of UV light (Philips 250 Watt High pressure Hg vapor lamp) for 1.5 h. The solvent and excess chlorine was removed, leaving a transparent film on the walls of the quartz vessel. The solid was dispersed in absolute alcohol under ultrasonication, filtered and washed with distilled water and absolute alcohol. The filtrate was then re-dispersed in 40 ml of distilled water, ultrasonicated for 2 min and centrifuged. The black supernatant obtained was separated and filtered using a polyvinylidene fluoride (PVDF) membrane (200 nm pore size). The yield from 15 mg graphene sample was around 3-4 mg.

Synthesis of brominated graphene (G-Br): In the case of bromination, 12 mg of graphene was taken in the quartz vessel, to which 20 mL of liquid bromine was added. The mixture was sonicated for 10 min using an ultrasonicator. To this 0.5 g of carbon tetrabromide was added. The quartz vessel was then heated to 250 ^{o}C with simultaneous irradiation of UV light just as in chlorination. The excess bromine was removed and the product washed with sodium thiosulphate. The solid residue was then washed with water and absolute alcohol several times to remove sodium thiosulphate and then dispersed in 40 mL distilled water and centrifuged. The black supernatant obtained was separated and filtered using a PVDF membrane (200 nm pore size). The yield from 12 mg sample was around 2-3 mg.

Photothermal experiment: Chlorinated graphene (3 mg) was dispersed in CCl_4 and taken in a quartz vessel. The solution was irradiated using the set up show in Figure 2. The temperature of the solutions is recorded every minute using a thermal sensor and this was continued for 45 min. Lambda physik KrF excimer laser (λ = 248 nm, τ = 30 ns, rep. rate = 5 Hz) was employed for this purpose. It is necessary to have a good dispersion of the graphene material in the solvent in order to spread the heat uniformly throughout the solution. Solvents to might get heated on laser radiation. It is, therefore, necessary to measure separately the effect of irradiation the solvent alone.

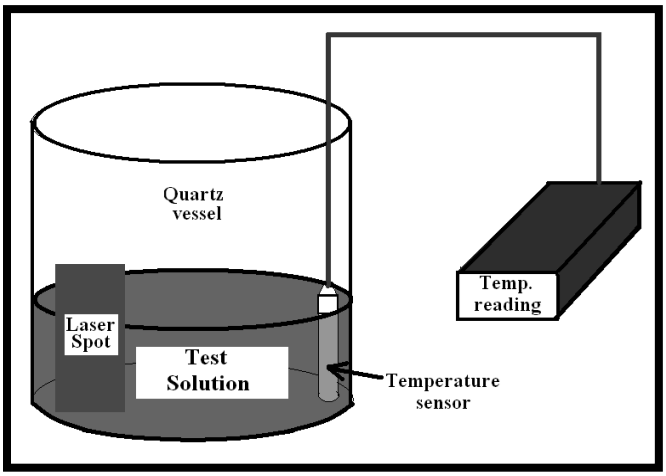

Figure 2. Photothermal experiment setup

4.1.4 Results and discussion

We have carried out halogenation studies on few-layer graphene since the presence of more than one layer is expected to favor the hydrogenation reaction.[3] We have used graphene samples with 2-4 layers for the present study. The graphene (G) sample was characterized by employing transmission electron microscopy (TEM), atomic force microscopy (AFM), X-ray photoelectron spectroscopy (XPS), Raman spectroscopy and infrared spectroscopy. Brunauer-Emmett-Teller (BET) surface area of the graphene was around 200 m^2/g. The Raman spectrum show the characteristic D (1323 cm^{-1}), G (1568 cm^{-1}) and 2D (2641 cm^{-1}) bands [6, 7]. The D and D'-bands are defect-induced features and are absent in defect-free samples. The G-band corresponds to the E_{2g} mode of graphene and arises from the vibration of sp^2 bonded carbon atoms. The 2D band originates from second order double resonant Raman scattering and varies with the number of layers.

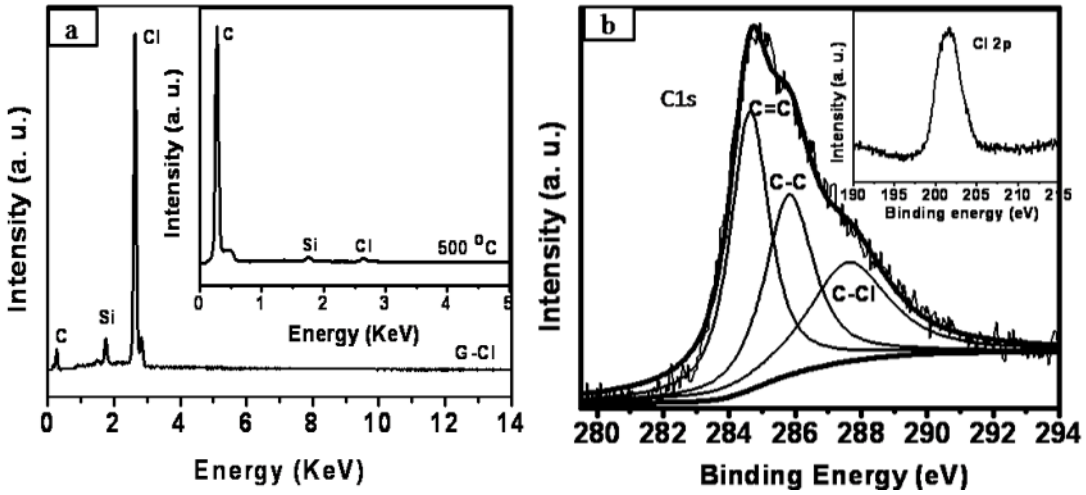

Figure 3 (a) EDAX spectrum of chlorinated graphene (G-Cl). Inset shows the EDAX spectrum after heating G-Cl at 500 °C for 4 h. (b) C1s core level XP spectrum of G-Cl. Inset shows the Cl 2p signal in XPS.

Chlorination of graphene was carried out by irradiation with UV light in liquid chlorine medium and the product examined by various techniques mentioned earlier. We show typical EDAX analysis of a chlorinated sample (G-Cl) in Figure 3(a). We could chlorinate graphene by this means up to 56 wt. % (30 at. %). It should be noted that

maximum possible chlorination 74.7 wt. %. We have estimated the composition of G-Cl by employing XPS (Figure 3(b)) as well. The X-ray photoelectron (XP) spectrum shows a is signal around 284.6 eV, assigned to C 1s and features due to chlorine 2p at 201.2 eV (see inset of Figure 3 (b)). Deconvolution of the C1s feature could be carried with three features centered at 284.6, 285.8 and 287.6 eV corresponding to sp^2 hybridized carbon, sp^3 hybridized carbon and C-Cl respectively. The composition of the sample was determined by the ratio of C-Cl peak intensity in Cl 2p to the C1s peak intensity taking into account the atomic sensitivity factors of Cl 2p and C 1s. This gave an estimate of 30 at. % of chlorine in agreement with EDAX analysis.

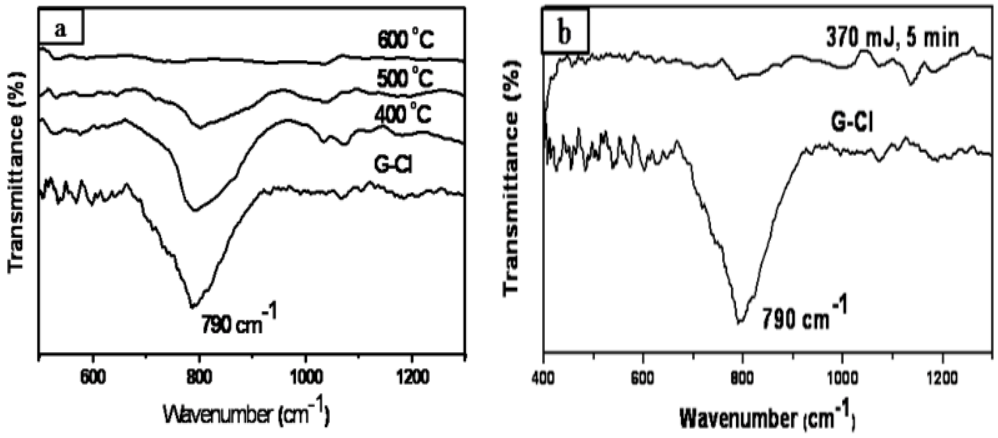

Figure 4(a) IR spectra of G-Cl heated for 4h at 400 °C, 500 °C and 600 °C. (b) IR spectra of G-Cl and G-Cl subjected to laser radiation (370 mJ, 5 min).

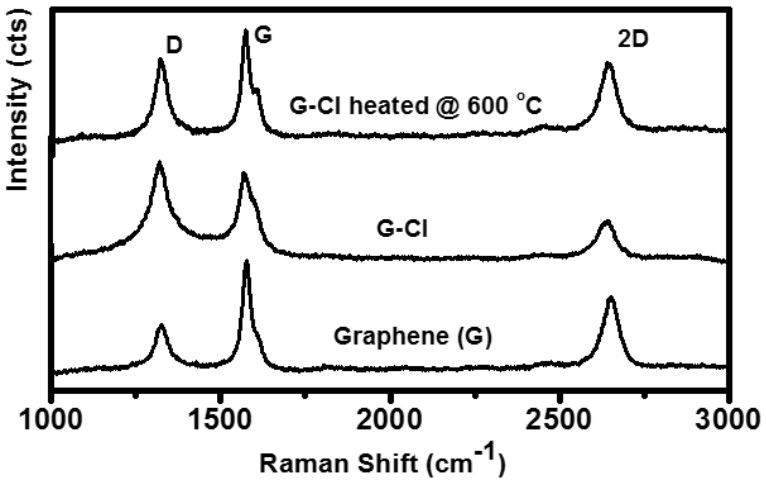

Figure 5. Raman spectra of graphene (G), chlorinated graphene (G-Cl) and G-Cl heated at 600 ^{o}C

The infrared spectrum of the chlorinated sample shows a band at 790 cm^{-1} due to the C-Cl stretching vibration as shown in Figure 4 (a) [8]. Thermogravimetric analysis supports the EDAX and XPS results. The chlorinated graphene (G-Cl) sample is stable under ambient condition and can be stored for long periods. We have examined the thermal stability of G-Cl in detail. In Figure 4(a), we show the infrared spectra of the chlorinated sample heated to different temperatures. We observe a decrease in C-Cl band intensity on heating progressively and completely disappears above 500 ^{o}C. In Figure 5 we show the Raman spectra of graphene (G), chlorinated graphene (G-Cl) and G-Cl heated at 600 ^{o}C. The Raman spectrum of the chlorinated sample shows an increase in the intensity of the D band relative to that of the G-band. On chlorination, due to the C-Cl sp^3 bond formation and breaking of C=C sp^2 translational symmetry, intensity of D band increases and 2D band decrease, thus resulting in increased defects in graphene lattice (due to sp^3 C-Cl bond formation). The Raman data of graphene and functionalized graphene is given in Table 1.

Table 1. The Raman data of graphene and functionalized graphene

Sample	**D band (cm^{-1})**	**G-Band (cm^{-1})**	**2D band (cm^{-1})**	**I_D/I_G**	**I_{2D}/I_G**
Graphene	1323	1568	2649	0.4	0.6
G-Cl	1320	1569	2645	1.1	0.4
G-Cl at 600 ^{o}C	1323	1571	2644	0.7	0.6

In Figure 6 we show the loss of chlorine from the chlorinated graphene with increase in temperature. The EDAX spectrum of the sample heated to 500 ^{o}C also shows the disappearance of the chlorine signal (see inset of Figure 3 (a)). Clearly all the chlorine is eliminated on heating G-Cl to 500 ^{o}C.

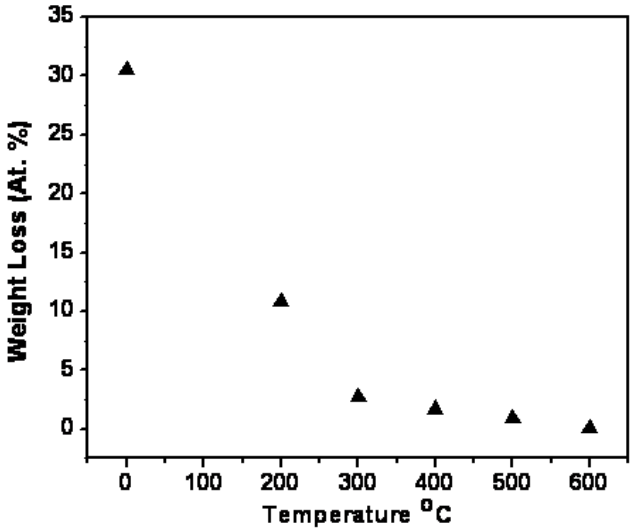

Figure 6. Loss of chlorine from chlorinated graphene with increase in temperature

We could also remove chlorine in G-Cl on irradiation with a laser (Lambda physik KrF excimer laser (λ = 248 nm, τ = 30 ns, rep. rate = 5 Hz, laser energy = 370 mJ)). We show the effect of laser irradiation in Figure 4 (b) which shows the absence of the C-Cl stretching band in the infrared spectrum on irradiation for 5 min. Dechlorination by laser irradiation shows photothermal effect. Thus, G-Cl dispersed in carbon tetrachloride shows an increase in temperature by 26 °C on irradiation (Figure 7).

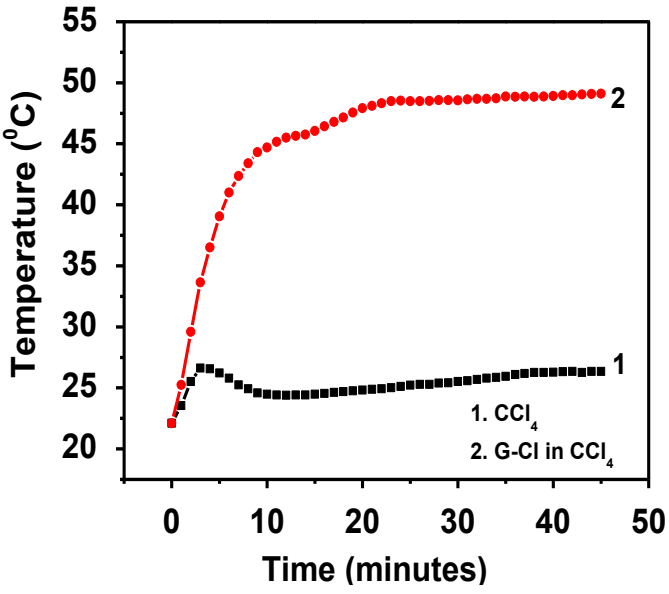

Figure 7. Changes in temperature of the solution with laser irradiation time for chlorinated graphene (G-Cl*)*

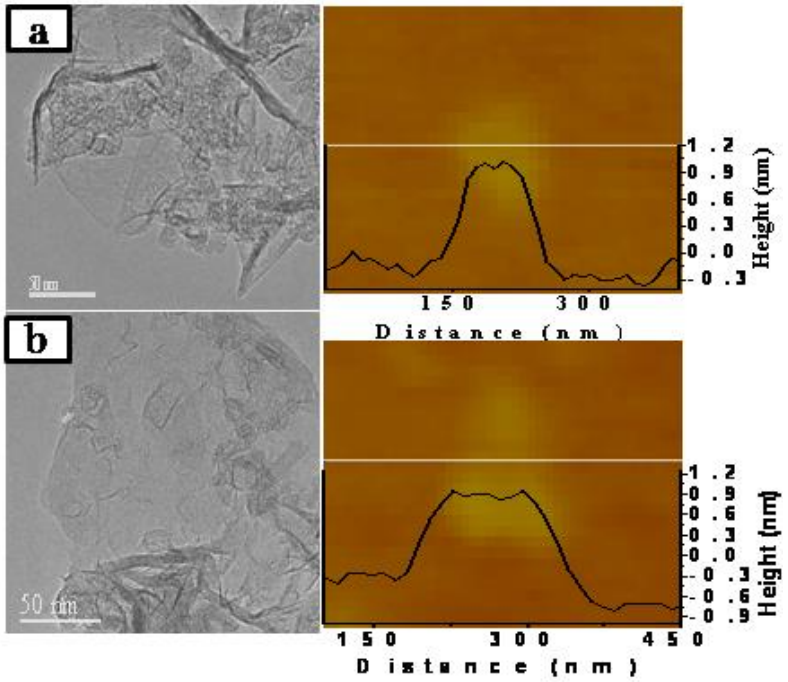

Figure 8. TEM images of (a) graphene and (b) dechlorinated graphene. AFM images of these samples are shown alongside

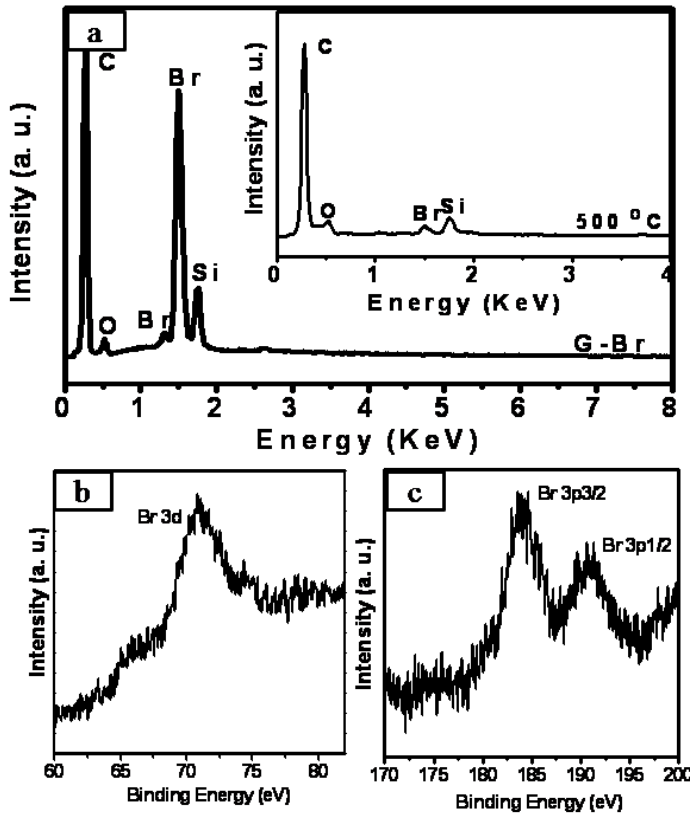

Figure 9 (a) EDAX spectrum of brominated graphene (G-Br). Inset shows the EDAX spectrum after heating at 500 °C for 4 h. Core level XP spectra of G-Br show (b) Br 3d and (c) Br 3p signals.

Interestingly, the nature of graphene was not affected on chlorination and dechlorination. In Figure 8 we compare the TEM images of the starting graphene sample and of the dechlorinated sample. AFM images of the two samples are also comparable. The dechlorinated samples can be chlorinated again satisfactorily. We have also carried out bromination of graphene. Figure 9 (a) shows a typical EDAX spectrum of graphene (G-Br) containing 25 wt. % (4.8 at. %). XPS analysis of the brominated sample shows Br 3d, $3p^{3/2}$ and $3p^{1/2}$ features at 70.9, 183.9 and 190.8 eV respectively as shown in Figures 9 (b) and (c). Bromine in the samples could be eliminated to heating at 500 ^{o}C as evidenced by the EDAX spectrum given in the inset of Figure 9 (a).

4.1.5 Conclusions

The present study demonstrates that one can achieve chlorination of few-layer graphene at least up to 56 wt. % by UV irradiation in liquid-chlorine medium. It may be possible to attain higher chlorine content by other means. The chlorinated graphene consists of sp^3 C-Cl bonds which are stable at room temperature. However, the chlorine can be removed on heating to around 500 ^{o}C or by laser irradiation. Clearly, dechlorination is associated with a small barrier just as the decomposition of hydrogenated graphene. The strain in the chlorinated sample appears to drive the dechlorination to form the more stable graphene. It is noteworthy that chlorination of graphene is reversible. The present study demonstrates that few-layer graphene can be used to store chlorine and bromine.

References

[1] Cotton. Advanced Inorganic Chemistry, 6th Edition. 1999:1376.

[2] Popov AI, Rygg RH. Studies on the Chemistry of Halogens and of Polyhalides. XI. Molecular Complexes of Pyridine, 2-Picoline and 2,6-Lutidine with Iodine and Iodine Halides1. J Am Chem Soc. 1957;79:4622-5.

[3] Carr P. Inert gas rejection system for metal halogen batteries. Google Patents; 1983.

[4] Subrahmanyam KS, Kumar P, Maitra U, Govindaraj A, Hembram KPSS, Waghmare UV, et al. Chemical storage of hydrogen in few-layer graphene. PNAS. 2011;108:2674-7.

[5] Tang S, Zhang S. Structural and Electronic Properties of Hybrid Fluorographene–Graphene Nanoribbons: Insight from First-Principles Calculations. J Phys Chem C. 2011;115:16644-51.

[6] Subrahmanyam KS, Panchakarla LS, Govindaraj A, Rao CNR. Simple Method of Preparing Graphene Flakes by an Arc-Discharge Method. J Phys Chem C. 2009;113:4257-9.

[7] Rao CNR, Sood AK, Subrahmanyam KS, Govindaraj A. Graphene: The New Two-Dimensional Nanomaterial. Angewandte Chemie International Edition. 2009;48:7752-77.

[8] C. N. R. Rao. Chemical Applications of Infrared Spectroscopy.Academic Press, New York, 1963.

.